HYDRODYNAMIC SCALING AND SOLIDS MIXING IN PRESSURIZED BUBBLING FLUIDIZED BED COMBUSTORS

by

Paul A. Farrell

M.S. Mech. Engr., The Pennsylvania State University (1990)
B.S. Mech. Engr., University of Notre Dame (1988)

Submitted to the Department of
Mechanical Engineering in Partial
Fulfillment of the Requirements
for the Degree of

Doctor of Philosophy in Mechanical Engineering

at the

MASSACHUSETTS INSTITUTE OF TECHNOLOGY

June 1996

Signature of Author_____
Department of Mechanical Engineering
May 21, 1996

Certified by_____
Leon R. Glicksman
Professor, Department of Mechanical Engineering
Thesis Supervisor

Accepted by_____
Ain A. Sonin
Chairman, Departmental Committee on Graduate Studies
Department of Mechanical Engineering

HYDRODYNAMIC SCALING AND SOLIDS MIXING IN PRESSURIZED BUBBLING FLUIDIZED BED COMBUSTORS

by

Paul A. Farrell

Submitted to the Department of Mechanical Engineering
on May 21, 1996 in Partial Fulfillment of
the Requirements for the Degree of Doctor of Philosophy in
Mechanical Engineering

ABSTRACT

A quarter-scale cold model of American Electric Power's 70 MW_e Tidd pressurized fluidized bed combustor (PFBC) has been constructed based on a simplified set of scaling parameters. Time-varying pressure drop data from the hot combustor and the cold model were used to compare the hydrodynamics of the two beds. Excellent agreement between the dimensionless probability density functions, the mean solid fraction profiles, and the bed expansions, provide a verification of the scaling parameters for commercial bubbling PFBC.

Some controversy has surrounded the importance of matching the solid-to-gas density ratio when scaling bubbling beds. Hydrodynamic scaling comparisons were conducted with all the scaling parameters matched with the exception of the density ratio. The comparisons indicate that to reliably scale the hydrodynamics of bubbling beds it is essential to match the solid-to-gas density ratio.

Bubbles provide the motive force for solids mixing in bubbling fluidized beds, prompting an investigation of the bubble characteristics in the cold model of the Tidd PFBC. A unique optical bubble probe design was used to measure bubble rise velocities, mean pierced lengths, and bubble frequency. Gas through-flow and bubble-growth rates appear to be significantly lower in pressurized beds than in atmospheric fluidized beds.

A thermal tracer technique has been implemented in the cold model of the Tidd PFBC. The technique involves thermally tagging bed particles, injecting them into the bed, and tracking their motion using an array of thermistors. The thermal tracer data suggest that the tube bank within the bed restricts solids mixing, making adequate mixing in the tube-free zone at the bottom of the bed of paramount importance. Increasing gas superficial velocity is shown to increase both axial and lateral mixing beneath the tube bank.

A mechanistic model of solids mixing in bubbling fluidized beds has been developed. Axial solids mixing is attributed to bubbles transporting solids vertically as they rise to the surface of the bed, while lateral mixing is associated with the lateral motion of bubbles as

they move to coalesce with neighboring bubbles. Comparisons of model with the thermal-tracer data and data from a previous study are encouraging; reasonable predictions of the data are achieved without adjusting the parameters of the model to fit the data.

Thesis Supervisor: Leon R. Glicksman
Title: Professor of Building Technology and Mechanical Engineering

ACKNOWLEDGMENTS

I would first like to acknowledge Leon Glicksman for giving me the opportunity to study and work at M.I.T.; for this, I am extremely grateful. I would also like to thank him for consistently challenging me and asking difficult questions while simultaneously being supportive and enthusiastic. His insights and guidance have greatly improved the quality of this thesis and of my graduate education.

In many respects, a thesis is a very individual effort, and yet, at least in my case, the opportunity to focus my time and energy on a singular goal was provided by the efforts of my wife, Susan. Susan, while simultaneously completing her own doctoral thesis work, has kept our lives running smoothly, demanding little from me in return. It is only through her sacrifices, both of her time and of the time that I did not spend with her, that this work was possible.

It is rare for a child to have the opportunity to publicly acknowledge the contributions their parents have made to their lives. But in many respects, these contributions lay the foundation on which a child achieves. Hence, I would be remiss if I did not thank both my parents for their guidance and support over the years.

I would like to acknowledge the contributions of my fellow graduate students to my education. In particular, I would like to thank Matt Hyre and Peter Noymer. I would like to thank Matt for being a model and mentor on how to conduct research and for his generous assistance throughout my time at M.I.T. I have learned a great deal about fluidization and many other disciplines as a result of our friendship. I would like to thank Peter for providing me with a forum to test ideas and for his help and suggestions throughout this project. I also would like to acknowledge Peter's contributions to my education as a classmate; the quality of my work was elevated through my collaborations with him.

I would like to thank the other members of my thesis committee–Professors János M. Beér, Peter Griffith, and Ain A. Sonin–for their time and suggestions.

I would like to acknowledge the efforts of individuals from Babcock and Wilcox and American Electric Power who were involved in testing at the Tidd Plant. I would particularly like to thank Tim Fuller of the Babcock & Wilcox, Alliance Research Center for all his efforts.

Finally, I would like to gratefully acknowledge the financial support of the U. S. Department of Energy through the Morgantown Energy Technology Center (Cooperative Agreement No. DE-FC21-92MC29264).

TABLE OF CONTENTS

ABSTRACT 3

ACKNOWLEDGMENTS 5

CHAPTER 1

1. INTRODUCTION 19

1.1 BACKGROUND 20

1.1.1 Advantages of Fluidized Bed Combustors 20

1.1.2 Pressurized Fluidized Bed Combustors (PFBC) 21

1.1.3 Regimes of Fluidization 23

1.2 THESIS RESEARCH OBJECTIVES AND MOTIVATION 24

1.2.1 Hydrodynamic Scaling 24

1.2.2 Solids Mixing in Pressurized Bubbling Fluidized Beds 26

1.3 ORGANIZATION OF THESIS 27

1.4 REFERENCES 29

CHAPTER 2

2. REVIEW OF FLUIDIZED BED HYDRODYNAMIC SCALING 31

2.1 OVERVIEW OF WORK RELATED TO HYDRODYNAMIC SCALING 31

2.2 DIMENSIONAL ANALYSIS AND SIMILARITY 31

2.2.1 Buckingham Pi Theorem 32

2.2.1.1 Buckingham Pi Theorem Procedure 32

2.2.1.2 Application of Buckingham Pi to Fluidized Bed Hydrodynamics 35

2.2.2 Nondimensionalization of Governing Equations and Boundary Conditions 36

2.2.3 Similarity 37

2.3 DEVELOPMENT OF HYDRODYNAMIC SCALING PARAMETERS 38

2.3.1 Two-Fluid Modeling 38

2.3.2 Governing Equations 39

2.3.3 Full Set of Scaling Parameters 42

2.3.3.1 Nondimensionalization of the Governing System 43

2.3.4 Simplifications to the Full Set of Scaling Parameters 46

2.3.4.1 Motivation for Pursuing Simplifications 47

2.3.4.2 Simplified Set of Scaling Parameters 49

2.3.4.3 Evaluation of the Error Due to the Simplifications 50

2.4 EXPERIMENTAL VERIFICATION OF THE HYDRODYNAMIC SCALING PARAMETERS 51

2.4.1 Bubbling Fluidized Beds 57

2.4.2 Circulating Fluidized Beds 62

2.5 NOMENCLATURE 67

2.6 REFERENCES 68

CHAPTER 3

3. EXPERIMENTAL SETUP FOR HYDRODYNAMIC SCALING STUDIES ___ 73

3.1 TIDD PFBC EXPERIMENTAL SETUP ___ 73

3.1.1 Tidd Pressure Measurement Setup ___ 74

3.1.1.1 Tidd Pressure Line Characterization ___ 75

3.1.2 Tidd Data Acquisition System ___ 83

3.2 HYDRODYNAMIC SCALING CALCULATIONS ___ 84

3.2.1 Error in Drag from Using the Simplified Set of Scaling Parameters ___ 91

3.3 MIT COLD MODEL EXPERIMENTAL SETUP ___ 93

3.3.1 Cold Model Pressure Measurement ___ 95

3.3.2 Cold Model Data Acquisition System ___ 96

3.3.3 Cold Model Air Flow Measurement ___ 97

3.4 NOMENCLATURE ___ 99

3.5 REFERENCES ___ 100

CHAPTER 4

4. VERIFICATION OF HYDRODYNAMIC SCALING FOR PFBC ____ 101

4.1 BASIS FOR SCALING COMPARISONS ____ 101

4.2 EXPERIMENTAL DATA ANALYSIS ____ 102

4.2.1 Solid Fraction Calculation ____ 102

4.2.2 Probability Density Function Analysis ____ 104

4.2.3 Power Spectral Density Analysis ____ 106

4.2.3.1 Power Spectral Density ____ 106

4.2.3.2 Filtering to Avoid Aliasing ____ 109

4.3 EXPERIMENTAL TEST PROCEDURES ____ 109

4.3.1 Tidd PFBC Test Procedure ____ 110

4.3.2 MIT Cold Model Test Procedure ____ 111

4.4 EXPERIMENTAL TEST CONDITIONS ____ 111

4.5 HYDRODYNAMIC SCALING COMPARISONS ____ 114

4.5.1 Voidage Comparisons ____ 114

4.5.1.1 Solid Fraction Profile Comparisons ____ 114

4.5.1.2 Bed Expansion Comparisons ____ 115

4.5.2 Probability Density Function Comparisons ____ 117

4.5.3 Frequency Domain Comparisons ____ 120

4.5.3.1 Power Spectral Density Comparisons ____ 120

4.5.3.2 Evaluation of Possible Source of Peaks in Power Spectra ____ 123

4.6 NOMENCLATURE ____ 128

4.7 REFERENCES ____ 130

CHAPTER 5

5. IMPORTANCE OF THE SOLID-TO-GAS DENSITY RATIO FOR SCALING BUBBLING FLUIDIZED-BED HYDRODYNAMICS ____ **133**

5.1 MOTIVATION FOR STUDY ____ 133

5.2 HYDRODYNAMIC SCALING TEST CONDITIONS ____ 135

5.3 EXPERIMENTAL DATA ACQUISITION AND ANALYSIS ____ 139

5.4 EXPERIMENTAL SETUP ____ 140

5.4.1 Bubbling Bed Experimental Setup ____ 140

5.4.2 Bubbling-Slugging Transition Experimental Setup ____ 142

5.5 HYDRODYNAMIC SCALING COMPARISONS ____ 143

5.5.1 Bed Expansion Comparison–u_o/u_{mf}=1.2 ____ 143

5.5.2 Bubbling Bed Scaling Comparisons ____ 144

5.5.3 Effect of Mismatched ρ_s / ρ_g on Bubbling-Slugging Transition ____ 153

5.6 NOMENCLATURE ____ 155

5.7 REFERENCES ____ 156

CHAPTER 6

6. REVIEW OF SOLIDS MIXING IN BUBBLING FLUIDIZED BEDS _____ 159

6.1 INTRODUCTION _____ 159

6.2 BASIC MECHANISMS OF SOLIDS MIXING IN BUBBLING FLUIDIZED BEDS _____ 159

6.2.1 Importance of Bubbles to Solids Mixing _____ 160

6.2.2 Summary of Solids Mixing Mechanisms _____ 163

6.3 SOLIDS MIXING MODELS _____ 164

6.3.1 Diffusion Model _____ 165

6.3.2 Counter-Current Backmixing Model _____ 167

6.4 SOLIDS MIXING EXPERIMENTAL STUDIES _____ 168

6.5 NOMENCLATURE _____ 172

6.6 REFERENCES _____ 173

CHAPTER 7

7. PFBC BUBBLE CHARACTERISTICS ____ 177

7.1 TECHNIQUES FOR MEASURING BUBBLE CHARACTERISTICS ____ 177

7.1.1 Capacitance Probes ____ 177

7.1.2 Optical Probes ____ 178

7.2 OPTICAL BUBBLE PROBE DEVELOPMENT ____ 179

7.2.1 Optical Bubble Probe Construction ____ 179

7.2.2 Bubble Probe Electronics ____ 181

7.2.2.1 Phototransistor Electronics ____ 181

7.2.2.2 Infrared Emitting Diode (IRED) Electronics ____ 184

7.2.3 Evaluation of Bubble Probe Performance ____ 185

7.2.3.1 Relationship Between Output Voltage and Solid Concentration ____ 185

7.2.3.2 Calibration Method ____ 186

7.3 OPTICAL BUBBLE PROBE DATA ANALYSIS ____ 189

7.3.1 Bubble Rise Velocity Determination ____ 189

7.3.2 Setting Bubble Threshold ____ 192

7.3.2.1 Relationship Between Voidage and Bubble Fraction ____ 193

7.3.2.2 Estimation of the Emulsion Voidage, ε_e ____ 194

7.3.2.3 Summary of Procedure for Setting Optical Probe Threshold ____ 204

7.3.3 Bubble Size Determination ____ 205

7.3.4 Bubble Frequency Determination ____ 206

7.4 OPTICAL PROBE RESULTS ____ 207

7.4.1 Bubble Rise Velocity, u_b ____ 209

7.4.2 Bubble Mean Pierced Length, $\bar{l}_b$ ____ 214

7.4.3 Bubble Frequency, f_b ____ 219

7.4.4 Sensitivity of Bubble Probe Results to Threshold ____ 224

7.5 GAS FLOW BALANCE AND PREDICTION OF BED EXPANSION ____ 225

7.6 COMPARISON OF DATA WITH BUBBLE GROWTH MODELS ____ 229

7.7 NOMENCLATURE ____ 233

7.8 REFERENCES ____ 235

CHAPTER 8

8. EXPERIMENTAL SETUP FOR SOLIDS MIXING STUDIES 237

8.1 THERMAL TRACER TECHNIQUE 237

8.1.1 Thermistor Probes 238

8.1.1.1 Thermistor Circuits 241

8.1.1.2 Thermistor Calibration 243

8.1.1.3 Thermistor Probe Time Response 244

8.1.1.4 Thermistor Array Configuration 246

8.1.2 Thermal Tracer Injection 246

8.1.2.1 Injector Configuration 247

8.1.2.2 Injection Procedure 250

8.2 NOMENCLATURE 252

8.3 REFERENCES 253

CHAPTER 9

9. SOLIDS MIXING IN PRESSURIZED BUBBLING FLUIDIZED BED COMBUSTORS 255

9.1 THERMAL TRACER DATA ANALYSIS 255

9.1.1 Temperature Normalization 255

9.1.1.1 Relationship Between Θ and the Tracer Concentration 256

9.1.2 Injection Time, t_0 259

9.1.3 Injection Temperature, T_{inj} 260

9.1.4 Delay Time, t_d 261

9.2 THERMAL TRACER DATA 263

9.2.1 Time Delay Data 263

9.2.2 Thermal Tracer Mixing Data 267

9.3 NOMENCLATURE 276

9.4 REFERENCES 277

CHAPTER 10

10. MODELING SOLIDS MIXING IN BUBBLING FLUIDIZED BEDS ____ 279

10.1 SOLIDS MIXING MECHANISMS ____ 279

10.2 SOLIDS MIXING MODEL ____ 281

10.2.1 Axial Mixing Model ____ 281

10.2.1.1 Comparison of Axial Mixing Model Against Sitnai (1981) Data ____ 290

10.2.2 Lateral Mixing Model ____ 295

10.2.2.1 Lateral Mixing Model Development ____ 296

10.2.3 Integrated Solids Mixing Model ____ 300

10.2.3.1 Mixing Model Inputs ____ 305

10.2.3.1.1 Axial Mixing Model Inputs ____ 306

10.2.3.1.2 Bubble Diameter in Each Region ____ 309

10.2.3.1.3 Bubble Coalescence Rate ____ 310

10.2.4 Calculational Procedure ____ 314

10.3 SAMPLE MODEL OUTPUT ____ 315

10.4 COMPARISON OF MIXING MODEL OUTPUT WITH THERMAL TRACER DATA ____ 319

10.5 ADVANTAGES OF MIXING MODEL OVER PREVIOUS MODELS ____ 323

10.6 NOMENCLATURE ____ 324

10.7 REFERENCES ____ 326

CHAPTER 11

11. CONCLUSIONS AND RECOMMENDATIONS ____ 329

11.1 CONCLUSIONS OF HYDRODYNAMIC SCALING STUDIES ____ 329

11.1.1 Hydrodynamic Scaling of the Tidd PFBC ____ 329

11.1.2 Importance of the Solid-to-Gas Density Ratio for Scaling Bubbling Fluidized Beds ____ 330

11.2 CONCLUSIONS OF SOLIDS MIXING STUDIES ____ 331

11.2.1 PFBC Bubble Characteristics ____ 331

11.2.2 Thermal Tracer Mixing Results ____ 333

11.2.3 Mechanistic Solids Mixing Model ____ 334

11.3 RECOMMENDATIONS FOR FUTURE WORK ____ 335

11.4 REFERENCES ____ 336

APPENDICES

Appendix A – Model of Tidd PFBC Pressure Lines _____ 337

Appendix B – Measurement of Particle Sphericity _____ 340

Appendix C – Tidd PFBC and Cold Model Particle Size Distributions _____ 341

Appendix D – Mean and Standard Deviation of Solid Fraction Data from Tidd PFBC and Cold Model _____ 343

Appendix E – Particle Size Distributions for ρ_s/ρ_g Studies _____ 346

Appendix F – Internal Angle of Friction Measurements for ρ_s/ρ_g Studies _____ 348

Appendix G – Bubble Fraction Data _____ 350

Appendix H – Bed Height Measurements _____ 353

Appendix I – Tabulated Optical Probe Data _____ 356

Appendix J – Bubble Characteristics Uncertainty Analysis _____ 358

Appendix K – Thermistor Calibration Constants _____ 362

1. Introduction

Initial interest in using fluidized beds for coal combustion developed during the late 1960s in response to environmental concerns related to burning fossil fuels (Tung and Williams, 1987). Fluidized beds offer the capability to simultaneously burn coal and clean the combustion gases, significantly lowering sulfur oxide (SO_x) emissions. They also operate at significantly lower temperatures than conventional pulverized-coal plants preventing the formation of thermal nitrogen oxides (NO_x). Both pollutants are thought to contribute to acid rain.

The United States has significant coal reserves, some estimate a 300 year supply (Whitney, 1992), making coal an important strategic energy resource. It became apparent during the energy crisis of the early 1970s that the U.S. needed to reduce its dependence on foreign energy sources. Fluidized beds represented an environmentally acceptable way of exploiting U.S. coal reserves, prompting an increase in research and development related to fluidized-bed coal combustion.

Although the underlying interest in fluidized beds is primarily related to their environmental performance, the hydrodynamics of a fluidized bed significantly influences both its environmental and thermal performance. Hence, understanding the hydrodynamics of fluidized beds is essential to fully capitalize on the benefits of fluidized-bed combustion. Pressurized fluidized bed combustors (PFBC) represent a new technology that offers higher cycle efficiencies than traditional atmospheric-fluidized-bed and pulverized-coal combustors. This study focuses on the hydrodynamics of pressurized fluidized bed combustors.

1.1 Background

1.1.1 Advantages of Fluidized Bed Combustors

Fluidized bed combustors (FBC) offer several advantages over conventional pulverized-coal (PC) combustors. These advantages include: greater fuel flexibility, improved environmental performance, and smaller boiler size.

High solids mixing rates promote temperature uniformity within the bed, even in the presence of highly exothermic combustion reactions. These high mixing rates and the large thermal inertia of the bed give fluidized beds the capability burn a broad range of fuels of varying quality; possible fuels include: inexpensive coals, lignites, wood, and waste products (Carpenter et al., 1991). In contrast, pulverized-coal combustors require much higher grade fuels. High mixing rates also make it possible to burn coal at relatively low temperatures. Fluidized bed combustors typically operate at temperatures of around 1100K; this is approximately half the combustion temperature commonly found in pulverized-coal plants. The low combustion temperatures prevent the formation of thermal nitrogen oxides, reducing overall nitrogen oxide emissions by up to 75% over PC plants (Carpenter et al., 1991).

Due to the high sulfur content of many coals, sulfur dioxide (SO_2) is a common byproduct of coal combustion. As mentioned previously, sulfur dioxide is an environmental pollutant that is believed to contribute to acid rain. PC plants typically use flue-gas scrubbers to control sulfur-dioxide emissions. Fluidized bed combustors have the advantage that they can burn coal and capture the sulfur dioxide in the combustion gases simultaneously. Fluidized bed combustors typically use CaO-based materials, such as limestone, for the bed solids (sorbent). The sulfur dioxide is captured by sulfation reactions with the bed material to form products such as calcium sulfate (Tung and Williams, 1987). These sulfation reactions are particularly effective at fluidized bed combustion temperatures.

The resulting sulfated sorbent is a much more manageable dry solid waste in comparison to the wet sludge produced by conventional flue-gas scrubber systems (Carpenter et al. 1991). Current fluidized-bed combustor designs can capture 90-98% of the sulfur released by the coal during combustion (Alvarez Cuenca and Anthony, 1995).

Fluidized beds offer heat transfer rates that are four to five times higher than those in conventional PC plants (Dept. of Energy, 1990). These high heat transfer rates provides the potential for significant reductions in boiler size. Bubbling beds have the heat transfer surface (boiler tubes) immersed within the bed and in water-cooled walls, permitting a particularly compact boiler design.

1.1.2 Pressurized Fluidized Bed Combustors (PFBC)

Pressurizing a fluidized-bed boiler provides the added potential for operating in a combined-cycle configuration. Conventional atmospheric fluidized bed combustors serve as the boiler for a Rankine cycle. Steam is generated as water flows through tubes immersed in the bed. PFBC plants use compressed air (up to 20 Mpa (Gogolek and Grace, 1995)) to fluidize the bed. The coal combustion in the bed increases the enthalpy of the air, providing the opportunity to expand the pressurized gases through a gas turbine to extract additional work from the system. Hence, PFBC plants typically operate with a Rankine cycle on the steam side and an open Brayton cycle on the gas side. Figure 1 illustrates a simple PFBC cycle. Direct coal-fired combined cycles have the potential to provide plant efficiencies of 40-43% (HHV) (Alvarez Cuenca and Anthony, 1995).

Due to their high energy release rates per unit bed volume, PFBC boilers have much deeper beds than atmospheric fluidized bed combustors. They also tend to have lower gas velocities (several times that required to fluidize the bed). These factors provide increased residence times, improving combustion efficiencies and sulfur capture over atmospheric designs.

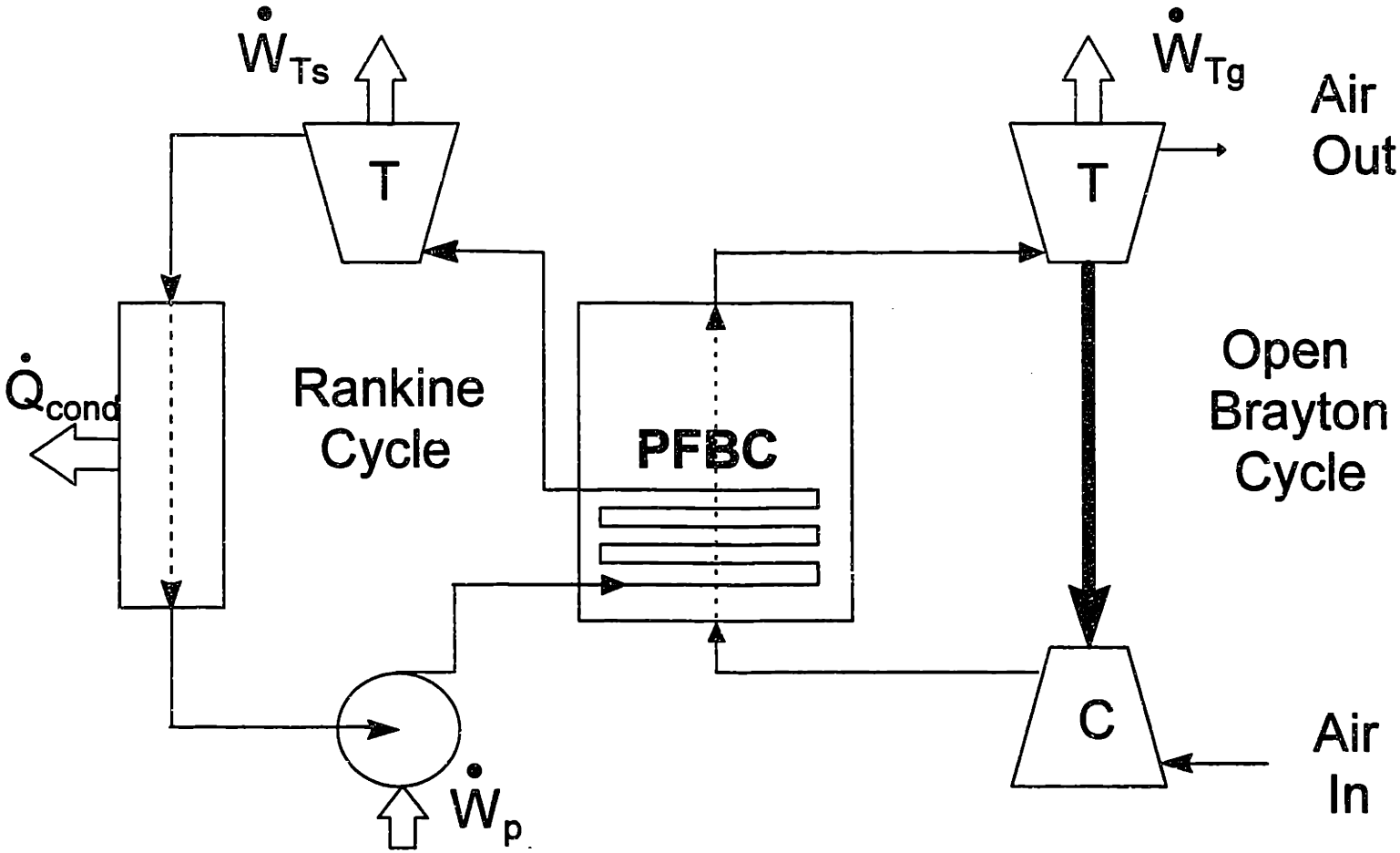

Figure 1: PFBC Combined Cycle

1.1.3 Regimes of Fluidization

Fluidized bed combustors typically operate in either bubbling or circulating regimes of fluidization. The circulating regime of fluidization is also commonly referred to as the fast fluidization regime. Figure 2 illustrates the two flow regimes.

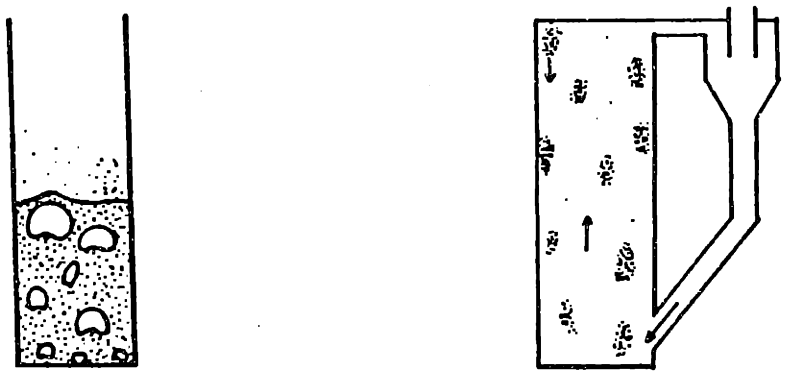

Bubbling Regime Circulating Regime

Figure 2: Bubbling and Circulating Regimes of Fluidization (Grace, 1982)

In bubbling beds, gas bubbles form at the distributor and rise through an emulsion of fluidized solids. The emulsion is typically assumed to be close to minimum fluidization conditions (i.e., the point at which the drag on the particles equals their weight). As bubbles rise through the bed, they can grow by coalescing with neighboring bubbles. Bubble growth is often limited by the presence of tubes immersed in the bed; the in-bed tubes have a significant effect on the bed hydrodynamics. The eruption of bubbles at the surface of the bed, ejects particles into the freeboard region above the bed surface. These particles undergo significant lateral dispersion across the surface of the bed.

In circulating fluidized beds (CFB) the bed has no distinct upper surface; particles are transported upward and out of the bed, captured using cyclone separators, and then recycled to the bottom of the bed. The hydrodynamics of a CFB are often described in terms of a core-annulus structure. Gas and particles, both single particles and particle clusters, flow upward in the core of a CFB. At the walls of the bed, an annulus of particle strands (frequently referred to as clusters) flows downward, but the net solids flux in a CFB is upward. Particle exchange takes place between the core and annulus regions through deposition and entrainment processes. Combustion can be staged in circulating fluidized bed making further reductions in NO_x emissions possible.

1.2 Thesis Research Objectives and Motivation

The work presented in this thesis focuses on two areas related to the hydrodynamics of pressurized bubbling fluidized bed combustors–hydrodynamic scaling and solids mixing.

1.2.1 Hydrodynamic Scaling

One of the most challenging problems encountered by a fluidized-bed designer is assessing how changes in bed geometry and operating conditions affect combustor performance. Typically, new combustor designs are based on operating experience from small pilot plants with power outputs in the neighborhood of 2 MW_t. Commercial fluidized bed combustors can generate well over 100 MW_e of power. (As of 1991, the largest atmospheric bubbling-bed plant was the Tennessee Valley Authority's Shawnee steam plant in Kentucky, which produces 160 MW_e of power (Makanski, 1991).) Hence it is essential that designers have the capability to reliably scale up pilot plant performance to commercially viable levels. Hydrodynamic scaling provides a rational approach to address this scale-up issue.

Hydrodynamic scaling also provides a way for designers to construct a laboratory-scale cold model that can be used to simulate the hydrodynamics of a hot combustor. A cold model of a combustor represents an inexpensive and convenient platform for conducting detailed hydrodynamic studies that would otherwise be impossible in the hostile environment of a fluidized bed combustor. For example, bubbles in bubbling fluidized beds play a central role in solids mixing and in gas flow patterns through the bed. Yet it is virtually impossible to measure the characteristics of the bubbles in a hot combustor. In contrast, the literature is replete with measurements of the bubbles in cold laboratory-scale fluidized beds (e.g., Olowson and Almstedt, 1990; Werther and Molerus, 1973a,b), although few studies have paid attention to proper hydrodynamic scaling to ensure that the data are relevant to the hydrodynamics of a hot combustor. Therefore, hydrodynamic scaling makes it possible to conduct fast and inexpensive tests, in the convenience of the laboratory, to evaluate the effects varying bed geometry and operating conditions on bed hydrodynamics.

The first objective of this study was to identify and verify a set of parameters for scaling the hydrodynamics of commercial-scale pressurized fluidized bed combustors (PFBC). Data from the Tidd PFBC 70 MW_e combustor were used as the basis for the scaling comparison. The data from the Tidd plant provide the unique opportunity to verify a set of scaling relationships for a truly commercial-scale fluidized bed combustor. The Tidd PFBC is a first-of-a-kind PFBC combined-cycle plant in the United States. Only two similar plants exist in the world–the Värtan plant in Sweden and the Escatrón plant in Spain. The Tidd plant is owned and operated by American Electric Power Company, Inc. and is located on the banks of the Ohio River in Brilliant, Ohio.

One of the scaling parameters used to scale the Tidd PFBC was the ratio of the solid particle density (ρ_s) to the density of the fluidizing gas (ρ_g). This scaling parameter has been found to be essential for scaling circulating fluidized (Glicksman et al. 1993), but some controversy remained over its importance for scaling bubbling fluidized beds. For example, Horio et al. (1986) and Horio et al. (1989) contend that the solid-to-gas density

ratio (ρ_s/ρ_g) is unimportant for scaling fluidized beds. This motivated an investigation to assess the importance of matching the density ratio when scaling bubbling fluidized beds.

1.2.2 Solids Mixing in Pressurized Bubbling Fluidized Beds

Coal is pumped into a PFBC in the form of a paste through fuel nozzles positioned near the bottom of the bed. The mixing of solids within the bed distributes the fuel. Although the complete combustion of the coal takes roughly 10 minutes, the coal devolatilizes in approximately 6 seconds (Andrei et al., 1985). The devolatilization time is comparable to the mixing times (Gogolek and Grace, 1995). Inadequate solids mixing can lead to the depletion of the oxygen in the vicinity of the fuel nozzles, producing plumes of unburned volatiles that rise through the bed into the freeboard. Once the volatiles reach the freeboard, there is sufficient oxygen for the volatiles to burn. Post-bed combustion can produce unsatisfactorily high freeboard and cyclone temperatures. An additional problem with the combustion in the freeboard is that there is insufficient sorbent in this region to adequately capture the sulfur dioxide produced by the combustion. This problem can be solved by reducing the fuel feedrate, but this reduces the capacity of the boiler. Alternatively, additional fuel feed points can be added, but this can substantially increase the cost of the boiler (~$250,000 for each feed-point pump). So there is a trade-off between performance and cost. An understanding of short-term solids mixing in PFBCs is required to estimate the location where the volatiles are released and the necessary feed-point spacing.

Early in its operation, Tidd experienced several problems related to insufficient solids mixing (McDonald, 1992). Failure to achieve sufficient distribution of the fuel led to plumes of volatiles burning in the freeboard and in the cyclones. Tidd also experienced high carbon carryover at low loads causing dip-leg fires. Baffles were installed above the fuel nozzles, among other measures, to improve the lateral distribution of fuel (McDonald,

1992). Hence, inadequate solids mixing is a very real and practical problem in PFBCs, and it is essential to obtain a better understanding of how solids mix in a PFBC.

As discussed in Section 1.2.1, cold scale models offer a convenient platform for conducting detailed hydrodynamic studies. In this study, the rare opportunity exists to use a cold model of an actual PFBC combustor–the Tidd PFBC–to investigate solids mixing in PFBCs.

1.3 Organization of Thesis

This thesis is divided into eleven chapters, including this introduction, followed by the appendices. Each chapter has its own nomenclature and reference sections for increased reader convenience. In an attempt to make the information in this thesis more accessible, experimental setups and experimental results are generally described in separate chapters.

Chapters 2 through 5 present the work done on hydrodynamic scaling. After a brief review of dimensional analysis and similarity, Chapter 2 presents a development of the scaling parameters used in this study and reviews previous experimental work on hydrodynamic scaling in both bubbling and circulating fluidized beds. Chapter 3 describes the experimental setups for both the Tidd plant and the cold model. Detailed information regarding the tube bank geometry has been omitted due to its proprietary nature. Chapter 4 presents the results of the hydrodynamic scaling comparisons. Finally, Chapter 5 discusses some small-scale tests that were conducted to investigate the importance of matching the solid-to-gas density ratio when scaling bubbling fluidized beds.

Chapters 6 through 10 address the work related to solids mixing in PFBCs. Chapter 6 reviews the relevant literature related to solids mixing in bubbling fluidized beds. As described in Chapter 6, the characteristics of the bubbles in the bed play a central role in the mixing of solids. This motivated the measurement of the bubble characteristics in the

cold model using a unique optical probe design. The results of these measurements are presented in Chapter 7. A thermal tracer technique has been used to study the motion of the solids within the cold model. This method of investigating solids mixing is described in Chapter 8, and the results are presented in Chapter 9. Chapter 10 presents the development of a mechanistic model of solids mixing in bubbling fluidized beds. Many of the bubble characteristics described in Chapter 7 are used as inputs to the model. The model described in Chapter 10 represents a completely new approach to modeling solids mixing in bubbling fluidized beds.

Finally, Chapter 11 summarizes the conclusions from both the hydrodynamic scaling and the solids mixing work presented in this thesis. This is followed by recommendations for future work.

1.4 References

Alvarez Cuenca, M. and Anthony, E.J., eds., 1995, Pressurized Fluidized Bed Combustion, Blackie Academic & Professional, London.

Andrei, M.A., Sarofim, A.F., and Beér, J.M., 1985, "Time-resolved Burnout of Coal Particles in a Fluidized Bed," *Combustion and Flame*, 61, pp. 17-27.

Carpenter, L., Langan, W., Dellefield, R., Nelkin, G., and Hand, T., 1991, "Pressurized Fluidized Bed Combustion: A Commercially Available Clean Coal Technology," Proceedings of the 1991 International Conference on Fluidized Bed Combustion, ed. E.J. Anthony, Montreal, pp. 467-474.

Department of Energy, 1990, "Tidd: The Nation's First PFBC Combined-Cycle Demonstration," Clean Coal Technology, Topical Report Number 1

Glicksman, L.R., Hyre, M., and Woloshun, K., 1993, "Simplified Scaling Relationships for Scaling Fluidized Beds," *Powder Technology*, 77, pp. 177-199.

Gogolek, P.E.G. and Grace, J.R., 1995, "Fundamental Hydrodynamics Related to Pressurized Fluidized Bed Combustion," *Prog. Energy Combust. Sci.*, 21, pp. 419-451.

Grace, J.R., 1982, "Fluidized-Bed Hydrodynamics," Chapter 8.1, Handbook of Multiphase Systems, ed. G. Hetsroni, Hemisphere, Washington, D.C.

Horio, M., Nonaka, A., Sawa, Y. and Muchi, I., 1986, "A New Similarity Rule For Fluidized Bed Scale-Up," *AIChE Journal*, 32, pp. 1466-1482.

Horio, M., Ishii, H., Kobukai, Y., and Yamanishi, N., 1989, A Scaling Law For Circulating Fluidized Beds," *Journal of Chemical Engineering of Japan*, 22, pp. 587-592.

Makanski, J., 1991, "Fluidized-bed boilers," *Power*, March, pp. 15-32.

McDonald, D.K., 1992, "PFBC Plant Operations–TIDD," Babcock & Wilcox Technical Paper, BR-1498, presented to Power-Gen '92, Orlando, FL.

Olowson, P.A. and Almstedt, A.E., 1990, "Influence of Pressure and Fluidization Velocity on the Bubble Behavior and Gas Flow Distribution in a Fluidized Bed," *Chemical Engineering Science*, 45, 7, pp. 1733-1741.

Tung, S.E. and Williams, G.C., 1987, Atmospheric Fluidized-Bed Combustion–A Technical Sourcebook, DOE Report DOE/MC/14536-2544.

Werther, J. and Molerus, O., 1973a, "The Local Structure of Gas Fluidized Beds - I. A Statistically Based Measuring System," *International Journal of Multiphase Flow*, 1, pp. 103-122.

Werther, J. and Molerus, O., 1973b, "The Local Structure of Gas Fluidized Beds - II. The Spatial Distribution of Bubbles," *International Journal of Multiphase Flow*, 1, pp. 123-138.

Whitney, S., 1992, "PFBC Applications in Utility Systems," Babcock & Wilcox Technical Paper, BR-1491A, presented to Power-Gen '92, Orlando, FL.

2. Review of Fluidized Bed Hydrodynamic Scaling

2.1 Overview of Work Related to Hydrodynamic Scaling

After briefly reviewing dimensional analysis and similarity, this chapter presents the development of a set of hydrodynamic scaling parameters. These parameters were used to specify the geometry and operating conditions of a cold model intended to simulate the hydrodynamics of the Tidd PFBC. This is followed by a review of the work done to experimentally verify hydrodynamic scaling for both bubbling and circulating fluidized bed hydrodynamics. Chapter 3 describes both the Tidd PFBC and the cold-model experimental setups. And Chapter 4 summarizes the work done to verify a set of hydrodynamic scaling parameters for use with commercial pressurized bubbling fluidized bed combustors. Finally, Chapter 5 presents the results from some additional small-scale experiments that were conducted to demonstrate the importance of matching the solid-to-gas density ratio when scaling bubbling fluidized beds.

2.2 Dimensional Analysis and Similarity

Dimensional analysis is a powerful analytical technique, particularly in situations where the equations governing a physical problem are either unknown or not easily solved. Dimensional analysis reduces the number of independent parameters on which a physical problem depends. The independent parameters are those that affect the value of dependent variable, and each independent parameter can be set without affecting the other independent parameters. Dimensional analysis is also useful for generalizing experimental results and aiding in their correlation. For example, dimensional analysis can be used to show how the friction factor (nondimensional wall shear stress) in turbulent pipe flow is a function of Reynolds number and dimensionless roughness height, or similarly how the lift coefficient (nondimensional lift force) for aerodynamic bodies depends on Reynolds

number and angle of attack. There are a number of dimensional analysis techniques; Buckingham's pi-theorem (Buckingham, 1914) and the method of nondimensionalizing the governing equations and boundary conditions (inspectional analysis) will be discussed.

Experiments on a full-size commercial prototype are often prohibitively expensive and complex. One of the additional benefits of dimensional analysis is that it provides a way of properly scaling between a full-size prototype (target) and a laboratory scale model. By matching the appropriate dimensionless parameters, which result from the dimensional analysis, between the model and the target prototype, dynamically similar behavior (similarity) will be achieved when it is expressed in the proper nondimensional form. These laws make it possible to obtain useful information regarding the behavior of a full-size prototype using a properly scaled model.

2.2.1 Buckingham Pi Theorem

Buckingham's pi theorem provides a simple method of forming the dimensionless parameters that govern a physical process. The resulting dimensionless parameters are the so-called pi groups.

Buckingham's pi theorem states that if a physical process depends on n independent parameters, it can be simplified to a relationship between (n-k) dimensionless parameters (pi groups). k is the number of dimensionally independent parameters, which is less than or equal to the number of dimensions (e.g., M=mass, L=length, t=time) in the original n parameters.

2.2.1.1 Buckingham Pi Theorem Procedure

The pi theorem is best demonstrated by an example; consider the case where the minimum fluidization velocity (u_{mf}) is the dependent parameter. Buckingham pi reduces the dependence of the minimum fluidization velocity on the relevant independent parameters to its simplest form.

The first step is to identify the complete set of dimensional independent parameters that are pertinent to the physical problem. It should be emphasized that the physics must be correct; if an important independent parameter is left out, the dimensional analysis will fail. Similarly, spurious independent parameters unnecessarily complicate the results of the dimensional analysis and reduce its utility. Again, the independent parameters are those that affect the value of a dependent parameter or variable, but can be set independent of each other. Typical examples include geometric or operating parameters that can be controlled independent of each other. In this particular example, it can be argued that the minimum fluidization velocity depends on the dominant forces on the particles and the particle geometry. We will assume that the dominant forces on the particles are: the force of buoyancy [$(\rho_s-\rho_g)g$], viscous forces (μ), and fluid inertia forces (ρ_g). Note that gravity appears combined with the difference in densities in the buoyancy term, not as a separate independent parameter. The particle geometry can be characterized by the mean particle diameter (d_p), the minimum fluidization voidage (ε_{mf}), and the particle sphericity (ϕ_s). Particle inertia, which would require the inclusion of ρ_s in the list of independent parameters, is assumed to be small for conditions near minimum fluidization.

$$u_{mf}=fcn\{(\rho_s-\rho_g)g,\ \mu,\ \rho_g,\ d_p,\ \varepsilon_{mf},\ \phi_s\} \qquad (1)$$

The next step is to list the dimensions of both the independent and the dependent parameters. The most common dimensions are mass (M), length (L), time (t), and temperature (T). In the case of the minimum fluidization velocity,

$$[u_{mf}] = L/t \qquad [\mu] = M/Lt \qquad [(\rho_s-\rho_g)g] = M/L^2t^2$$
$$[\rho_g] = M/L^3 \qquad [d_p] = L \qquad [\varepsilon_{mf}] = 1 \qquad (2)$$
$$[\phi_s] = 1.$$

Temperature does not appear in this case.

A dimensionally independent subset of the independent parameters must be specified; the dimensionally independent parameters are used to nondimensionalize the remaining parameters. In order for the parameters to be dimensionally independent, it should not be possible to construct a dimensionless parameter (pi group) from them. Typically, the number of dimensionally independent parameters is equal to the number of dimensions in the problem. Selecting ρ_g (M/L^3), μ (M/Lt), and d_p (L) as the dimensionally independent parameters, and nondimensionalizing the remaining independent parameters and the dependent parameter using these gives

$$\frac{\rho_g u_{mf} d_p}{\mu} = \text{fcn}\left(\frac{(\rho_s-\rho_g)\rho_g g d_p^3}{\mu^2}, \varepsilon_{mf}, \phi_s\right) . \qquad (3)$$

This can be written more concisely as,

$$Re_{mf} = \text{fcn}(Ar, \varepsilon_{mf}, \phi_s), \qquad (4)$$

where Re_{mf} is the particle Reynolds number at minimum fluidization, and $Ar \equiv (\rho_s-\rho_g)\rho_g g d_p^3/\mu^2$ is the Archimedes number. A functional form for this relationship is given by the Ergun equation (Ergun, 1952), which at minimum fluidization conditions is given by

$$\frac{1.75}{\varepsilon_{mf}^3 \phi_s} Re_{mf}^2 + \frac{150(1-\varepsilon_{mf})}{\varepsilon_{mf}^3 \phi_s^2} Re_{mf} = Ar . \qquad (5)$$

Wen and Yu (1966) assumed that ε_{mf} is only a function of ϕ_s and showed that over a wide range of conditions $1/(\phi_s \varepsilon_{mf}^3)$ and $(1-\varepsilon_{mf})/(\phi_s^2 \varepsilon_{mf}^3)$ are approximately constant. Solving for Re_{mf} and assuming that the coefficients are constant gives

$$Re_{mf} = \sqrt{C_1^2 + C_2 Ar} - C_1, \qquad (6)$$

where Grace (1982) recommends values of 27.2 and 0.0408 for C_1 and C_2, respectively.

This example illustrates the application of the Buckingham pi approach of dimensional analysis. It also shows how with additional physical insight into the problem simplifications are possible. If ρ_g, ρ_s, and g had been listed individually as independent parameters, which would have occurred if no additional physical insight had been used, two additional independent dimensionless parameters would have resulted. The larger the number of independent dimensionless parameters the more complicated the task of correlating experimental data.

2.2.1.2 Application of Buckingham Pi to Fluidized Bed Hydrodynamics

The Buckingham pi procedure, presented in Section 2.2.1.1, can be applied to determine the dimensionless groups that govern the hydrodynamic behavior of fluidized beds. If we take the pressure drop as the dependent parameter of interest, we can use Buckingham pi to determine the independent dimensionless parameters on which it depends.

To maintain generality, we will resist the temptation to simplify and take the complete list of the independent parameters to be

$$\Delta p = \text{fcn}(u_o, g, D, L, d_p, \rho_s, \rho_g, \mu, \phi_s). \tag{7}$$

These parameters have the dimensions:

$[\Delta p]=M/(Lt^2)$	$[u_o]=L/t$	$[g]=L/t^2$
$[D]=L$	$[L]=L$	$[\phi_s]=1$
$[\rho_s]=M/L^3$	$[\rho_g]=M/L^3$	$[\mu]=M/(Lt)$.
$[d_p]=L$		

(8)

Choosing u_o (L/t), D (L), and ρ_g (M/L^3) as the dimensionally independent parameters and nondimensionalizing the remaining parameters with these gives:

$$\frac{\Delta p}{\rho_g u_o^2} = \text{fcn}\left(\frac{\rho_s}{\rho_g}, \frac{gD}{u_o^2}, \frac{L}{D}, \frac{D}{d_p}, \frac{\rho_g u_o D}{\mu}, \phi_s\right). \tag{9}$$

This set of dimensionless parameters is identical to the scaling laws developed by Glicksman (1984), which resulted from the nondimensionalization of the Jackson (1971)

equations of motion for fluidized beds. The number of nondimensional independent parameters is fixed unless simplifications can be justified, but they can be arbitrarily arranged in different forms. For example, the Archimedes number when $\rho_s >> \rho_g$ (which is common in gas fluidized beds) results from

$$Ar \approx \left(\frac{\rho_g u_o d_p}{\mu}\right)^2 \cdot \left(\frac{g d_p}{u_o^2}\right) \cdot \left(\frac{\rho_s}{\rho_g}\right) \tag{10}$$

It is important to note that Ar cannot be used to replace the three parameters, it can only be substituted for one such that the number of independent parameters remains the same. Simplifications result from physical insight, not mathematical manipulation.

2.2.2 Nondimensionalization of Governing Equations and Boundary Conditions

The Buckingham pi approach to dimensional analysis quickly and easily produces a set of dimensionless parameters, but it provides no way of determining whether the initial list of independent parameters is complete. The method of nondimensionalization of the governing equations and boundary conditions does not suffer from this limitation if the governing equations and boundary conditions can be completely specified.

If the scales of the problem can be identified, nondimensionalizing the governing equations using the scales normalizes the equations such that each term is of order unity or less. This makes it possible to look at the order of magnitude of each term for a particular situation to determine when certain terms are negligible relative to others (referred to as order-of-magnitude or scale analysis). Order-of-magnitude analysis can also provide information regarding the functional form of the solution to the equation. Order-of-magnitude arguments are used, for example, to simplify the Navier-Stokes equations in the development of the boundary layer equations. Kline (1965) provides a detailed discussion on nondimensionalizing the governing equations and boundary conditions.

The first step in nondimensionalizing the governing equations is to define the dimensionless dependent variables. Next, each term in the governing equations and the boundary conditions must be written in terms of the dimensionless variables. Finally, the coefficient of a term in each governing equation and boundary condition is chosen and each term in the equation or boundary condition is divided through by it. The resulting dimensionless coefficients of the terms in the normalized equations and boundary conditions are the relevant dimensionless independent parameters. This procedure is followed in the development of the hydrodynamic parameters presented below.

The more complete the governing equations and boundary conditions are, the more widely applicable the results of the dimensional analysis will be. It is important to realize the limitations of the method of nondimensionalizing the governing equations. As with the Buckingham pi method, if all the important terms representing the independent physical processes are not included in the equations, the dimensional analysis will be incomplete or it will fail.

2.2.3 Similarity

One of the benefits of dimensional analysis is that it provides the scaling laws between a model and a target prototype such that the two systems will exhibit dynamically similar behavior.

Geometric similarity is a prerequisite to dynamic similarity. A model and a prototype are geometrically similar when all of their linear dimensions are related by a constant scale factor. They also must have the same shape (e.g. all angles must be preserved, etc.). In the fluidization example in Section 2.2.1.2 the nondimensional groups L/D and d_p/D are terms that would have to be matched between a model and a prototype to achieve geometric similarity.

A model and a target prototype will exhibit dynamically similar behavior if they are geometrically similar and if all the values of the relevant independent dimensionless parameters are matched between the two. In terms of the Buckingham-pi dimensional analysis, by matching all the independent pi groups the nondimensional dependent variables will be identical. Using the drag on an arbitrary body as an example, if the model and the prototype are geometrically similar, and the Reynolds numbers of the flows over the two are identical, the drag on the target prototype is related to the drag on the model by

$$F_{D_t} = F_{D_m} \frac{(\rho u^2 L^2)_t}{(\rho u^2 L^2)_m}, \tag{11}$$

where the subscript m is for the model and t is for the target prototype. In other words, the nondimensional drag force on the model and the prototype are identical.

Similarly, if the same dimensionless governing equations and boundary conditions govern both a full-size target prototype and a scale model, the dimensionless solution will be identical. Hence, if the dimensionless parameters in the nondimensional governing equations and boundary conditions are matched between the prototype and the model, they will exhibit similar behavior when it is expressed in nondimensional form.

2.3 Development of Hydrodynamic Scaling Parameters

2.3.1 Two-Fluid Modeling

Two-fluid models represent the state-of-the-art in modeling two-phase flows. Two-fluid models involve separate mass, momentum, and energy conservation equations for each phase. This results in two sets of conservation equations, one set for each phase (i.e., six equations total), that are coupled through interaction terms. The gas (subscript g) and solid particle emulsion (subscript s) are the phases in fluidization. Due to the considerable uncertainty that exists in the location of the individual phases at any particular instant in

time, averaging methods are typically used to develop the governing equations. The averaging process transforms, what Ishii (1975) calls the "local instant" equations, which represent two phases that alternately occupy a spatial location, into averaged equations that represent two interpenetrating continuous phases simultaneously existing at each point in the flow. Averaging eliminates essential characteristics of the flow that must be reintroduced into the equations through appropriate constitutive equations. This is analogous to the need to constitute the Reynolds-stress term in turbulent single-phase fluid mechanics. The identification of satisfactory constitutive equations continues to be an important area of research. In general, limitations in constitutive equations continue to hamper efforts to accurately predict the hydrodynamics of gas-solid flows.

A two-fluid model of a gas-solid suspension will be nondimensionalized to identify the scaling parameters that govern the hydrodynamics of bubbling fluidized beds. Drew (1992) provides the detailed development of the governing equations. Drew's equations are comprehensive and general. Assumptions are made, particularly with respect to constitutive relationships, to make the governing equations specific to fluidization. The approach to nondimensionalizing these equations is similar to that of Glicksman (1984) and Glicksman et al. (1993b).

The validity of the continuum assumption can be debated, particularly in the leaner regions of bubbling beds and in circulating fluidized beds. Glicksman et al. (1994) develop the same set of scaling relationships using the equation of motion for a single particle, demonstrating that it is not necessary to make the continuum assumption.

2.3.2 Governing Equations

As discussed in Section 2.3.1, two-fluid models involve separate conservation equations for each phase. Vigorous mixing in fluidized beds provides a relatively uniform temperature distribution throughout the bed; this feature of fluidized beds is often

exploited in fluidized-bed chemical reactors. Assuming that the fluidized bed is isothermal eliminates the need for an energy equation. Hence, only continuity and momentum equations are considered for scaling fluidized-bed hydrodynamics.

Neglecting mass transfer between the phases due to chemical reaction, the gas and solid-phase continuity equations are given by

$$\frac{\partial}{\partial t}\left(\varepsilon \rho_g\right)+\nabla\cdot\left(\varepsilon \rho_g \vec{u}_g\right)=0 \tag{12}$$

and

$$\frac{\partial}{\partial t}\left[(1-\varepsilon)\rho_s\right]+\nabla\cdot\left[(1-\varepsilon)\rho_s \vec{u}_s\right]=0, \tag{13}$$

respectively.

Similarly, each phase has its own momentum equation. Drag is the dominant gas-solid interaction force and is assumed to be the primary source of momentum exchange between the phases. Other forces, such as virtual mass and history effects, and the gas-phase shear stress are negligible in gas-fluidized systems (Clift and Rafailidis, 1993). The drag between the phases is expressed in the form of a particle-assembly drag coefficient, β. The resulting gas-phase momentum equation is given by

$$\frac{\partial}{\partial t}\left(\varepsilon \rho_g \vec{u}_g\right)+\nabla\cdot\left(\varepsilon \rho_g \vec{u}_g \vec{u}_g\right)=-\nabla(\varepsilon p)+\varepsilon \rho_g \vec{g}-\beta\left(\vec{u}_g-\vec{u}_s\right). \tag{14}$$

Defining an appropriate solid-phase momentum equation is more difficult due to the additional complication of constituting a solid-phase stress tensor. Inviscid flow theory has been used extensively in fluidization. For example, Davidson's (1961) seminal model of a single bubble rising in an infinite bed used potential flow theory to treat the movement of the dense phase around a spherical bubble. Davies and Taylor (1950) used inviscid flow theory to derive an expression for the rise velocity of a gas bubble in a liquid. Davidson et al. (1959) showed, experimentally, that this expression was also valid for gas bubbles rising in a fluidized bed. Unlike solid bodies, the free surface of bubbles have an

extremely small shear stress. Bagnold (1954) found, experimentally, that the inter-particle shear stress should become small in regions where the shear rate is zero. Clift and Rafailidis (1993) use these observations to explain why the particle phase moves like an ideal fluid around the upper surface of a bubble and to provide support for the use of inviscid flow theory to model certain phenomenon in fluidization. But they also concede that the high shear rates in bubble wakes invalidate the ideal fluid assumption in this region. Hence, although high effective viscosities have been measured in fluidized beds, modeling the solids-phase as an inviscid flow has been shown to provide useful information on aspects of fluidized-bed hydrodynamics.

The solid-phase shear stress has been treated several ways in computational studies. In some early investigations (e.g., Gidaspow and Ettehadieh, 1983), it was assumed that the normal component of the solid-phase stress is a function of the voidage (ε). Experimental data were then used to establish the functional dependence of the normal stress on voidage. Massoudi et al. (1992) showed that the empirical fits used in different investigations differ by orders of magnitude, and yet the numerical results were shown to be insensitive to the fit that was chosen. This raised serious questions over the validity of this approach. More recently, granular flow theory has been used to develop expressions for the solid-phase stress tensor (e.g., Ding and Gidaspow, 1990). Granular flow theory attributes the stress in the solid phase to inter-particle collisions and is based on the kinetic theory of dense gases (e.g., Chapman and Cowling, 1970). But Clift and Rafailidis (1993) refute the notion that interactions between particles produce significant particle-particle stress. Based on the data of Campbell and Wang (1991) and Rathbone et al. (1989) they conclude that solid-phase stress is due primarily to the momentum of "packets" of particles transported by bubbles, not kinetic interactions between individual particles.

There is currently no satisfying model of the solid-phase stress tensor in fluidization. State-of-the-art computational programs use elaborate stress-tensors based on granular flow theory. But as just discussed, it is not clear that this is the correct model for the stress in the solids phase. And even these elaborate models require bold assumptions to

simplify Boltzmann's equation to provide a workable expression for the granular temperature. (The granular temperature is a dependent variable in the model which characterizes the kinetic energy of the random particle fluctuations.) The solid-phase stress tensor has been omitted from the following momentum equation for clarity. When the granular-flow-based stress tensor used by Boemer et al. (1995) is nondimensionalized, the coefficient of restitution is the only parameter that arises in addition to what will be referred to as the full set of scaling parameters. Litka and Glicksman (1985) found that the coefficient of restitution had a negligible effect on the hydrodynamics of bubbling fluidized beds. For this reason, it has been excluded from the list of scaling parameters. If particle-particle interactions were the primary mechanism of the solids phase stress, one would anticipate that the particle coefficient of restitution would have a significant effect on the hydrodynamics. Litka and Glicksman's results raise additional questions over the validity the granular flow model of solid-phase stress. Glicksman (1984) presented the first systematic development of the full set of scaling parameters; this development omitted the solid-phase stress tensor. Since then, these relationships have been verified extensively for atmospheric fluidized beds, as will be discussed in Section 2.4. This at least suggests that the dependence of the solid-phase stress tensor is embodied in the current list of scaling parameters.

The following solid-phase momentum equation is used in the subsequent scaling-parameter development.

$$\frac{\partial}{\partial t}\left[(1-\varepsilon)\rho_s \vec{u}_s\right] + \nabla\cdot\left[(1-\varepsilon)\rho_s \vec{u}_s \vec{u}_s\right] = (1-\varepsilon)\rho_s \vec{g} + \beta\left(\vec{u}_g - \vec{u}_s\right). \qquad (15)$$

2.3.3 Full Set of Scaling Parameters

2.3.3.1 Nondimensionalization of the Governing System

Let the dimension D represent a reference bed dimension, such as the tube pitch. The superficial gas velocity, u_o, will be used as the reference gas velocity. It is assumed that the solids velocity is related to the upward motion of bubbles and that the bubble size (d_b) is defined by the tube pitch (D). Hence, the functional form of Davies and Taylor's (1950) bubble rise velocity, which is proportional to $\sqrt{g d_b}$, will be used as the reference solid-phase velocity. The pressure drop in a bubbling bed is dominated by the weight of the bed material (i.e., hydrostatic); the reference pressure is defined as such. The dimensionless forms of the variables in the governing equations, in terms of these independent reference parameters, are given by:

$$\nabla' \equiv D\nabla, \tag{16}$$

$$t' \equiv t\frac{u_o}{D}, \tag{17}$$

$$\vec{u}'_g \equiv \frac{\vec{u}_g}{u_o}, \tag{18}$$

$$\vec{u}'_s \equiv \frac{\vec{u}_s}{\sqrt{gD}}, \text{ and} \tag{19}$$

$$p' \equiv \frac{p}{\rho_s g D}. \tag{20}$$

Assuming both phases are incompressible, the governing equations–(12) through (15)–written in terms of the dimensionless variables given by (16) to (20) are:

$$\frac{\partial \varepsilon}{\partial t'} + \nabla' \cdot \left(\varepsilon \vec{u}'_g\right) = 0 \tag{21}$$

$$\frac{\partial}{\partial t'}(1-\varepsilon)+\left(\frac{\sqrt{gD}}{u_o}\right)\nabla'\cdot\left[(1-\varepsilon)\vec{u}'_s\right]=0 \tag{22}$$

$$\frac{\partial}{\partial t'}\left(\varepsilon\vec{u}'_g\right)+\nabla'\cdot\left(\varepsilon\vec{u}'_g\vec{u}'_g\right)=-\left(\frac{\rho_s}{\rho_g}\right)\left(\frac{gD}{u_o^2}\right)\nabla'(\varepsilon p')+\varepsilon\left(\frac{\vec{g}D}{u_o^2}\right)-\left(\frac{\beta D}{\rho_s u_o}\right)\left(\frac{\rho_s}{\rho_g}\right)\left(\vec{u}'_g-\frac{\sqrt{gD}}{u_o}\vec{u}'_s\right) \tag{23}$$

$$\frac{\partial}{\partial t'}\left[(1-\varepsilon)\vec{u}'_s\right]+\left(\frac{\sqrt{gD}}{u_o}\right)\nabla'\cdot\left[(1-\varepsilon)\vec{u}'_s\vec{u}'_s\right]=(1-\varepsilon)\frac{\sqrt{\vec{g}D}}{u_o}+\left(\frac{\beta D}{\rho_s u_o}\right)\left(\frac{u_o}{\sqrt{gD}}\vec{u}'_g-\vec{u}'_s\right) \tag{24}$$

The dimensionless parameters that result from nondimensionalizing the governing equations are

$$\frac{u_o^2}{gD}\quad\frac{\rho_s}{\rho_g}\quad\frac{\beta D}{\rho_s u_o}. \tag{25}$$

But β is not a constant, and hence, the dependence of the dimensionless drag term must be given further consideration. The drag expression proposed by Ergun(1952) is frequently used for bubbling beds and will be used here. It is important to note that other drag relationships have been shown to give the same results (e.g., Glicksman et al., 1994). Thus the scaling relationships do not hinge on a specific drag relationship. Ergun's (1952) drag expression is given by

$$\beta=150\frac{(1-\varepsilon)^2}{\varepsilon}\frac{\mu}{\left(\phi_s d_p\right)^2}+1.75(1-\varepsilon)\frac{\rho_g\left|\vec{u}_g-\vec{u}_s\right|}{\left(\phi_s d_p\right)}. \tag{26}$$

Writing (26) in the dimensionless form found in (25) gives

$$\frac{\beta D}{\rho_s u_o}=150\frac{(1-\varepsilon)^2}{\varepsilon}\left(\frac{\rho_g}{\rho_s}\right)\frac{\mu}{\rho_g u_o\left(\phi_s d_p\right)}\left(\frac{D}{\phi_s d_p}\right)+1.75(1-\varepsilon)\left(\frac{\rho_g}{\rho_s}\right)\left(\frac{D}{\phi_s d_p}\right)\left|\vec{u}'_g-\frac{\sqrt{gD}}{u_o}\vec{u}'_s\right| \tag{27}$$

Upon inspection of (27), equation (25) can be rewritten as

$$\frac{u_o^2}{gD}\quad\frac{\rho_s}{\rho_g}\quad\frac{\rho_g u_o d_p}{\mu}\quad\frac{D}{d_p}\quad\phi_s. \tag{28}$$

In order to get the same dimensionless solution to the governing equations, the dimensionless boundary conditions must also be the same for the two beds. Hence, the boundary conditions must also be nondimensionalized. Geometric similarity is one scaling requirement that arises from nondimensionalizing the boundary conditions. For example, consider the no-slip boundary condition for the gas velocity (i.e., $\vec{u}_g = 0$) at an arbitrary solid boundary at z=L, say, where z is the direction opposite gravity.
Nondimensionalizing this boundary condition in terms of the dimensionless variables given in (16) and (18) gives:

$$\text{at } z' = \frac{L}{D},\ \vec{u}'_g = 0. \tag{29}$$

The dimensionless scaling parameter L/D reflects the need for the hot and cold-model beds to be geometrically similar.

Boundary conditions must be specified and nondimensionalized for the four dependent variables: $\vec{u}_g$, $\vec{u}_s$, ε, and p. Let the subscripts x and y denote the directions tangential and normal to a surface, respectively.

- Gas-phase velocity, $\vec{u}_g$

  At the distributor, $u_{gx}=0$ and $u_{gy} = u_o/\Delta$, where Δ is the fraction of open area in the distributor (i.e., A_{open}/A_{xs}). No new groups arise from the first boundary condition. Δ appears when the second boundary condition is nondimensionalized and reflects the need for geometric similarity. At all other solid surfaces $u_{gx}=u_{gy}=0$, which introduces no new parameters.

- Solid-phase velocity, $\vec{u}_s$

  The solid-phase velocity boundary conditions are less obvious. The solid phase velocity normal to a surface (u_{sy}) can be assumed to be 0, introducing no new parameters. Tangential to a surface, two assumptions are common–no-slip ($u_{sx}=0$) and free-slip boundary conditions ($\partial u_{sx}/\partial y = 0$). Again neither of these limiting conditions introduces any new parameters. Boundary conditions involving the particle and wall roughness can be envisioned; these additional factors are not considered here.

- Voidage, ε

  Voidage is a dimensionless variable. Hence, nondimensionalizing boundary conditions on the voidage (e.g., Dirichlet or Neumann) will only produce parameters requiring geometric similarity.

- Pressure, p

  Considering variations in pressure along the vertical axis of the bed, the freeboard is typically treated as a constant pressure outflow boundary (e.g., Syamlal et al. 1993). But the absolute pressure does not change sufficiently to influence the thermodynamic properties of the fluid; hence, parameters that depend on the absolute pressure are neglected in this development.

Finally, (28) can be expanded to give

$$\frac{u_o^2}{gD} \quad \frac{\rho_s}{\rho_g} \quad \frac{\rho_g u_o d_p}{\mu} \quad \frac{D}{d_p} \quad \frac{L}{D} \quad \phi_s \quad \text{PSD}. \tag{30}$$

These dimensionless groups will be referred to as the full set of scaling parameters. The first two parameters arise directly from nondimensionalizing the governing equations (Eqns. (21)-(24)). The particle Reynolds number must be matched in order for the dimensionless drag to be the same between two beds (Eqn. (27)). The remaining parameters are statements requiring geometric similarity between both the bed and the particle geometry. D/d_p and ϕ_s appear in the dimensionless drag term; ϕ_s and d_p are separated to maintain geometric similarity between the particles. Similarly, the dimensionless particle size distribution (PSD) is listed as an independent parameter to ensure geometric similarity between the distribution of particle sizes of both the hot and cold-model beds.

2.3.4 Simplifications to the Full Set of Scaling Parameters

2.3.4.1 Motivation for Pursuing Simplifications

The full set of scaling parameters have been verified extensively for atmospheric fluidized bed combustors (see Section 2.4). A scale model of an atmospheric fluidized bed combustor based on the full set of scaling parameters and fluidized with ambient air has dimensions that are one-quarter those of the hot combustor. But the full set of scaling parameters provides no size reduction for a scale model of a PFBC fluidized with ambient air. This is most easily demonstrated with an example.

Consider a pressurized fluidized bed combustor with the following geometry and operating conditions.

Operating/Geometric Parameter	Value
p (atm)	10
T (K)	1100
ρ_g (kg/m^3)	3.21
μ (kg/m-s)	4.5×10^{-5}
u_o (m/s)	1
D (m)	1
d_p (mm)	1

Only three of the dimensionless groups in (30) are required to determine the scale factor provided by the full set of scaling parameters–u_o^2/gD, $\rho_g u_o d_p/\mu$, and D/d_p. For this example, these three groups have the following values.

u_o^2/gD	0.102
$\rho_g u_o d_p/\mu$	71.3
D/d_p	1000

Now consider defining a cold model fluidized with ambient air and pressure that has the same values for these three groups. Matching these groups fixes the cold model: superficial gas velocity (u_o), overall bed dimensions (D), and mean particle size (d_p). The cold model geometry and operating conditions that satisfy the full set of scaling parameters are summarized in the following table.

Operating/Geometric Parameter	Value
p (atm)	1
T (K)	300
ρ_g (kg/m^3)	1.18
μ (kg/m-s)	1.9×10^{-5}
u_o (m/s)	1.05
D (m)	1.1
dp (mm)	1.1

The cold model has dimensions that are 10% larger than those of the hot combustor (i.e., $D_{cold}/D_{hot}=1.1$). For a large pressurized combustor, such as the Tidd PFBC scaled in this study, the required size of the cold model is impractical. Hence, it is desirable to identify a reduced set of scaling relationships that permits a scale factor to be supplied as a scaling input rather than determined by the scaling parameters themselves. The so-called simplified set of scaling parameters, which are developed in the next section, provide this additional flexibility.

2.3.4.2 Simplified Set of Scaling Parameters

The simplified set of scaling relationships arise by considering the dimensionless drag term, given by (27), in the limits of low and high particle Reynolds number. This behavior is clarified when (27) is written in terms of the minimum fluidization velocity (u_{mf}). Expressions for the minimum fluidization velocity in the two Reynolds number limits are developed using the Ergun (1952) drag equation. At minimum fluidization, the weight of the bed material is balanced by the drag on the particles, hence

$$\rho_s g(1-\varepsilon_{mf}) = 150\frac{(1-\varepsilon_{mf})^2}{\varepsilon_{mf}^3}\frac{\mu u_{mf}}{(\phi_s d_p)^2} + 1.75\frac{(1-\varepsilon_{mf})}{\varepsilon_{mf}^3}\frac{\rho_g u_{mf}^2}{\phi_s d_p}. \tag{31}$$

At low particle Reynolds numbers, the first term on the right hand side of (31) dominates. Neglecting the second term and solving for u_{mf} gives the following expression, which is valid in the limit of low particle Reynolds numbers.

$$u_{mf} = \frac{\rho_s g \varepsilon_{mf}^3 (\phi_s d_p)^2}{150(1-\varepsilon_{mf})\mu}. \tag{32}$$

At high particle Reynolds numbers, the second term on the right hand side of (31) dominates. Neglecting the first term and solving for u_{mf} gives the following high particle Reynolds number u_{mf} expression.

$$u_{mf} = \sqrt{\frac{(\phi_s d_p)\rho_s g \varepsilon_{mf}^3}{1.75\rho_g}}. \tag{33}$$

Similarly, at low particle Reynolds numbers, the first term on the right hand side of (27) dominates. Neglecting the second term on the right hand side of (27) and combining this with (32) gives

$$\frac{\beta D}{\rho_s u_o} = \frac{\varepsilon_{mf}^3}{\varepsilon}\frac{(1-\varepsilon)^2}{(1-\varepsilon_{mf})}\left(\frac{u_o}{u_{mf}}\right)\left(\frac{gD}{u_o^2}\right). \tag{34}$$

At high particle Reynolds numbers, the second term on the right hand side of (27) dominates. Neglecting the first term on the right hand side of (27) and combining this with (33) gives

$$\frac{\beta D}{\rho_s u_o} = \left(\frac{u_o}{u_{mf}}\right)^2 \left(\frac{gD}{u_o^2}\right) \varepsilon_{mf}^3 (1-\varepsilon) \left| \vec{u}'_g - \frac{\sqrt{gD}}{u_o} \vec{u}'_s \right| . \tag{35}$$

Comparing (34) and (35) shows that in the limits of both low and high Reynolds numbers, (25) can be rewritten as

$$\frac{L}{D} \quad \frac{u_o^2}{gD} \quad \frac{\rho_s}{\rho_g} \quad \frac{u_o}{u_{mf}} \quad \phi_s \quad \text{PSD}, \tag{36}$$

where ϕ_s and PSD are included to match ε_{mf} between two beds. The groups listed in (36) are referred to as the simplified set of scaling parameters. The assumption behind the simplified set of scaling parameters is that since the parameters are exact in the limits of high and low particle Reynolds numbers, they should be at least approximately valid for intermediate Reynolds numbers. There is an error associated with using the simplified set of scaling parameters at intermediate particle Reynolds numbers. The particle Reynolds number is no longer matched between the two beds, producing a mismatch in the dimensionless drag term, (27). An expression is developed in the following section to assess the magnitude of this error.

2.3.4.3 Evaluation of the Error Due to the Simplifications

Although the simplified set of scaling parameters give the same results in the limits of low and high particle Reynolds numbers, an error is introduced for intermediate Reynolds numbers. Equation (27) can be recast to evaluate this error. Dividing the left hand side of (27) by the first term on its right hand side gives

$$\left(\frac{\beta D}{\rho_s u_o}\right) \frac{\varepsilon \rho_s u_o (\phi_s d_p)^2}{150(1-\varepsilon)^2 \mu D} = 1 + \frac{1.75}{150} \left(\frac{\varepsilon \phi_s}{1-\varepsilon}\right) \left(\frac{\rho_g u_o d_p}{\mu}\right) \left| \vec{u}'_g - \frac{\sqrt{gD}}{u_o} \vec{u}'_s \right| . \tag{37}$$

Performing the same operation on (31) gives

$$\frac{\rho_s g \varepsilon_{mf}^3 (\phi_s d_p)^2}{150(1-\varepsilon_{mf}) \mu \varepsilon_{mf}} = 1 + \frac{1.75 \phi_s}{150(1-\varepsilon_{mf})} \left(\frac{u_{mf}}{u_o}\right) \left(\frac{\rho_g u_o d_p}{\mu}\right) . \tag{38}$$

Defining the particle Reynolds number as

$$Re_{dp} \equiv \frac{\rho_g u_o d_p}{\mu}, \tag{39}$$

and dividing (37) by (38) and introducing (39) gives

$$\frac{\beta D}{\rho_s u_o} = \left(\frac{\varepsilon_{mf}^3}{\varepsilon}\right)\frac{(1-\varepsilon)^2}{(1-\varepsilon_{mf})}\left(\frac{gD}{u_o^2}\right)\left(\frac{u_o}{u_{mf}}\right)\frac{1+\frac{1.75}{150}\left(\frac{\varepsilon\phi_s}{1-\varepsilon}\right)Re_{dp}\left|\vec{u}'_g - \frac{\sqrt{gD}}{u_o}\vec{u}'_s\right|}{1+\frac{1.75}{150}\left(\frac{u_{mf}}{u_o}\right)\frac{\phi_s}{(1-\varepsilon_{mf})}Re_{dp}}. \tag{40}$$

The error in the dimensionless drag parameter can be evaluated using (40) to calculate $\beta'_{cold}/\beta'_{hot}$ over a range of Re_{dp}, where $\beta' \equiv \beta D/\rho_s u_o$. The particle Reynolds number for the cold model is different from that of the hot bed because the particle diameter is not scaled down by the scale factor. Hence, even at a condition where all the simplified scaling parameters are matched, the particle Reynolds numbers between the two beds will be different. Chapter 3 presents an evaluation of the error associated with using the simplified set of scaling parameters to scale the Tidd PFBC.

2.4 Experimental Verification of the Hydrodynamic Scaling Parameters

A summary of the work done to experimentally verify hydrodynamic scaling in bubbling and circulating fluidized beds is presented below. Three unique sets of scaling laws were used in the experimental studies. To be consistent with the previous scaling law development, they will be referred to as: the full set of scaling laws (equation (30)), the simplified set of scaling laws (equation (36)), and the viscous-limit scaling laws. The viscous-limit scaling parameters are equivalent to the simplified set of scaling parameters except that they do not include the solid-to-gas density ratio. They are based on the assumption that the gas convective terms in (14) are negligible at low particle Reynolds numbers. The CFB scaling law proposed by Horio et al. (1989) can be shown to be equivalent to the simplified set of scaling laws. Horio et al. (1989) also discussed

simplifications to this set of scaling laws in which the solid-to-gas density ratio is omitted. This simplified law is equivalent to the bubbling bed scaling laws proposed earlier by Horio et al. (1986a) and have been shown by Glicksman (1988) to be equivalent to the viscous-limit scaling laws. As will be shown in Chapter 5, the solid-to-gas density ratio is not a parameter that can be omitted when scaling fluidized beds.

A number of studies have been conducted to establish the validity of the scaling relationships. Tables 1 and 2 give the values for the full set of scaling parameters for the bubbling bed and the circulating bed experimental studies, respectively. The values of other parameters used for scaling are included in the "Other Parameters" column. It was not the objective of all the studies to match each of these parameters, but the tables provide a summary of what groups were matched and how closely they were matched for each of the studies. Table 2, the circulating fluidized bed scaling summary table, includes the dimensionless solids flux ($G_s/\rho_s u_o$), which is an additional parameter that must be matched when scaling circulating fluidized beds. G_s is the solids flowrate recycled to the riser from the cyclone exit.

Table 1: Scaling Parameter Values for Bubbling Fluidized Bed Experimental Studies

Reference	Hot/Cold	$\rho_g u_o D / \mu$	$u_o^2 / g D$	ρ_s / ρ_g	L / D	D / d_p	ϕ_s	Scaling Laws	d_p (μm)	Other Parameters
Fitzgerald and Crane (1980)	Cold	8915-11138	.018-.027	126	1.0	234	N/A	Full	2068	Re_{dp}=38.1-47.6
	Cold	9259-11562	.018-.026	110	1.0	235			240	Re_{dp}=39.4-49.2
Fitzgerald, Bushnell, Crane, and Shieh (1984)	Hot	28881	0.33	8224	3.0	915	N/A	Full	2000	Re_{dp}=31.6
	Cold	32000	0.31	8214	3.0	920			500	Re_{dp}=34.8
Nicastro and Glicksman (1984)	Hot	4658	0.143	7280	7.21	901	0.80	Full	677	Re_{dp}=5.2
	Cold	4781	0.145	5920	7.21	897	0.80		170	Re_{dp}=5.3
Horio, Nonaka, Sawa, and Muchi (1986a)	Cold	3514	0.021	2117	Scaled	638	N/A	Simplified	376	Re_{dp}=5.5 u_o/u_{mf}=2.00
	Cold	954	0.022	2117		328			305	Re_{dp}=2.9 u_o/u_{mf}=1.97
	Cold	247	0.021	2117		174			236	Re_{dp}=1.4 u_o/u_{mf}=2.00
Horio, Takada, Ishida, and Tanaka (1986b)	Cold	4448	0.0024	2203	0.325	3297	N/A	Simplified	182	Re_{dp}=1.4 u_o/u_{mf}=4.4
	Cold	1520	0.0023	2203	0.327	2000			150	Re_{dp}=0.8 u_o/u_{mf}=4.6
	Cold	537	0.0023	2203	0.333	1163			129	Re_{dp}=0.5 u_o/u_{mf}=5.3
	Cold	105	0.0024	2203	0.340				106	Re_{dp}=0.2 u_o/u_{mf}=4.7
Newby and Keairns (1986)	Cold	1134-2523	.00068-.0034	2091	1.67	1800	N/A	Full	200	Re_{dp}=0.63-1.40 u_o/u_{mf}=1.0-2.2
	Cold	1134-2523	.00068-.0034 .00062-.0032	2484	1.67	1800			200	Re_{dp}=0.63-1.40 u_o/u_{mf}=1.1-2.5
	Cold	1059-2406		2332	1.67	1800			100	Re_{dp}=0.59-1.34 u_o/u_{mf}=1.1-2.5
Zhang and Yang (1987)	Cold	65784	0.135	2208	0.462	1137	Matc	Simplified	805	Re_{dp}=58 u_o/u_{mf}=1.8
	Cold	12658	0.135	2208	0.422	529	hed		577	Re_{dp}=24 u_o/u_{mf}=1.8
	Cold	77147	0.185	2208	0.462	1137			805	Re_{dp}=68 u_o/u_{mf}=2.1
	Cold	14792	0.184	2208	0.422	529			577	Re_{dp}=28 u_o/u_{mf}=2.1
	Cold	88510	0.244	2208	0.462	1137			805	Re_{dp}=78 u_o/u_{mf}=2.4
	Cold	16984	0.243	2208	0.422	529			577	Re_{dp}=32 u_o/u_{mf}=2.4

Table 1: Scaling Parameter Values for Bubbling Fluidized Bed Experimental Studies

Reference	Hot/Cold	$\rho_g u_o D / \mu$	$u_o^2 / g D$	ρ_s / ρ_g	L / D	D / d_p	ϕ_s	Scaling Laws	d_p (μm)	Other Parameters
Roy and Davidson (1989)	Hot	923	0.462	6667	N/A	225	N/A	Full/Vis-	600	Re_{dp}=4.1 u_o/u_{mf}=5.2
	Cold	1375	0.490	5882		250		cous Limit	180	Re_{dp}=5.5 u_o/u_{mf}=5.0
	Cold	2970	2.100	5882		90			500	Re_{dp}=33 u_o/u_{mf}=1.6
	Cold	5250	5.950	5882		50			900	Re_{dp}=105 u_o/u_{mf}=1.3
	Cold	1388	0.436	2041		188			240	Re_{dp}=7.4 u_o/u_{mf}=6.1
	Cold	5835	0.026	3030		1167			240	Re_{dp}=5 u_o/u_{mf}=13.5
	Cold	6664	0.026	3448		833			120	Re_{dp}=8 u_o/u_{mf}=16.0
	Cold	1250	0.029	2041		833			120	Re_{dp}=1.5 u_o/u_{mf}=8.5
	Cold	4667	0.032	2041		1167			240	Re_{dp}=4 u_o/u_{mf}=4.6
	Cold	11636	0.058	3448		182			550	Re_{dp}=64 u_o/u_{mf}=2.7
	Cold	2184	0.084	2041		182			550	Re_{dp}=12 u_o/u_{mf}=2.1
Almstedt and Zakkay (1990)	Hot	54135	0.21	913	3.13	811	0.82	Full	962	Re_{dp}=66.8
	Cold	53861	0.21	1068	3.12	811	0.75		486	Re_{dp}=66.4
	Cold	53861	0.21	911	3.12	811	0.82		486	Re_{dp}=66.4
	Cold	53861	0.21	911	3.12	410	0.82		962	Re_{dp}=131.4
Di Felice, Rapagna, and Foscolo (1992a)	Cold	1468-8922	.009-.331	1126	N/A	322	1.0	Full	597	Re_{dp}=4.6-27.7 u_o/u_{mf}=1.0-5.3
	Cold	1351-8025	.010-.340	1128		305	1.0		348	Re_{dp}=4.4-26.3 u_o/u_{mf}=1.0-5.4
	Cold	1395-8367	.009-.333	1136		313	1.0		158	Re_{dp}=4.6-26.7 u_o/u_{mf}=1.0-5.0
	Cold	1173-7330	.007-.290	1007		304	0.6		163	Re_{dp}=3.9-24.1 u_o/u_{mf}=0.4-2.7
	Cold	1468-8809	.009-.323	24444		552	1.0		348	Re_{dp}=2.7-16.0 u_o/u_{mf}=1.1-6.5
Di Felice, Rapagna, Foscolo, and Gibilaro (1992b)	Cold	31.3-500.4	$(.21\text{-}53)10^{-5}$	769	5.5	3536	N/A	Full	14	Re_{dp}=0.0009-0.14
	Cold	18.4-402.6	$(.14\text{-}65)\ 10^{-5}$	794	4.5	2824			68	Re_{dp}=0.007-0.14
	Cold	2078-6928	.0216-.2405	1100	2.8,5.6*	305			348	Re_{dp}=6.8-22.7
	Cold	2186-7765	.0192-.2420	1105	2.6,5.2*	322			597	Re_{dp}=6.8-24.1
* Slugging Cases	Cold	15242-35564	.346-1.89	2000	1.0,2.0*	112			950	Re_{dp}=136.1-317.5
	Cold	24714-37895	.834-1.96	2036	1.1,2.1*	115			2400	Re_{dp}=214.9-329.5
Glicksman and Farrell (1995)	Hot	188330	0.025	898	scaled	3995	0.82	Simplified	851	Re_{dp}=47.1 u_o/u_{mf}=3.8
	Cold	22637	0.025	835		1396	0.85		609	Re_{dp}=16.2 u_o/u_{mf}=3.8

Table 2: Scaling Parameter Values for Circulating Fluidized Bed Experimental Studies

Reference	Hot/Cold	$\rho_g u_o D / \mu$	$u_o^2 / g D$	ρ_s / ρ_g	L / D	D / d_p	$G_s/\rho_s u_o$	ϕ_s	Scaling Laws	d_p (μm)	Other Parameters
Horio, Ishii, Kobukai, and Yamanishi (1989)	Cold Cold	9885-16063 1236-2008	0.33-0.86 0.33-0.86	1508 1508	8 8	2528 816	.0028-.0052 .0028-.0052	N/A	Simplified	79 61	Re_{dp}=3.9-6.4 u_o/u_{mf}≈229-371 Re_{dp}=1.5-2.5 u_o/u_{mf}≈190-310
Ishii and Murakami (1991)	Cold Cold	9885-14827 1236-1853	.326-.734 .326-.734	1508 1508	N/A	3263 1078	.0056-.0037 .0056-.0037	N/A	Simplified	61 46	Re_{dp}=3.0-4.5 u_o/u_{mf}=381-571 Re_{dp}=1.1-1.7 u_o/u_{mf}=333-500
Tsukada, Nakanishi, Takei, Ishii, and Horio (1991)	Cold Cold Cold	1518 2736 5327	0.510 0.510 0.510	1534 852 437	8 8 8	1078 1078 1078	0.0067 0.0067 0.0067	N/A	Viscous Limit	46 46 46	Re_{dp}=1.4 u_o/u_{mf}=417 Re_{dp}=2.5 u_o/u_{mf}=417 Re_{dp}=4.9 u_o/u_{mf}=417
Glicksman, Westphalen, Brereton, and Grace (1991)	Hot Cold	6984 6785	66.94 66.54	8700 6000	48.7 48.0	822 646	0.0017 0.0016	N/A N/A	Full	185 52	Re_{dp}=8.5 Re_{dp}=10.5
Chang and Louge (1992)	Cold Cold Cold Cold	15630 22977 53454 22977	13.84 9.34 4.20 9.34	4800 4961 4966 4961	35 35 35 35	855 1835 2985 1835	0.0044 0.0042 0.0020 0.0020	0.69 1.0 0.73 1.0	Full	234 109 67 109	Fr^*=131 M=21 Ar^*≈45 R≈4880 Fr^*=131 M=10 Ar^*≈47 R≈4964
Glicksman, Hyre, and Westphalen (1993a)	Hot Cold	29170 30369	5.26 5.63	8500 6200	11.43 11.25	2917 2759	0.0013 0.0011	N/A	Full	240 58	Re_{dp}=10.0 Re_{dp}=11.0

Table 2: Scaling Parameter Values for Circulating Fluidized Bed Experimental Studies

Reference	Hot/Cold	$\rho_g u_o D/\mu$	u_o^2/gD	ρ_s/ρ_g	L / D	D / d_p	$G_s/\rho_s u_o$	ϕ_s	Scaling Laws	d_p (μm)	Other Parameters
Glicksman, Hyre, and Woloshun (1993b)	Cold	3211-5352	7.1-19.7	2117	14.2	412	$(4\text{-}7)10^{-3}$	1.0	Viscous	79	Re_{dp}=7.8-13.0 u_o/u_{mf}=106-176
	Cold	3211-5352	7.1-19.7	1167	14.2	326	$(4\text{-}7)10^{-3}$	.6-.8	Limit	100	Re_{dp}=9.9-16.5 u_o/u_{mf}=176-294
	Cold	25699-45146	7.1-19.6	2117	14.1	1158	$(4\text{-}7)10^{-3}$	1.0	Simplified	112	Re_{dp}=22.2-39.0 u_o/u_{mf}=104-174
	Cold	3171-5286	7.2-19.9	2117	14.4	407	$(4\text{-}7)10^{-3}$	1.0		79	Re_{dp}=7.8-13.0 u_o/u_{mf}=106-176
	Cold	24030-43020	7.1-19.6	1167	14.1	900	$(2\text{-}3)10^{-3}$	.6-.8	Simplified	145	Re_{dp}=26.7-47.8 u_o/u_{mf}=200-333
	Cold	3188-5313	7.2-19.9	1167	14.4	322	$(2\text{-}3)10^{-3}$	.6-.8		100	Re_{dp}=9.9-16.5 u_o/u_{mf}=176-294
	Hot	27975-36938	5.6-9.9	8400	12.2	2716	$(.5\text{-}1.8)10^{-3}$	N/A	Full /	243	Re_{dp}=10.3-13.6
	Cold	25008-31993	7.1-12.5	6200	14.1	2253	$(.5\text{-}1.8)10^{-3}$	.6-.8	Simplified	58	Re_{dp}=11.1-14.2 u_o/u_{mf}=214-286
	Cold	3891-5075	5.7-10.2	6200	14.4	1538	$(.5\text{-}1.8)10^{-3}$	.6-.8		26	Re_{dp}=2.5-3.3 u_o/u_{mf}=200-267
Glicksman, Hyre, Torpey, and Wheeldon (1995)	Hot	43430	3.66	758	40.9	1230	0.016	0.84	Simplified	165	Re_{dp}=35.3 u_o/u_{mf}=113
	Cold	12530	3.62	758	40.9	564	0.016	0.85		180	Re_{dp}=22.2 u_o/u_{mf}=107
	Hot	53149	4.40	681	40.9	1230	0.016	0.84	Simplified	165	Re_{dp}=43.2 u_o/u_{mf}=124
	Cold	13771	4.38	758	40.9	564	0.016	0.85		180	Re_{dp}=24.4 u_o/u_{mf}=118
	Hot	48228	4.02	718	40.9	1230	0.015	0.84	Simplified	165	Re_{dp}=39.2 u_o/u_{mf}=118
	Cold	13207	4.01	758	40.9	564	0.015	0.85		180	Re_{dp}=23.4 u_o/u_{mf}=113
	Hot	49212	3.85	688	40.9	1230	0.0035	0.84	Simplified	165	Re_{dp}=40.0 u_o/u_{mf}=116
	Cold	12925	3.85	758	40.9	564	0.00.5	0.85		180	Re_{dp}=22.9 u_o/u_{mf}=111

2.4.1 Bubbling Fluidized Beds

Fitzgerald and Crane (1980) performed one of the first evaluations of the full set of hydrodynamic scaling parameters. They compared the hydrodynamics of two scaled beds using pressure fluctuation measurements and movies. In one bed, cork particles were fluidized with air; the other consisted of sand fluidized with pressurized refrigerant-12 vapor. Movies showed qualitative agreement between bubble growth and the solids flow in the beds. The ratio of the bed minimum fluidization velocities was within 20% of the theoretical value; the difference was attributed to the angular shape of the cork particles (ϕ_s was not matched between the beds). The fast Fourier transform of the pressure fluctuations was used to determine the average frequency of the fluctuations. The ratio of average frequencies for the two beds was in fair agreement with the theoretical velocity-time scale factor. The pressure fluctuation data were taken with a single bed pressure tap. This may be responsible for level of agreement in the frequency ratios. Some additional qualitative slugging comparisons were made using movies of bed behavior; the slugs appeared to have the same scaled lengths and velocities.

Fitzgerald et al. (1984) measured pressure fluctuations in an atmospheric fluidized bed combustor and a quarter scale cold model. The full set of scaling parameters was matched between the beds. The autocorrelation function of the pressure fluctuations was similar for the two beds but not within the 95% confidence levels they anticipated. The amplitude of the autocorrelation function for the hot combustor was significantly lower than that for the cold model. Also, the experimentally determined time-scaling factor differed from the theoretical value by 24%. They suggested that the differences could be due to electrostatic effects. Particle sphericity and size distribution were not discussed; failure to match these could also have influenced the hydrodynamic similarity of the two beds. Bed pressure fluctuations were measured using a single pressure point which may not accurately represent the local hydrodynamics within the bed. Similar results were obtained

between two two-dimensional beds–a bed of reacted limestone fluidized with helium and a half-scale bed of copper fluidized with air.

Nicastro and Glicksman (1984) experimentally verified the full set of scaling laws for bubbling fluidized beds. They compared the time-resolved differential pressure measurements from a bubbling fluidized bed combustor and a scaled cold model. Good agreement was obtained between the spectral content and the probability density distribution of the differential pressure fluctuations of the hot combustor and the cold model. They concluded that hydrodynamic similarity had been achieved between the hot combustor and the cold model. When actual hot-bed material was used in the cold model, a violation of the scaling laws, the model's behavior was shown to be different from that of the hot bed.

Horio et al. (1986a) used three geometrically similar bubbling beds, fluidized with ambient air, to verify their proposed scaling laws. The solid-to-gas density ratio was not varied in the experiments although it was not one of their proposed scaling parameters. By including the density ratio, Horio et al. (1986a), in essence, used the simplified set of scaling parameters. Video analysis of bubble eruptions at the bed surface was used to determine the cross-sectional average: bubble diameter, bubble diameter distribution, and radial distribution of superficial bubble velocity. Similarity was achieved in these hydrodynamic parameters when bed Froude number, density ratio, and the ratio of superficial-to-minimum fluidization velocities were matched.

Horio et al. (1986b) verified Horio's (1986a) bubbling bed scaling laws for solid mixing and segregation. Sand was used as a bed material in straight and tapered bed geometries. A bed sectioning technique was used to measure the transient radial dispersion coefficient and the distribution of float tracers. They concluded that bed mixing and the behavior of floating bodies obey the scaling laws in both straight and tapered beds. The solid-to-gas density ratio was held constant in the tests, satisfying the simplified set of scaling laws.

Newby and Keairns (1986) made bubbling bed scaling comparisons between two cold models using the full set of scaling laws. One bed fluidized two different 200 μm glass powders using ambient air. The second bed, which was a half-scale model of the first, used pressurized air to fluidize 100 μm steel powder. High-speed movies showed good agreement between the nondimensional bubble frequencies in the two beds. They also found reasonably good agreement between the nondimensional amplitudes of the pressure fluctuations in the beds.

Zhang and Yang (1987) carried out scaling comparisons between two two-dimensional beds with u_o^2/gD and u_o/u_{mf} matched between them. They also inadvertently kept the solid-to-gas density ratio constant and thus matched the simplified scaling parameters. They found, through photographs, that the beds appeared qualitatively similar. The beds also had similar dimensionless freeboard entrainment rates and dimensionless bed heights over a range of u_o/u_{mf}.

Roy and Davidson (1989) considered the validity of the full and viscous limit scaling laws at elevated pressures and temperatures. The nondimensional dominant frequency and amplitude of the pressure-drop fluctuations were used as the basis of the comparison. They concluded that when the full set of scaling parameters is matched, similarity is achieved. They also suggested that it is not necessary to match the density ratio (ρ_s/ρ_g) and d_p/D for particle Reynolds numbers (Re_{dp}) less than 30 (i.e., viscous limit scaling). Although, the run with Re_{dp} of 33 had the same density ratio as the low Re_{dp} runs. These conclusions may be open to different interpretations. As shown in Table 1, the scaling parameters were neither matched closely nor varied in a systematic manner.

Almstedt and Zakkay (1990) made scaling comparisons between a hot PFBC and a pressurized cold scale model using the full set of scaling laws. A capacitance probe was used to measure the mean values of the: bubble frequency, mean pierced length, bubble rise velocity, and bubble volume fraction. Scaling comparisons were made using the dimensionless form of these dependent hydrodynamic parameters. Three different bed

materials were used in the cold bed–Olivine sand and two different size distributions of the hot-bed material. One of the hot-bed material size distributions was properly scaled and the other was out of scale. The sand had a lower sphericity and higher density than the hot-bed material, making it possible to investigate the sensitivity of the scaling to small variations in the density ratio and the particle sphericity. The out-of-scale hot-bed material was also used to illustrate the sensitivity of the scaling to the D/d_p parameter. The nondimensional form of the capacitance probe measurements agreed within 25% for the sand and the properly scaled hot-bed material; the agreement was best in the upper part of the bed. The properly scaled hot-bed material showed only slightly better agreement than that for the sand, but the mismatch in the density ratio and the sphericity for the sand was small. The improperly scaled hot-bed material had a maximum deviation of 38% from the hydrodynamics of the hot-bed combustor. They concluded that a properly scaled cold model can be used to achieve hydrodynamic behavior that is similar to that of a pressurized fluidized bed combustor.

Di Felice et al. (1992a) investigated the validity of the full set of scaling laws for bubbling and slugging fluidized beds. They used an experimental facility that permitted the pressurization of different diameter test sections to match the scaling parameters. Minimum fluidization measurements, video measurements of bed expansion, and pressure fluctuation data were used to compare the similarity of five different bed configurations. Three of the beds were scaled properly, the fourth had a mismatched particle sphericity, and the fifth bed was purposely mis-scaled relative to the others (see Table 1). The voidage at minimum fluidization was found to be the same for all the beds except the one with the different particle sphericity. In the bubbling regime, good agreement in the nondimensional bed expansion measurements was obtained for all but the bed with the mis-scaled particle sphericity. The lower particle sphericity increased u_{mf} for the system which effectively shifted the bed expansion curve for this case. The pressure fluctuations for the three properly scaled beds in the bubbling regime showed good agreement, while the mis-scaled beds exhibited poor agreement with the other three. The two sets of data that deviate from the other three correspond to the mis-scaled beds.

In the slugging regime Di Felice et al. (1992a) found that the bed expansion characteristics were similar to those in the bubbling regime, but the pressure fluctuation characteristics for all five beds were in poor agreement with each other. They attributed this to the importance of particle material properties and particle-particle interactions, which are not accounted for in the full set of scaling laws.

Di Felice et al. (1992b) evaluated the full set of scaling laws for three different Geldart (1973) powder categories (A,B, and D) in the bubbling and slugging fluidization regimes. Pressure fluctuations were used as the basis for the scaling comparisons. In the bubbling regime, the RMS and dominant frequencies of the pressure fluctuations showed good agreement for all three powder categories. Only Geldart groups B and D were considered in the slugging regime. They exhibited fair agreement in the RMS of their pressure fluctuations, but their dominant frequencies agreed poorly. They found that the full set of scaling laws are valid for bubbling beds fluidizing powders in Geldart groups A, B, and D. They also concluded that the full set of scaling laws should not be used for slugging beds where particle-particle interactions are thought to be important.

Glicksman and Farrell (1995) verified the simplified set of scaling parameters for use with pressurized bubbling fluidized bed combustors. Chapters 3 and 4 describe this work in detail.

He et al. (1996) investigated hydrodynamic scaling in spouted beds. They found that it was necessary to supplement Glicksman's (1984) full set of scaling parameters with two additional dimensionless groups–the internal angle of friction and the loose-packed voidage. These parameters characterize the particle-particle interaction forces that are believed to be important in the annulus of spouted beds, which behaves like a moving packed bed. They found that when the original full set of scaling parameters plus the internal angle of friction and the loose-packed voidage were matched between two

spouted beds, good agreement was obtained between their maximum spoutable bed height, spout diameter, fountain height, and longitudinal pressure profiles.

2.4.2 Circulating Fluidized Beds

Horio et al. (1989) experimentally verified their proposed circulating fluidized bed (CFB) scaling laws. The solid-to-gas density ratio was not varied in the tests, hence they effectively verified the simplified set of scaling laws. Two cold scaled CFBs fluidized using ambient air were used in the verification. Good agreement in the axial solid fraction profiles was obtained for most of the conditions tested. A "choking-like transition" was found to occur for cases with higher solids fluxes and lower gas superficial velocities. A discrepancy in the "choking" transition point for the two beds was attributed to differences in the geometry of the bed exit and the solids recycle lines. The transition point was found to be very sensitive to the particle-size ratio. An optical probe was used to verify similarity in the annular flow structures and the cluster velocities.

Ishii and Murakami (1991) evaluated Horio et al.'s (1989) CFB scaling relationships using two cold CFB models. Solids flux, pressure drop, and optical probe measurements were used to measure a large number of hydrodynamic parameters to serve as the basis for the comparison. Fair-to-good similarity was obtained between the beds. Dependent hydrodynamic parameters such as: pressure drop and pressure fluctuation characteristics, cluster length and voidage, and the core diameter were compared between the two beds. The gas-to-solid density ratio was not varied between the beds. As seen in Table 2, the dimensionless solids flux decreased as the superficial velocity was increased because the solids flux was held constant.

Tsukada et al. (1991) applied Horio et al.'s (1989) CFB scaling laws at several different elevated pressures (viscous-limit scaling laws). A single bed and bed material were used in the study. A pressure vessel was used to vary the gas pressure. The bed was fluidized

with ambient temperature air at three different pressures (0.1, 0.18, and 0.35 MPa). Axial solid fraction profiles and optical probe measurements were used as the basis for their similarity comparison. They found that as the pressure was increased the axial solid fraction profile changed, indicating a change in the hydrodynamics. It was suggested that the effect on the axial solid fraction profile could be due to reaching a Reynolds number limit; e.g., the upper boundary for the viscous limit. They also suggest that it could be due to a change in gas bypassing between the riser and the downcomer. The only parameter that was not matched in this study that had been matched in previous verifications of Horio et al.'s (1989) scaling relationships is the solid-to-gas density ratio. It is likely, based on the recent results of Glicksman et al. (1993b), that this is the cause of the pressure effect on the bed hydrodynamics.

Glicksman et al. (1991) made scaling comparisons between an experimental circulating fluidized bed combustor and a scaled cold model based on the full set of scaling laws. The time-resolved pressure fluctuations and the time-averaged pressure drop were measured. Due to uncertainties in the hot-bed solid circulation measurements, the cold-bed solids flux was adjusted until the average bed solid fraction matched that of the hot bed. The vertical solid fraction profiles, and the probability density function and the Fourier transform of the pressure fluctuations were compared between the hot and cold bed. Good agreement was obtained between the vertical solid fraction profiles except near the top of the beds. It was suggested that the differences in the solid fraction profiles at the top of the bed could be due to protrusions or wall roughness in the hot bed that were not modeled in the cold bed. Good agreement was also obtained in the comparison of the probability density distributions and the Fourier transforms of the pressure fluctuations.

Chang and Louge (1992) carried out tests on a circulating bed in which they could vary the gas composition. By combining this with particles of different density and size, they are able to scale a series of different size hot commercial beds with diameters up to five times larger than the cold bed. Comparisons between glass and plastic particles show identical mean vertical solids fraction profiles. $Fr^{*}=u_o^2/g\phi_s d_p$ was matched in the

comparisons, whereas Froude number based on bed diameter (D) could not be matched since the experimental bed diameter was fixed in the tests. The inability to alter the bed diameter also made it impossible to match the D/d_p scaling parameter. Particle sphericity is not explicitly included as an independent parameter, rather it is included with the particle diameter based on a combination of the gas-to-particle drag coefficient. The values of the parameters matched for scaling are presented in the "Other Parameters" column of Table 2. Steel and glass particles were also compared. The level of agreement when steel and glass were used was poor because the bed using the steel particles was choked while the bed with glass particles was not. Yang's (1983) correlation indicates that choking is a strong function of the Froude number based on bed diameter (Fr_D). Fr_D could not be matched between the beds, which caused them to choke under different conditions.

Glicksman et al. (1993a) evaluated the full set of scaling laws for circulating fluidized beds. Solid fraction data were obtained from the 2.5 MW_{th} Studsvik CFB prototype. The full set of scaling laws were evaluated through solid fraction profile comparisons between the Studsvik bed and a 1/4 scale cold model. Fairly good agreement was obtained; the profiles most closely matched in the top of the beds. Differences between the profiles were attributed to uncertainty in the hot-bed solid flux measurements and to the mismatch in the solid-to-gas density ratio.

The viscous-limit scaling laws were also evaluated by Glicksman et al. (1993b) in a series of two tests with circulating beds. Scaling was attempted between glass-steel and glass-plastic (i.e., different density ratios) in the same bed. The average solid fraction profiles, the solid fraction probability density functions, and the power spectral densities were all in poor agreement. It is believed that the beds were operating near the point of incipient choking condition, as predicted by the Yang (1983) correlation. Because this correlation indicates that choking is a strong function of the solid-to-gas density ratio, it was concluded that the viscous-limit scaling parameters are unable to model bed hydrodynamics near the boundary between different flow regimes. They concluded that since low u_o is required for the viscous-limit scaling to be valid, while sufficiently high u_o is

required to prevent choking, the applicability of the viscous-limit scaling parameters for CFBs is limited.

The simplified set of scaling laws were used by Glicksman et al. (1993b) to scale between properly-sized plastic and glass particles in two geometrically similar beds. The average solid fraction profiles showed excellent agreement. The probability density functions and power spectral densities also agreed well. In contrast to the viscous-limit scaling results, the simplified scaling laws gave good agreement even for conditions where Yang's (1983) correlation predicted the beds were choked.

Glicksman et al. (1993b) verified the simplified scaling laws for hot beds by comparing the solid fraction profiles for the Studsvik CFB prototype, the 1/4 scale cold model, and a 1/16 scale cold model. The average solid fraction profiles were in good agreement for most of the conditions tested. The agreement was excellent between the 1/4 scale cold model, which utilized the full set of scaling laws, and the 1/16 scale model, which utilized the simplified set of scaling laws. Hence, any disagreement between the Studsvik bed and the 1/16 scale model is not due to the simplifications of the full set of scaling laws. The density ratio was not matched exactly between the hot bed and the two cold beds, which may have affected the agreement. They concluded that the simplified set of scaling laws, which includes the solid-to-gas density ratio, gives acceptable results over a wide range of particle densities and bed sizes, even when the length ratio is as small as 1/16.

Glicksman et al. (1995) verified the simplified set of scaling parameters for use with pressurized circulating fluidized bed combustors in a study done in parallel with this thesis. They compared the hydrodynamics of a Foster Wheeler pressurized CFB and a half-scale cold model. The dimensionless pressure fluctuations were compared between the two beds. Good agreement was obtained between the solid fraction profiles, the probability density functions, and the fast Fourier transforms of the pressure data from the two beds.

The validity of the full set of scaling parameters has been demonstrated for bubbling and circulating fluidized beds. The viscous-limit scaling parameters do not appear generally applicable. The simplified set of scaling parameters, which includes the viscous-limit scaling parameters and the solid-to-gas density ratio, has been verified for atmospheric and pressurized circulating beds. The verification of the simplified set of scaling parameters for pressurized bubbling beds is the subject of the present work.

2.5 Nomenclature

A_{open}	open area of distributor
Ar	Archimedes number=$\left(\rho_s - \rho_g\right)\rho_g g d_p^3 / \mu^2$
A_{xs}	bed cross-sectional area
D	reference bed dimension
d_p	mean particle diameter
F_D	drag force
Fr_D	Froude number based on reference bed dimension, D; $= u_o^2/gD$
g	acceleration due to gravity=9.807 m/s^2
G_s	CFB solids flux
L	bed dimension
p	gas pressure
p'	dimensionless gas pressure=$p/\rho_s gD$
PSD	dimensionless particle size distribution
Re_{mf}	particle Reynolds number at minimum fluidization conditions
Re_{dp}	particle Reynolds number at operating superficial gas velocity, u_o
t	time
t'	dimensionless time=tu_o/D
T	temperature
$\vec{u}_g$	gas-phase velocity
$\vec{u}'_g$	dimensionless gas-phase velocity= $\vec{u}_g/u_o$
u_o	superficial gas velocity
u_{mf}	minimum fluidization velocity
$\vec{u}_s$	solid-phase velocity
$\vec{u}'_s$	dimensionless solid-phase velocity = $\vec{u}_s/\sqrt{gD}$

Greek Symbols

β	particle-assembly drag coefficient
β'	dimensionless drag coefficient = $\beta D/\rho_s u_o$
Δ	fraction of distributor area that is open
Δp	differential pressure drop
ε	local voidage
ε_{mf}	voidage at minimum fluidization conditions
ϕ_s	particle sphericity
μ	gas viscosity
ρ_g	gas density
ρ_s	solid density

2.6 References

Almstedt, A.E. and Zakkay, V., 1990, "An Investigation of Fluidized-Bed Scaling - Capacitance Probe Measurements in a Pressurized Fluidized-Bed Combustor and a Cold Model Bed," *Chemical Engineering Science*, 45, No. 4, pp. 1071-1078.

Bagnold, R.A., 1954, "Experiments on a gravity-free dispersion of large solid spheres in a Newtonian fluid under shear," *Proc. Royal Soc. London*, A225, pp. 49-63.

Boemer, A., Qi, H., Renz, U., Vasquez, S., and Boysan, F., 1995, "Eulerian Computation of Fluidized Bed Hydrodynamics-A Comparison of Physical Models," Proceedings of the 13th International Conference on Fluidized Bed Combustion, Kissimmee, FL, pp. 775-787.

Buckingham, E., 1914, "On Physically Similar Systems: Illustrations of the Use of Dimensional Equations," Physical Review, Vol. 4, p. 345.

Campbell, C.S. and Wang, D.G., 1991, "Particle pressures in gas-fluidized beds," *Journal of Fluid Mechanics*, 227, pp. 495-508.

Chang, H., and Louge, M., 1992, "Fluid Dynamic Similarity of Circulating Fluidized Beds," *Powder Technology*, 70, p. 259.

Chapman, S. and Cowling, T.G., 1970, The Mathematical Theory of Non-Uniform Gases, 3rd Edition, Cambridge University Press., Cambridge.

Clift, R. and Rafailidis, S., 1993, "Interparticle Stress, Fluid Pressure, and Bubble Motion in Gas-Fluidised Beds," *Chemical Engineering Science*, 48, 9, pp. 1575-1582.

Davidson, J.F., Paul, R.C., Smith, M.J.S., and Duxbury, H.A., 1959, "The Rise of Bubbles in a Fluidised Bed," *Trans. Inst. Chem. Engrs.*, 37, pp. 323-328.

Davidson, J.F., 1961, *Trans. Inst. Chem. Engrs.*, 39, p. 230. Davidson, J.F. and Harrison, D., 1963, Fluidised Particles, Cambridge University Press, Cambridge.

Davies, R.M., and Taylor, G.I, 1950, "The mechanics of large bubbles rising through extended liquids and through liquids in tubes," *Proceedings of the Royal Society of London*, A200, p. 375-390.

Di Felice, R., Rapagna, S., and Foscolo, P.U., 1992a, "Dynamic Similarity Rules: Validity Check for Bubbling and Slugging Fluidized Beds," *Powder Technology*, 71, pp. 281-287.

Di Felice, R., Rapagna, S., Foscolo, P.U., and Gibilaro, L.G., 1992b, "Cold Modelling Studies of Fluidised Bed Reactors," *Chemical Engineering Science*, 47, 9-11, pp. 2233-2238.

Ding, J. and Gidaspow, D., 1990, "A Bubbling Fluidization Model Using Kinetic Theory of Granular Flow," *AIChE Journal*, 36, 4, pp. 523-538.

Drew, D.A., 1992, "Analytical Modeling of Multiphase Flows," Modern Developments and Advances in Boiling Heat Transfer, ed. R.T. Lahey, Jr., Elsevier, pp. 31-84.

Ergun, S., 1952, "Fluid Flow Through Packed Columns," *Chemical Engineering Progress*, 48, pp. 89-94.

Fitzgerald, T. J. and Crane, S.D., 1980, "Cold Fluidized Bed Modeling," Proceedings of The Sixth International Conference on Fluidized Bed Combustion, Volume III, Atlanta, GA, pp. 815-820.

Fitzgerald, T., Bushnell, D., Crane, S., and Shieh, Y., 1984, "Testing of Cold Scaled Bed Modeling for Fluidized-Bed Combustors," *Powder Technology*, 38, pp. 107-120.

Geldart, D., 1973, "Types of Gas Fluidization," *Powder Technology*, 7, pp. 285-292.

Gidaspow, D., and Ettehadieh, B., 1983, "Fluidization in Two-Dimensional Beds with a Jet: 2. Hydrodynamics Modeling," *I&EC Fundamentals*, 22, p. 193.

Glicksman, L.R., 1984, "Scaling Relationships for Fluidized Beds," Chemical Engineering Science, Vol. 39, No. 9, pp. 1373-1379.

Glicksman, L.R., 1988, "Scaling Relationships for Fluidized Beds," *Chemical Engineering Science*, 43, 6, pp. 1419-1421.

Glicksman, L.R., Westphalen, D., Brereton, C., and Grace, J., 1991, "Verification of the Scaling Laws for Circulating Fluidized Beds," in Circulating Fluidized Bed Technology III, P. Basu, M. Horio, and M. Hasatani, eds., Pergamon Press, p. 119.

Glicksman, L.R., Hyre, M.R., and Westphalen, D., 1993a, "Verification of Scaling Relations for Circulating Fluidized Beds," Proceedings of the 12th International Conference on Fluidized Bed Combustion, San Diego, p. 69.

Glicksman, L.R., Hyre, M.R., and Woloshun, K., 1993b, "Simplified Scaling Relationships for Fluidized Beds," *Powder Technology*, 77, pp. 177-199.

Glicksman, L.R., Hyre, M.R., and Farrell, P.A., 1994, "Dynamic Similarity in Fluidization," *International Journal of Multiphase Flow*, 20, Supplement, pp. 331-386.

Glicksman, L.R. and Farrell, P.A., 1995, "Verification of the Simplified Hydrodynamic Scaling Parameters for Commercial Pressurized Fluidized Bed Combustors: Part 1-

Bubbling Fluidized Beds," Proceedings of the 13th International Conference on Fluidized Bed Combustion, Kissimmee, FL, p. 981-990.

Glicksman, L.R., Hyre, M.R., Torpey, M., and Wheeldon, J., 1995, "Verification of the Simplified Hydrodynamic Scaling Parameters for Commercial Pressurized Fluidized Bed Combustors: Part 2- Circulating Fluidized Beds," Proceedings of the 13th International Conference on Fluidized Bed Combustion, Kissimmee, FL, p. 991-1000.

Grace, J.R., 1982, "Fluidized-Bed Hydrodynamics," Chapter 8.1, Handbook of Multiphase Systems, ed. Hetsroni, G., Hemisphere, Washington, D.C.

He, Y-L., Lim, C.J., and Grace, J.R., 1996, "Scale-up Studies of Spouted Beds," *Chemical Engineering Science*, in press.

Horio, M., Nonaka, A., Sawa, Y., and Muchi, I., 1986a, "A New Similarity Rule for Fluidized Bed Scale-up," *AIChE Journal*, 32, 9, pp. 1466-1482.

Horio, M., Takada, M. Ishida, M. and Tanaka, N., 1986b, "The Similarity Rule of Fluidization and its Application to Solid Mixing and Circulation Control," in Fluidization V, K. Ostergaard and A. Sorensen, eds., p. 159.

Horio, M., Ishii, H., Kobukai, Y., and Yamanishi, N., 1989, "A Scaling Law for Circulating Fluidized Beds," *Journal of Chemical Engineering of Japan*, 22, 6, p. 587.

Ishii, M., 1975, Thermo-Fluid Dynamic Theory of Two-Phase Flow, Eyrolles.

Ishii, H. and Murakami, I., 1991, "Evaluation of the Scaling Law of Circulating Fluidized Beds in Regard to Cluster Behaviors," in Circulating Fluidized Bed Technology III, P. Basu, M. Horio, and M. Hasatani, eds., Pergamon Press, p. 125.

Jackson, R., 1971, "Fluid Mechanical Theory," In Fluidization, eds. Davidson, J.F. and Harrison, D., Academic Press, New York.

Kline, S.J., 1965, Similitude and Approximation Theory, McGraw Hill: New York.

Litka, T. and Glicksman, L.R., 1985, "The Influence of Particle Mechanical Properties on Bubble Characteristics and Solids Mixing in Fluidized Beds," *Powder Technology*, 42, pp. 231-239.

Massoudi, M., Rajagopal, K.R., Ekmann, J.M., and Mathur, M.P., 1992, "Remarks on the Modeling of Fluidized Systems," *AIChE Journal*, 38, 3, pp. 471-472.

Newby, R.A. and Keairns, D.L., 1986, "Test of the Scaling Relationships for Fluid-Bed Dynamics," Fluidization V, Engineering Foundation, New York, pp. 31-38.

Nicastro, M.T. and Glicksman, L.R., 1984, "Experimental Verification of Scaling Relationships for Fluidized Bed," *Chemical Engineering Science*, 39, 9, pp. 1381-1391.

Rathbone, R.R., Ghadiri, M., and Clift, R., 1989, "Measurement of particle velocities and associated stresses on immersed surfaces in fluidised beds," in Fluidization VI (eds. Grace, J.R., Shemilt, L.W., and Bergougnou, M.A., Engineering Foundation, New York, pp. 629-635.

Roy, R. and Davidson, J.F., 1989, "Similarity Between Gas-Fluidized Beds at Elevated Temperature and Pressure," Fluidization VI, Engineering Foundation, New York, pp. 293-300.

Syamlal, M., Rogers, W., and O'Brien, T.J., 1993, MFIX Documentation Theory Guide, DOE/METC-94-1004.

Tsukada, M., Nakanishi, D., Takei, Y., Ishii, H., and Horio, M., 1991, "Hydrodynamic Similarity of Circulating Fluidized Bed Under Different Pressure Conditions," Proceedings of the 11th International Conference on Fluidized Bed Combustion, Montreal, p. 829.

Wen, C.Y. and Yu, Y. H., 1966, "A Generalized Method for Predicting the Minimum Fluidization Velocity," *AIChE Journal*, 12, pp. 610-612.

Yang, W.C., 1983, "Criteria for Choking in Vertical Pneumatic Conveying Lines," *Powder Technology*, 35, pp. 143-150.

Zhang, M.C. and Yang, R.Y.K., 1987, "On the Scaling Laws for Bubbling Gas-Fluidized Bed Dynamics," *Powder Technology*, 51, pp. 159-165.

This page intentionally blank

3. Experimental Setup for Hydrodynamic Scaling Studies

3.1 Tidd PFBC Experimental Setup

The Tidd plant is a first-of-a-kind PFBC combined-cycle plant in the United States that can generate up to 70 MW_e of power (79% steam cycle/21% gas cycle). The Tidd PFBC boiler operates at roughly 10 atm of pressure and a temperature between 838 and 860°C (McDonald, 1990). Figure 1 is a schematic of the Tidd boiler. As shown in the figure, boiler tubes pass through the bed in a serpentine arrangement to generate steam, and there is a large freeboard region above the tube bank. Fuel and sorbent are injected into the bottom of the bed beneath the tube bank. At full load, the expanded bed height is 3.6 m (McDonald, 1990).

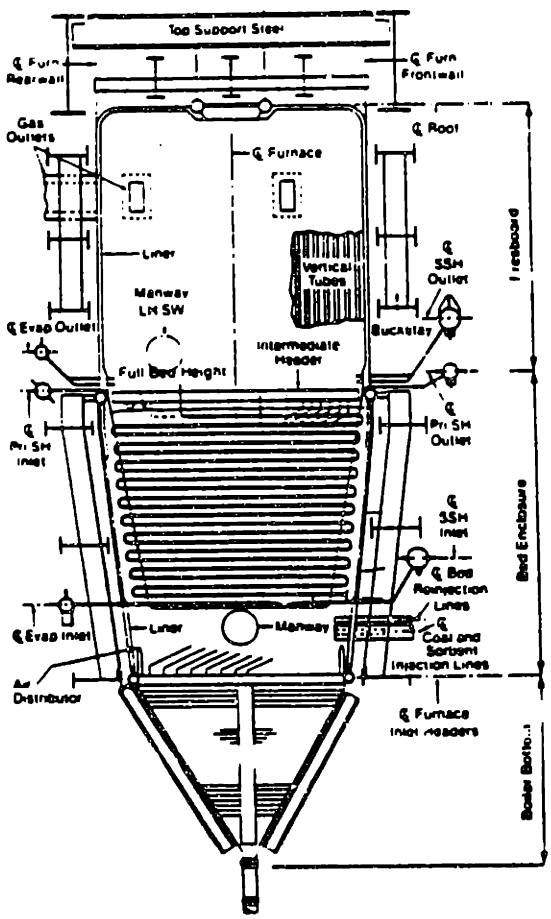

Figure 1: Tidd Boiler Schematic (McDonald, 1990)

3.1.1 Tidd Pressure Measurement Setup

The Tidd PFBC is a demonstration plant, and as such, is equipped to provide measurements that would not typically be available from a standard boiler. The Tidd plant is equipped with 8 experimental pressure taps positioned vertically along the boiler wall. The taps protrude approximately 46 cm into the bed and have a 1.3 cm inner diameter. These taps were used to obtain time-varying pressure drop data. In addition to the experimental taps, the bed is fitted with pressure taps to provide data for plant operations. The so-called POPS (Plant Operational Performance System) system provides static pressure drop measurements over several elevations in the bed. The POPS system provides the opportunity to cross-check data taken from the experimental taps. As will be discussed in Chapter 4, the POPS system data were also used to estimate the voidage in the bottom of the Tidd plant, due to problems with the experimental taps in this region. Figure 2 shows the relative location of the two sets of pressure taps. H represents the height of the tube bank, and z is the distance above the distributor.

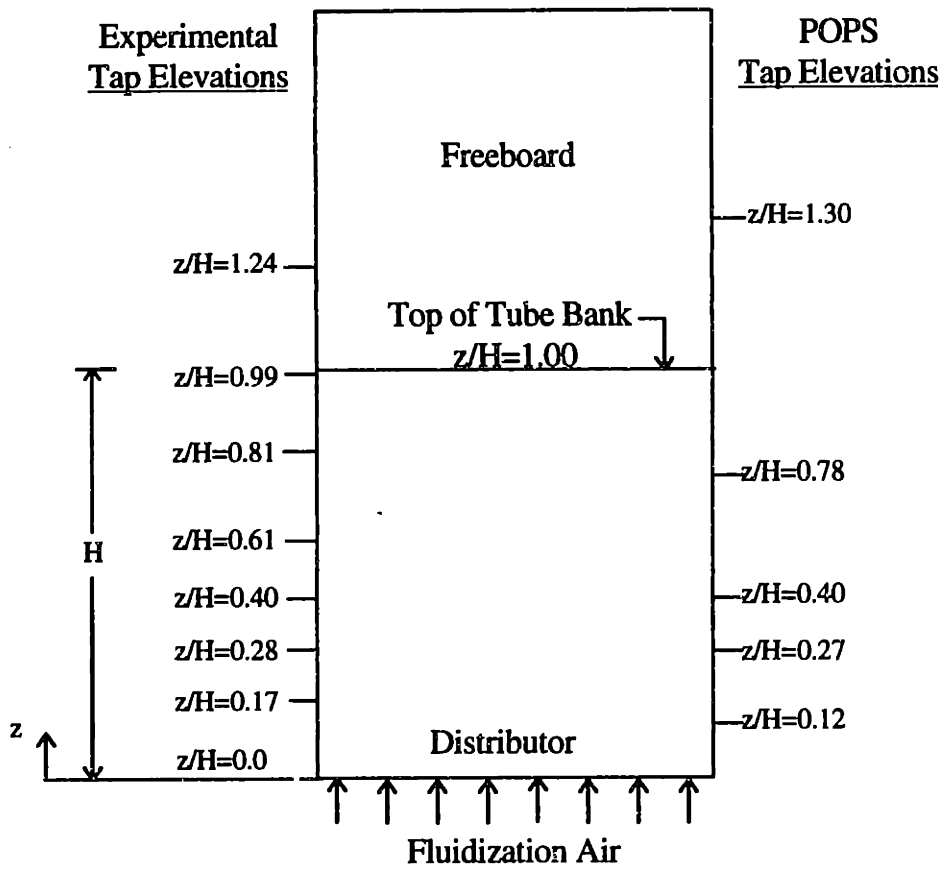

Figure 2: Tidd Pressure Tap Locations

3.1.1.1 Tidd Pressure Line Characterization

The Tidd pressure lines are quite long; Babcock & Wilcox estimated their length to be approximately 15 m (Fuller, 1995). This raised concerns over whether the pressure lines could transmit a dynamic pressure signal without significantly distorting it. Babcock & Wilcox (Fuller, 1995) conducted some limited tests to obtain more information on the effects of the pressure lines on a time-varying pressure signal. An analytical model of the pressure-line dynamics has been developed; the details of the model are given in Appendix A. Babcock & Wilcox's test results have been used in conjunction with the model to assess the frequency response of the Tidd pressure lines.

During a shutdown of the Tidd PFBC boiler, Babcock & Wilcox tested the Tidd pressure line-dynamics at ambient conditions. They applied a 30 Hz sinusoidal pressure signal to the boiler-end of a pressure line while simultaneously measuring both the pressure signal into and out of the line. The 30 Hz pressure signal was generated using a modified vane pump. Three purge-air configurations were tested. (Purge air is introduced through a "T" in the pressure line. The third leg of the "T" contains a critical-flow orifice that experiences the line pressure on one side and the pressure-vessel pressure on the other. Purge air is used to prevent the pressure taps from becoming plugged during boiler operation.) The configuration with the purge-air line blocked off was experimentally found to alter the pressure signal either comparably or more significantly than the other two configurations and is the simplest to model. Hence, the following discussion and the analytical model developed in Appendix A are based on the Tidd pressure lines with no purge air effects. Fuller (1995) provides additional analysis of the data with simulated purge air.

The model of the pressure lines presented in Appendix A is a linear lumped-parameter model that includes the effects of: fluid inertance, capacitance, and resistance. The constitutive equations for each fluid-system element were taken from Rowell and Wormley (1994). The resulting model is a second-order system with an undamped natural frequency, ω_n, and a damping ratio, ζ.

Figure 3 shows a segment of the Tidd pressure line test data. The data designated "Input" were taken from a pressure transducer positioned at the source of the 30 Hz pressure signal. The "Output" data were taken from a pressure transducer connected to the opposite end of the pressure sensing line. As shown in Figure 3, the pressure line amplifies the 30 Hz input signal by approximately a factor of 2.3. Based on the model developed in Appendix A, the pressure line should behave as a second-order system. Underdamped second-order systems will amplify a sinusoidal input signal when they are excited near their undamped natural frequency (ω_n). According to the pressure line model, the damping ratio (ζ) for the pressure line at the test conditions is approximately

0.06. This is a low damping ratio, suggesting that the pressure line should behave like an underdamped system (i.e., $0<\zeta<1$). This implies that the undamped natural frequency of the pressure lines is in the vicinity of 30 Hz at the test conditions. The shape of the "Output" data shown in Figure 3, which are for a frequency that is much higher than those typical of fluidized-bed hydrodynamics, is not significantly distorted from the input signal. This suggests that nonlinear effects are not very important, in this case, and provides support for using a linear model of the pressure-line dynamics.

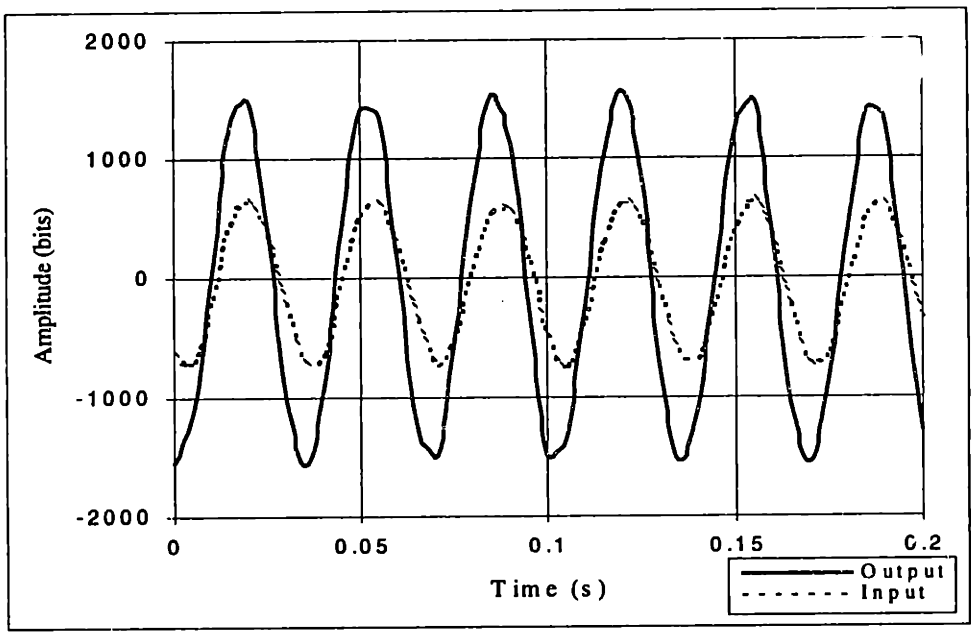

Figure 3: Segment of Data from Pressure Line Characterization Tests

A system's frequency response relates the magnitude of its output to the magnitude of a sinusoidal input over a range of frequency. Bode plots are the standard way of plotting system frequency response (Rowell and Wormley, 1994). Figure 4 presents the Bode plot for the Tidd pressure line based on the analytical model; the input parameters for this analysis are given in Table 1. The conditions presented in Table 1 are for air at ambient temperature and pressure, which correspond approximately to the conditions of the pressure-line tests. The ordinate on the Bode plot is the ratio of the system output magnitude to the input magnitude in decibels. For example, if the ratio of the output and input magnitudes is unity, the "Gain" in decibels is $20\log_{10}(1)=0$ dB. Hence, Figure 4

shows that the magnitude of the output equals the input (i.e., 0 dB Gain) for low angular frequencies (ω). Figure 4 is given in terms of the angular frequency (ω); angular frequency is related to the frequency in Hz (f) by

$$\omega = 2\pi f \,. \tag{1}$$

According to the test data, the input is amplified by a factor of 2.3, or approximately 7 dB, at a frequency of 30 Hz; this corresponds to an angular frequency of 188 s^{-1}. Although the model predicts the underdamped behavior of the pressure line (i.e., the amplification of the input), a comparison of the measurements with the model shows that it clearly does not predict the frequency at which this behavior occurs. Figure 4 shows that the model predicts an undamped natural frequency of roughly 21 s^{-1}, or 3.3 Hz, which is far from the measured frequency of 188 s^{-1} with a gain of 7 dB. The model involves three lumped fluid-system parameters: inertance, capacitance, and resistance. Deficiencies in the model's predictive abilities may be due to limitations in the constitutive relationships used for the inertance and capacitance of the fluid in the lines (see Appendix A for the details); the natural frequency is independent of the resistance. It is desirable to find a way to "correct" for the model's deficiencies to permit an assessment of the pressure line frequency response under normal boiler operation.

According to the model, the undamped natural frequency for the pressure lines is given by

$$\omega_n = \sqrt{\frac{\gamma \cdot R \cdot T}{l^2}} \,. \tag{2}$$

Equation (2) implies that the undamped natural frequency, the quantity the model predicted poorly, depends on: gas properties (γ and R), temperature (T), and pressure-line length (l). Of particular interest is the dynamic behavior of the pressure lines at the elevated temperature they experience during boiler operation. In an attempt to compensate for the model's deficiencies, while accounting for the effect of temperature on ω_n, an effective pressure line length (l_{eff}) will be calculated to match the model to the data at the pressure-line test conditions. This effective line length should provide better predictions of the pressure line dynamics under the conditions the lines experience during boiler operation.

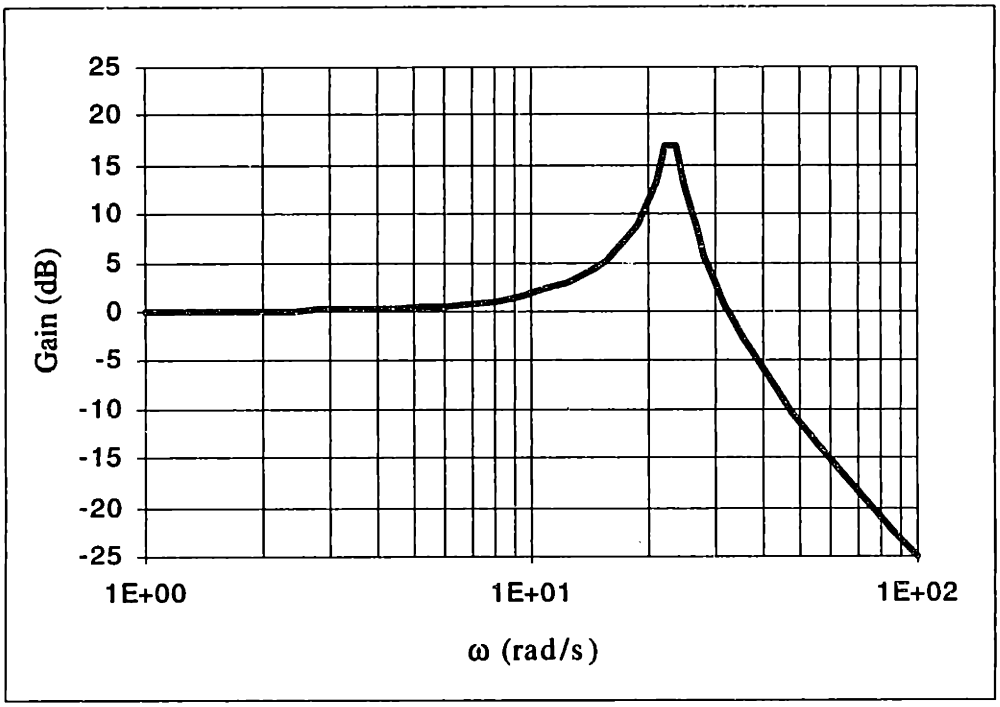

Figure 4: Bode Plot for Pressure Line Model at Test Conditions

Table 1: Model Inputs at Pressure Line Test Conditions

Model Parameter	Value
l (m)	15.0
d (m)	0.0127
μ (kg/m-s)	1.8×10^{-5}
γ	1.4
p (N/m^2)	1.013×10^5
T (K)	300
ρ_g (kg/m^3)	1.18
R (J/kg-K)	287

For low damping ratios, the undamped natural frequency corresponds approximately to the peak frequency (ω_p) on the Bode plot (i.e., $\omega_n \approx \omega_p$ for low ζ since $\omega_p = \omega_n \sqrt{1-2\zeta^2}$). Assuming the model predicts the behavior around the natural

frequency, just not the actual value of the natural frequency, Figure 4 shows that the ratio of the frequency at which the gain is 7 dB (ω_{7dB}) and the peak/natural frequency is

$$\frac{\omega_{7dB}}{\omega_n} \approx 1.2 . \tag{3}$$

Experimentally, Babcock & Wilcox found that $\omega_{7dB} = 188\,s^{-1}$. Using this experimental result and (3), the undamped natural frequency of the pressure lines at the test condition is 157 s^{-1}. Using this value for ω_n, (2), and the values in Table 1, gives an effective pressure line length of

$$l_{eff} = \sqrt{\frac{\gamma \cdot RT}{\omega_n^2}} = 2.2\text{m} . \tag{4}$$

This effective line length can now be used as an input to the analytical model to predict the frequency response of the Tidd pressure lines during boiler operation. The pressure lines run between the boiler enclosure and the wall of the pressure vessel. The temperature inside the pressure vessel while the Tidd PFBC boiler is running is approximately 590 K. The boiler operates under pressurized conditions, hence the absolute pressure in the lines is approximately equal to the boiler pressure, which is typically around 10 atm. Table 2 summarizes the pressure line model inputs parameters to simulate conditions during boiler operation. The effective pressure line length was used to calculate the fluid inertance and capacitance. The actual estimated pressure line length (l) was used to calculate the fluid resistance. The frequency response was also determined using l_{eff} to calculate the resistance; this was found to have a very small effect on the results.

Table 2: Model Inputs at Boiler Operating Conditions

Model Parameter	Value
l_{eff} (m)	2.2
l (m)	15.0
d (m)	0.0127
μ (kg/m-s)	29.4×10^{-6}
γ	1.4
p (N/m^2)	1.013×10^6
T (K)	590
ρ_g (kg/m^3)	6
R (J/kg-K)	287

Figure 5 presents the Bode plot for the pressure line at the conditions listed in Table 2. The fidelity of the input signal is maintained by the pressure lines out approximately to an angular frequency of 80 s^{-1}, or 13 Hz. According to the model, components of the pressure signal at this frequency would be amplified by 15%. Chapter 7 describes measurements of the bubble characteristics in a cold-scale model of the Tidd PFBC. At the scaled Tidd operating conditions, the maximum bubble frequency was measured to be approximately 7 Hz. If scaled properly, the dimensionless bubble frequency in the cold model should be equivalent to that in the Tidd PFBC. This implies that

$$\left.\frac{fD}{u_o}\right|_{cold} = \left.\frac{fD}{u_o}\right|_{hot} . \tag{5}$$

As will be discussed in Section 3.2, the cold model has dimensions one-quarter those of the Tidd PFBC (i.e., a scale factor of 4); hence $D_{cold}=D_{hot}/4$. In order to match the Froude number between the two beds, the cold model superficial velocity must be equal to the Tidd PFBC superficial velocity divided by the square-root of the scale factor (i.e., $u_o|_{cold} = u_o|_{hot}/\sqrt{4}$). Using these scaling requirements in (5) gives

$$f_{hot} = \frac{u_o|_{hot}}{u_o|_{cold}} \cdot \frac{D_{cold}}{D_{hot}} \cdot f_{cold} = \frac{f_{cold}}{2}. \qquad (6)$$

Since $f_{cold} \approx 7$ Hz, (6) implies that $f_{hot} \approx 3.5$ Hz. Thus, the mean bubble frequency in the Tidd PFBC should be well below the frequency at which the pressure line begins to amplify the pressure signal. As long as the frequency of the signal is not too broadband, the pressure line should not significantly alter the input pressure signal.

Although there are some unsatisfying aspects to the previous analysis, it sheds some light on the Tidd pressure line dynamics and the possible pitfalls associated with their length. The analysis suggests that the expected dominant frequencies of the pressure signal should be transmitted by the Tidd pressure lines unamplified. And Babcock & Wilcox's data suggest that the signal should remain undistorted. But it also implies that higher frequency components of the pressure signal could be artificially amplified due to resonance in the pressure lines. It is anticipated that these effects would manifest themselves in the power spectrum of the Tidd pressure signal. As will be discussed in Chapter 4, the Tidd power spectrum has unusual features; the pressure lines are a possible source of the observed aberrant behavior.

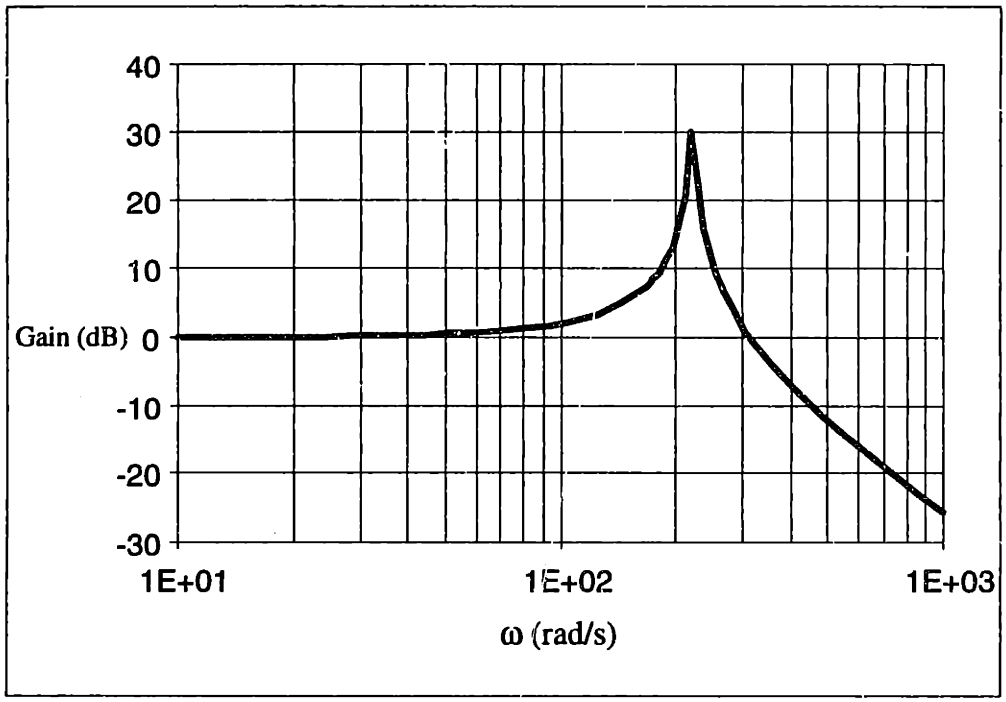

Figure 5: Bode Plot for Pressure Line Model at Boiler Operating Conditions

3.1.2 Tidd Data Acquisition System

The time-varying pressure drop data from the Tidd PFBC demonstration plant were acquired using a personal-computer-based data acquisition system. A 486-33MHz personal computer equipped with a 12-bit analog-to-digital conversion board was used to sample the pressure transducer output. The Tidd data were obtained using a single, 0-5 psi, differential pressure transducer connected to a pressure manifold system. The manifold system permitted any two of the eight experimental pressure taps to be connected to the pressure transducer. An electronic filter was installed between the data acquisition system and the pressure transducer to prevent aliasing and to eliminate any high frequency noise.

3.2 Hydrodynamic Scaling Calculations

Table 3 lists the Tidd PFBC geometric and operating parameters. The particle density (ρ_S) was determined by measuring the displacement of a known mass of the Tidd bed material (dolomite). The particle sphericity (ϕ_S) was determined by evaluating a digitized picture of the Tidd bed material; image-analysis software[1] was used to estimate its average apparent circularity. Chang and Louge (1992) found that the square of the apparent circularity provided a good estimate of the particle sphericity. Additional details on the particle sphericity measurements are provided in Appendix B. The minimum fluidization velocity was predicted using an expression proposed by Grace (1982). Experiments were conducted at ambient conditions that showed that this expression predicts the minimum fluidization velocity of the Tidd bed material well. The surface-volume mean particle diameter (d_p=851 μm) was determined through sieve analysis of a Tidd bed sample taken from the sorbent reinjection vessels during testing. (The surface-volume mean particle diameter is used since the friction on the particle is proportional to its area, and the gravitational force is proportional to its mass.) It is not currently possible to obtain a sorbent sample from the center of the bed. This introduces some uncertainty in the exact size of the particles within the bed. Detailed information on the Tidd PFBC particle size distribution is given in Appendix C. The dimension D is an arbitrary reference bed dimension; the value for D in Table 3 is the width of the scaled section of the Tidd PFBC. (The scaled section is illustrated in Figure 6.)

The values of the parameters listed in Table 3 were used to calculate the values of the simplified scaling parameters for the Tidd PFBC. Table 4 lists the values of the simplified scaling parameters for the Tidd PFBC. These dimensionless groups must be matched between the combustor and a cold model in order for the model to simulate the combustor's hydrodynamics. In addition to the parameters listed in Table 4, a cold model must be geometrically similar to the Tidd PFBC, and the dimensionless particle size

[1] Image 1.47 developed by the U.S. National Institutes of Health

distribution (PSD) must be matched between the two beds. Geometric similarity requires that all length scales change by the same scale factor. This is equivalent to matching L/D between two beds, where L is any bed dimension.

Table 3: Tidd PFBC Operating Parameters

Parameter	Value of Parameter for Tidd PFBC
T (K)	1135
p (N/m^2-abs)	9.04×10^5
μ (kg/m-s)	4.6×10^{-5}
ρ_g (kg/m^3)	2.8
ρ_s (kg/m^3)	2513
ϕ_s	0.82
u_{mf} (m/s)	0.24
u_o (m/s)	0.91
D (m)	3.4
d_p (μm)	851

Table 4: Tidd PFBC Simplified Scaling Parameters

Scaling Parameter	Tidd PFBC
ρ_s/ρ_g	898
u_o^2/gD	0.025
u_o/u_{mf}	3.8
ϕ_s	0.82

The procedure for determining the dimensions and operating conditions for a *cold* model using the values of the simplified set of scaling parameters for the *hot* combustor follows.

1. Calculate the cold model particle density that matches the hot-bed solid-to-gas density ratio;

$$\rho_s|_{cold} = \rho_g|_{cold}\left(\frac{\rho_s}{\rho_g}\right)\Bigg|_{hot}.$$

2. Choose a scale factor. In this case, for example, a quarter-scale cold model was constructed;

$$D_{cold} = \frac{D_{hot}}{4}.$$

Hydrodynamic similarity requires that the cold model be geometrically similar to the hot bed. Hence, all the dimensions of the hot bed must be scaled down by the scale factor and all angles must be maintained (e.g., $L_{cold}=L_{hot}/4$). In this case, d_p is not scaled by the same factor.

3. Calculate the cold-model gas superficial velocity that matches the hot-bed Froude number;

$$u_o|_{cold} = u_o|_{hot}\sqrt{\frac{D_{cold}}{D_{hot}}}.$$

4. Calculate the cold-model minimum fluidization velocity that matches the hot-bed u_o/u_{mf};

$$u_{mf}|_{cold} = \frac{u_o|_{cold}}{\left(u_o/u_{mf}\right)\Big|_{hot}}.$$

5. Calculate the cold-model particle diameter that, using the particle density calculated in Step 1, agrees with u_{mf} calculated in Step 4. The expression proposed by Grace (1982) was solved for particle diameter (d_p) in the current study. Grace's u_{mf} relationship is

$$\frac{\rho_g u_{mf} d_p}{\mu} = \sqrt{(27.2)^2 + 0.0408\frac{\rho_g\left(\rho_s-\rho_g\right)g d_p^3}{\mu^2}} - 27.2.$$

6. The dimensionless particle size distribution (PSD) and the particle sphericity (ϕ_s) must be matched between the hot bed and the cold model.

A cold-scale model of a section of the Tidd PFBC has been constructed using the simplified set of scaling laws. Figure 6 illustrates the scaling from the Tidd PFBC to the cold model. A two-dimensional slice of the Tidd boiler enclosure is illustrated in Figure 6. The dashed lines represent the section of the Tidd combustor that was scaled. The cold scale model, including the tube bank, has linear dimensions that are one-quarter those of the section illustrated in Figure 6. The decision to scale only a section of the combustor was based on the observations of Glicksman and McAndrews (1985) and Glicksman et al. (1987). They found that the bubble distribution is nearly uniform throughout the bed cross-section for large-particle bubbling fluidized beds containing a large array of horizontal tubes. The walls have a minimal influence on the conditions near the center of the bed when the bed diameter is 3-4 times larger than the maximum bubble size.

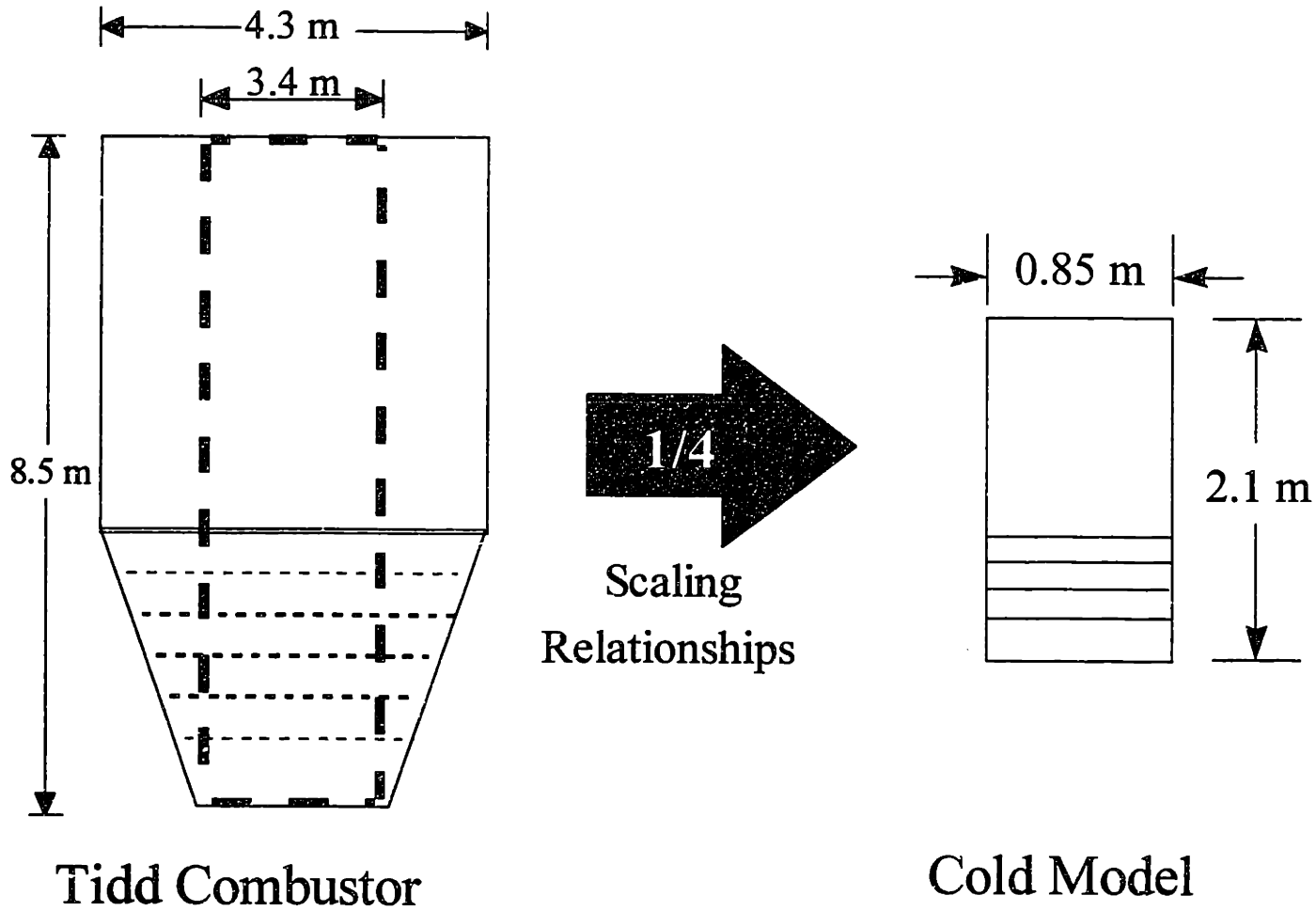

Figure 6: Scaling from Large Combustor to Cold Model

Table 5 summarizes the results of the scaling exercise described previously for the quarter-scale cold model of the Tidd PFBC. The second column in Table 5 lists the values for the cold model geometry and operating parameters required to exactly satisfy the scaling relationships; the adjacent column gives the values that were actually achieved. A granular linear low-density polyethylene manufactured by Union Carbide (GRSN 7047) was chosen as the cold bed material; it has a solid density of 918 kg/m^3 versus the 988 kg/m^3 required to exactly match the solid-to-gas density ratio. The cold-bed material particle sphericity is 0.85. Its value was measured in the same manner as for the Tidd bed material; the measurement procedure is described in Appendix B. The particles were segregated in an attempt to achieve the required scaled particle size; the deviation between the exact and actual mean particle diameter are small enough that it has a negligible effect on the minimum fluidization velocity.

Table 5: Cold Model Operating Parameters

Parameter	Value for Exact Cold Model	Value for Actual Cold Model
T (K)	311	311
p (N/m^2-abs)	1.01×10^5	1.01×10^5
μ (kg/m-s)	1.9×10^{-5}	1.9×10^{-5}
ρ_g (kg/m^3)	1.1	1.1
ρ_s (kg/m^3)	988	918
ϕ_s	0.82	0.85
u_{mf} (m/s)	0.12	0.12
u_o (m/s)	0.46	0.46
D (m)	0.85	0.85
d_p (μm)	581	609

Table 6 compares the values of the simplified set of scaling parameters for the Tidd PFBC and the cold model. The polyethylene bed material allows the hot-bed density ratio to be matched within 8%, and the particle sphericity matches the Tidd bed value within 4%. An attempt was also made to match the dimensionless particle size distribution. Figure 7 compares the dimensionless particle size distributions (PSD) of the Tidd PFBC and the MIT cold model; the PSDs of the two beds matched closely. The details of both the Tidd and the cold-model particle size distributions are provided in Appendix C.

Table 6: Comparison of Simplified Scaling Parameters

Scaling Parameter	Tidd PFBC	Cold Model
ρ_s/ρ_g	898	835
u_o^2/gD	0.025	0.025
u_o/u_{mf}	3.8	3.8
L/D	geom. similar	geom. similar
ϕ_s	0.82	0.85
PSD	matched	matched

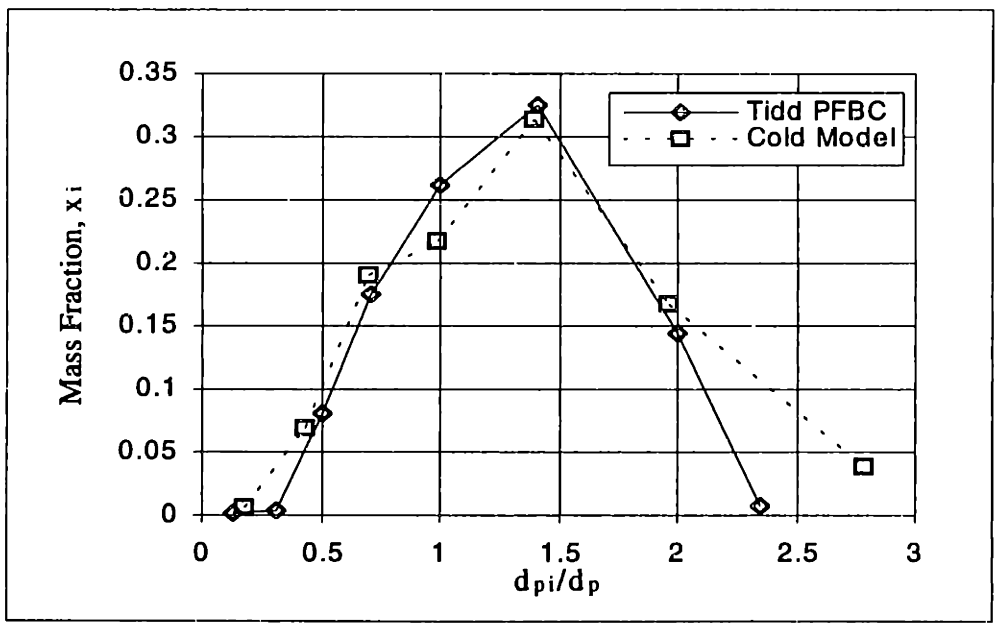

Figure 7: Comparison of the Tidd PFBC and the Cold Model Particle Size Distributions

3.2.1 Error in Drag from Using the Simplified Set of Scaling Parameters

In Chapter 2, it was shown that the simplification in going from the full to the simplified set of scaling parameters introduces a scaling error because the particle Reynolds number is no longer matched between the two beds. Failure to match the particle Reynolds number produces a mismatch between the hot-bed and cold-model dimensionless drag parameters ($\beta' \equiv \beta D/\rho_s u_o$). An expression was developed in Section 2.3.4.3 to compare the dimensionless drag parameters over a range of particle Reynolds number. This relationship is given by

$$\frac{\beta D}{\rho_s u_o} = \left(\frac{\varepsilon_{mf}^3}{\varepsilon}\right)\frac{(1-\varepsilon)^2}{(1-\varepsilon_{mf})}\left(\frac{gD}{u_o^2}\right)\left(\frac{u_o}{u_{mf}}\right)\frac{1+\frac{1.75}{150}\left(\frac{\varepsilon\phi_s}{1-\varepsilon}\right)Re_{dp}\left|\bar{u}'_g-\frac{\sqrt{gD}}{u_o}\bar{u}'_s\right|}{1+\frac{1.75}{150}\left(\frac{u_{mf}}{u_o}\right)\frac{\phi_s}{(1-\varepsilon_{mf})}Re_{dp}}. \qquad (7)$$

Evaluating (7) for the Tidd PFBC and the cold model requires assumptions for the gas and solids velocities (u_g and u_s). Two limiting conditions are considered.

1. For the drag due to the gas flow through the particle emulsion, it is reasonable to assume that $u_g=u_{mf}/\varepsilon$ and $u_s=0$.
2. For the drag associated with the motion of the bubbles, the gas velocity can be assumed to be the bubble rise velocity plus $3u_{mf}$ (i.e., $u_g=u_b+3u_{mf}$ and $u_s=0$). Measurements in the cold model (see Chapter 7) indicate that at the scaled Tidd operating condition $u_b\approx0.9$ m/s. According to the scaling relationships, this would correspond to a bubble rise velocity of 1.8 m/s in the Tidd PFBC.

For the first case, assuming that $\varepsilon\approx\varepsilon_{mf}$, there is no error in the dimensionless drag terms introduced by using the simplified set of scaling parameters. Figure 8 shows the error for the second case over a range of hot-bed particle Reynolds numbers. The hot-bed has a particle Reynolds number of 48. As shown in the figure, at this Reynolds number the dimensionless drag coefficient for the cold model is 31% lower than that of the hot bed.

The figure also shows that, as discussed in Chapter 2, in the limits of both high and low particle Reynolds numbers, the dimensionless drag terms are equivalent because the simplified set of scaling relationships are equivalent to the full set of scaling relationships in these limits.

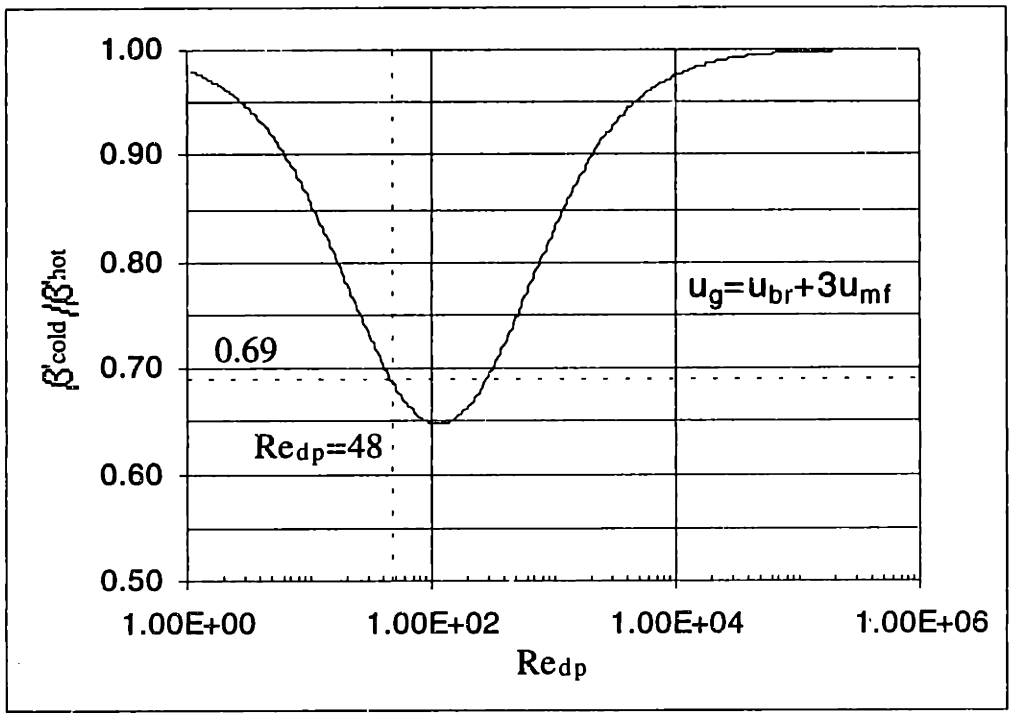

Figure 8: Error in Dimensionless Drag Parameter

The results of these two limiting cases suggest that the error in the dimensionless drag term at different locations in the bed should vary roughly between 0 and 31%. Although in bubbling beds, most of the drag is associated with the gas flow required to fluidize the particle emulsion and not the bubbles, this does not provide any information on how any error affects the local hydrodynamics.

3.3 MIT Cold Model Experimental Setup

Figure 9 is a sketch of the MIT cold model. A blower supplies air to the cold model through 6 in. PVC piping. The blower is capable of supplying up to 1200 cfm at 12 psi. Under typical operating conditions, the cold model requires 380 cfm at roughly 4 psi. The airflow to the bed is regulated by a valve in the air line upstream of the bed.

Air from the blower enters the inlet plenum of the model and then passes through a perforated plate distributor. The distributor is constructed of two perforated steel plates with 48% open area. Two layers of cloth and a layer of 325 mesh screen are sandwiched between the two plates to support the particles and provide a pressure drop sufficient to achieve a uniform flow distribution.

The cross-section of the cold model is 0.85 m wide and 0.46 m deep. The bed is constructed of ¾ in. plywood, supported by a steel Dexion[2] frame. Wooden dowels were used to simulate the presence of the boiler tubes in the Tidd PFBC. The cold model dowel array was constructed to be geometrically similar to the Tidd tube bank; the detailed tube bank geometry is not provided due to its proprietary nature.

[2] Dexion Incorporated, Woodside 77, NY.

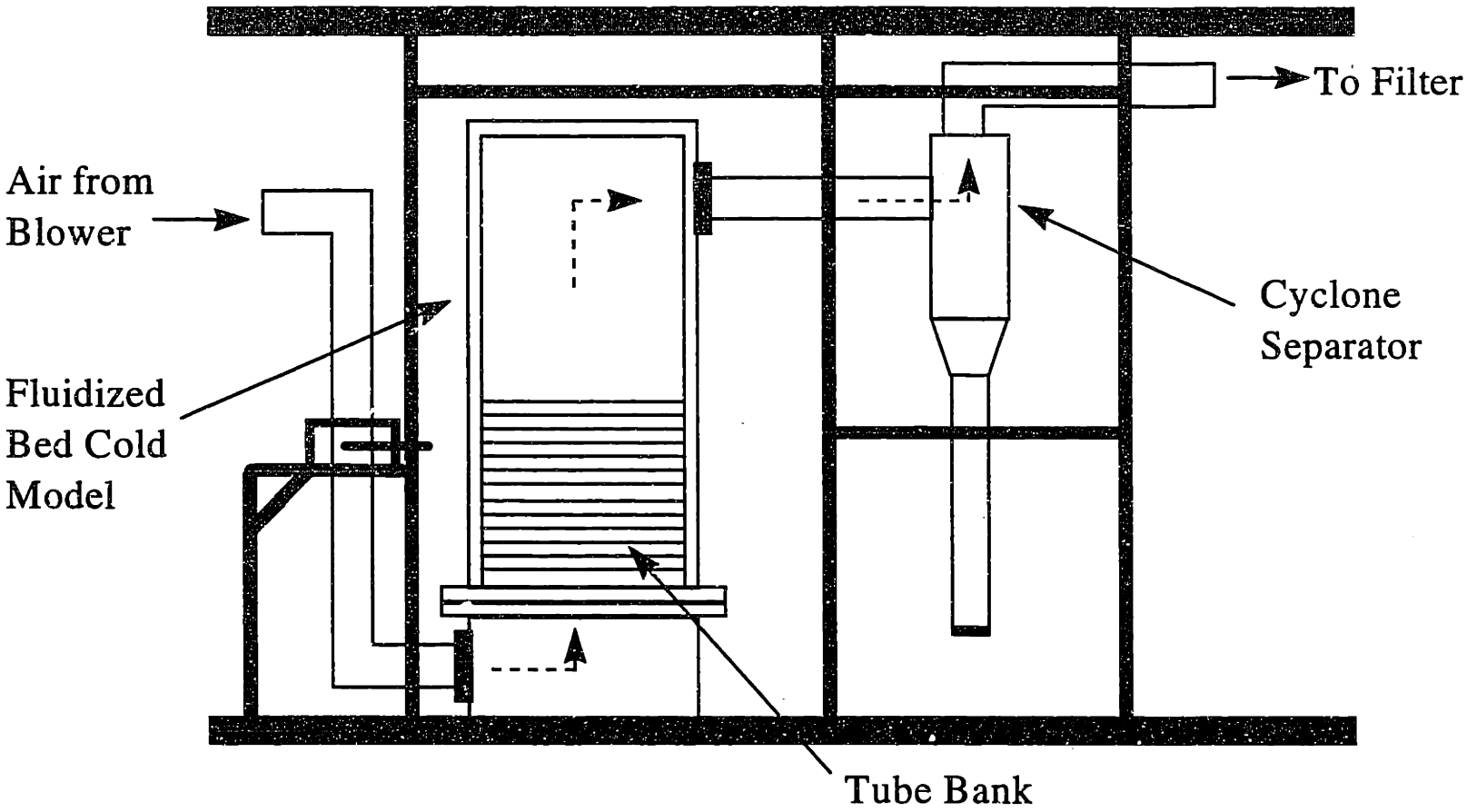

Figure 9: Illustration of Cold-Scale Model

The air leaving the bed passes through a cyclone to capture any elutriated bed material. The cyclone was approximately 33 cm in diameter and 96 cm tall and was manufactured by Pemm Corp[3]. Only a small amount of solids are carried out of the bubbling bed, making it unnecessary to continuously reintroduce the captured solids back into the bed. The solids captured by the cyclone collected in a vertical 6 in. PVC pipe connected to the bottom of the cyclone. To avoid significantly altering the particle size distribution in the bed, the collected solids were periodically removed from the pipe through a drain at its bottom and reintroduced into the bed.

After leaving the cyclone, the fluidization air passes through a filter box prior to exhausting into the laboratory

3.3.1 Cold Model Pressure Measurement

The cold model pressure taps are positioned at the same dimensionless elevations (z/H) as the Tidd experimental taps shown in Figure 2. The cold-model taps were flush with the wall, while the Tidd taps extended 46 cm into the bed. The effect of having the taps protrude into the bed was evaluated in the cold model and found to have a negligible effect on the pressure-drop data. The lines to the pressure taps were short lengths (< 30 cm) of plastic tubing. Plugging of the pressure taps was not a problem. The pressure lines were blown out prior to conducting a test; tests were repeated several times to verify the repeatability of the data.

The cold model is instrumented to simultaneously measure the pressure drop between all the successive pressure taps, but the final time-varying data were filtered prior to digitization using a single-channel analog filter. This required that the cold model data used in the scaling comparisons presented in Chapter 4 be obtained using a single, 0-5 in. H_2O, fast-response pressure transducer. Therefore, as with the Tidd differential pressure

[3] PEMM Corp Process Equipment & Mfg. Corp., Cold Spring, NY.

data, the data for each level in the cold model were taken sequentially rather than simultaneously. The pressure transducers were made by AutoTran, Inc.[4] (Series 600).

3.3.2 Cold Model Data Acquisition System

The cold model data acquisition system is illustrated in Figure 10. The time-varying pressure drop measurements from the MIT cold model were sampled using a personal computer-based data acquisition system. A 386SX-33MHz Dell computer equipped with Keithley-Metrabyte's DAS-1601 data acquisition board and EASYEST LX™ data acquisition software were used to sample the pressure transducer signal. The DAS-1601 is a high-speed 12-bit analog-to-digital converter that can accommodate up to 16 single-ended inputs.

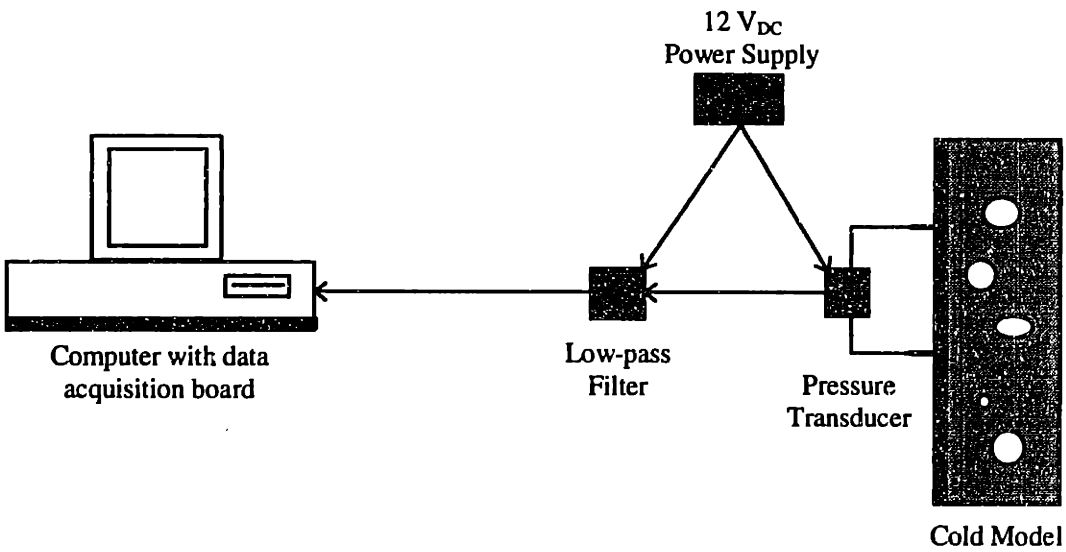

Figure 10: MIT Cold Model Data Acquisition System

As mentioned in Section 3.3.1, the data from the cold model were electronically filtered prior to digitization. A D68L8B-100Hz analog anti-aliasing filter manufactured by

[4] AutoTran Incorporated, Hopkins, Minnesota

Frequency Devices[5] was used. The filter is an 8-Pole low-pass Butterworth filter with a 100 Hz cutoff frequency (-3 dB). The 8-Pole Butterworth filter was chosen for its flat pass band and steep 48 dB/octave roll-off. The performance of the cold-model anti-aliasing filter was evaluated using an electronic signal generator. The attenuation provided by the filter was verified by supplying sinusoidal inputs over a range of frequencies and measuring the attenuation of the input amplitude. Figure 11 presents the measured performance of the electronic filter.

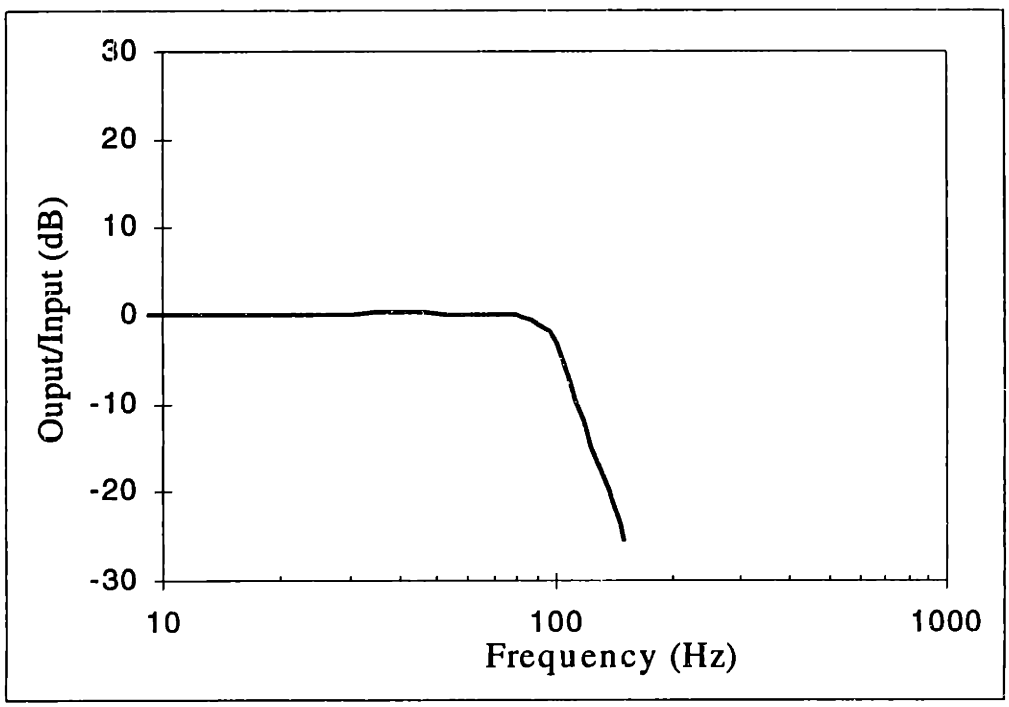

Figure 11: Measured Performance of Electronic Filter

3.3.3 Cold Model Air Flow Measurement

The air flowrate through the cold model was measured using a concentric-bore orifice plate manufactured by Meriam Instrument[6]. The orifice plate was made of 304 stainless

[5] Frequency Devices Inc., Haverhill, MA
[6] Meriam Instrument, Cleveland, OH

steel and had a bore of 2.7794 in., giving it a diameter ratio ($\beta_{orif} = d_{bore}/d_{pipe}$) of 0.458. The orifice plate was installed between a pair of orifice flanges, also manufactured by Meriam Instrument, that were equipped with corner pressure taps for measuring the pressure drop across the orifice plate. The orifice pressure drop was measured using a water manometer. As recommended by the manufacturer, the orifice plate was installed with a minimum of 10 pipe diameters of straight pipe upstream of the plate and 5 pipe diameters of straight pipe downstream from the orifice plate.

The air flowrate was calculated using measurements of the orifice pressure-drop, the temperature of the air in the line, and the gage pressure in the line, in conjunction with the procedure described in Chapter 9 of the Flow Measurement Engineering Handbook (Miller, 1989).

3.4 Nomenclature

D	reference bed dimension
d	pressure line diameter
d_{bore}	diameter of hole in orifice plate
d_{pipe}	diameter of the pipe in which the orifice plate is installed
d_p	surface-volume mean particle diameter
$\overline{d}_{p_i}$	mean aperture of adjacent sieves
f	frequency (Hz)
g	acceleration due to gravity, 9.807 m/s^2
H	distance from the distributor to the top of the tube bank
l	pressure line length
l_{eff}	effective pressure line length
L	bed dimension
p	pressure
PSD	dimensionless particle size distribution
R	perfect gas constant for air=287 J/kg-K
Re_{dp}	particle Reynolds number based on the gas superficial velocity
T	absolute temperature
u_b	bubble rise velocity
u_g	local gas velocity
u_o	gas superficial velocity
u_{mf}	minimum fluidization velocity
u_s	solid velocity
x_i	fraction of particle sample mass in interval i
z	distance above the distributor

Greek Symbols

β	particle-assembly drag coefficient
β'	dimensionless particle-assembly drag coefficient
β_{orif}	orifice plate diameter ratio=d_{bore}/d_{pipe}
ε	local voidage
ε_{mf}	minimum fluidization voidage
ϕ_s	particle sphericity
γ	ratio of specific heats, c_p/c_v
μ	gas viscosity
ω	angular frequency (s^{-1})
ω_n	undamped natural frequency
ω_p	peak frequency on Bode plot
ρ_g	gas density
ρ_s	solid density
ζ	damping ratio

3.5 References

Chang, H. and Louge, M., 1992, "Fluid Dynamic Similarity of Circulating Fluidized Beds," *Powder Technology*, 70, pp. 259-270.

Fuller, T.A., 1995, "Application of Scaiing Laws to PFBC–Final Report," Babcock & Wilcox Report No.: RDD:95:43109-001-000:08.

Grace, J.R., 1982, "Fluidized-Bed Hydrodynamics," Chapter 8.1, Handbook of Multiphase Systems, ed. G. Hetsroni, Hemisphere, Washington, D.C.

McDonald, D.K., 1992, "PFBC Plant Operations–TIDD," Babcock & Wilcox Technical Paper, BR-1498, presented to Power-Gen '92, Orlando, FL.

Miller, R.W., 1989, Flow Measurement Engineering Handbook, 2nd Edition, McGraw-Hill, New York.

Rowell, D. and Wormley, D.N., 1994, System Dynamics: An Introduction, Course Notes for: 2.02 *Introduction to System Dynamics*, Department of Mechanical Engineering, Massachusetts Institute of Technology.

4. Verification of Hydrodynamic Scaling for PFBC

4.1 Basis for Scaling Comparisons

Numerous techniques have been used to experimentally verify hydrodynamic scaling in fluidized beds. The ultimate objective of these techniques is to measure the important dependent hydrodynamic phenomena for use as a basis for comparing scaled beds. When two fluidized beds are hydrodynamically similar, their dependent hydrodynamic phenomena when expressed in dimensionless form will be identical. In bubbling beds, methods such as video analysis (e.g., Newby and Keairns, 1986) and capacitance probe methods (e.g., Almstedt and Zakkay, 1990) have been used to directly measure bubble properties such as their: diameter, growth rate, diameter distribution, frequency, and rise velocity. Similarly, optical probes have been used in circulating fluidized beds to measure variables such as cluster velocity and length to serve as a basis for scaling comparisons (e.g., Ishii and Murakami, 1991). With these methods, the approach is to directly measure local dependent hydrodynamic variables.

A second approach, which is more common due to its ease and accuracy, is to use time-resolved differential pressure measurements as the dependent hydrodynamic phenomena. In general, this is the only viable approach when scaling hot commercial beds. In this approach, pressure measurements are used to characterize the hydrodynamics of the fluidized bed. Lirag and Littman (1971) used statistical analysis of pressure fluctuations to estimate the average size of bubbles leaving a bubbling bed. Fan et al. (1981) concluded that bubble motion and coalescence are responsible for pressure fluctuations in fluidized beds. They also found that the amplitude of the pressure fluctuations is related to bubble size. Hence, pressure fluctuations reflect bed hydrodynamics. To characterize local bed behavior, the differential pressure measurements should be made over a modest bed level. Roy and Davidson (1989) found that the maximum pressure difference between two

closely spaced pressure taps is related to the bubble diameter at that level in the bed. Use of a single bed pressure point can make it difficult to interpret results since pressure fluctuations can be due to local effects, bubbles erupting at the bed surface, or even fluctuations in the air supply system. For example, Roy and Davidson (1989) found that pressure fluctuations measured using a single pressure point are primarily due to surface bubbles. They also concluded that the dominant frequency and amplitude measured at a single pressure point are independent of position in the bed.

Differential pressure drop measurements were employed in the current study. Time-varying pressure drop measurements were obtained from both the Tidd PFBC demonstration plant and the cold-scale model. The experimental setups for both beds were described in Chapter 3. When scaling between two laboratory-scale models, using either direct measurements of the hydrodynamics or differential pressure measurements are equally viable. But the Tidd PFBC is a large power-producing (70 MW_e) commercial boiler. It is neither practical nor permissible to insert probes into the bed to measure the local bubble characteristics. In this instance, differential pressure measurements provide the only way to characterize the hydrodynamics of the Tidd PFBC.

4.2 Experimental Data Analysis[1]

4.2.1 Solid Fraction Calculation

Differential pressure drop (Δp) is one of the few quantities that can be measured relatively easily and accurately in fluidized beds. Assuming that the weight of the particles between two pressure taps (say, taps 1 and 2) is the sole contributor to the pressure drop (i.e., negligible contributions from friction or acceleration), the solid fraction ($1-\varepsilon$) between the taps is given by

[1] Bendat and Piersol (1986) provides an excellent discussion on data analysis; this book served as the primary reference for Sections 4.2.2-4.2.3.

$$\left[1-\varepsilon(t)\right]_{1-2}=\frac{\rho_g}{\rho_g-\rho_s}+\frac{\Delta p_{1-2}(t)}{\left(\rho_s-\rho_g\right)\cdot g\cdot \Delta h_{1-2}}, \tag{1}$$

where Δh_{1-2} is the elevation between taps 1 and 2. Gravity dominates the pressure drop in bubbling fluidized beds, and for gas fluidized beds where $\rho_s \gg \rho_g$, (1) can be simplified by neglecting ρ_g with respect to ρ_s giving

$$\left[1-\varepsilon(t)\right]_{1-2}=\frac{\Delta p_{1-2}(t)}{\rho_s\cdot g\cdot \Delta h_{1-2}}. \tag{2}$$

As discussed in Chapter 2, scaling comparisons must be made on a dimensionless basis. Hydrodynamic scaling provides similarity between the *dimensionless* dependent variables from the two beds under consideration. Differential pressure drop is a dependent variable. Solid fraction is a dimensionless form of differential pressure drop that physically reflects the voidage or porosity in the interval. Hence, solid fraction is an important characteristic of fluidized bed hydrodynamics, and because it is dimensionless, provides an appropriate basis for comparing the hydrodynamics of two scaled beds. Note that even when the solid fraction is not given by (1), such as when friction or acceleration are not negligible, variations in the dimensionless pressure drop still provide a useful basis of comparison since pressure drop is a dependent hydrodynamic phenomenon.

The time-varying solid fraction (pressure drop) measurements are ergodic (i.e., stationary and random) and can be characterized in several ways. The most obvious characteristic of the time series is its mean value. The mean solid fraction in an interval can be calculated from a series of discrete measurements using

$$\overline{(1-\varepsilon)}=\frac{1}{N}\cdot\sum_{i=1}^{N}(1-\varepsilon)_i, \tag{3}$$

where N is the number of solid fraction measurements. By acquiring pressure drop data at several levels in the bed, the solid fraction profile can be constructed. The solid fraction profile shows how the voidage varies vertically as a function of distance from the distributor.

The mean pressure measurements can also be used to calculate the expanded bed height (H_b). The fluidizing gas causes the bed to expand from its initial loose-packed state to accommodate bubbles. Thus, the expanded bed height is related to, and a reflection of, the bed hydrodynamics. More specifically, it reflects the overall bed voidage. For the same scaled bed inventories, hydrodynamically similar beds will have the same dimensionless expanded bed heights.

Beyond using the mean pressure drop data to compare the solid fraction profiles and the dimensionless expanded bed heights of two scaled beds, additional comparisons are possible by considering the fluctuating nature of the data. In this study, two additional characterizations–the probability density function and the power spectral density function–have been calculated for the dimensionless pressure-drop data. These analyses are discussed in Sections 4.2.2 and 4.2.3.

4.2.2 Probability Density Function Analysis

The probability density function (PDF) characterizes the distribution of solid fraction values, or alternatively void values, in the solid fraction data. The distribution of voidage values is related to the size of the bubbles in the bed. Hence, beyond the mean solid fraction, the PDF shows how broadly the magnitudes of the fluctuations are distributed about the mean. It also shows the shape of the distribution (e.g., normal or otherwise). So the PDF provides a much more complete statistical characterization of the solid fraction data than the mean value alone.

The PDF is a normalized histogram; a histogram is simply a plot of the number of solid fraction measurements that fall in specified solid fraction intervals. For example, out of 100 measurements, 5 lie between 0.1 and 0.2, 20 of the 100 lie between 0.2 and 0.3, etc. The value of the probability density function over a finite solid fraction interval, is the

probability per unit interval width that the solid fraction at any time t will have a value in the interval. By normalizing the probability by the interval width, the area under the PDF curve is unity.

Bendat and Piersol (1986) present a detailed procedure for calculating the probability density function. This procedure is summarized below.

Consider a series of N discrete solid fraction measurements (i.e., $(1-\varepsilon)_i$ where i=1,N), where it is desired to construct the PDF over solid fractions ranging from $(1-\varepsilon)_{lb}$ to $(1-\varepsilon)_{ub}$. The subscripts "lb" and "ub" refer to the lower and upper bounds of the range of solid fraction over which the PDF is to be constructed. These bounds are defined by the analyst, and may or may not correspond to the minimum and maximum solid fraction values in the data under consideration. Divide the range of solid fraction into K equal-sized intervals; the width of each interval can be calculated using

$$W = \frac{(1-\varepsilon)_{ub} - (1-\varepsilon)_{lb}}{K}. \tag{4}$$

Let N_k represent the number of the $(1-\varepsilon)_i$ measurements that lie in the interval k, where k=0,(K+1). The probability density function defined at the midpoint of interval k is given by

$$PDF_k = \frac{N_k}{N \cdot W}. \tag{5}$$

Equation (5) shows that the PDF is just the probability (N_k/N) per interval width (W) that $(1-\varepsilon)_i$ will lie between $[(1-\varepsilon)_{lb} + (k-1)\cdot W]$ and $[(1-\varepsilon)_{lb} + k \cdot W]$. The values of N_k can be determined for each value of $(1-\varepsilon)_i$ as follows.

1. For $(1-\varepsilon)_i \leq (1-\varepsilon)_{lb}$, $N_0 = N_0 + 1$.
2. For $(1-\varepsilon)_{lb} < (1-\varepsilon)_i \leq (1-\varepsilon)_{ub}$, calculate $I_{chk} = [(1-\varepsilon)_i - (1-\varepsilon)_{lb}]/W$. The interval index k is the largest integer that is less than or equal to I_{chk}. $N_k = N_k + 1$.
3. For $(1-\varepsilon)_{ub} < (1-\varepsilon)_i$, $N_{K+1} = N_{K+1} + 1$.

It should be noted that the PDF is not unique, it depends on the value specified for K. If K is too small, the PDF will provide only a course resolution of the distribution. Conversely, if K is too large, there may be intervals in the middle of the distribution that contain no samples, leading to an erratic distribution. When comparing two PDFs, the number and width of the intervals should be kept the same. In the current study, solid fraction intervals 0.02 wide were found to provide detailed and well-behaved PDF curves.

4.2.3 Power Spectral Density Analysis

4.2.3.1 Power Spectral Density

The power spectral density, $P_x(f)$, describes the rate at which the mean squared amplitude of a quantity x varies with frequency, f. $P_x(f)$ shows how the "power" in x is distributed over the range of frequencies. For example, the power spectral density of a sine wave with a frequency f_o involves a delta function at f_o. This indicates, not surprisingly, that all the power in the sine wave lies at a single frequency.

To calculate the power spectral density, it is first necessary to convert x(t), in the time domain, to X(f), in the frequency domain. This is accomplished by Fourier transforming the data. The Fourier transform of x(t) is given by (Press et al., 1989)

$$X(f) = \int_{-\infty}^{\infty} x(t) \cdot e^{j2\pi ft} dt, \tag{6}$$

where $j = \sqrt{-1}$, and X(f) is generally a complex number. But for discrete data, x(t) will only be known over a finite time interval, say between 0 and T. In this case, the Fourier transform of x(t) is

$$X(f,T) = \int_{0}^{T} x(t) \cdot e^{j2\pi ft} dt \tag{7}$$

When x(t) is represented by discrete values, the transformation expressed in (7) is typically accomplished using fast finite Fourier transform (FFT) procedures on a digital computer. The (one-sided) power spectral density of x(t) can be calculated using

$$P_x(f) = 2 \cdot \lim_{T \to \infty} \frac{1}{T} \left\langle |X(f,T)|^2 \right\rangle. \tag{8}$$

$|X(f,T)|$ is the magnitude of X(f,T), and $\langle\ \rangle$ represents the ensemble averaging operation. Real data have a finite T, and hence the averaging can only be done for a finite number of ensemble elements. The ensemble averaging is accomplished by breaking a record of length, T_T, into n continuous segments of length T, where $T_T = n \cdot T$. Each segment is then Fourier transformed, and the expected value for $|X(f)|^2$ is estimated by averaging the values for every segment at each frequency. Increasing the number of data segments reduces the random error in the power spectrum estimate (more specifically, it reduces the standard deviation of the estimate by $1/\sqrt{n}$). But for a fixed record length, T_T, increasing the number of segments reduces the resolution of the estimate. Thus, longer record lengths reduce the random error in the power spectrum estimate while making it possible to maintain resolution.

The discontinuities at the beginning and end of a finite digital data record can cause power in the spectrum to "leak". This power leakage can distort the spectrum, causing the power at frequencies on either side of a spectral peak to be overestimated. This problem is addressed by applying a window function to the data that eliminates the discontinuities at the ends of the time-history data. Many window functions have been proposed (e.g., see Press et al., 1989), one of the most common is the Hanning window. A Hanning window was used in the power spectrum estimates for this study.

One problem with applying a window to the data is that it reduces the resolution of the analysis. This resolution can be recovered by increasing the segment length T for each FFT. But for a fixed record length, this results in fewer data segments, increasing the random error in the power spectrum estimate. This is prevented by dividing the record

into segments that overlap, typically by 50%. The one disadvantage of overlapping is that it doubles the number of FFTs that must be calculated.

The power spectral density estimates shown in this study were calculated using MATLAB which is a mathematical analysis software package developed by The Mathworks, Inc. (The MathWorks, Inc., 1993). The power spectrum estimates presented in this chapter are based on approximately 30,000 data points. Segment sizes ranging from 256 to 2024 points were evaluated. Segments of 256 points were found to satisfactorily resolve the features of the power spectrum while minimizing the random error. As mentioned previously, a Hanning window was used in the power spectrum estimates. The data segments were overlapped by 50% to compensate for the reduced resolution caused by the window.

In summary, the solid fraction power spectral density estimates presented in Section 4.5.3.1 are based on 128 Hanning-windowed, 256-point, overlapping data segments.

Finally, it is important to make one additional observation. Remember that $P_x(f)$ describes the rate at which the mean square amplitude of a quantity x varies with frequency, f. This implies that if the input quantity under consideration were voltage as a function of time, for example, the units on the power spectral density would be volts^2/Hz. Here we are interested in the power spectral density of solid fraction as a function of time. Since solid fraction is dimensionless, the units on the power spectral density are 1/Hz, or seconds. Hence, the power spectral densities of solid fraction data from two scaled beds require additional nondimensionalized before they can be compared. The power spectral densities and frequencies compared in Section 4.5.3.1 are nondimensionalized by the factor (u_o/D).

4.2.3.2 Filtering to Avoid Aliasing

When sampling an analog signal, the higher the frequency to be resolved, the higher the sampling rate required. For example, one would need to sample at a much higher rate to capture the features of a 60 Hz sine wave than would be necessary to resolve a 3 Hz sine wave. In the lower limit of a steady signal, only one sample is required. The Nyquist frequency (f_N) defines the highest frequency accurately resolved for a specified sampling rate. The Nyquist frequency is given by

$$f_N = \frac{f_s}{2} = \frac{1}{2 \cdot \Delta t}, \tag{9}$$

where f_s is the sampling frequency, which can alternatively be expressed as the time between samples (Δt). So, for example, the 60 Hz sine wave requires a sampling rate of 120 samples per second (i.e., Δt=0.0083 s) to be accurately sampled.

One additional problem is that if the sampling frequency is insufficient for the bandwidth of the analog signal, the frequencies above the Nyquist frequency (i.e., $f > f_s/2$) will appear as lower frequencies in the digitized data. This phenomenon is referred to as aliasing.

In the case of the solid fraction measurements, the exact bandwidth of the signal is not known *a priori*. The best approach to prevent aliasing is to limit the bandwidth of the continuous signal by analog filtering. Analog filtering the signal prior to digitization defines the signal bandwidth. The signal can then be sampled at a rate above the Nyquist frequency corresponding to the specified bandwidth. As discussed in Sections 4.3.1 and 4.3.2, the data acquired from both the Tidd PFBC and the cold-scale model were electronically filtered prior to digitization.

4.3 Experimental Test Procedures

4.3.1 Tidd PFBC Test Procedure

The Tidd PFBC time-varying pressure drop data were taken by a team of engineers from Babcock & Wilcox's (B&W's) Alliance Research Center. A summary of their efforts is provided in Fuller (1995). Although B&W acquired the data from the Tidd plant, the Tidd data were analyzed as part of this study.

Prior to digitization, the signal from the pressure transducer was electronically low-pass filtered (50 Hz) to prevent aliasing and to eliminate any high frequency noise. It was also high-pass filtered (0.1 Hz) to remove the mean from the data, leaving only the fluctuating component of the signal. The static differential pressure drop was subsequently measured by resetting the filters to remove the dynamic component of the signal. At each level in the bed, 30000 points were acquired at a sampling rate of 294 Hz (i.e., 102 seconds of data).

As discussed in Chapter 3, because the Tidd PFBC is a demonstration plant, it is equipped to provide measurements that would not typically be available from a standard boiler. One of these special features is a set of 8 experimental pressure taps. These taps were used to obtain the time-varying pressure drop data. One problem that arose during testing at Tidd was that the lowest experimental pressure tap was plugged. But pressure-drop measurements in the bottom of the bed were of particular interest. There are no boiler tubes in the bottom of the bed, creating a region with unique hydrodynamics. In addition to the experimental taps, the bed is fitted with standard pressure taps for plant operations. The so-called POPS (Plant Operational Performance System) system provides static pressure-drop measurements over several elevations in the bed. The POPS data served two purposes. First, they made it possible to independently check the mean pressure

profile measured using the experimental taps and the high-speed data acquisition system. And second, they provided some limited information on the hydrodynamics of the bottom of the bed (i.e., the mean solid fraction).

4.3.2 MIT Cold Model Test Procedure

The data from the cold model were filtered prior to digitization. The filter could only accommodate one channel at a time, hence the cold model data were obtained using a single, 0-5 in. H_2O, fast-response pressure transducer. Therefore, as with the Tidd differential pressure data, the data for each level in the cold model were taken sequentially rather than simultaneously. At each level in the bed, 33000 points were sampled at 500 Hz (i.e., 66 seconds of data). Fluidized-bed hydrodynamic frequencies are modest, typically less than 10 Hz (Gogolek and Grace, 1995), so a sampling rate of 500 Hz is excessive. But individuals from Babcock & Wilcox were interested in performing data analyses that they felt required high sampling rates (Fuller, 1995); the 500 Hz sampling rate was chosen to accommodate their request.

4.4 Experimental Test Conditions

Table 1 summarizes the test conditions for the Tidd PFBC and the MIT cold model scaling comparison.

Table 1: Summary of Tidd PFBC and MIT Cold Model Test Conditions

	Tidd PFBC	MIT Cold Model
T (K)	1135	311
p (Pa-abs)	9.04×10^5	1.013×10^5
μ (kg/m-s)	4.6×10^{-5}	1.9×10^{-5}
ρ_g (kg/m^3)	2.8	1.1
ρ_s (kg/m^3)	2513	918
ϕ_s	0.82	0.85
u_{mf} (m/s)	0.24	0.12
u_o (m/s)	0.91	0.46
D (m)	3.4	0.85
d_p (μm)	851	609

As shown in Table 1, the Tidd data were taken at a bed temperature of 1135 K (1583 °F) and 9 atm. pressure. The cold model fluidizing air was essentially at ambient temperature and pressure. The Tidd PFBC uses dolomite as a sorbent material. A granular polyethylene was used in the cold model to closely match the solid-to-gas density ratio between the two beds. D represents the bed width; Table 1 shows that the cold model dimensions are one-quarter those of the Tidd PFBC. Note that the bed dimension chosen for D is arbitrary since all dimensions are scaled down by a factor of four. The simplified set of scaling parameters relaxes the requirement that the particle size also scale down by the scale factor. The error associated with using the simplified set of scaling parameters was evaluated in Section 3.2.1. The cold model particle size was chosen to match u_o/u_{mf} between the hot bed and the cold model.

Table 2 compares the values of the simplified set of scaling parameters for the two beds. The values of the simplified scaling parameters were closely matched between the cold

model and the Tidd PFBC. The granular polyethylene used in the cold model matches the hot-bed solid-to-gas density ratio within 8%, and it matches the particle sphericity (ϕ_s) within 4%. In addition, the dimensionless particle size distribution (PSD) was matched between the two beds (see Section 3.2).

A detailed discussion on calculating the cold-bed geometry and operating parameters listed in Table 1 is given in Chapter 3, Section 3.2.

Table 2: Summary of Tidd PFBC and MIT Cold Model Simplified Scaling Parameters

	Tidd PFBC	MIT Cold Model
ρ_s / ρ_g	898	835
$u_o^2 / g \cdot D$	0.025	0.025
u_o / u_{mf}	3.8	3.8
L / D	geom. similar	geom. similar
ϕ_s	0.82	0.85
PSD	matched	matched

The Tidd plant operates at a fixed volumetric flowrate. Due to seasonal changes in the ambient air density, mass flowrate limitations prohibit the Tidd PFBC from operating at full bed height during the summer months. The expanded bed height at full load coincides approximately with the top of the tube bank (H). The data used in the following scaling comparisons were taken at a single operating condition with reduced bed load and bed height. The expanded bed height in the Tidd plant at the tested operating condition was z/H=0.58, where H is the height of the tube bank relative to the distributor. Since the bed was not operating at its full height, comparisons of the time-resolved pressure drop data were only made at three bed elevations (measured midway between the pressure taps):

z/H = 0.22, 0.34, 0.50. The four taps used to take the pressure drop data were located at: z/H = 0.17, 0.28, 0.40, and 0.61 (see Figure 2 in Chapter 3).

4.5 Hydrodynamic Scaling Comparisons

4.5.1 Voidage Comparisons

4.5.1.1 Solid Fraction Profile Comparisons

Solid fraction can be calculated from differential pressure drop measurements using (1). The solid fraction represents the fraction of the total volume between two pressure taps that is solid. Or, alternatively, the solid fraction is one minus the voidage (the fraction of the total volume that is gas). The local mean solid fraction is an important characteristic of fluidized-bed hydrodynamics.

Figure 1 compares the cold model and the Tidd PFBC solid fraction profiles. The upper dashed line denotes the location of the bed surface, and the lower dashed line identifies the bottom of the tube bank. Two sets of data from the Tidd plant are plotted on Figure 1. One set was taken using the experimental taps ("Expt. Taps") used to obtain the time-varying pressure drop data, and the other data set, designated "Plant Taps", is plant operating data from the POPS system. Figure 2 in Chapter 3 shows the relative location of the two sets of taps. Data from the plant taps were used since, as discussed in Section 4.3.1, the lowest experimental tap was plugged. The POPS system only provides time-averaged data.

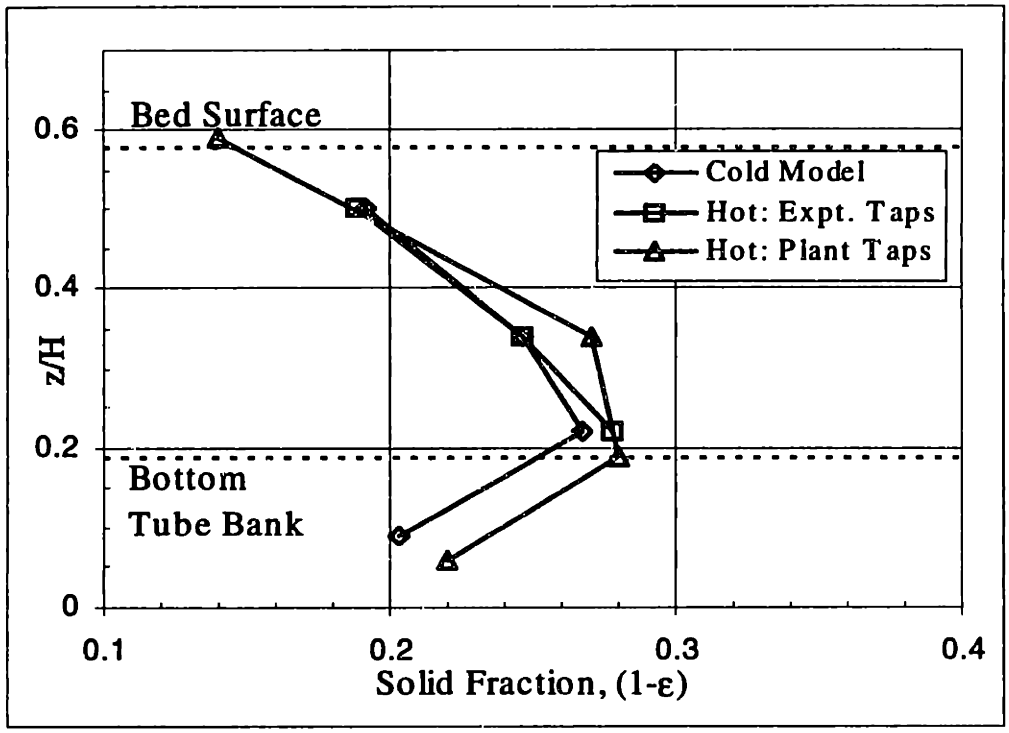

Figure 1: Comparison of Tidd PFBC and Cold Model Solid Fraction Profiles

Figure 1 shows that the agreement between the cold model and the Tidd Expt. Taps solid fraction profiles is extremely good. Good agreement is also obtained in the bottom of the bed between the plant-data solid fraction profile and the cold-model profile. The solid fraction is lower (higher voidage) in the bottom of the bed most likely due to the presence of many small, slow moving bubbles. As the bubbles coalesce, they rise faster causing an increase in the solid fraction (reduced voidage). The tube bank tends to restrict further bubble growth causing a flattening of the profile. The presence of the bed surface in the uppermost pressure drop interval leads to a reduced solid fraction at the top bed location. The numerical data used to generate Figure 1 are given in Appendix D.

4.5.1.2 Bed Expansion Comparisons

Figure 1 compares the *local* solid fractions, or alternatively voidages, between the Tidd PFBC and the cold model. The bed expansion reflects the *integrated*, or overall, bed

voidage. For the same scaled bed solid inventories (i.e., $V_{s\text{-}cold}=V_{s\text{-}hot}/4^3$), if the cold model is scaled properly, it should have the same dimensionless expanded bed height. The bed expands to accommodate rising bubbles, and thus the expanded bed height reflects the hydrodynamics of the bed.

Although the solid inventories of the two beds were not measured, they can be deduced from the expanded bed height (H_B) and the solid fraction profile, each determined from pressure-drop measurements. Since bed height and solid fraction are easier to measure than bed solid volume, the particle inventory in the cold model was adjusted until the measured expanded bed height matched the properly-scaled bed height (i.e., $H_{B\text{-}cold} = H_{B\text{-}hot}/4$). The solid fraction is the solid volume per total volume (gas plus solid). In this case, by setting the expanded bed height, the scaled total volume was matched since the dimensions of the cross-section were scaled. The solid volume was then calculated using the measured solid fractions. The objective was to show that if the scaled total volumes were matched, the solid volumes would also scale properly. Since the total volume consists of gas and solid, this is another way saying that the overall bed voidage should be the same between the hot bed and the cold model.

The expanded bed heights were determined from the pressure profiles in the beds. The pressure-drop data were plotted in the form $(p(z)-p_{fb})$ versus distance from the distributor (z), where p_{fb} is the freeboard pressure. The expanded bed height was found by linearly extrapolating the pressure profile to the elevation where $(p-p_{fb})=0$. The expanded bed height (H_B) is the distance from the distributor where the pressure (p) equals the freeboard pressure (p_{fb}). The expanded bed height of the Tidd PFBC was estimated to be 2.13 m, requiring the cold model bed inventory to be adjusted to achieve a bed height of 53 cm.

The Tidd bed total volume ($V_{T\text{-}hot}$) under consideration is 13.866 m^3. This corresponds to a cold bed total volume ($V_{T\text{-}cold}$) of 0.217 m^3, such that

$$\frac{V_{T-hot}}{V_{T-cold}} = 4^3 = 64 . \qquad (10)$$

The bed total volumes were calculated by taking the product of the expanded bed height and the area of the bed cross-section under consideration. Assuming that the solid fraction in the bottom of the Tidd PFBC is that measured by the POPS system and using the data from the experimental taps for the other levels in the bed, the volume of solids in each pressure-drop interval can be calculated. Table 3 summarizes the local and total solid volumes for the Tidd PFBC and the cold model. The volume of solids in an interval is the product of the local solid fraction, determined from pressure drop measurements, and the total volume (solids plus gas) of the interval (V_{T_i}).

Table 3: Solid Volume in Pressure Drop Interval

z/H	Tidd PFBC $(1-\varepsilon)_i$	Tidd PFBC $Vs_i=(1-\varepsilon)_i \cdot V_{T-hot_i}$	Cold Model $(1-\varepsilon)_i$	Cold Model $Vs_i=(1-\varepsilon)_i \cdot V_{T-cold_i}$
0.09	0.22	3.051	0.203	0.044
0.22	0.278	3.855	0.267	0.058
0.34	0.246	3.411	0.246	0.053
0.50	0.188	2.607	0.192	0.042
		$Vs_{hot}=12.924\ m^3$		$Vs_{cold}=0.197\ m^3$

If the cold model perfectly simulates the Tidd combustor, Vs_{hot}/Vs_{cold} would equal 64. The actual ratio is 65.6 which is within 2.5% of the theoretical value. This is well within the experimental uncertainty and reflects the overall agreement between the solid fraction profiles shown in Figure 1.

4.5.2 Probability Density Function Comparisons

Figures 2 to 4 present the probability density functions of the solid fraction data for the three bed elevations. The largest disagreement occurs between the standard deviations at

z/H=0.22. But, in general, the figures show exceptional agreement between the mean (as shown in Section 4.5.1.1) and the standard deviation of the time-varying solid fraction measurements at all three bed levels. The figures show that the hydrodynamics (i.e., the distribution of scaled bubble sizes at each elevation), as reflected in these comparisons, are very similar.

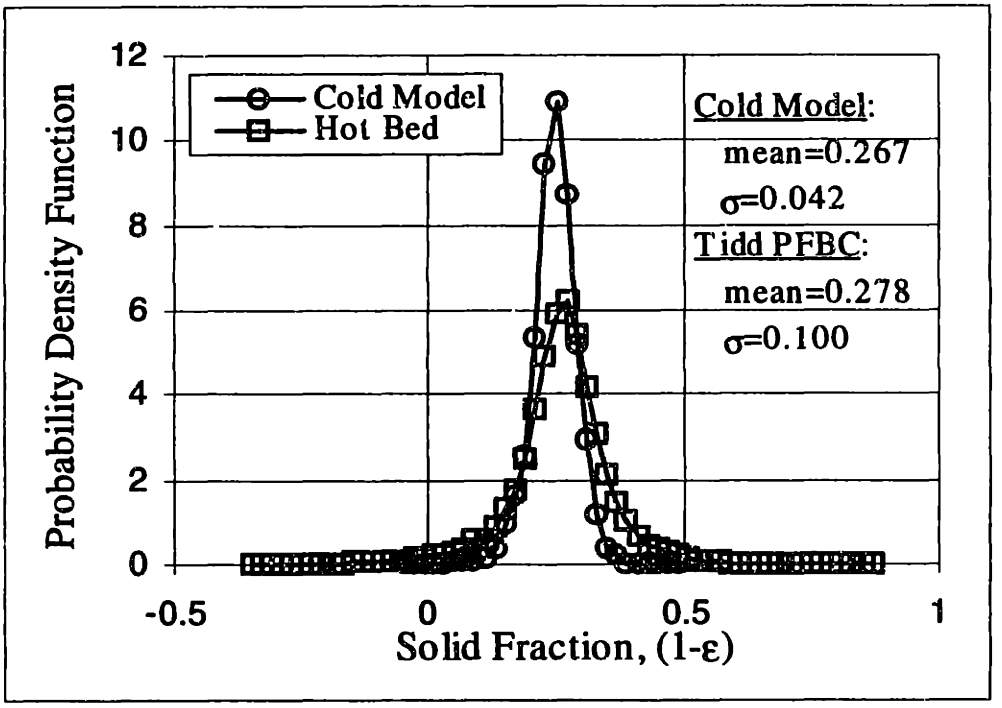

Figure 2: Probability Density Function Comparison at z/H=0.22

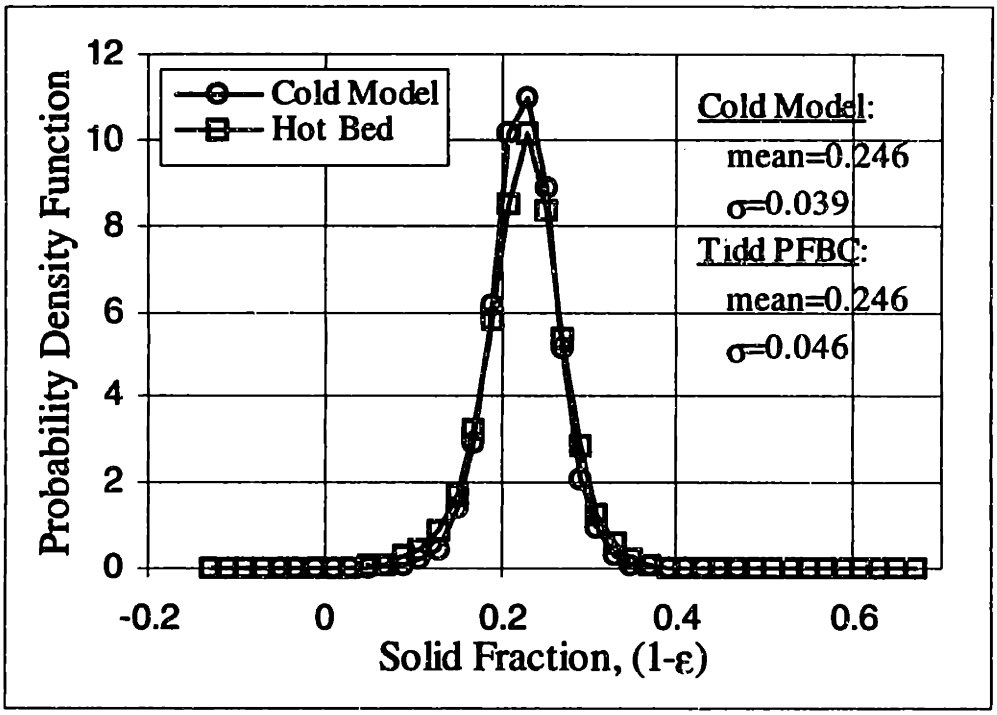

Figure 3: Probability Density Function Comparison at z/H=0.34

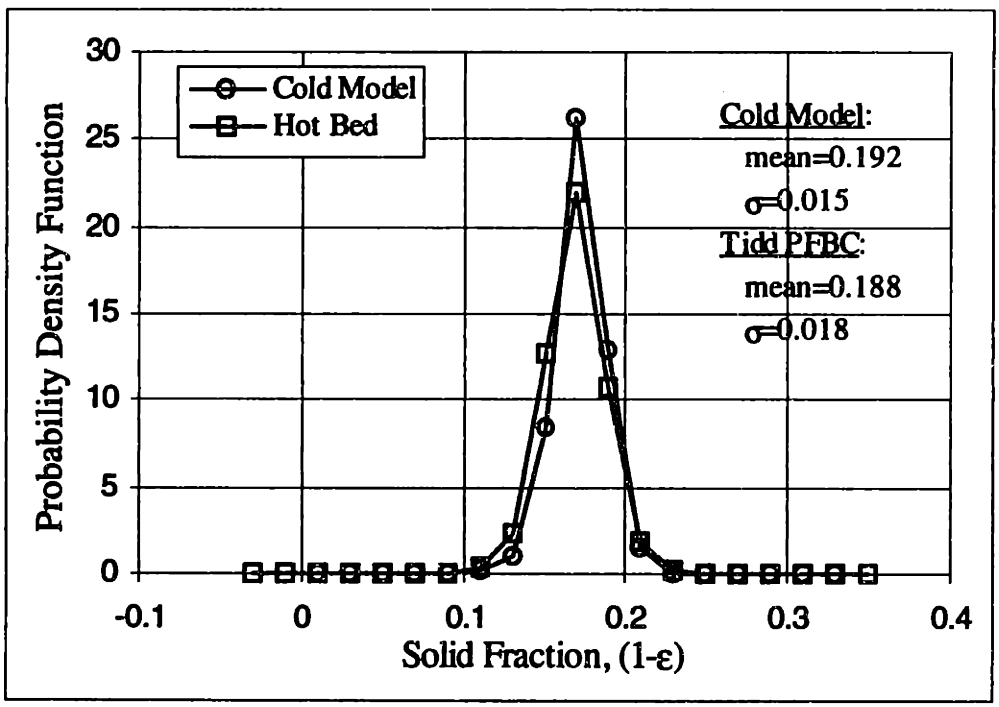

Figure 4: Probability Density Function Comparison at z/H=0.5

4.5.3 Frequency Domain Comparisons

4.5.3.1 Power Spectral Density Comparisons

As discussed in Section 4.2.3.1, the dimensionless power spectral density is used to compare the frequency content of the hot bed and the cold-scale model pressure fluctuations. Figures 5 to 7 compare the dimensionless power spectral densities of the Tidd PFBC and the cold model pressure data at z/H = 0.22, 0.34, and 0.50; in general, the agreement is poor.

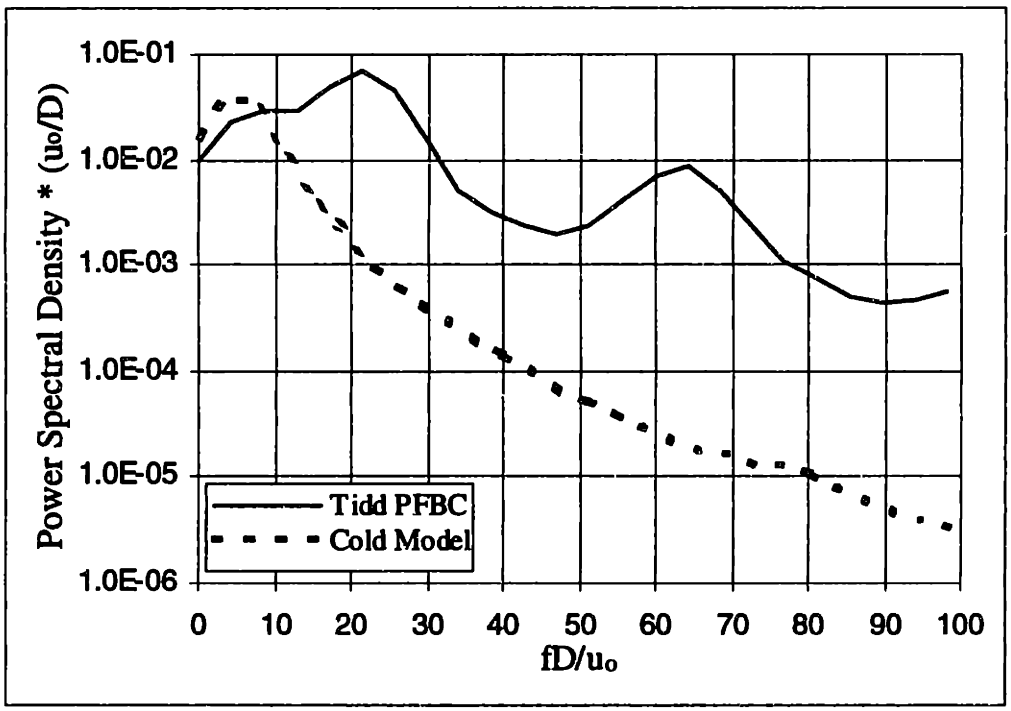

Figure 5: Power Spectral Density Comparison at z/H=0.22

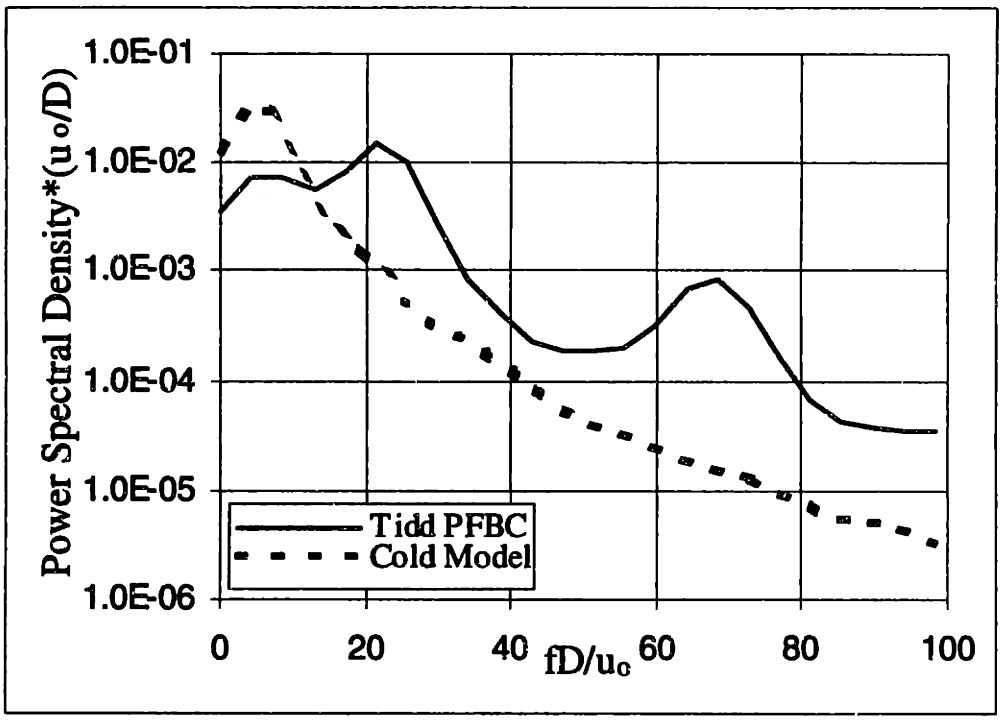

Figure 6: Power Spectral Density Comparison at z/H=0.34

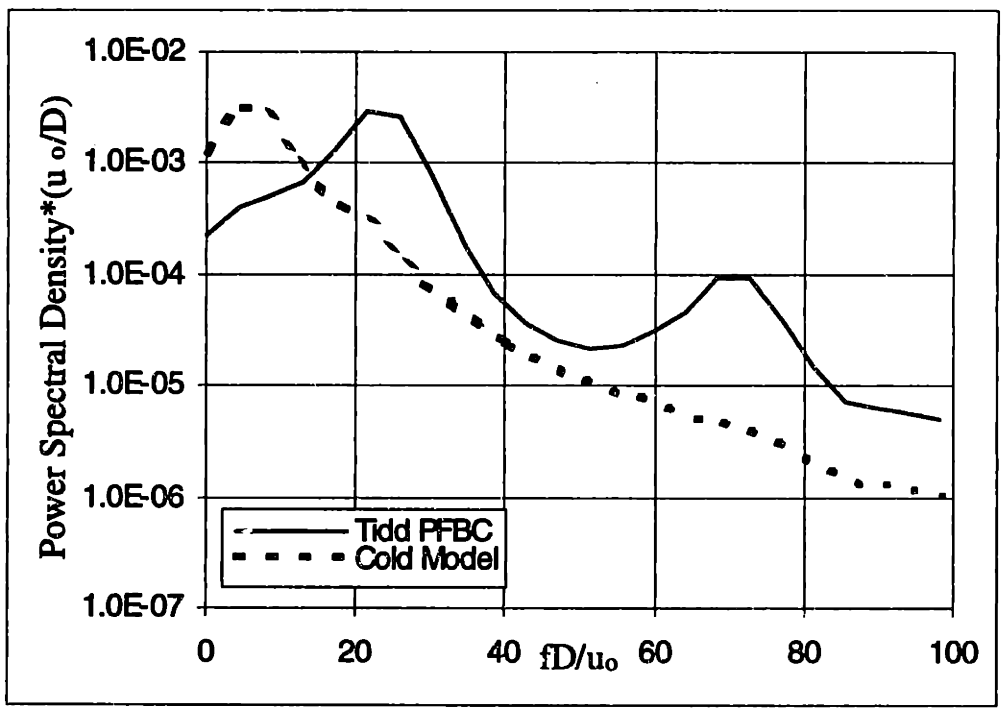

Figure 7: Power Spectral Density Comparison at z/H=0.50

The Tidd power spectrum contains pronounced peaks while the cold model power spectrum decays from a single dominant frequency. Based on prior experience (e.g., Nicastro and Glicksman, 1984), the cold model power spectra exhibit the anticipated behavior; the Tidd power spectra are quite unusual. The Tidd power spectrum is most likely higher than the cold model power spectrum at higher frequencies due to the amplification of the pressure signal in the Tidd pressure lines. The analysis in Section 3.1.1.1 suggests that components of the pressure signal with frequencies above roughly 13 Hz will be amplified by a resonance in the Tidd pressure lines.

Figure 8 shows the dimensional power spectrum estimates for two locations in the Tidd PFBC over a broader frequency range than that shown in Figures 5 to 7. The z/H=0.22 power spectrum is from data taken within the fluidized portion of the combustor, while the z/H=1.12 data were taken in the open freeboard region well above the surface of the bed. (The bed surface coincides with z/H=0.58.) Both plots contain distinct peaks at the same frequencies, suggesting that the source of the peaks is unrelated to the fluidization characteristics. (The power spectral density of the pressure data at all levels in the Tidd bed contain these peaks.) The power spectra have peaks at frequencies around 6, 17, 30 and 42 Hz; the last three peaks are well above expected hydrodynamic frequencies. (According to Gogolek and Grace (1995), the hydrodynamic fluctuations caused by the passage of bubbles and the pressure waves produced by bubbles bursting at the bed surface are between 1 and 10 Hz.) This suggests that structural vibration or other sources are responsible for the peaks. The frequency content of the Tidd PFBC pressure drop data appear to be contaminated.

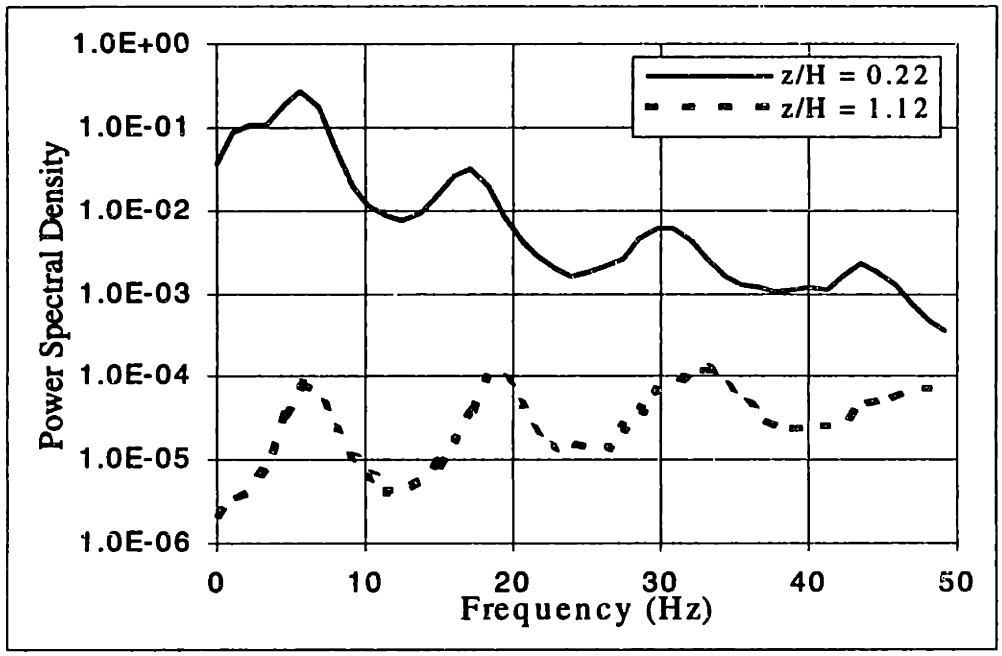

Figure 8: Illustration of Peaks in Tidd Power Spectra-Within and Above the Bed

4.5.3.2 Evaluation of Possible Source of Peaks in Power Spectra

The following discussion suggests that tube vibrations could be one possible source of the contamination. The Tidd PFBC has not experienced excessive erosion or mechanical failure rates, which implies that any vibration is structurally insignificant. One would expect large amplitude vibrations to also affect the bed hydrodynamics. The exceptional agreement in the solid fraction and probability density function comparisons shown in Figures 1 to 4 suggest that any vibration must be small enough to have a minimal effect on the hydrodynamics.

Turner et al. (1982) remark that the forces on an immersed tube bank decrease with increasing distance from the distributor, with the lowest tubes experiencing the highest forces. This is consistent with the deviations of the Tidd power spectra from those of the cold model shown in Figures 5 and 6. Turner et al.'s observations suggest that the forces on the tube bank are higher at z/H = 0.22 (Figure 5) than for z/H = 0.34 (Figure 6),

enhancing any tube vibration in the lower level. Figures 5 and 6 show that the deviation between the magnitude of the Tidd power spectrum and that of the cold model is greatest at the lowest level in the bed where the forces are highest.

As discussed by Païdoussis (1982), tightly-spaced tube arrays in dense fluids have been shown to be susceptible to strong hydrodynamic coupling between tubes. The acceleration of one tube can create a pressure wave that causes adjacent tubes to vibrate. Therefore, it would not be surprising if pressure waves from vibrating tubes were reflected in pressure measurements.

Vincent et al. (1987) concluded that tubes in a fluidized-bed with clamped supports respond like a beam with fixed end conditions. The equation for the natural frequencies of a uniform fixed-end beam of length ℓ, under a uniform load per unit length, w, is given by (Barber, 1992)

$$f_n = \frac{k_n}{2\pi} \cdot \sqrt{\frac{EIg}{w\,\ell^4}}, \qquad (11)$$

where E is the modulus of elasticity and I is the moment of inertia. k_n is a constant for each beam mode. In this case, k_1, k_2, k_3, and k_4 are equal to: 22.4, 61.7, 121, and 200, respectively. Equation (11) shows that the ratios of the natural frequencies, for the same beam, are constant and equal to the ratios of the values of k_n. Table 4 shows that these ratios for a uniform fixed-end beam closely agree with the ratios of the peak frequencies shown in Figure 8. This suggests that a possible source of the peaks in the Tidd power spectra could be the excitation of the natural frequencies of the tubes in the bed. The exact values of the frequencies depend on the tube bank construction. The tubes in the Tidd bed are supported in a complicated manner, which makes estimating *l* and the other parameters in (11) extremely difficult. But using a very rough estimate of the parameters in (11) indicates that the first natural frequency of the tube bank should be between 15 and 20 Hz. The value of the first peak frequency (6 Hz) is within the range of the natural frequencies of fluidized-bed heat exchanger tubes quoted in the literature (e.g. Vincent et al., 1987; Turner et al., 1982).

Table 4: Comparison of Tidd PFBC Peak Frequencies and Fixed-End Beam Natural Frequencies

i	Fixed End Beam $f_n(i+1)/f_n(i)$	Tidd PFBC $f_p(i+1)/f_p(i)$
1	2.8	2.8
2	2.0	1.8
3	1.7	1.4

The cold-model tube bank would not exhibit any vibration that might be present in the hot bed. No attempt was made to scale the structural/materials characteristics of the hot-bed tube bank. Damping was added to the cold model tube bank to prevent vibrations from affecting the hydrodynamics.

The natural frequencies of the tubes in the Tidd PFBC depend on the detailed geometry of the tube bank and the characteristics of the fluidization. To accurately determine the natural frequencies would require detailed measurements on the tubes while the bed was running since the natural frequencies of the tubes are influenced by the presence of the bed material due to added-mass effects (Vincent et al., 1987). Detailed hot in-bed measurements were beyond the scope of the current study.

Babcock and Wilcox (B&W), the designers of the Tidd tube bank, suggested fluctuations in the coal and limestone feed and fluctuations in the air flow as other possible explanations for the peaks in the Tidd power spectra. The analysis presented in Section 3.1.1.1 also points to the Tidd pressure lines as a possible source of problems. This analysis and Babcock & Wilcox's data (Fuller, 1995) show that resonance is a possible problem with the lines. Fuller (1995) has also expressed concerns over nonlinear behavior distorting the pressure signal as it travels through the pressure lines. Their pressure line

test data do not exhibit significant pressure-signal distortion, just amplification, but the data were only taken for a single frequency.

Another hypothesis is that the flow past the pressure taps, which extend 46 cm into the bed, sets up standing waves in the pressure lines. Treating the pressure line as a pipe that is closed at one end, the natural frequencies are given by (Serway, 1983)

$$f_n = n\frac{c}{4 \cdot l}, \tag{12}$$

where only the odd harmonics are present (i.e., n=1,3,5,7,...). l is the length of the pressure lines and c is the speed of sound in the air in the pressure lines. The speed of sound (c) is given by

$$c = \sqrt{\gamma RT} \tag{13}$$

where γ is the ratio of specific heats, R is the ideal gas constant, and T is the absolute temperature. For air, γ=1.4 and R=287 J/kg-K. The Tidd PFBC pressure lines are located within the Tidd pressure vessel. During boiler operation, the temperature of air in the pressure vessel is around 590 K. Assuming that the air in the pressure lines is in thermal equilibrium with the air in the pressure vessel, and using (13) to calculate the speed of sound in the pressure lines gives: c=487m/s. Fuller (1995) estimated that the Tidd pressure lines were roughly 15 m long. It was neither possible to get an exact measurement of the pressure line length, nor was it possible to know exactly what the speed of sound is in the pressure lines. But if it is assumed that the lines were actually 20 m long (i.e., l=20m) and that the speed of sound in the lines (c) is 487m/s, according to (12) the first harmonic frequency is 6 Hz. This is equivalent to the first peak frequency in the Tidd power spectrum. Since only the odd harmonics are present, the third, fifth and seventh natural frequencies would be: 18, 30, and 42 Hz, respectively. These frequencies are essentially the same as those found in the Tidd power spectrum. Hence, another possible source of the peaks in the Tidd power spectrum is that the flow past the pressure taps sets up standing waves in the pressure lines that manifest themselves in the frequency content of the pressure signal. Note that for shorter line lengths the frequencies are

higher, and thus pressure lines of more moderate length would have harmonic frequencies at high enough frequencies that they would most likely go unnoticed.

4.6 Nomenclature

c	speed of sound
D	bed width
d_p	surface-volume mean particle diameter
E	modulus of elasticity
f	frequency
f_n	natural frequency
f_N	Nyquist frequency
f_p	frequency of peaks in Tidd power spectrum
f_s	sampling frequency
g	acceleration due to gravity, 9.807 m/s^2
H	distance from the distributor to the top of the tube bank
H_B	expanded bed height
I	moment of inertia
I_{chk}	index for constructing PDF
j	$\sqrt{-1}$
k_n	constant for each mode of a fixed-end beam
K	number of bins used to construct the PDF
l	pressure line length
ℓ	fixed-end beam length
L	bed dimension
n	number of records of length T comprising the total record length T_T or the harmonic frequency number
N	number of discrete measurements
N_k	number of measurements that fall into bin k
p	pressure
p_{fb}	freeboard pressure
$P_x(f)$	one-sided power spectral density of x(t)
PDF	probability density function
PSD	dimensionless particle size distribution
R	perfect gas constant for air=287 J/kg-K
T	absolute temperature or length of record for which the $P_x(f)$ is calculated
T_T	total record length
t	time
u_o	gas superficial velocity
u_{mf}	minimum fluidization velocity
V_S	volume of solids
V_T	total volume, gas plus solid
w	uniform load per unit length on a fixed-end beam
W	width of the bins used to construct the PDF
x(t)	variation of x with time
X(f)	Fourier transform of x(t)

z distance above the distributor

Greek Symbols

Δh distance between pressure taps
Δp differential pressure drop
Δt time between discrete data sampling
ε local voidage
$(1-\varepsilon)$ solid fraction
$(1-\varepsilon)_{lb}$ lower solid fraction bound for the PDF
$(1-\varepsilon)_{ub}$ upper solid fraction bound for the PDF
ϕ_s particle sphericity
γ ratio of specific heats, c_p/c_v
μ gas viscosity
ρ_g gas density
ρ_s solid density
σ standard deviation of the time-varying solid fraction measurements

4.7 References

Almstedt, A.E. and Zakkay, V.,1990, "An Investigation of Fluidized-Bed Scaling - Capacitance Probe Measurements in a Pressurized Fluidized-Bed Combustor and a Cold Model Bed," *Chemical Engineering Science*, 45, No. 4, pp. 1071-1078.

Barber, A., 1992, Handbook of Noise and Vibration Control, 6th Edition, Elsevier, Oxford, U.K.

Bendat, J.S. and Piersol, A.G., 1986, Random Data–Analysis and Measurement Procedures, Second Edition, John Wiley & Sons, New York.

Fan, L.T., Ho, T.C., Hiraoka, S., and Walawender, W.P., 1981, "Pressure Fluctuations in a Fluidized Bed," *AIChE Journal*, 27, No. 3, pp. 388-396.

Fuller, T.A., 1995, "Application of Scaling Laws to PFBC - Final Report," Babcock & Wilcox Report No.: RDD:95:43109-001-000:08.

Gogolek, P.E.G. and Grace, J.R., 1995, "Fundamental Hydrodynamics Related to Pressurized Fluidized Bed Combustion," *Prog. Energy Combust. Sci.*, 21, pp. 419-451.

Ishii, H. and Murakami, I., 1991, "Evaluation of the Scaling Law of Circulating Fluidized Beds in Regard to Cluster Behaviors," in Circulating Fluidized Bed Technology III, P. Basu, M. Horio, and M. Hasatani, eds., Pergamon Press, p. 125.

Lirag, R.C. and Littman, H., 1971, "Statistical Study of the Pressure Fluctuations in a Fluidized Bed," AIChE Symposium Series, No. 116, 67, pp. 11-22.

Newby, R.A. and Keairns, D.L., 1986, "Test of the Scaling Relationships for Fluid-Bed Dynamics," Fluidization V, Engineering Foundation, New York, pp. 31-38.

Nicastro, M.T. and Glicksman, L.R., 1984, "Experimental Verification of Scaling Relationships for Fluidized Bed," *Chemical Engineering Science*, 39, 9, pp.1381-1391.

Païdoussis, M.P., 1982, "A review of flow-induced vibrations in reactors and reactor components," *Nuclear Engineering Design*, 74, p. 31-60.

Press. W.H., Flannery, B.P., Teukolsky, S.A., and Vetterling, W.T., 1989, Numerical Recipes - The Art of Scientific Programming, Cambridge University Press, Cambridge.

Roy, R. and Davidson, J.F., 1989, "Similarity Between Gas-Fluidized Beds at Elevated Temperature and Pressure," Fluidization VI, Engineering Foundation, New York, pp. 293-300.

Serway, R.A., 1983, Physics for Scientists and Engineers with Modern Physics, Saunders College Publishing, Philadelphia.

The MathWorks, Inc., 1993, Signal Processing Toolbox User's Guide, Natick, MA.

Turner, M.J. and Irving, D., 1982, "Forces on Tubes Immersed in a Fluidised Bed," Proceedings of the Seventh International Conference on Fluidized-Bed Combustion, Philadelphia, PA, pp. 831-839.

Vincent, R.Q., Hart, D.E., and Siddall, W.F., 1987, "Dynamic Forces on Tubes Immersed in Bubbling AFBC," Proceedings of the Ninth International Conference on Fluidized-Bed Combustion, Boston, MA, pp. 567-574.

This page intentionally blank

5. Importance of the Solid-to-Gas Density Ratio for Scaling Bubbling Fluidized-Bed Hydrodynamics

5.1 Motivation for Study

In 1984, Glicksman (1984) developed, what were referred to in Chapter 2 as, the full set of scaling parameters. The full set of scaling relationships is given by

$$\frac{\rho_s}{\rho_g} \quad \frac{u_o^2}{gD} \quad \frac{\rho_g u_o d_p}{\mu} \quad \frac{D}{d_p} \quad \frac{L}{D} \quad \phi_s \quad \text{PSD}. \tag{1}$$

In the same paper, Glicksman (1984) proposed a reduced set of scaling parameters–the viscous-limit scaling parameters–for use in the limit of low particle Reynolds number (Re_{dp} less than roughly 4). Horio et al. (1986) later proposed what appeared to be a different set of scaling parameters specifically for bubbling beds. But Glicksman (1988) showed that Horio et al.'s (1986) bubbling bed scaling parameters were a subset of the full set of scaling parameters and equivalent to the viscous-limit scaling parameters. The viscous-limit/Horio-bubbling-bed scaling parameters are given by

$$\frac{u_o^2}{gD} \quad \frac{u_o}{u_{mf}} \quad \frac{L}{D} \quad \phi_s \quad \text{PSD}. \tag{2}$$

Note that the solid-to-gas density ratio does not appear in the list of viscous-limit scaling parameters.

In the late 1980s, interest grew in scaling the hydrodynamics of circulating fluidized beds (CFBs). In response, Horio et al. (1989) developed a set of CFB scaling parameters. The scaling parameters were based on Ishii et al.'s (1989) clustering annular flow model (CAFM). The CAFM views the flow in a CFB in terms of particle clusters moving upward in the core and downward at the wall (annulus). In addition to the parameters listed in (2), the resulting set of scaling parameters included the solid-to-gas density ratio (ρ_s/ρ_g). But Horio et al. (1989) argued that by sacrificing similarity in cluster size

(seemingly a bold assumption considering the central role clusters play in the CAFM), it was possible to neglect the solid-to-gas density ratio, leaving the original bubbling bed scaling parameters (Equation (2)). Horio and his colleagues conducted several experimental studies to verify (2) for scaling CFBs (e.g., Horio et al., 1989 and Ishii and Murakami, 1991). In the studies where the hydrodynamics of two scaled CFBs were found to be similar, the density ratio was not varied. In Tsukada et al. (1991), the one study where the solid-to-gas density ratio was varied, they found that the hydrodynamics of the CFB changed as the density ratio changed.

In Glicksman et al. (1993), attempts were made to verify the viscous-limit scaling parameters (Equation (2)) for use with circulating fluidized beds. They found that it was not possible to achieve hydrodynamic similarity without matching the solid-to-gas density ratio between two scaled beds. In tests where the viscous-limit scaling parameters were used, the agreement between the hydrodynamics of the two beds was poor. Glicksman et al. (1993) proposed that the hydrodynamics of the beds were different because, based on Yang's (1983) choking correlation, one of the beds was choked and the other was not. Interestingly, Yang's (1983) choking correlation depends strongly on the solid-to-gas density ratio ($\sim\left(\rho_g/\rho_s\right)^{2.2}$). Hence, by not matching the density ratio, it was not possible to simulate the flow regime transition. These observations led to the development of the simplified set of scaling parameters, which are given by

$$\frac{\rho_s}{\rho_g} \quad \frac{u_o^2}{gD} \quad \frac{u_o}{u_{mf}} \quad \frac{L}{D} \quad \phi_s \quad \text{PSD}. \tag{3}$$

The detailed development of these scaling parameters is presented in Chapter 2.

The results of Glicksman et al. (1993) and Tsukada et al. (1991) indicate that it is essential to match the solid-to-gas density ratio when scaling circulating fluidized beds. But some controversy remains as to whether Horio et al.'s (1986) scaling parameters (Equation (2)) can be reliably used to scale the hydrodynamics of bubbling fluidized beds. Broadhurst and Becker (1973) developed correlations for the superficial gas velocity and voidage at

minimum bubbling conditions, and a criterion for the onset of slugging. Each of these three phenomenon were found to depend on the solid-to-gas density ratio, suggesting that it is also important to match this parameter when scaling bubbling fluidized beds. The objective of the work presented in this chapter was to determine whether it was important to match the density ratio when scaling bubbling beds. In addition, the results from previous studies on scaling CFBs and the Broadhurst and Becker (1973) study suggest that the density ratio plays an important role in flow regime transitions. Therefore, the effect of the density ratio on the bubbling-slugging transition is also considered.

5.2 Hydrodynamic Scaling Test Conditions

The approach taken here was to compare the hydrodynamics of two beds that have all the simplified set of scaling parameters with the exception of the solid-to-gas density ratio matched between them (i.e., match (2)). Scaling comparisons were made by fluidizing two different density bed materials in the same bed. The experimental setups for the bubbling bed comparisons and the evaluation of the bubbling-slugging transition are described in Sections 5.4.1 and 5.4.2, respectively.

Limestone and polyethylene were chosen as the two bed materials. The density of the limestone was measured to be 2670 kg/m^3 using displacement methods. The polyethylene is the same bed material as that used to scale the hydrodynamics of the Tidd PFBC and has a density of 918 kg/m^3. Tests were conducted using ambient air (ρ_g=1.18 kg/m^3), providing a mismatch in the density ratio between the two bed materials of 290%.

Since the hydrodynamics of the two bed materials were compared using the same bed (i.e., same D), in order to match the Froude number (u_o^2/gD), the bed materials had to be fluidized at the same gas superficial velocity (u_o). And if the beds operate at the same u_o, the bed materials must have the same minimum fluidization velocity (u_{mf}) to match the ratio of the superficial-to-minimum fluidization velocities (u_o/u_{mf}). Hence, it was first

necessary to sieve both the limestone and the polyethylene particles to construct particle size distributions that provided both the same u_{mf} and the same dimensionless particle size distributions (PSD) for the two materials. The limestone has a higher density than the polyethylene and therefore must have a smaller mean particle diameter (d_p) to provide the same u_{mf}. The final particle size distributions for the two bed materials are given in Appendix E. The mean particle size of the limestone was 379 μm, while the mean particle size for the polyethylene was 653 μm. Measurements of the minimum fluidization velocities of the two particle types showed that the polyethylene particles had a u_{mf} of 0.23 m/s, and the limestone particles had a u_{mf} of 0.24 m/s. These minimum fluidization velocities were sufficiently close that they were assumed to be equivalent in the scaling calculations. The dimensionless particle size distributions are compared in Figure 1; the PSDs matched closely.

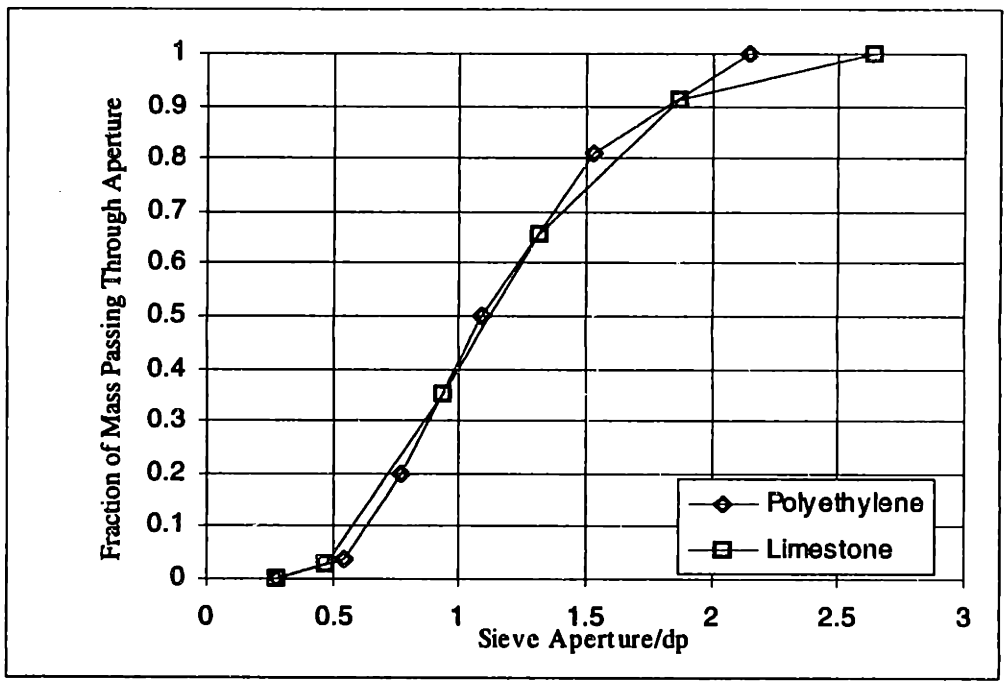

Figure 1: Comparison of Particle Size Distributions

Particle sphericity (ϕ_s) must also be matched between the two bed materials. The particle sphericity for the polyethylene and the Tidd PFBC bed material were measured for the

work described in Chapters 3 and 4. (The sphericity measurements are described in Appendix B.) The polyethylene particles used here were the same as those used in the cold model of the Tidd PFBC; the sphericity of the polyethylene was measured to be 0.85. Fluidized bed combustor sorbents typically have sphericities of around 0.8. The Tidd PFBC bed material had a measured sphericity of 0.82. The sphericity of the limestone was not measured, but, based on visual inspection, it appeared to be typical of fluidized-bed combustor sorbents and was assumed to be approximately 0.82.

Particle-particle interactions are not accounted for in the full set of scaling relationships (Equation (1)). The viscous-limit scaling relationships (Equation (2)) are a simplification of the full set of scaling parameters and hence, also neglect particle-particle interactions. These effects require further consideration when scaling slugging beds. Di Felice et al. (1992) verified Glicksman's (1984) set of scaling parameters (Equation (1)) for bubbling fluidized beds, but found that these relationships failed to provide hydrodynamic similarity between slugging fluidized beds. Chen et al. (1995) explained this by demonstrating that the hydrodynamics of the slugging regime are a function of the frictional characteristics of the particles. They proposed characterizing the particle-particle friction effects using the internal angle of friction (α). This approach is similar to that of Thiel and Potter (1977) who found that the internal angle of friction influenced the characteristics of the slugs in slugging fluidized beds. Since we are also interested in evaluating the bubbling-slugging transition, an additional parameter must be matched between the two beds–the internal angle of friction, α. It is necessary to match α to ensure that particle-particle friction effects are not responsible for any differences in the behavior of the two beds. In this study, an attempt was made to match α in addition to the parameters listed in (2). The internal angle of friction was measured for the polyethylene and found to be 36°, and for the limestone it was found to be 40°. Thus, the internal angles of friction agree within 11%. He et al. (1996) obtained good agreement between the hydrodynamics of two spouted beds with internal angles of friction that agreed within 7.7%. Particle-particle interaction forces are important in the annulus of spouted beds. The measurements of the

internal angle of friction for the materials used in this study are described in Appendix F; the measurement approach was the same as that used by He et al. (1996).

Table 1 summarizes the properties of the two bed materials used in this study.

Table 1: Summary of the Polyethylene and Limestone Particle Properties

Property	Polyethylene	Limestone
ρ_s (kg/m^3)	918	2670
d_p (μm)	653	379
u_{mf} (m/s)	0.23	0.24
ϕ_s	0.85	0.82
α (°)	36	40

The bubbling bed comparisons were conducted at three values of u_o/u_{mf}: 1.0, 1.2, and 2.4, which correspond to gas superficial velocities (u_o) of: 0.23, 0.28, and 0.55 m/s. The simplified set of scaling parameters for the two bed materials are compared in Table 2. Tests in the bubbling regime were conducted in a bed with a diameter (D) of 10.16 cm (4 in.); this value was used to calculate the Froude numbers (u_o^2/gD) in Table 2. Note that the only significant mismatch between the polyethylene and the limestone scaling parameters is the solid-to-gas density ratio. The other scaling parameters are matched closely between the two bed materials.

Table 2: Comparison of Simplified Set of Scaling Parameters for Bubbling-Regime Tests

Scaling Parameter	Polyethylene	Limestone
ρ_s/ρ_g	778	2263
u_o^2/gD	0.053,0.079,&0.304	0.053,0.079,&0.304
u_o/u_{mf}	1.0,1.2, & 2.4	1.0,1.2, & 2.4
L/D	matched	matched
ϕ_s	0.85	0.82
PSD	matched	matched
α (°)	36	40

5.3 Experimental Data Acquisition and Analysis

As was done in Chapter 4, the bubbling-regime hydrodynamics of the two bed materials were compared based on the characteristics of time-varying differential pressure fluctuations. A different approach was taken to evaluate the bubbling-slugging transition; this approach is described in Sections 5.4.2 and 5.5.3. The bubbling bed data were taken over three differential elevations. A single-channel low-pass analog filter was used to prevent aliasing[1]. This made it necessary for the data at each level in the bed to be taken sequentially, using a single pressure transducer, rather than simultaneously. The data acquisition system described in Section 3.3.2 was used to sample the pressure transducer output. Several sampling rates and sample lengths were considered; a rate of 300 Hz for 13.6 seconds (4096 points) was found to be sufficient.

The time-varying pressure drop measurements for the bubbling-bed comparisons were analyzed using the same methods described in Section 4.2. The pressure-drop measurements were first nondimensionalized, expressing them in terms of a solid fraction,

[1] Frequency Devices Inc., model D6L8B-100Hz

(1-ε). The mean, standard deviation, and probability density function (PDF) were then calculated for the solid fraction values. Finally, the power spectral density of the solid fraction values was determined to evaluate the frequency content of the measurements.

5.4 Experimental Setup

5.4.1 Bubbling Bed Experimental Setup

Figure 2 illustrates the bubbling bed experimental setup. The bed was constructed of a 10.16 cm (4 in.) diameter clear PVC pipe. A mock tube bank was inserted in the bed to break up the bubbles to prevent slugging. The mock tube bank was constructed of four rows of 0.6 cm (1/4 in.) diameter dowels spaced vertically 2.54 cm apart. Each row included two dowels, laterally spaced 2.54 cm apart, that spanned the width of the bed. Shop air was used to fluidize the bed material. The air flowrate was measured using one of two rotameters–400 cfh or 30 cfm–depending on the superficial velocity of the run. A bed inventory of 1000 ml was used for both bed materials.

The experimental rig was equipped with four pressure taps, their relative position is shown in Figure 2. As discussed in Section 5.3, the pressure drops between the taps were measured one at a time; the unused taps were sealed while these data were taken. For example, Figure 2 shows the apparatus configured to measure $\Delta P_{3\text{-}4}$; taps 1 and 2 would be sealed while these measurements were made. A 0-5 in. H_2O fast-response pressure transducer[2] was used to measure the pressure drop for the bubbling bed comparisons.

[2] AutoTran, Inc., Model 600

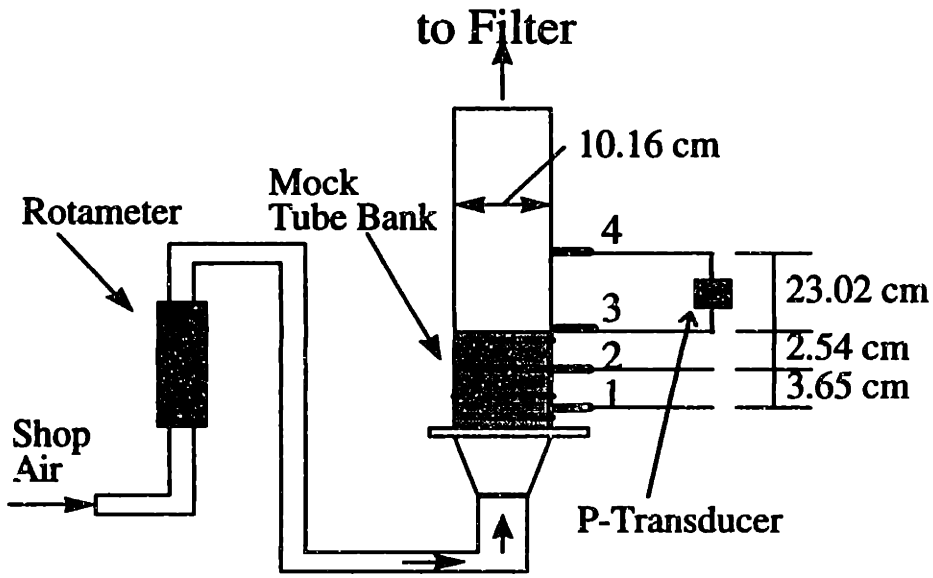

Figure 2: Bubbling Bed Experimental Setup

5.4.2 Bubbling-Slugging Transition Experimental Setup

Figure 3 illustrates the experimental apparatus used to evaluate the effects of the solid-to-gas density ratio on the bubbling-slugging transition. The experimental apparatus is a 1:6.5 scale cold model of a Foster Wheeler CFB pilot plant. Due to its high aspect ratio, it was suitable for operating in both the bubbling and slugging regimes of fluidization. The bed is constructed of a 5.08 cm (2 in.) diameter clear PVC pipe. Shop air was used to fluidize the bed material, and the air flowrate was measured using a 15 cfm rotameter. A bed inventory of 1000 ml was used for both bed materials.

Horio et al. (1992) proposed a method for evaluating flow regime transitions that uses the root-mean-square (RMS) of the gage pressure fluctuations (i.e., $p'_{gage} = p_{gage}(t) - \overline{p}_{gage}$) from a single pressure point located within the dense region of a fluidized bed. Hence, as shown in Figure 3, the high-pressure-side of a pressure transducer was connected to a single pressure point within the bed, with the low-pressure side open to the atmosphere. A 0-10 in. H_2O fast-response pressure transducer was used in the bubbling-slugging transition experiments.

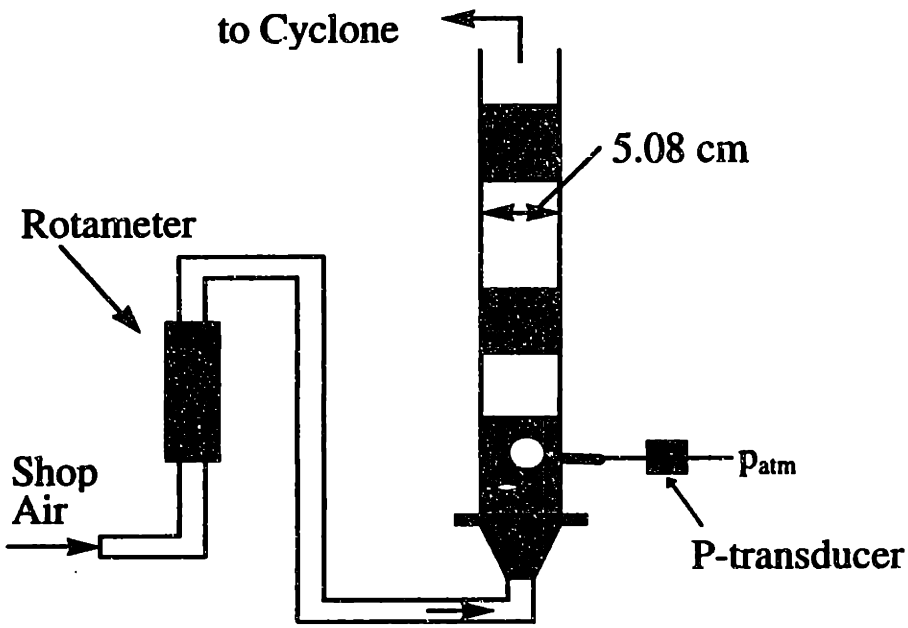

Figure 3: Bubbling-Slugging Transition Experimental Setup

5.5 Hydrodynamic Scaling Comparisons

5.5.1 Bed Expansion Comparison–u_o/u_{mf}=1.2

Figure 4 presents the pressure profiles in the bubbling bed apparatus (Figure 2) for both the polyethylene and the limestone when u_o/u_{mf}=1.2. By linearly extrapolating the pressure profile to the point where the pressure (p) is equal to the freeboard pressure (p_{fb}), it is possible to estimate the expanded bed height (H). As shown on the figure, the limestone expands 14% more than the polyethylene; the expanded bed heights for the limestone (H_{lime}) and the polyethylene (H_{poly}) are 22.7cm and 19.9cm, respectively. Hence, the overall voidage in the bed of limestone bed is higher than it is in the bed of polyethylene. This shown more clearly in Section 5.5.2 where the solid fraction profiles for this case are compared. This indicates that the hydrodynamics of the bed materials with different density ratios are not similar.

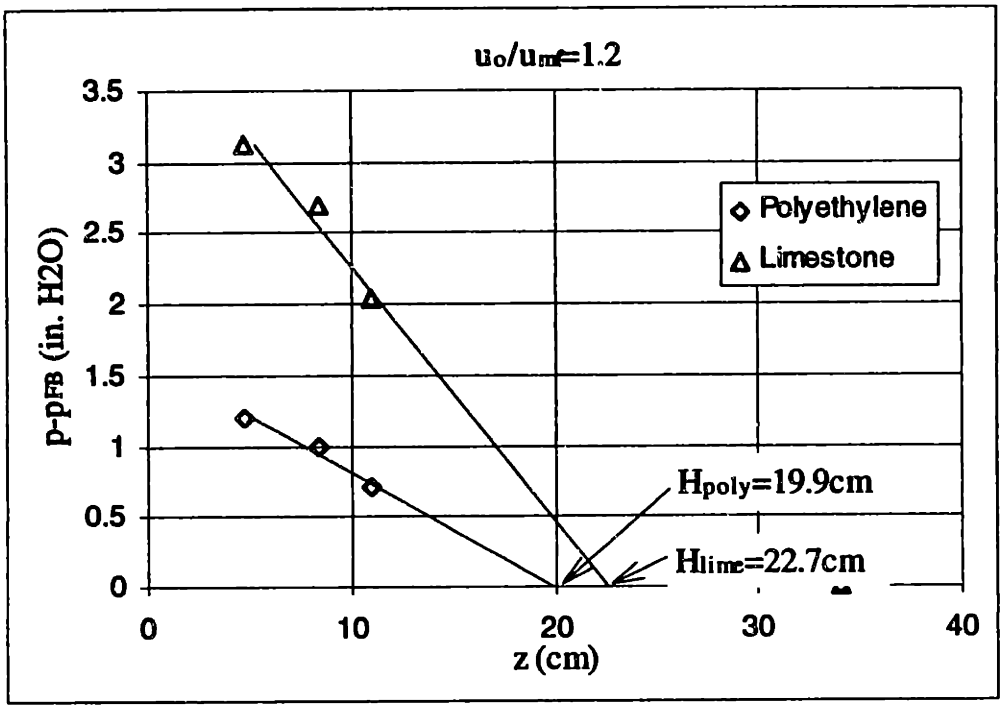

Figure 4: Bed Expansion Comparisons for Two Bed Materials–u_o/u_{mf}=1.2

5.5.2 Bubbling Bed Scaling Comparisons

Differential pressure drop data were taken over the three measurement intervals shown in Figure 2 (i.e., taps 1-2, taps 2-3, and taps 3-4). Figures 5 through 10 show the probability density functions (PDF) and power spectral densities of the dimensionless time-varying pressure drop (solid fraction) data taken from taps 2-3 for u_o/u_{mf}=1.0, 1.2, and 2.4. These plots are provided to present a representative sampling of the PDF and power spectral density comparisons over a range of conditions. The power spectral densities are compared in dimensional form because the length and velocity scales are the same for both materials. Hence, nondimensionalizing the power spectral densities and frequencies for the two materials will not change their relative values. For example, the power spectral density results presented in Chapter 4 were nondimensionalized by (D/u_o); this factor is the same for both of the tested bed materials. The behavior at the other levels in the bed are illustrated through comparisons of the mean solid fraction profiles and the profiles of the

standard deviation (σ) of the solid fraction. The mean and the standard deviation characterize the position and width of the PDF. Hence, these comparisons summarize how the PDF varies with elevation in the bed. Figures 11-16 present profiles of the mean solid fraction and the standard deviation of the solid fraction for u_o/u_{mf}=1.0, 1.2, and 2.4.

Differences in the behavior of the two bed materials are apparent in Figures 5 and 6, where u_o/u_{mf}=1.0. The limestone has a broader PDF than the plastic, while the plastic has a higher mean solid fraction (lower voidage). In addition, the peak in the power spectrum occurs at a higher frequency for the limestone than for the polyethylene. Figure 11 shows that for u_o/u_{mf}=1.0, the overall mean solid fraction in the bed of polyethylene is higher than in the bed of limestone; although they are equivalent at the top of the bed. Figure 12 shows that for u_o/u_{mf}=1.0, the standard deviation of the solid fraction measurements is higher in the bed of limestone than in the bed of polyethylene, except at the bottom of the bed where they are the same.

Figures 11 and 12 show that, for the same operating condition, it is possible for the mean solid fractions to agree at a location where the standard deviation of the solid fraction disagree, and vice versa. For example, in Figure 11 the mean solid fractions for the limestone and the polyethylene are equivalent at the top of the bed. But as shown in Figure 12, the standard deviation of the solid fractions are different for the two bed materials in the top pressure-drop measurement interval. The converse is true in the bottom of the bed. If the density ratio were not important, these curves would lie on top of each other. Therefore, these results indicate that the solid-to-gas density ratio is important for scaling bubbling fluidized beds.

The behavior shown in Figures 7-8 and 13-14 for u_o/u_{mf}=1.2 is similar to that for u_o/u_{mf}=1.0. However, the standard deviation of the solid fraction (Figure 14) is no longer equivalent for the two bed materials in the bottom of the bed as it was in Figure 12. The bed expansion comparison presented in Section 5.5.1 (Figure 4) corresponds to the solid fraction profiles compared in Figure 13. This comparison indicated that the polyethylene

had a lower bed expansion than the limestone, and this was attributed to the polyethylene having a lower voidage (higher solid fraction) than the limestone. Figure 13 shows that the overall bed solid fraction for the polyethylene is higher than that of the limestone. Again, this implies that the hydrodynamics of the two materials are different.

Finally, for u_o/u_{mf}=2.4, Figure 10 shows that the power spectral densities for the two bed materials agree well at taps 2-3. But Figure 9 shows that PDFs do not exhibit the same level of agreement at the same position in the bed.

Differences in the mean and the standard deviation of the solid fraction, and the power spectral densities reflect potentially important differences in the hydrodynamics of the two beds. For example, the standard deviation of the solid fraction is thought to be related to the distribution of bubble sizes in the bed, and the power spectral density reflects the bubble frequency. The bubble size and bubble frequency significantly affect important hydrodynamic characteristics of the bed such as solids mixing and the split of gas between the bubble and dense phases. Hence, by failing to match the solid-to-gas density ratio between two beds, important hydrodynamic quantities could potentially be different between them.

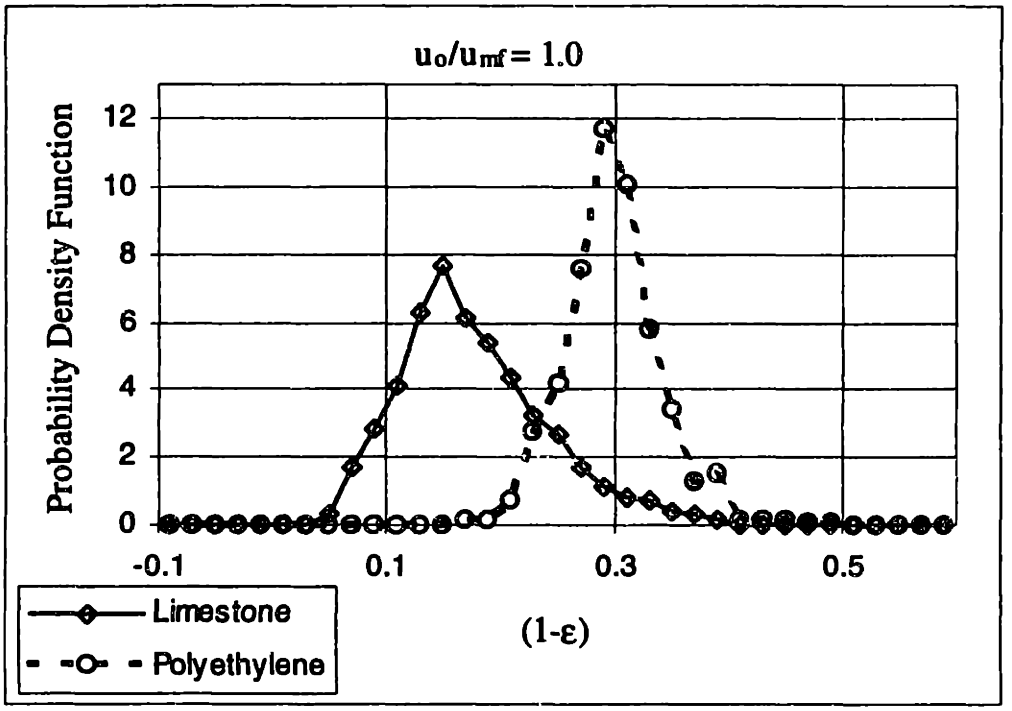

Figure 5: PDF of (1-ε) Data Taken From Taps 2-3–u_o/u_{mf}=1.0

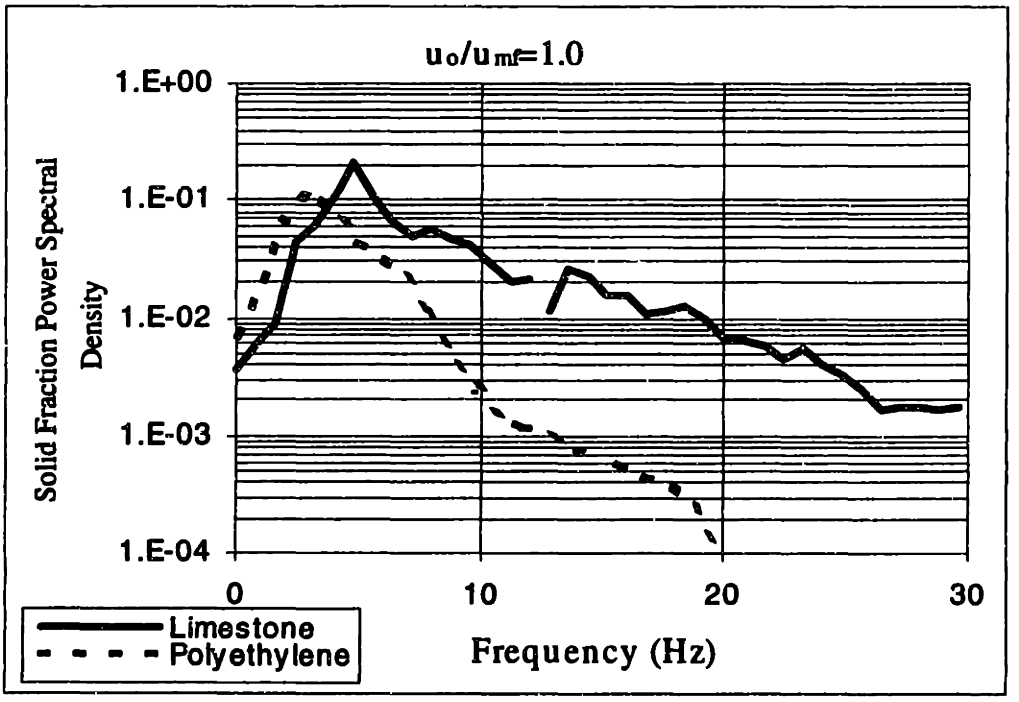

Figure 6: Power Spectrum of (1-ε) Data Taken From Taps 2-3–u_o/u_{mf}=1.0

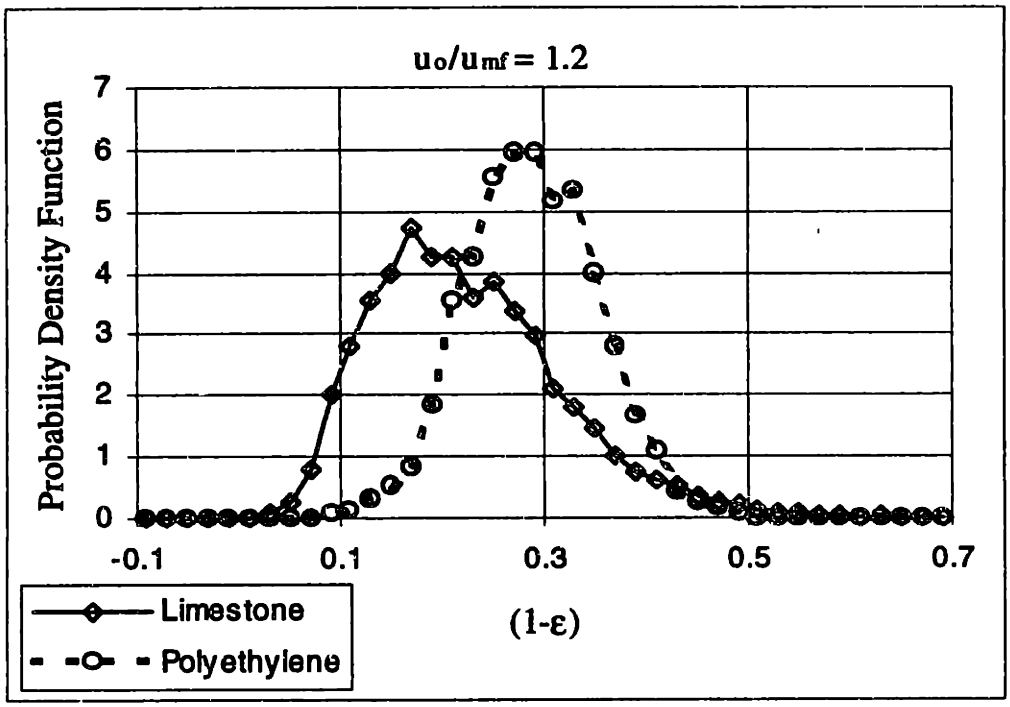

Figure 7: PDF of (1-ε) Data Taken From Taps 2-3–u_o/u_{mf}=1.2

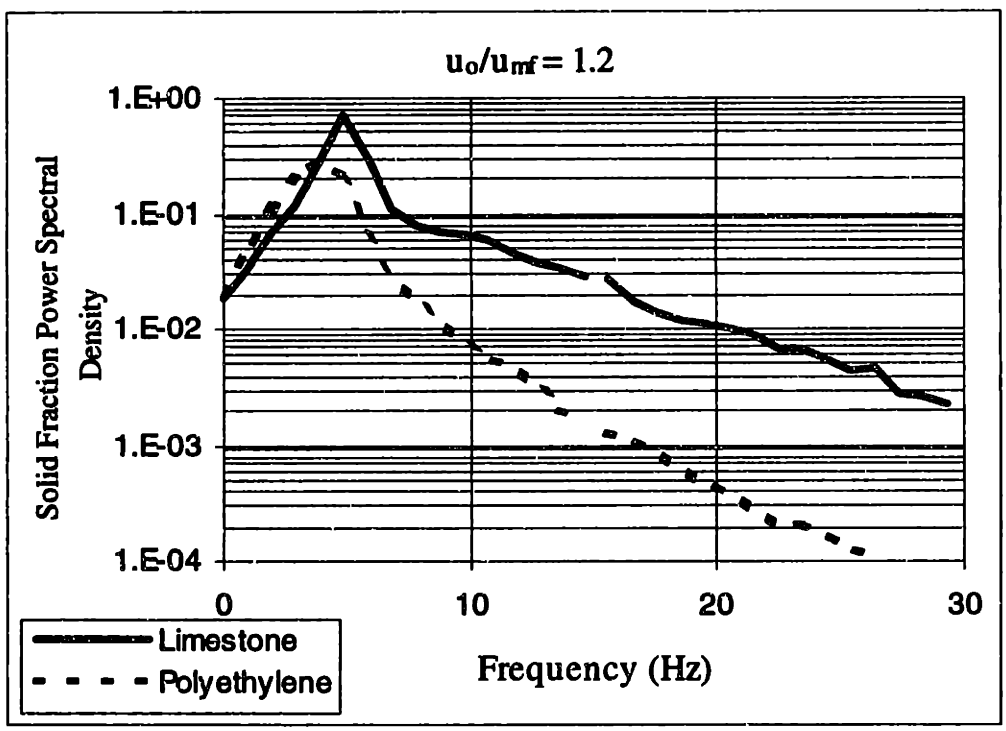

Figure 8: Power Spectrum of (1-ε) Data Taken From Taps 2-3–u_o/u_{mf}=1.2

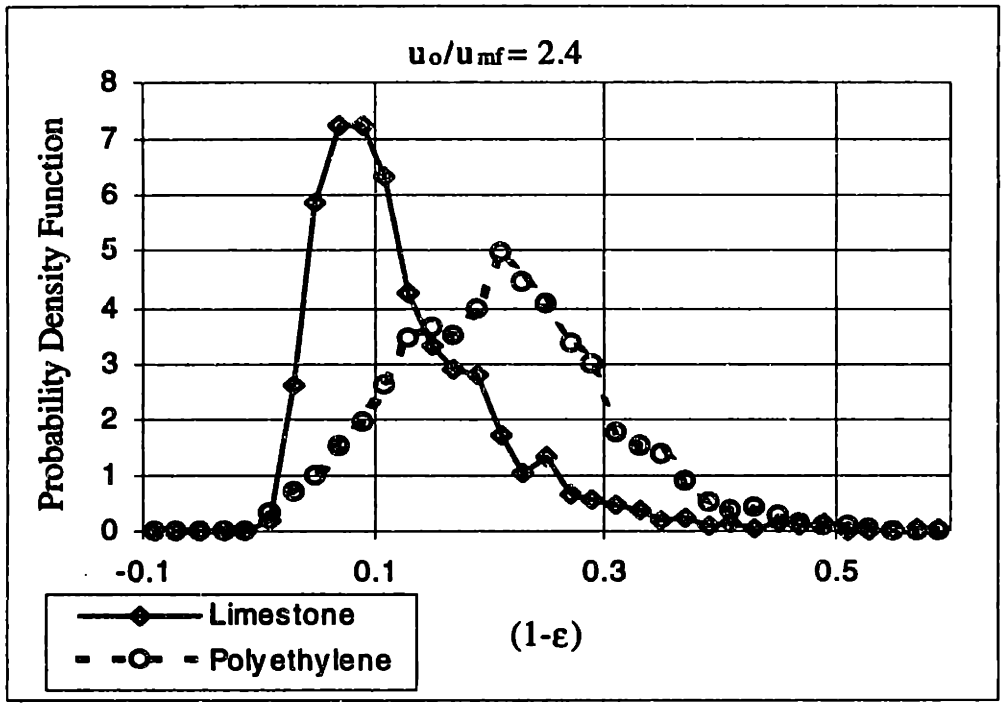

Figure 9: PDF of (1-ε) Data Taken From Taps 2-3–u_o/u_{mf}=2.4

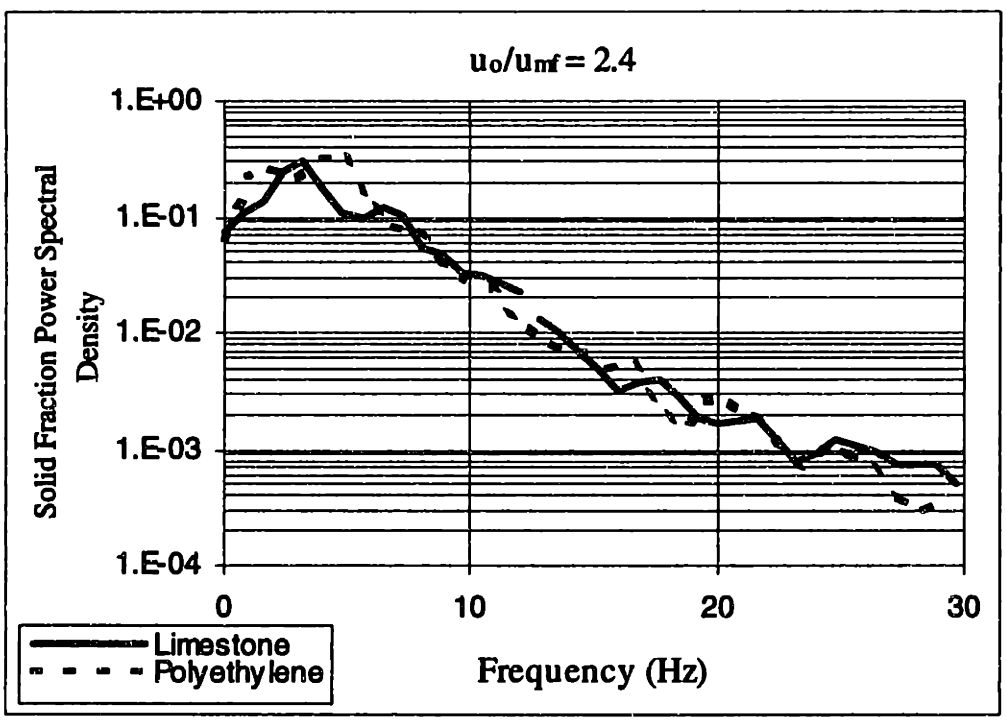

Figure 10: Power Spectrum of (1-ε) Data Taken From Taps 2-3–u_o/u_{mf}=2.4

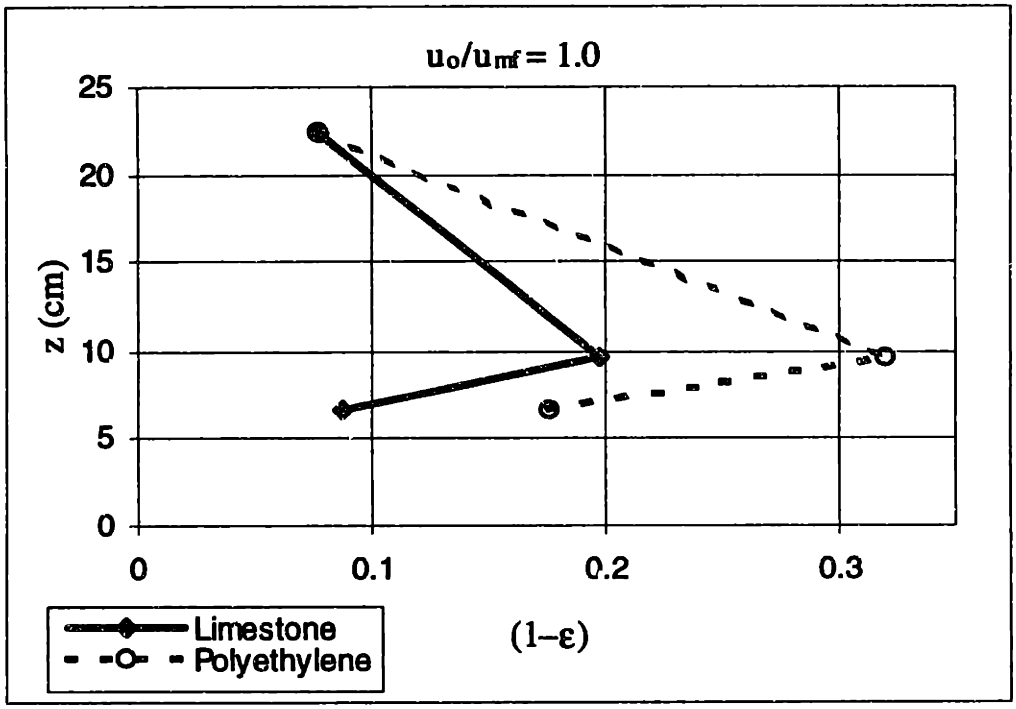

Figure 11: Solid Fraction Profile–u_o/u_{mf}=1.0

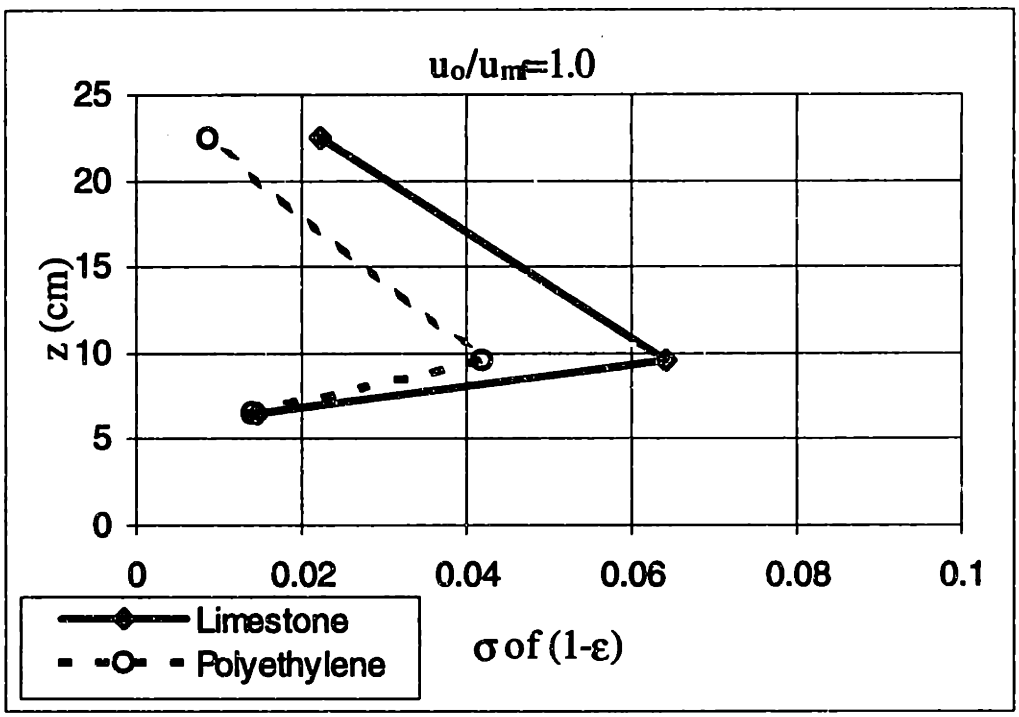

Figure 12: σ of (1-ε) Profile–u_o/u_{mf}=1.0

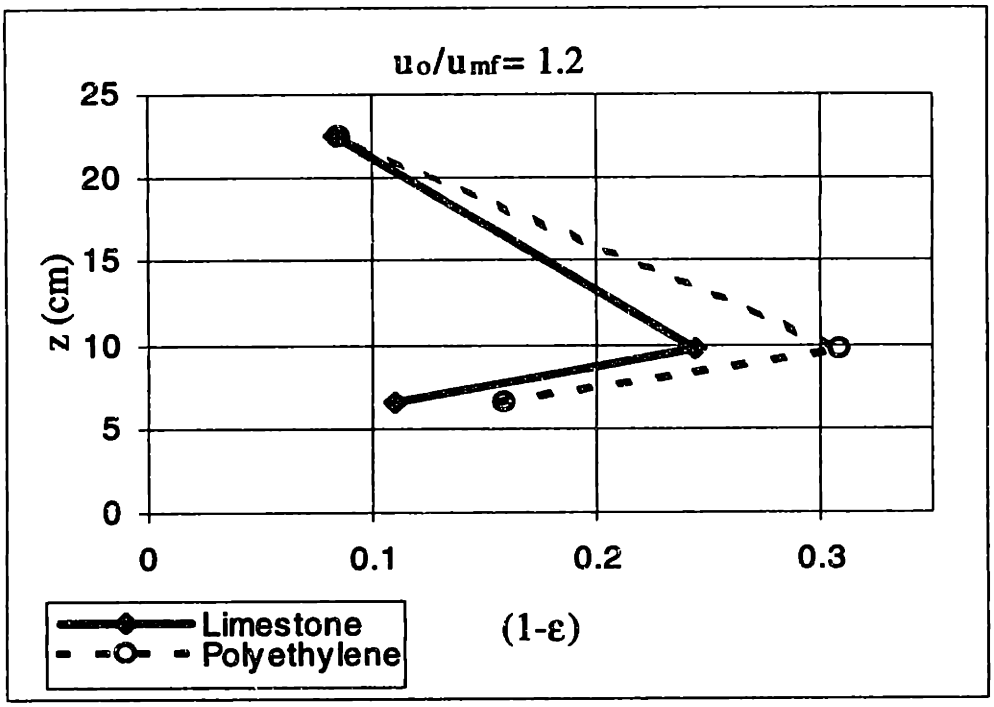

Figure 13: Solid Fraction Profile–u_o/u_{mf}=1.2

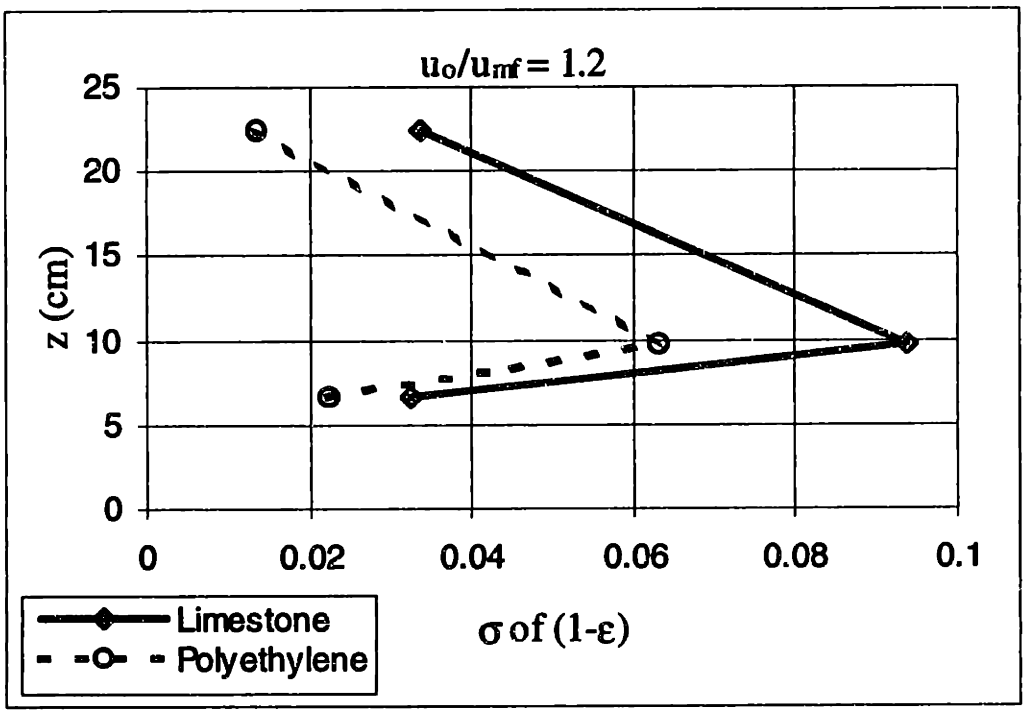

Figure 14: σ of (1-ε) Profile–u_o/u_{mf}=1.2

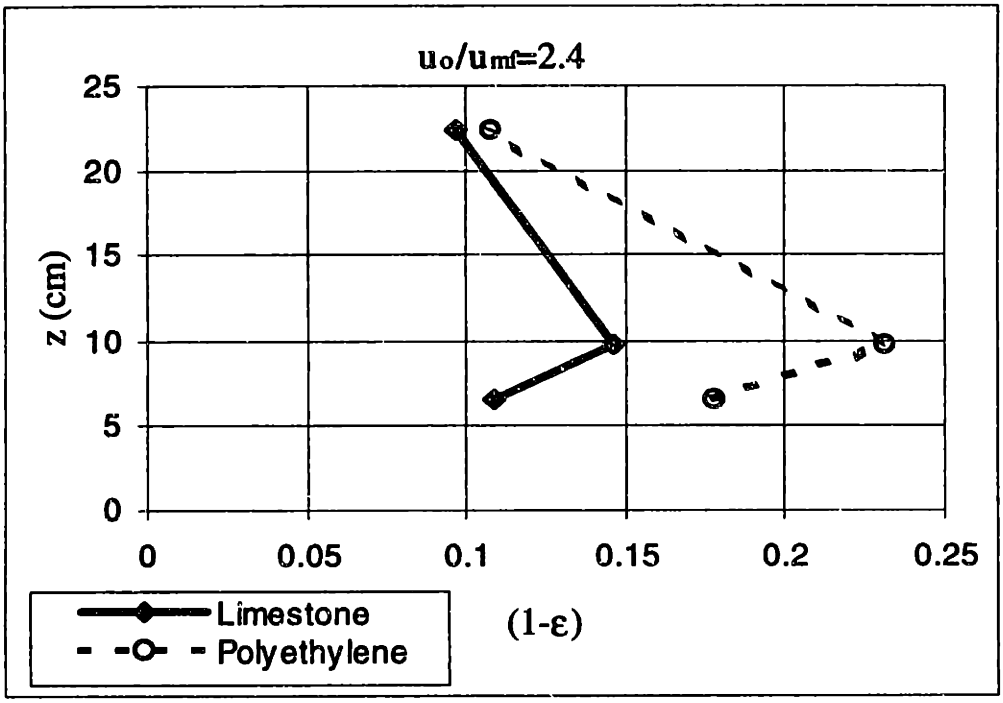

Figure 15: Solid Fraction Profile–u_o/u_{mf}=2.4

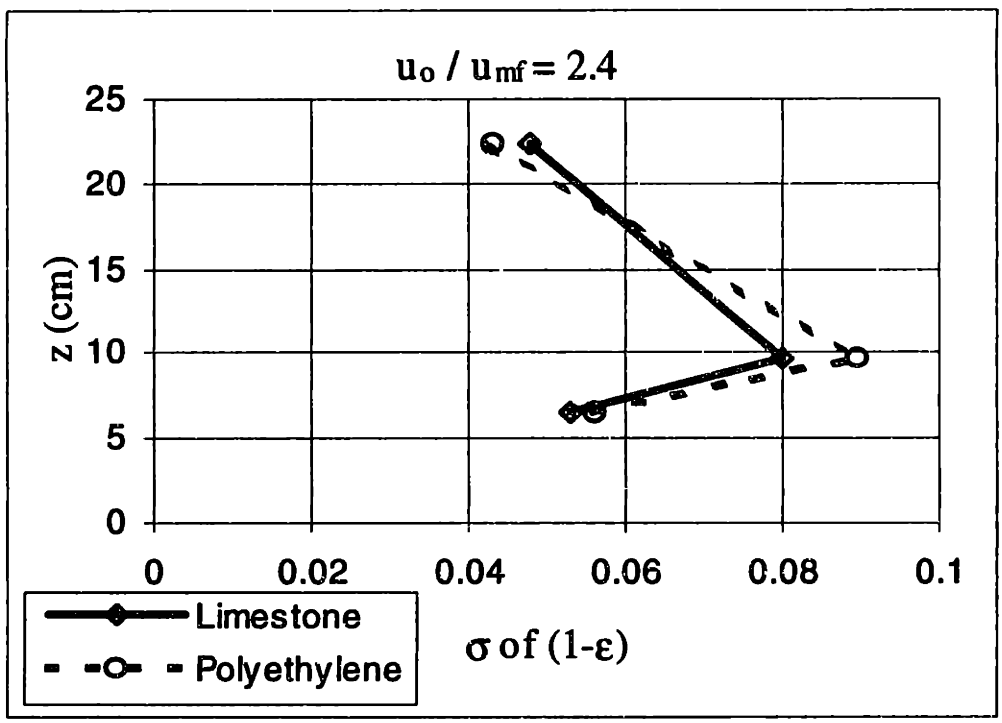

Figure 16: σ of (1-ε) Profile–u_o/u_{mf}=2.4

5.5.3 Effect of Mismatched ρ_s / ρ_g on Bubbling-Slugging Transition

As discussed in Section 5.4.2, Horio et al.'s (1992) approach to identifying flow regime transitions is used here to evaluate the effect of not matching the solid-to-gas density ratio on the flow regime boundaries. Horio et al. (1992) plotted the RMS of gage pressure fluctuations (p'_{gage}) versus gas superficial velocity and used changes in the slope of the curve to identify flow regime transitions. Figure 17 is a plot of the RMS of p'_{gage} versus u_o/u_{mf} taken from the apparatus shown in Figure 3 for the two bed materials. Lines have been added to the figure to identify the flow regime boundaries based on Horio et al.'s (1992) method and visual observations of the bed. As indicated on Figure 17, the bed appears to begin fully slugging at approximately the same u_o/u_{mf}, and both the limestone and the polyethylene are bubbling at low u_o/u_{mf}. But the nature of the transition between the flow regimes appears to be different. The limestone remains in the bubbling regime up to u_o/u_{mf} of 2.1. Whereas the polyethylene begins the transition from bubbling to slugging at u_o/u_{mf}=1.7. Hence the results in Figure 17 imply that the polyethylene transitions between the two flow regimes over a broader range of u_o/u_{mf} than the limestone.

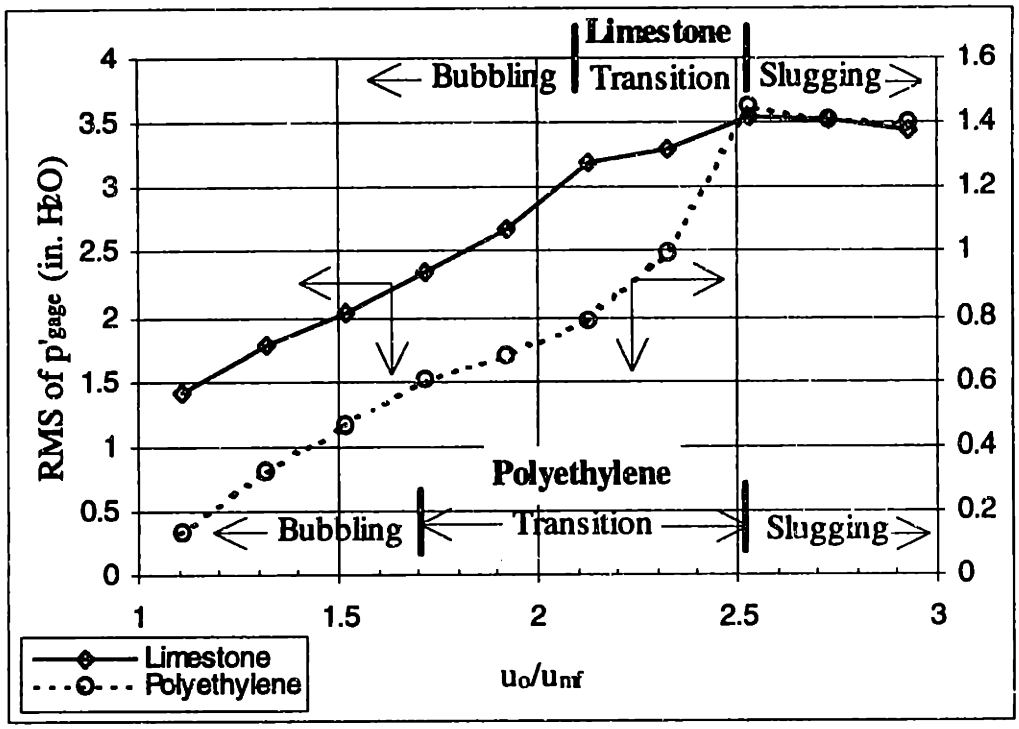

Figure 17: Evaluation of ρ_s/ρ_g on Bubbling-Slugging Transition

5.6 Nomenclature

D	bed diameter
d_p	surface-volume mean particle diameter $= 1/\sum_i x_i/\bar{d}_{p_i}$
$\bar{d}_{p_i}$	mean aperture of adjacent sieves defining interval i
g	acceleration due to gravity, 9.807m/s^2
H	expanded bed height
L	bed dimension
p	pressure
p_{fb}	freeboard pressure
p_{gage}	gage pressure measured at a point within the bed, $p(t)-p_{atm}$
p'_{gage}	$p_{gage}(t) - \bar{p}_{gage}$
PDF	probability density function
PSD	dimensionless particle size distribution
u_{mf}	minimum fluidization velocity
u_o	gas superficial velocity
x_i	fraction of particle sample's mass residing in interval i
z	distance above the distributor

Greek Symbols

α	internal angle of friction
ε	voidage
$(1-\varepsilon)$	solid fraction
ϕ_s	particle sphericity
μ	gas dynamic viscosity
ρ_g	gas density
ρ_s	particle solid density
σ	standard deviation of $(1-\varepsilon)$ measurements

5.7 References

Broadhurst, T.E. and Becker, H.A., 1973, "The Application of the Theory of Dimensions to Fluidized Beds," Proc. Int. Symp. Ste. Chimie Indust., Toulouse, pp. 10-27.

Chen, Z., Rapagná, S., Di Felice, R., Gibilaro, L.G., and Foscolo, P.U., 1995, "Particle-Particle and Particle-Wall Frictional Effects in Fluidized Beds," Fluidization VIII, Engineering Foundation.

Di Felice, R., Rapagná, S., and Foscolo, P.U., 1992, "Dynamic Similarity Rules: Validity Check for Bubbling and Slugging Fluidized Beds," *Powder Technology*, 71, pp. 281-287.

Glicksman, L.R., 1984, "Scaling Relationships for Fluidized Beds," *Chemical Engineering Science*, 39, pp. 1373-1379.

Glicksman, L.R., 1988, "Scaling Relationships for Fluidized Beds," *Chemical Engineering Science*, 43, pp. 1419-1421.

Glicksman, L.R., Hyre, M.R., and Woloshun, K., 1993, "Simplified Scaling Relationships for Fluidized Beds," *Powder Technology*, 77, pp. 177-199.

He, Y-L., Lim, C.J., and Grace, J.R., 1996, "Scale-up Studies of Spouted Beds," *Chemical Engineering Science*, in press.

Horio, M., Nonaka, A., Sawa, Y., and Muchi, I., 1986, "A New Similarity Rule for Fluidized Bed Scale-Up," *AIChE Journal*, 32, pp. 1466-1482.

Horio, M., Ishii, H., Kobukai, Y., and Yamanishi, N., 1989, "A Scaling Law for Circulating Fluidized Beds," *Journal of Chemical Engineering of Japan*, 22, pp. 587-592.

Horio, M., Ishii, H., and Nishimuro, M., 1992, "On the Nature of Turbulent and Fast Fluidized Beds," *Powder Technology*, 70, pp. 229-236.

Ishii, H., Nakajima, T., and Horio, M., 1989, "The Clustering Annular Flow Model of Circulating Fluidized Beds," *Journal of Chemical Engineering of Japan*, 22, 5, p. 484.

Ishii, H. and Murakami, I., 1991, "Evaluation of the Scaling Law of Circulating Fluidized Beds in Regard to Cluster Behavior," In Circulating Fluidized Bed Technology III (eds. Basu, P., Horio, M., and Hasatani, M.), Pergamon Press, Oxford.

Thiel, W.J. and Potter, O.E., 1977, "Slugging in Fluidized Beds," *Ind. Eng. Chem., Fundam.*, 16, 2, pp. 242-247.

Tsukada, M., Nakanishi, D., Takei, Y., Ishii, H., and Horio, M., 1991, "Hydrodynamic Similarity of Circulating Fluidized Bed Under Different Pressure Conditions," Proceedings 11th International Conference on Fluidized Bed Combustion, pp. 829-834.

Yang, W.C., 1983, "Criteria for Choking in Vertical Pneumatic Conveying Lines," *Powder Technology*, 35, pp. 143-150.

This page intentionally blank

6. Review of Solids Mixing in Bubbling Fluidized Beds

6.1 Introduction

In Chapter 4, a cold model was shown to have similar hydrodynamics to the Tidd PFBC. This makes the cold model a convenient platform for performing detailed solids mixing studies; studies that could not be conducted in the hostile environment of a PFBC.

This chapter provides an overview of the more germane experimental and theoretical work done on solids mixing. The discussion highlights the important role bubbles play in the solids mixing process. This motivated the measurement of the bubble characteristics in the cold model; this work is described in Chapter 7. A thermal tracer technique was used to study solids mixing in the cold model. The experimental setup for the mixing studies is provided in Chapter 8, and Chapter 9 discusses the results of the studies. Finally, Chapter 10 presents the development of a mechanistic model of solids mixing in bubbling fluidized beds.

6.2 Basic Mechanisms of Solids Mixing in Bubbling Fluidized Beds

Several researchers have conducted experiments to identify the mechanisms of solids mixing in bubbling fluidized beds. These studies clearly show the central role that bubbles play in the mixing of solids within a bubbling fluidized bed.

In these studies, the researchers typically formed a bed of two particle layers, where the particles in each layer were distinguishable from those in the other (e.g., by color or X-ray attenuation characteristics). Then while passing air through the bed at a velocity just below that required to form bubbles, they injected a single bubble from an orifice in the distributor. The mixing of the two particle layers was then evaluated, often by dissecting

the bed into thin layers to determine particle displacement produced by the bubble. The studies described in Section 6.2.1 generally followed this approach, except where otherwise noted.

Before proceeding with a detailed discussion of the relationship between bubbles and solids mixing, it is important to differentiate between axial and lateral mixing. Axial, or vertical, mixing takes place along the vertical axis of the bed. Lateral, or horizontal, mixing takes place in the direction normal to the vertical axis of the bed. Distinctions will be made in the following discussion between these two types of mixing, and their mechanisms will be examined.

6.2.1 Importance of Bubbles to Solids Mixing

One of the earliest studies on the mechanisms of solids mixing in bubbling fluidized beds was conducted by Rowe et al. (1965). Experiments were conducted with particles ranging in size from less than 53 μm up to 460 μm to evaluate the effect of particle size on the mixing mechanisms. They identified three solids mixing mechanisms.

- The first is often referred to as bubble-induced "drift" due to the similar appearance of the particle displacement profile to that derived by Lighthill (1956) for the passage of a sphere through an inviscid fluid.
- The second mechanism is the vertical solids transport in the wake of the bubble. The bubble wake sheds particles and is continuously replenished as the bubble rises through the bed. Particles from different locations in the bed mix in the wake and are then shed after rising with the bubble for some distance. When the bubble erupts at the bed surface, the material above the bubble and in the wake is dispersed, contributing to the lateral solids mixing.
- Finally, they observed that particles smaller than 60 μm in diameter experience an additional mixing mechanism that they describe as "eddy-diffusive mixing".

Rowe et al. (1965) conclude that bubbles alone are responsible for solids mixing in bubbling fluidized beds of all but the smallest particles. They also show results that refute the idea that mixing is caused by inter-particle diffusion. They describe the mixing induced by the bubbles as a convection process, where upward convection is observed along the bubble path and downward convection is produced in the area surrounding the bubble.

Woollard and Potter (1968) conducted similar experiments to those of Rowe et al. (1965), using 380 μm glass spheres. Their primary objective was to better quantify the particle motion produced by a bubble's motion. In particular, they measured the volume of particles displaced by a bubble as it crosses a level in the bed. Comparisons were made between their measurements and the theoretical displacement produced by a sphere moving through an inviscid fluid (Lighthill, 1956). According to inviscid flow theory, as a sphere moves through an unbounded ideal fluid, it displaces a volume equal to 50% of the volume of the sphere. (This estimate does not account for wake transport). Woollard and Potter's (1968) measurements suggest that the actual displaced volume is approximately 30-40% of the bubble's volume, including both wake and drift transport.

Abrahami and Resnick (1974) also considered the particle displacement produced by a single bubble using particles ranging in size from 420 to 707 μm. Their measurements indicate that a bubble displaces a volume of particles (wake plus drift) approximately equal to one bubble volume. They found that a bubble must rise a distance of roughly 2.0 bubble diameters after forming to achieve a fully developed wake. This suggests that bubble-induced mixing would be less in shallow beds (i.e., when $H \sim d_B$). They also concluded that the height of the particle *drift* profile was always approximately 1.7 bubble diameters.

The previous studies were conducted with particle diameters ranging from less than 53 μm up to 707 μm. Cranfield (1978) measured particle displacements using much larger particles with mean diameters between 1520 and 1760 μm. Based on bed dissection and video measurements, he concluded that the only mechanism of vertical solids transport in

large-particle beds is bubble-induced drift. His experiments showed no signs of the wake transport observed with smaller particles. Larger particles typically fall into the Geldart (1973) group D particle classification, which characteristically produce bubbles with very small wakes. Hence, for large particles drift is the dominant solids-mixing mechanism. By measuring the drift profile in a two-dimensional bed, he estimated the average upward particle displacement to be approximately one bubble diameter and the average downward displacement of the surrounding particles to be approximately one-eighth of a bubble diameter. These are average displacements, not the peak height of the drift profile measured by Abrahami and Resnick (1974). Based on a sketch of the drift profile in Cranfield's (1978) paper, his drift-profile height appears to be consistent with that measured by Abrahami and Resnick (1974). He also found that bubbles in large-particle beds displace a volume of particles approximately equal to one bubble volume.

Valenzuela and Glicksman (1984) developed a unique approach to studying particle motion in freely-bubbling fluidized beds. They conducted experiments in a two-dimensional bed making it possible to observe the bubble motion. Particle motion was followed by thermally tagging bed particles and then tracking their motion using thermistor probes attached to light emitting diodes (LEDs). A LED was energized when thermal tracers were sensed by its associated thermistor. This experimental setup made it possible to relate the bubble motion to the particle motion in a freely-bubbling fluidized bed. They found that vertical solids transport is due to both bubble-induced drift and wake transport. In addition, they concluded that significant lateral particle motion is produced by the horizontal motion of bubbles as they move to coalesce with surrounding bubbles. Lateral mixing due to bubble coalescence acts in addition to the lateral wake-mixing mechanism postulated by Kunii and Levenspiel (1969). Valenzuela and Glicksman (1984) also estimated that in their two-dimensional bed, bubbles displace a volume of particles (wake plus drift) equal to approximately one-third of the bubble's volume.

6.2.2 Summary of Solids Mixing Mechanisms

The studies described in Section 6.2.1 highlight the central role that bubbles play in the mixing of solids in bubbling fluidized beds. They show that the volume of particles and the distance they are displaced is governed by bubble size. Since particle motion is induced by the bubble motion, the mixing rates in bubbling fluidized beds should be controlled by the bubble frequency. Bubble coalescence is a function of the distance between bubbles which depends on the bubble fraction and the bubble size.

The studies discussed in Section 6.2.1 identify mechanisms of both axial and lateral solids mixing; Figure 1 illustrates several of these mechanisms.

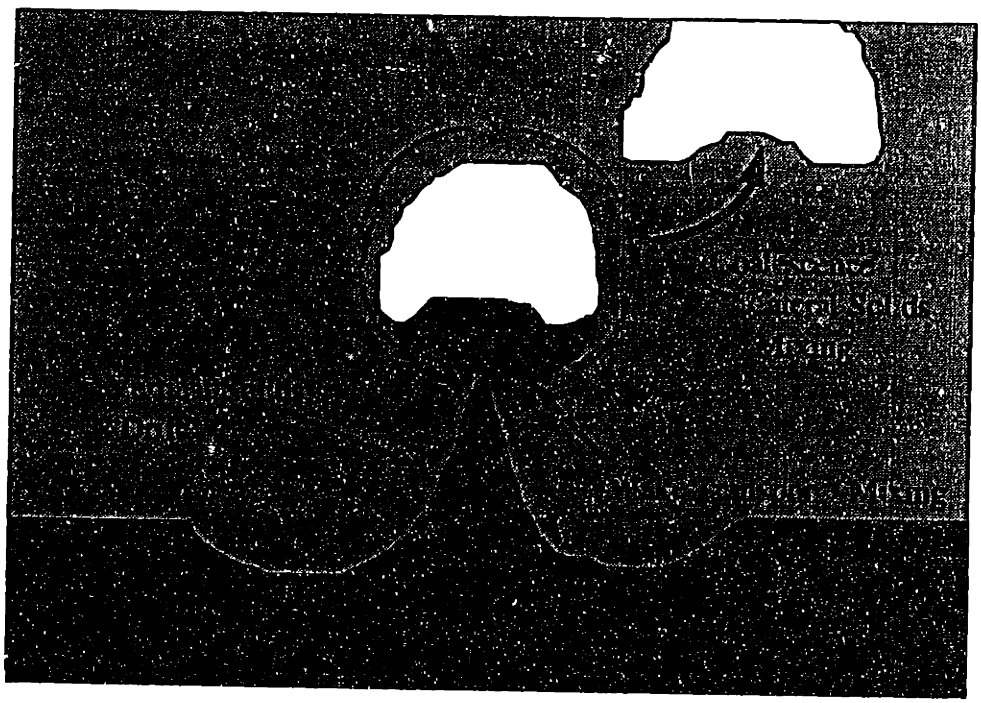

Figure 1: Mechanisms of Solids Mixing

As Figure 1 shows, axial mixing is produced by bubble-induced drift and wake transport. Solids mix laterally as bubbles move to coalescence with neighboring bubbles. And additional mixing takes place within the wake of the bubble. Significant lateral mixing is also produced when a bubble erupts at the surface of the fluidized bed, dispersing the

contents of its wake across the surface of the bed. In general, inter-particle diffusion contributes negligibly to the solids mixing process.

Particles that are less than approximately 60 μm in diameter appear to experience an additional mixing mechanism that is analogous to turbulent eddy diffusion. This eddy mixing is not present in bubbling fluidized beds of particles larger than approximately 100 μm in diameter. Solids mixing in larger-particle beds is caused only by the motion of bubbles.

Due to the preferential upward motion of the bubbles, axial mixing is anisotropic. Upward mixing rates are significantly higher than downward and lateral mixing rates. Upward mixing is controlled by the length and time scales of the bubbles. According to Valenzuela and Glicksman (1984), the downward particle motion proceeds at a lower velocity and consists of "a uniform flow of a more cohesive particle group." This suggests that it is futile to attempt to develop a general diffusion/dispersion model of the mixing process. A mixing model based on the mechanisms described above is developed in Chapter 10.

6.3 Solids Mixing Models

There are two common approaches to modeling solids mixing in bubbling fluidized beds– the diffusion and counter-current backmixing models. Both models require empirical input coefficients.

Verloop et al. (1968/1969) found that diffusion coefficient measurements were difficult to compare. Most experimental studies that used a diffusion coefficient to describe their data were conducted in small-diameter beds without internals, causing the diffusion coefficient to be a function of the bed diameter. This dependence would not be expected in a bed of large particles with a tube bank as long as the bed diameter is several times larger than the tube pitch. In this case, Glicksman et al. (1987) found that the bubbles are distributed

randomly across the bed cross-section and the bubble size is controlled by the tube pitch. When Sitnai (1981) tried to calculate a diffusion coefficient for his data, he found that it was necessary to vary the coefficient by a factor of 7 between two levels in the bed. Jinescu et al. (1966) found that measured diffusion coefficients varied both in space and time. In addition, no attention has been paid to hydrodynamic scaling in these studies. For example, Sitnai (1981) conducted mixing studies in an experimental rig, which operated at ambient conditions, that was geometrically representative of a fluidized bed combustor. Sand was used as the bed material, which has roughly the same density as typical combustor bed materials. Nicastro and Glicksman (1984) showed that when actual combustor bed material is fluidized in a geometrically similar cold model, the cold-model hydrodynamics are different from those of the hot combustor. All these issues raise serious doubts over the applicability of using coefficients measured in previous studies for predicting solids mixing in PFBCs.

The diffusion and counter-current backmixing models and their assumptions are summarized below. These models are also described in reviews by Potter (1971) and van Deemter (1985).

6.3.1 Diffusion Model

The diffusion model has found widespread use as a solids mixing model in bubbling fluidized beds. The diffusion model in cylindrical coordinates for both lateral (radial) and axial mixing is given by

$$\frac{\partial c_i}{\partial t} = D_{sa}\frac{\partial^2 c_i}{\partial z^2} + D_{sr}\frac{1}{r}\frac{\partial}{\partial r}\left(r\frac{\partial c_i}{\partial r}\right). \qquad (1)$$

c_i is the concentration of species i, and D_{sa} and D_{sr} represent the axial and radial diffusion coefficients, respectively.

The problem with using the diffusion model as a model of solids mixing in bubbling beds is that solids mixing is not a diffusion process. The following are some of the assumptions inherent in the diffusion model. Each assumption is followed by a brief description of the inconsistencies between the assumption and the behavior of bubbling fluidized beds.

1. *The system is homogeneous.* But, for example, the cold model solid fraction measurements exhibit significant voidage variations along the vertical axis of the bed. And bubbles represent a local nonhomogeneity.
2. *Due to their stochastic nature, diffusion processes assume that the interaction distance is small with respect to the dimensions of the system.* As shown by investigators such as: Rowe et al. (1965), Woollard and Potter (1968), and Abrahami and Resnick (1974), particles are displaced a distance on the order of the bubble diameter. Hence, for shallow beds the diffusion model will be particularly poor. But even with the deeper beds found in PFBCs, the number of interactions before a particle would reach the boundaries of the bed should be relatively small.
3. *The particle motion is random.* Rowe et al.'s (1965) "experiments show that the particle movement is not random but that mixing is a result of a definite pattern of displacement accompanying each bubble as it passes through the bed."

The previous discussion suggests that a diffusion model is generally inappropriate for modeling solids mixing, and particularly axial solids mixing, in bubbling fluidized beds. Verloop et al. (1968/1969) tabulated the experimental results from studies that attempted to describe their experiments in terms of a diffusion coefficient. They found that the measured diffusion coefficients varied between studies by up to five orders of magnitude, and described the results as "difficult to compare" and "contradictory". Many investigators such as: Morris et al. (1964), Fitzgerald et al. (1977), Sitnai (1981), Valenzuela and Glicksman (1984), Avidan and Yerushalmi, (1985), among others, have highlighted the inadequacy of modeling solids mixing in bubbling fluidized beds as a diffusion process. Morris et al. (1964) concluded that solids mixing in "fluidised beds cannot be described by a simple diffusional mechanism."

6.3.2 Counter-Current Backmixing Model

The counter-current backmixing model was first developed by van Deemter (1967), and was subsequently enhanced by researchers such as Gwyn et al. (1970) and Sitnai (1981). In its simplest form, the model treats the axial flow in a bed in three layers–two counter-current flowing solid streams and a single gas flow layer. Figure 2 illustrates the model's layers (Kunii and Levenspiel,1991).

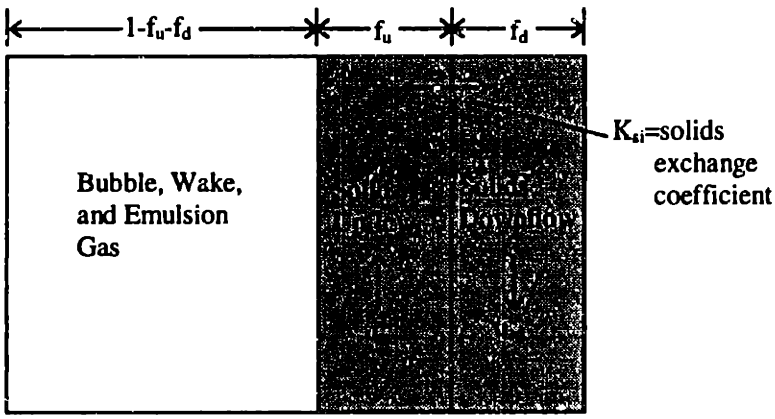

Figure 2: Counter-Current Backmixing Model

The two layers of solids move in plug flow; the upflow velocity is u_{su} and the downflow velocity is u_{sd}. f_u and f_d are the fraction of the bed volume in the upflow and downflow layers. The upflowing solids layer represents the solids displaced vertically in the wakes of bubbles and by bubble-induced drift. To satisfy the requirement that there be zero net mass flux at any level in the bed, a downflowing layer of solids must be present, and

$$f_u \cdot u_{su} = f_d \cdot u_{sd} . \tag{2}$$

Species i is exchanged between the two layers through a solids exchange coefficient, K_{s_i} (m^3_i/m^3-s). Conservation of species i requires that

$$f_d \frac{\partial c_{sd_i}}{\partial t} + f_d u_{sd} \frac{\partial c_{sd_i}}{\partial z} + K_{s_i}\left(c_{sd_i} - c_{su_i}\right) = 0 \tag{3}$$

and

$$f_u \frac{\partial c_{su_i}}{\partial t} + f_u u_{su} \frac{\partial c_{su_i}}{\partial z} + K_{s_i}\left(c_{su_i} - c_{sd_i}\right). \qquad (4)$$

c_{sd_i} and c_{su_i} are the concentrations of species i (m^3_i/m^3) in the downflow and upflow layers, respectively. This model has five input parameters: f_u, f_d, u_{su}, u_{sd}, and K_{s_i}. Only four of these parameters are independent due to the additional constraint imposed by (2).

Sitnai (1981) extended the counter-current backmixing model by including an additional downflowing solids layer to account for the faster solids downflow frequently present at the boundaries of bubbling fluidized beds. This layer is assigned a unique velocity and volume fraction. This model has 9 independent parameters that were chosen to fit axial mixing data taken from a model of an atmospheric fluidized bed combustor.

More recently, Shen et al. (1995) added lateral mixing effects to the counter-current backmixing model by discretizing the width of bed and introducing a lateral diffusion model for the solids exchange between the downflowing layers in adjacent elements.

The physical assumptions of the counter-current backmixing model make it more appropriate for modeling solids mixing in high aspect ratio beds, where distinct upflowing and downflowing layers are more clearly defined. Aside from a thin layer flowing down at the walls, the hydrodynamics of the larger, shallower beds found in combustors do not exhibit this layered behavior. Extensions of the counter-current backmixing model, such as those proposed by Shen et al. (1995), should enhance the predictive ability of the model for low aspect ratio beds.

6.4 Solids Mixing Experimental Studies

Solids mixing has been studied for many decades (e.g., Gilliland and Mason, 1949; May, 1959). But these early and most subsequent studies focused on solids mixing in fluidized bed chemical reactors. This is reflected in the small particles (d_p~100 μm) and large

height-to-diameter ratios used in these investigations. Bubbling fluidized bed combustors typically have large particles (d_p~1000 μm) and height-to-diameter ratios of 1 or less. An additional, and critical, feature of fluidized bed combustors is the presence of a horizontal tube bank. The presence of even a sparse tube bank has been found to significantly retard solids motion in bubbling beds (Highley and Merrick,1971; Chen et al.,1984). The tube bank geometry, in many ways, governs the bed hydrodynamics. In particular, it limits bubble growth, making the bubble properties a strong function of the tube bank geometry and independent of the overall bed dimensions. Rowe et al. (1965) showed that bubbles play a central role in the mixing of solids in fluidized beds. This is supported by Mori and Nakamura's (1966) finding that their diffusion coefficients were proportional to bubble diameter squared (i.e., $D \sim d_B^2$). Many of the mixing studies related to chemical reactors show a strong influence of bed diameter on the mixing; this would not be expected in a bed where the bubble properties are independent of the overall bed dimensions.

As mentioned previously, there is an additional concern over whether the hydrodynamics measured in experiments represent those found in a hot combustor. Many of the mixing studies related to fluidized-bed combustion used bed materials similar to those found in combustors but were fluidized using ambient air. Nicastro and Glicksman (1984) found significant disagreements between the hydrodynamics of a combustor and those of a cold-scale model using the hot-bed material. So although many solids mixing studies have been conducted, their relevance to solids mixing in PFBCs is tenuous at best.

Potter (1971) provides a comprehensive review of the experimental studies through the late 1960s. A more recent review, emphasizing solids mixing developments since 1976, is given by Fan et al. (1990). This review discusses developments in solids mixing related to a broad range of disciplines, including fluidization. A recent review by Lim et al. (1995) also provides an overview of recent developments in solids mixing related to gas-solid fluidization. Some of the more relevant experimental studies will be briefly reviewed here.

Highley and Merrick (1971) studied lateral solids mixing in a 1.52 m diameter fluidized bed. The bed had a small aspect ratio, with bed heights of 0.3 and 0.6 m. Lateral solids mixing was studied by introducing a radioactive tracer into the bed. Samples were drawn from 12 locations in the bed; a sample was taken from each probe every 2 seconds for 30 seconds after the tracer was introduced into the bed. Tracer concentrations were determined by analyzing the samples in a scintillation counter, providing tracer concentration data as a function of time at the 12 sampling locations in the bed. Eighteen tests were conducted to evaluate the effects of: tracer particle size and density, superficial velocity, bed height, and the presence of a tube bank, on the lateral solids mixing in their bed. They quantified their data by determining the lateral diffusion coefficient that best fit a diffusion model, assuming perfect mixing in the axial direction (i.e., one-dimensional diffusion). They concluded that for these low tracer concentrations, particle size and the particle density had no effect on the lateral diffusion coefficient. The lateral diffusion coefficient was found to increase in proportion to an increase in the gas superficial velocity. And without tubes in the bed, doubling the bed height produced a small increase in the lateral mixing. The presence of tubes in the bed reduced the lateral diffusion coefficient by a factor of 2.

Fitzgerald et al. (1977) studied three-dimensional solids mixing in 1 m square fluidized bed containing an array of horizontal tubes. Ferrite was used as a tracer, and its movement was followed using 64 inductance probes. The inductance probes were integrated into the the tube bank, eliminating non-prototypic disruptions of the flow. They found that for the same operating conditions, the tracer did not always spread in the same way, supporting a view of solids mixing as a stochastic phenomenon. Their results also suggest that the tracer moves from the injection point in clumps, rather than spreading smoothly as would be predicted by a diffusion model. Not surprisingly, they found that mixing rates were higher for higher superficial velocities. Kunii and Levenspiel (1991) show that in studies conducted in beds without tube bundles, the lateral diffusion coefficient is roughly an order of magnitude lower than axial diffusion coefficients. In contrast, Fitzgerald et al.

(1977) found that in their bed, which had a tube bank, the mixing rate was approximately the same in all directions–vertically, and laterally both normal and parallel to the tubes.

Sitnai (1981) studied axial mixing in a 1 m square bed with a horizontal tube bank. Mixing was measured by distributing an iron-ore tracer across the surface of the bed and then continuously drawing samples from 7 locations in the bed. The average tracer concentrations were determined over 5 second intervals, providing tracer concentration as a function of time at each of the sampling locations. Sitnai (1981) initially tried to fit the data to a diffusion model, but found that the diffusion coefficient varied by a factor of seven between two elevations in the bed. He then developed a three-layer counter-current backmixing model. The model had nine independent parameters; the axial mixing data were used to help establish values for these parameters.

Chen et al. (1984) tracked the motion of a radioactive tracer particle in a 19 cm diameter fluidized bed, both with and without a tube bank. They found that even sparse tube bundles can significantly reduce solids velocities and hence solids mixing. For example, at $u_o/u_{mf}=6$ the average axial solids velocity was reduced from 26 cm/s with no tube bank (100% open cross-section) to 15 cm/s with a sparse tube bank (85% open cross-section) to 2 cm/s with a dense tube bank (67% open cross-section). Thus, as found by Fitzgerald et al. (1977) and Highley and Merrick (1971), the presence of the tube bank has a significant effect on the motion of the solids in the bed.

6.5 Nomenclature

c_i	concentration of species i
c_{sd_i}	concentration of species i in the solids downflow region
c_{su_i}	concentration of species i in the solids upflow region
d_B	bubble diameter
d_p	particle diameter
D_{sa}	axial solids diffusion coefficient
D_{sr}	radial/lateral solids diffusion coefficient
f_d	fraction of the bed volume in the downflow region
f_u	fraction of the bed volume in the upflow region
K_{s_i}	solids exchange coefficient for species I
r	radial coordinate
u_{mf}	minimum fluidization velocity
u_o	gas superficial velocity
u_{sd}	velocity of the solids downflow region
u_{su}	velocity of the solids upflow region
z	axial coordinate

6.6 References

Abrahami, S.N. and Resnick, W., 1974, "Fluidised Bed Behavior Near Incipient Fluidization in a Three-Dimensional Bed," *Transactions of the Institution of Chemical Engineers (Great Britain)*, 52, pp. 80-87.

Avidan, A. and Yerushalmi, J., 1985, "Solids Mixing in an Expanded Top Fluid Bed," *AIChE Journal*, 31, 5, pp. 835-841.

Chen, M.M., Chao, B.T., and Liljegren, J., 1984, "The Effects of Bed Internals on the Solids Velocity Distribution in Gas Fluidized Beds," *Proceedings of the Fourth International Conference on Fluidization*, eds. D. Kunii and R. Toei, Engineering Foundation, pp. 203-210.

Cranfield, R.R., 1978, "Solids Mixing in Fluidized Beds of Large Particles," Fluidization: Application to Coal Conversion Processes, *AIChE Symposium Series* No. 176, 74, pp. 54-59.

Fan, L.T., Chen, Yi-Ming, and Lai, F.S., 1990, "Recent Developments in Solids Mixing," *Powder Technology*, 61, pp. 255-287.

Fitzgerald, T., Catipovic, N., and Jovanovic, G., 1977, "Solid Tracer Studies in a Tube-Filled Fluidized Bed," Proceedings of the Fifth International Conference on Fluidized Bed Combustion, 3, Washington, D.C., pp. 135-152.

Geldart, D., 1973, "Types of Gas Fluidization," *Powder Technology*, 7, pp. 285-292.

Gilliland, E.R. and Mason, E.A., 1949, "Gas and Solid Mixing in Fluidized Beds," *Industrial and Engineering Chemistry*, 41, 6, pp. 1191-1196.

Glicksman, L.R., Lord, W.K., and Sakagami, M., 1987, "Bubble Properties in Large-Particle Fluidized Beds," *Chemical Engineering Science*, 42, 3, pp. 479-491.

Gwyn, J.E., Moser, J.H., and Parker, W.A., 1970, "A Three-Phase Model For Gas-Solids Fluidized Beds," *Chemical Engineering Progress Symposium Series* No. 101, 66, pp. 19-27.

Highley, J. and Merrick, D., 1971, "The Effect of the Spacing Between Solid Feed Points on the Performance of a Large Fluidized-Bed Reactor," *AIChE Symposium Series No. 116*, 67, pp. 219-227.

Jinescu, G., Teoreanu, L., and Ruckenstein, E., 1966, *Canadian Journal of Chemical Engineering*, 44, p. 73.

Kunii, D. and Levenspiel, O., 1969, "Lateral Dispersion of Solid in Fluidized Beds," *Journal of Chemical Engineering of Japan*, 2, 1, pp. 122-124.

Kunii, D. and Levenspiel, O., 1991, Fluidization Engineering, Second Edition, Butterworth-Heinemann, Boston.

Lighthill, M.J., 1956, "Drift," *Journal of Fluid Mechanics*, 1, pp. 31-53.

Lim, K.S., Zhu, J.X., and Grace, J.R., 1995, "Hydrodynamics of Gas-Solid Fluidization," *International Journal of Multiphase Flow*, 21 (Suppl.), pp. 141-193.

May, W.G., 1959, "Fluidized-bed reactor studies," *Chemical Engineering Progress*, 55, 12, pp. 49-56.

Mori, Y., and Nakamura, K., 1966, *Kagaku Kogaku*, 4, p.154.

Morris, D.R., Gubbins, K.E., and Watkins, S.B., 1964, "Residence Time Studies in Fluidized and Moving Beds with Continuous Solids Flow," *Transactions of the Institution of Chemical Engineers (Great Britain)*, 42, pp. T323-T333.

Nicastro, M.T. and Glicksman, L.R., 1984, "Experimental Verification of Scaling Relationships for Fluidized Bed," *Chemical Engineering Science*, 39, 9, pp. 1381-1391.

Potter, O.E., 1971, "Mixing," Chapter 7 in Fluidization, eds. J.F. Davidson and D. Harrison, Academic Press, London, pp. 293-381.

Rowe, P.N., Partridge, B.A., Cheyenne, A.G., Henwood, G.A., and Lyall, E., 1965, "The Mechanisms of Solids Mixing in Fluidized Beds," *Transactions of the Institution of Chemical Engineers (Great Britain)*, 43, pp. T721-T286.

Shen, L., Zhang, M., and Xu, Y., 1995, "Solids Mixing in Fluidized Beds," *Powder Technology*, 84, pp. 207-212.

Sitnai, O., 1981, "Solids Mixing in a Fluidized Bed with Horizontal Tubes," *Ind. Eng. Chem. Process Des. Dev.*, 20, pp. 533-538.

Valenzuela, J.A. and Glicksman, L.R., 1984, "An Experimental Study of Solids Mixing in a Freely Bubbling Two-Dimensional Fluidized Bed," *Powder Technology*, 38, pp. 63-72.

van Deemter, J.J., 1967, In the Proceedings of the International Symposium on Fluidization, ed. A.A.H. Drinkenburg, Netherlands University Press, Amsterdam, pp. 334-347.

van Deemter, J.J., 1985, "Mixing", Chapter 9 in Fluidization, 2nd Edition, eds. J.F. Davidson et al., Academic Press, London, pp. 331-353.

Verloop, J., de Nie, L.H., and Heertjes, P.M., 1968/1969, "The Residence Time of Solids in Gas-Fluidized Beds," *Powder Technology*, 2, pp. 32-42.

Woollard, I.N.M. and Potter, O.E., 1968, "Solids Mixing in Fluidized Beds," *AIChE Journal*, 14,3, pp. 388-391.

This page intentionally blank

7. PFBC Bubble Characteristics

7.1 Techniques for Measuring Bubble Characteristics

Bubbles play a central role in the hydrodynamics of bubbling fluidized beds; in particular, they supply the motive force for the mixing of solids. So to begin to understand how solids mix in fluidized beds, it is essential to start by determining the characteristics of the bubbles. Of particular interest are the bubble diameter and the bubble frequency since these two variables dictate the length and time scales of the mixing within the bed. The bubble fraction is also important; the bubble size and the bubble fraction control the spacing between bubbles. Bubble coalescence rates, and thus lateral mixing, depend strongly on the bubble spacing. The two most common techniques for measuring bubble characteristics in fluidized beds are capacitance and optical probes. Both types of measurement devices will be briefly discussed. Yates and Simons (1994) provide a more detailed description of these and other experimental methods in fluidization.

7.1.1 Capacitance Probes

If a pair of conductive surfaces at different voltages are placed adjacent to each other in a gas-solid mixture, charges will accumulate on the two surfaces. The total charge is equal to the voltage difference times the capacitance of the intervening mixture. The capacitance of a gas-solid mixture is a function of the mixture's solids concentration. Capacitance probes measure bubble properties by responding to the change in capacitance between the probe's surfaces caused by the passage of a gas bubble. Riley and Louge (1989) provide a detailed discussion of capacitance probes and their application to measuring solids concentration in gas-solid flows.

Capacitance probes have been used to study fluidization back as early as 1951 (Morse and Ballou, 1951). Geldart and Kelsey (1972) highlighted the difficulty in interpreting capacitance probe output and the importance of calibration. Werther and Molerus (1973a,b) made detailed bubble measurements using a miniature needle capacitance probe. The probe's small size minimized its disturbance of the bed hydrodynamics, but their approach to identifying passing bubbles is suspect.

7.1.2 Optical Probes

Optical probes represent a relatively simple approach to measuring bubble characteristics. The two basic elements of an optical probe are a light source and a photodetector. When the light source is positioned opposite the photodetector, the detector's output will vary in response to changes in the attenuation provided by the medium between the two elements. In a fluidized bed, the output of the photodetector will vary depending on whether a bubble or the particle emulsion is present in the intervening region.

Optical probes also have a long history of use in fluidization research. Yasui and Johanson (1958) used optical probes as early as the late 1950s. Many other researchers have used optical bubble probes. Glicksman et al. (1987) used two fiber-optic probes to measure the bubble properties in a large-particle fluidized bed. The first probe consisted of two vertically aligned emitter-detector pairs for measuring bubble rise velocities. The second probe was an elaborate three-dimensional array of light sensors surrounding a single light source; they used the probe to measure bubble shape. Mainland and Welty (1995) provide a more detailed discussion of studies using optical probes to characterize bubble behavior. They also describe an optical probe suitable for use in high-temperature combustor applications.

Both optical and capacitance probes require methods of interpreting their output. Fluctuations in the voidage surrounding the probe produce fluctuations of varying

magnitude in the probe output. The objective of methods of interpreting the output is to rationally identify a threshold beyond which a change in output is classified as being produced by the passage of a bubble.

7.2 Optical Bubble Probe Development

Capacitance probes were considered for use in this study, but a unique optical probe was devised that made it possible to measure the bubble properties less intrusively and at lower cost.

7.2.1 Optical Bubble Probe Construction

A set of four optical probes were constructed to measure the bubble characteristics in the cold-scale model of the Tidd PFBC. The four probes were positioned different vertical distances from the distributor (z=13.3, 20.6, 27.6, and 31.4 cm), to provide detailed information on the bubble characteristics at several elevations in the bed.

The probe design takes advantage of the fact that the cold model requires an array of rods to simulate the boiler tubes of the hot combustor. The tight proximity of the rods in the cold model makes it possible to replace two adjacent rods with a light probe constructed to maintain geometric similarity with the combustor tube bank. Figure 1 illustrates the optical probe design used in the cold model.

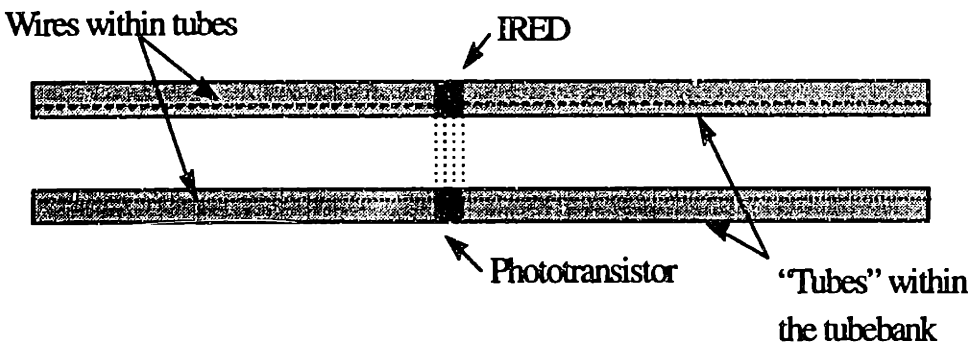

Figure 1: Top View of Optical Bubble Probe

An infrared emitting diode (IRED) serves as the probe's "light" source. The gallium aluminum arsenide (GaAlAs) diode[1] emits over a narrow band of wavelengths in the infrared spectrum, with peak emission at a wavelength of 880 nm. The IRED emits outside the visible spectrum, thus the term "light" is somewhat of a misnomer. A planar silicon phototransistor[2] acts as the probe's photodetector. Silicon phototransistors are highly sensitive to the emission wavelength of GaAlAs emitting diodes, providing an efficient coupling between the emitter and the detector. The sensitivity of the phototransistor to the emission from the IRED is sufficiently high that changes in the visible background lighting had a negligible effect on its output.

Pairs of rods in the cold-model tube bank were replaced with hollow copper tubing of the same diameter, which, as shown in Figure 1, accommodates the necessary optoelectronic devices and their wiring. The IRED and the phototransistor were epoxied into the tubing opposite each other, with just their lenses exposed through holes milled into the tube wall. The wiring runs along the inside of the tubes, leaving the tubing through holes milled into the top of the tube ends. The wires for each of the four probes were bound together, run up the wall of the bed, and then run out of the bed through a single fitting in each of the side walls. This unique design made it possible to measure the characteristics of the bubbles with minimal intrusion into the flow.

[1] Quality Technologies F5D3 GaAlAs infrared emitting diode
[2] Motorola MDR-310 planar silicon phototransistor

The probe positioned 13.3 cm above the distributor required a modified design since it was located below the bottom of the tube bank. (The bottom of the tube bank is 17.2 cm above the distributor.) A side view of the modified probe design is shown in Figure 2. A pair of dowels in the bottom row of the tube bank were replaced with hollow copper tubing of the same diameter. But rather than installing the phototransistor/IRED pair in the tubing as shown in Figure 1, holes where milled in the bottom of the tubing and a vertical section was attached that extended into the region below the tube bank. The phototransistor/IRED pair were installed in these vertical segments of tubing. The wiring for the optoelectronic components was run up through the hole in bottom of the horizontal section and then routed in the same manner as the other probes.

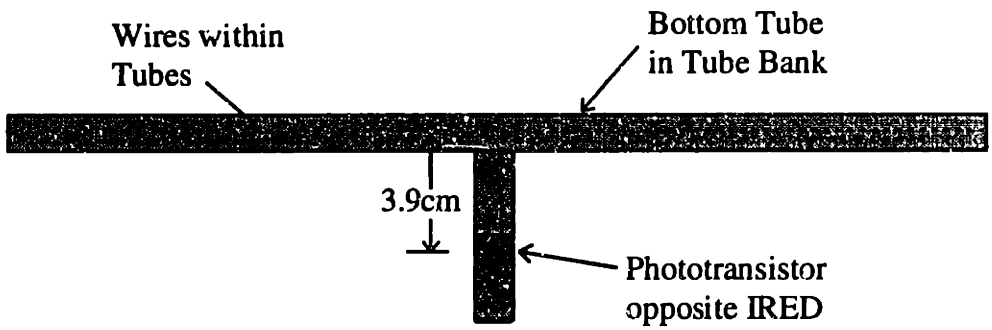

Figure 2: Side View of Probe Positioned Below Tube Bank at z=13.3cm

7.2.2 Bubble Probe Electronics

7.2.2.1 Phototransistor Electronics

Phototransistors behave like ordinary transistors. A transistor is shown schematically in Figure 3.

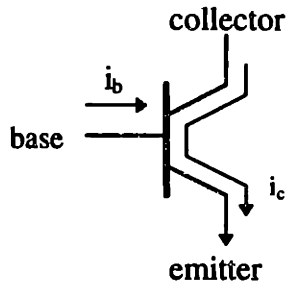

Figure 3: Transistor Schematic

Light incident on a phototransistor creates a photocurrent in the base-collector junction. This photocurrent supplies the base current of the transistor (i_b). A transistor can be thought of, in simple terms, as a current amplifier (Horowitz and Hill, 1989) where the collector current (i_c) is equal to the base current (i_b) times a gain. The relationship between i_c and i_b is given by

$$i_c = \beta \cdot i_b , \tag{1}$$

where β is the current gain, which typically has a value of around 100. Hence, a change in the intensity of the light incident on the transistor will alter the base current (i_b), producing a change in the much larger collector current (i_c).

The phototransistor requires power input to operate ($P=i_c \cdot v_{ce}$, where v_{ce} is the collector-emitter voltage difference), and also current is not typically a convenient quantity to measure. So additional electronics must accompany the phototransistor. Figure 4 presents the optical probe's phototransistor circui

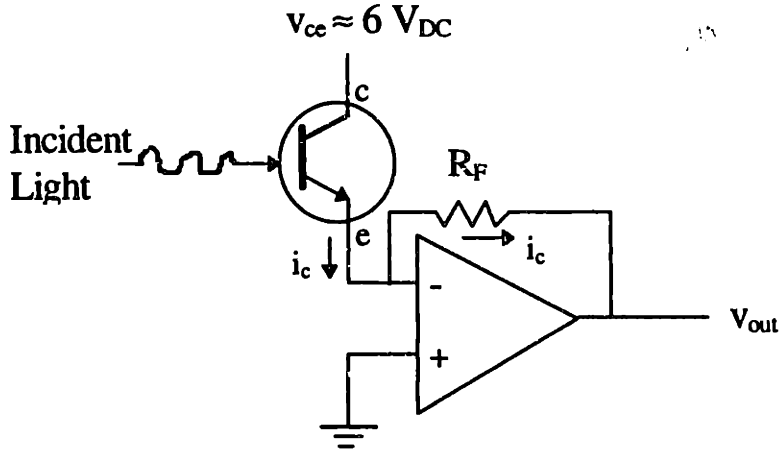

Figure 4: Phototransistor Circuit

A 12 V_{DC} power supply powers the phototransistor circuit. A differential-voltage operational amplifier circuit (see for example, Beckwith et al., 1993) reduced the 12 V_{DC} power supply to provide the 6 V_{DC} collector voltage (v_c). One-percent resistors were used in the differential amplifier to provide precise resistor matching to achieve a high common-mode rejection ratio.

The phototransistor circuit, shown in Figure 4, uses a general-purpose LF411 operational amplifier (op-amp) manufactured by National Semiconductor. The op-amp serves two purposes.

- The op-amp maintains the emitter voltage (v_e) equal to ground, and hence the collector-emitter voltage ($v_{ce}=v_c-v_e$) equal to 6 V_{DC}. Horowitz and Hill's (1989) first "golden rule" of op-amp behavior is: "The output attempts to do whatever is necessary to make the voltage difference between the inputs zero." Since the positive input terminal of the op-amp is grounded, the op-amp will attempt to maintain the negative terminal at ground. The voltage of the negative terminal is equivalent to the emitter terminal voltage (v_e) on the phototransistor, so that v_{ce} will be maintained at 6 V_{DC}. A collector-emitter voltage (v_{ce}) of 6 V_{DC} was chosen because the phototransistor base current (i_b) is independent of v_{ce} in the vicinity of this voltage. This simplifies the relationship between the intensity of the light incident on the

phototransistor and the light current generated. This will be discussed further in Section 7.2.3.

- The second purpose of the op-amp in the phototransistor circuit is to convert the collector current (i_c) to a voltage. Current is typically not a convenient quantity to measure; data acquisition systems are commonly configured to measure voltage. Therefore, it is necessary to convert the current leaving the phototransistor (i_c) to an output voltage (v_{out}) that varies as the current varies. Horowitz and Hill's (1989) second "golden rule" for op-amps is that "the inputs draw no current." The LF411's input current is approximately 0.2 nA (Horowitz and Hill (1989)). Hence, as illustrated in Figure 4, the negative terminal draws no current causing all the current leaving the phototransistor (i_c) to flow through the resistor R_F. Using Ohm's law, $v_{out}=-R_F i_c$, providing a simple relationship between the current from the transistor and the op-amp voltage output. The value of R_F was set individually for each probe to achieve a broad range of output; R_F typically ranged from 6-10 kΩ.

7.2.2.2 Infrared Emitting Diode (IRED) Electronics

Figure 5 shows the circuit for the IRED.

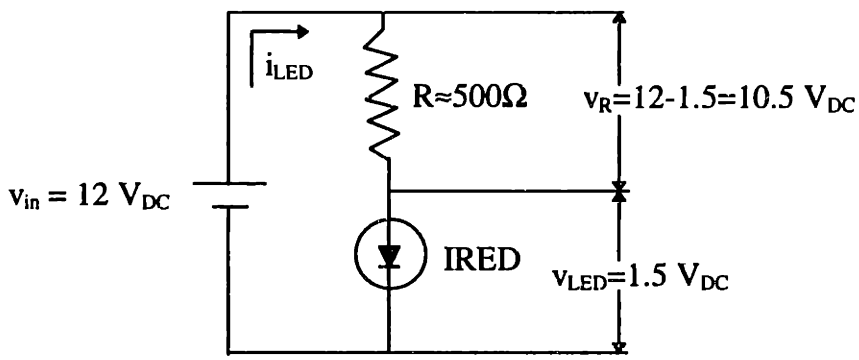

Figure 5: Infrared Emitting Diode Circuit

Diodes operate at approximately a constant forward voltage. For a typical operating current (i_{LED}) of 20 mA, the forward voltage (v_{LED}) of the Quality Technologies F5D3 IRED is roughly 1.5 V_{DC}. (At a maximum continuous current of 100 mA, the forward voltage is 1.7 V_{DC}.) The circuit is powered by a 12 V_{DC} power supply. In the voltage divider circuit configuration shown in Figure 5, the voltage drop across the resistor (v_R) must be equal to the difference between the supplied voltage (v_{in}) and the voltage drop across the IRED (v_{LED}). The resistance R is specified such that the current through the circuit (i_{LED}) is roughly 20 mA. Ohm's law gives: $R = v_R/i_{LED} \approx 500\Omega$.

7.2.3 Evaluation of Bubble Probe Performance

7.2.3.1 Relationship Between Output Voltage and Solid Concentration

The functional relationship between the output voltage from the phototransistor circuit (v_{out}) and the solid fraction ($1-\varepsilon$) can be determined from the circuit design and the phototransistor specifications. This functional form can then be used with calibration data to obtain a better understanding of the optical probe's performance.

As mentioned in Section 7.2.2.1, if the collector-emitter voltage (v_{ce}) is maintained at 6 V_{DC}, based on the phototransistor specifications, the phototransistor base current (i_b) is independent of v_{ce}. In this instance, according to the phototransistor specifications, the relationship between the base current and the irradiance (E_e) is given by

$$i_b = C_1 E_e^m, \tag{2}$$

where C_1 and m are constants. Combining (1) and (2) gives

$$i_c \simeq \beta \cdot C_1 E_e^m. \tag{3}$$

The output voltage from the thermistor circuit is related to the collector current (i_c) by

$$v_{out} \approx -R_F \cdot i_c. \tag{4}$$

The minus sign appears in (4) because the op-amp shown in Figure 4 is wired in an inverting configuration. Combining equations (3) and (4) provides a relationship between the output voltage (v_{out}) and the irradiance (E_e),

$$v_{out} = -R_F \cdot \beta \cdot C_1 E_e^m . \tag{5}$$

Finally, the Beer-Lambert Law will be used to relate the irradiance incident on the phototransistor to the solid fraction, i.e.,

$$E_e = e^{-a(1-\varepsilon)} . \tag{6}$$

a is a constant that indicates the attenuation characteristics of the intervening medium. Finally, substituting (6) into (5) gives

$$v_{out} = -B \cdot e^{-A \cdot (1-\varepsilon)}, \tag{7}$$

where $B=(R_F \cdot \beta \cdot C_1)$ and $A=(a \cdot m)$. A and B are constants that are determined from calibration data. Equation (7) is used with the calibration method described in the following section to characterize the optical probe performance.

7.2.3.2 Calibration Method

To assess the performance of the optical probes, they were immersed in a homogeneous gas-particle mixture of known solid concentration (1-ε). The difficulty lies in generating gas-particle mixtures over a range of known solid concentration. This was accomplished using the drop-tube apparatus illustrated in Figure 6. The drop-tube was constructed of a 2.4 m long piece of 5.08 cm diameter clear PVC pipe. The drop-tube had a particle reservoir at its top, with a valve to regulate the particle flow, and a collection bucket at its base. A coarse screen was placed in the tube at the exit of the upper particle reservoir to create a homogeneous mixture. The optical probe was installed in the base of the tube, where the particles flowed over it as they exited the drop-tube into the collection bucket.

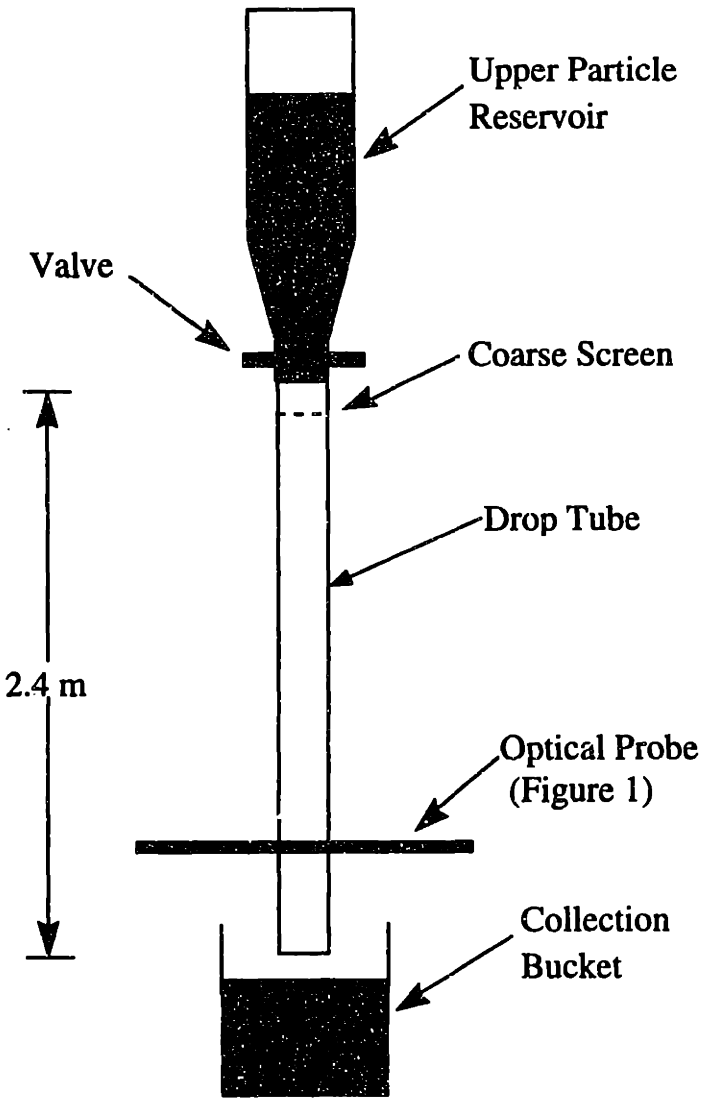

Figure 6: Optical Probe Calibration Apparatus

To estimate the solid concentration of the gas-particle mixture, the mass flowrate of the particles was measured using a stopwatch to determine the time that particles flow through the tube. By weighing the particles that accumulate in the collection bucket, it was possible to estimate the particle mass flowrate. From mass conservation, the average solid concentration of the mixture flowing through the tube is given by

$$(1-\varepsilon) \approx \frac{M}{t \cdot \rho_s \cdot u_{fall} \cdot A_{xs}}, \tag{8}$$

where:

M=the mass of particles collected in the collection bucket during time, t;

t=collection time;

ρ_s=particle solid density;

u_{fall}=the fall velocity of the particles; and

A_{xs}=the cross-sectional area of the drop tube.

The falling velocity of the particles (u_{fall}) past the optical probe was measured using high-speed video system and found on average to be 5.7 m/s.

Hence, by determining the mean optical probe output voltage (v_{out}) during the time that the particles were flowing over the probe, and using (8) to estimate the solid fraction, a set of calibration points can be obtained to specify A and B in (7). Figure 7 is a typical plot of v_{out} versus solid fraction. The "Curvefit" line represents (7) with the best-fit values for A and B. The data and the curve show that the optical probes are very sensitive to changes in solid concentration up to solid fractions of approximately 3% (i.e., $d\, v_{out}/d(1-\varepsilon)$ is large for $(1-\varepsilon)<0.03$). For solid fractions above 3%, much of the intensity of the light from the LED is attenuated, reducing the sensitivity of the probe.

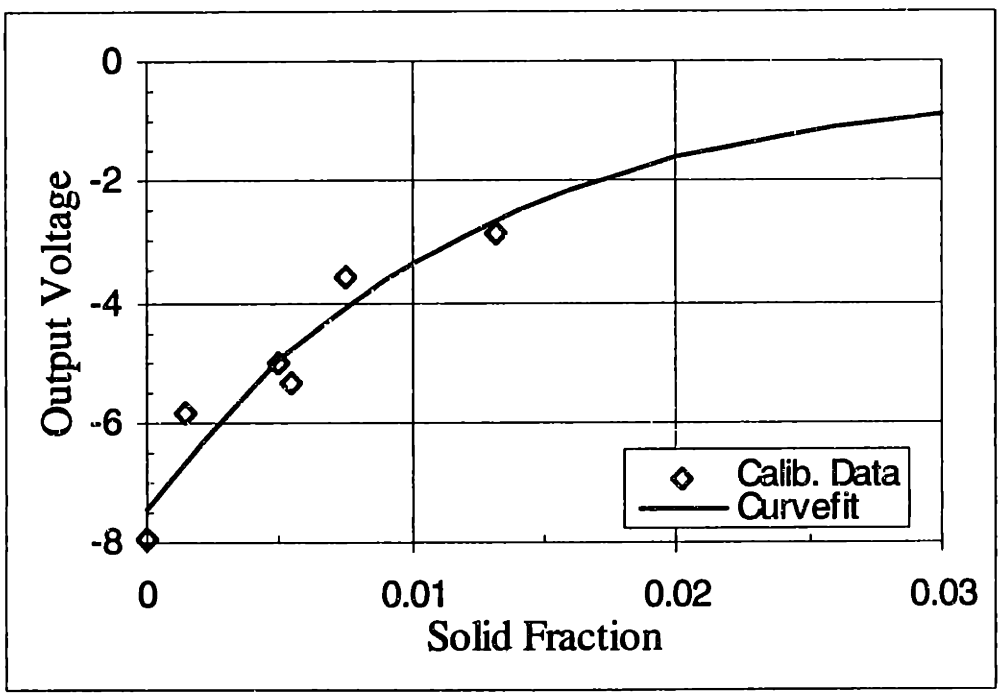

Figure 7: Typical Optical-Probe Voltage Output as a Function of Solid Concentration

7.3 Optical Bubble Probe Data Analysis

7.3.1 Bubble Rise Velocity Determination

The mean bubble rise velocity is measured using the output of two vertically aligned probes. The two probes will respond similarly to the passage of a bubble, but the response of the higher probe will lag behind the lower probe's response due to the finite rise velocity of the bubble. Figure 8 shows a bubble rising between two vertically aligned probes. As illustrated in the figure, there will be a delay between when the leading edge of the bubble passes the lower probe and when it reaches the upper probe.

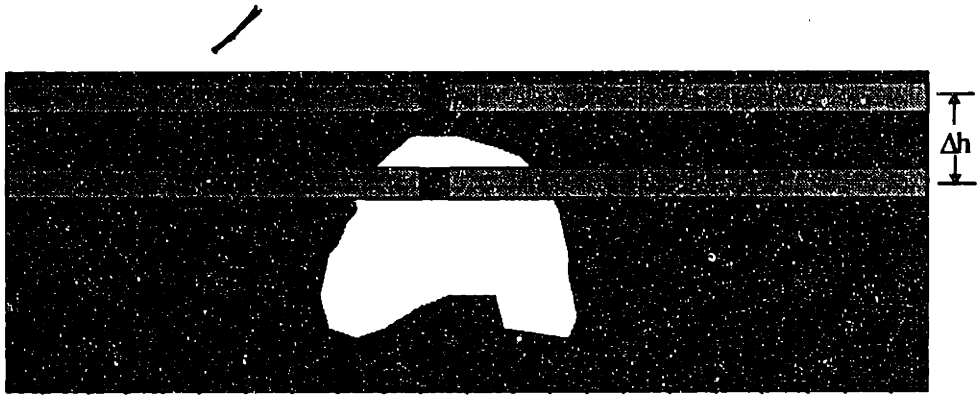

Figure 8: Illustration of Bubble Rising Between Vertically Aligned Probes

By measuring the distance separating the leading edges of the two probes (Δh) and estimating the mean time lag (τ_b), it is possible to calculate the mean bubble rise velocity using

$$u_b = \frac{\Delta h}{\tau_b}. \tag{9}$$

The instantaneous bubble rise velocity depends on many factors; the size and position of neighboring bubbles are two examples. So it is more useful to measure the local mean bubble rise velocity, rather than individual bubble velocities. The time lag between the

two probe outputs (τ_b), or equivalently the time it takes the bubble to rise a distance Δh, can be estimated using correlation methods. The cross-correlation function $R_{xy}(\tau)$ for the two stationary random processes x(t) and y(t) is given by (Bendat and Piersol, 1986)

$$R_{xy}(\tau) = \lim_{T \to \infty} \frac{1}{T} \int_0^T x(t) \cdot y(t+\tau) dt . \tag{10}$$

The cross-correlation function characterizes the correlation between two variables at different values of τ. Equation (10) defines the cross-correlation function, but it must be modified to accommodate discrete values of x(t) and y(t) and a finite sampling time (T). The procedure described below was used to estimate the most highly correlated time lag from the digital output of two optical probes (Bendat and Piersol, 1986). Let u_i and v_i represent discrete values of two data series, where i=1,N and N is the number of samples taken over a finite sampling time, T.

1. Least squares procedures were used to remove any trend in the data. A trend is a frequency component of the data that has a period longer than the sampling time.
2. The mean values of the two data records were computed using

$$\bar{u} = \frac{1}{N} \cdot \sum_{i=1}^{N} u_i \quad \text{and} \quad \bar{v} = \frac{1}{N} \cdot \sum_{i=1}^{N} v_i . \tag{11}$$

3. The data were transformed to have a zero mean value. Define

$$x_i = u_i - \bar{u} \quad \text{and} \quad y_i = v_i - \bar{v} , \tag{12}$$

such that $\bar{x}$ and $\bar{y}$ are zero.

4. The cross-correlation function is commonly normalized such that its value lies between +1 (perfect positive correlation) and -1 (perfect negative correlation). The normalized sample cross-correlation function is referred to as the sample cross-correlation coefficient [$\hat{\rho}_{xy}(\tau)$]. (A cross-correlation coefficient of zero indicates an absence of correlation.) For the two discrete data sets, the cross-correlation coefficient was calculated using

$$\hat{\rho}_{xy}(r \cdot \Delta t) = \frac{\hat{R}_{xy}(r \cdot \Delta t)}{\sqrt{\hat{R}_x(0)} \cdot \sqrt{\hat{R}_y(0)}} , \tag{13}$$

where r is the lag number which ranges from 0 to m. Higher lag numbers correspond to higher time lags ($\tau = r \cdot \Delta t$). (The ^ over each of the terms represents that they were calculated for finite sample times, T.) For discrete data, the sample cross-correlation function is given by

$$\hat{R}_{xy}(r \cdot \Delta t) = \frac{1}{N-r} \cdot \sum_{i=1}^{N-r} x_i \cdot y_{i+r} \cdot \tag{14}$$

$\sqrt{\hat{R}_x(0)}$ and $\sqrt{\hat{R}_y(0)}$ are estimates of the root mean square of x_i and y_i and were calculated using

$$\hat{R}_x(0) = \frac{1}{N} \cdot \sum_{i=1}^{N} (x_i)^2 \quad \text{and} \quad \hat{R}_y(0) = \frac{1}{N} \cdot \sum_{i=1}^{N} (y_i)^2 . \tag{15}$$

The sample cross-correlation coefficient, $\hat{\rho}_{xy}(\tau)$, was calculated from the voltage output of two adjacent probes in the bed. The outputs from the four optical bubble probes were used to estimate three values of the mean time lag (τ_b), one for each interval between the probes. The mean time lag was determined by plotting the cross-correlation coefficient versus time lag (τ) to graphically show the most highly correlated lag time (i.e, τ_b). Figure 9 presents a sample cross-correlation coefficient versus time lag plot. In this particular example, the output of the two probes have a correlation coefficient of 0.46 at a time lag (τ_b) of 0.4 s. Figure 9 also shows a periodicity in the signals. The probe outputs are strongly correlated not just for a single time lag corresponding to the passage of the same bubble, but also with what appears to be the subsequent bubble passing approximately 0.19 s later. This corresponds to a bubble frequency of roughly 5.3 Hz. This is consistent with the bubble frequency measurements described in Section 7.4.3. The average of the bubble frequencies measured by the two probes whose output was used to generate Figure 9 is 5.1 Hz. The correlation of the two signals is not always as strong as that shown in Figure 9 making this an unreliable approach to determining bubble frequency.

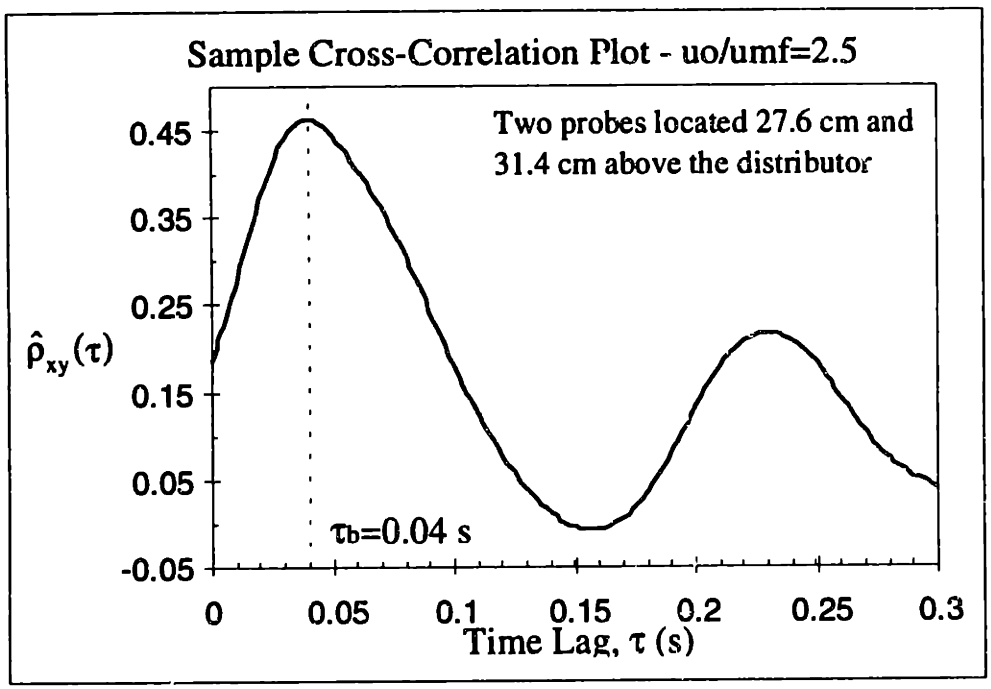

Figure 9: Sample Cross-Correlation of Light Probe Output to Determine τ_b

7.3.2 Setting Bubble Threshold

As mentioned in Section 7.1.2, it is essential to rationally establish a threshold beyond which variations in the optical probe output are interpreted as resulting from the passage of a bubble. One method, used in previous studies (Glicksman et al., 1987), is to calibrate the probe in a two-dimensional bed where variations in the probe's output are directly related to visual observations of the bubble motion in the bed. A different technique has been developed for this study. The approach is to independently estimate the bubble fraction (δ) from pressure drop measurements and the dense phase voidage; this will be described in detail in the following section. The optical probe threshold can then be set such that the bubble fraction measured by the probe matches the bubble fraction determined from the pressure-drop measurements. With the threshold established, it is possible to determine other bubble characteristics such as bubble size and frequency.

7.3.2.1 Relationship Between Voidage and Bubble Fraction

Differential pressure drop (Δp) is one of the few quantities that can be measured relatively easily and accurately in fluidized beds. Assuming that the weight of the particles between two pressure taps, say taps 1 and 2, is the sole contributor to the pressure drop (i.e., negligible contributions from friction or acceleration), it is possible to estimate the mean voidage between the taps using

$$\bar{\varepsilon}_{1-2} = \frac{\rho_s}{\rho_s - \rho_g} - \frac{\Delta p_{1-2}}{(\rho_s - \rho_g) \cdot g \cdot \Delta h_{1-2}}. \qquad (16)$$

Gravity dominates the pressure drop in bubbling fluidized beds, and for gas fluidized beds, where $\rho_s \gg \rho_g$, (16) can be simplified by neglecting ρ_g with respect to ρ_s.

To estimate the mean bubble fraction using the mean voidage ($\bar{\varepsilon}_{1-2}$), several modeling assumptions are necessary (Kunii and Levenspiel, 1968).

1. At any level in the bed, the cross-section consists of either a bubble or the particle emulsion.
2. The particle emulsion has a uniform and constant voidage (ε_e) throughout the bed.
3. The voidage within the bubble (ε_b) is approximately unity.

Figure 10 illustrates the model of a segment of a bubbling fluidized bed cross-section.

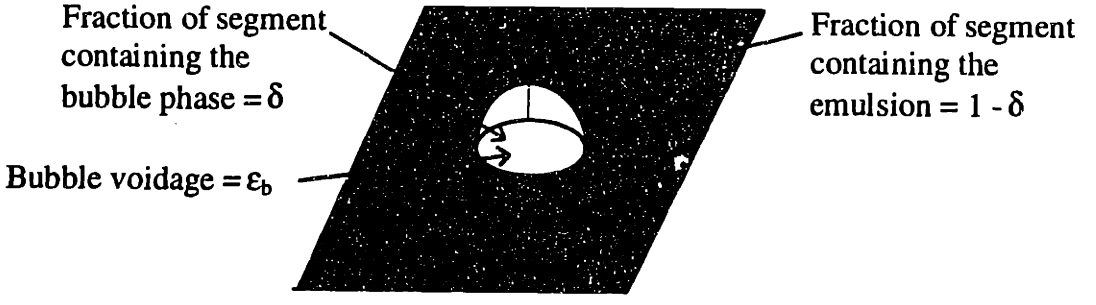

Figure 10: Model of a segment of bubbling bed cross-section

From the model of the bubbling fluidized bed cross-section shown in Figure 10, the mean voidage of the cross-section can be related to the local bubble fraction using

$$\bar{\varepsilon}_{1-2}(z) = \delta_{1-2}(z) \cdot \varepsilon_b + (1 - \delta_{1-2}(z)) \cdot \varepsilon_e . \tag{17}$$

Solving (17) for the bubble fraction and assuming that $\varepsilon_b \approx 1$ gives

$$\delta_{1-2}(z) = \frac{\bar{\varepsilon}_{1-2}(z) - \varepsilon_e}{1 - \varepsilon_e} . \tag{18}$$

7.3.2.2 Estimation of the Emulsion Voidage, ε_e

Using equation (18) to calculate the bubble fraction requires an estimate for the emulsion voidage, ε_e. Typically the emulsion voidage is assumed to be the voidage at minimum fluidization conditions (ε_{mf}). The minimum-fluidization voidage is roughly equivalent to the loose-packed voidage (ε_{lp}) of the bed material. Hence, it is common to assume that the emulsion voidage (ε_e) is approximately equivalent to the minimum-fluidization voidage (ε_{mf}), which in turn can be estimated by measuring the loose-packed voidage (ε_{lp}). In the approach described below, the minimum-fluidization-voidage estimate begins with the measured loose-packed voidage. The loose-packed voidage is then corrected for the bed expansion that occurs as the superficial gas velocity is increased from the loose-packed condition (no air flow) to the minimum-fluidization condition. This estimate of ε_{mf} provides a good estimate of the emulsion voidage for superficial gas velocities greater than that required to fluidize the bed (i.e., $u_o > u_{mf}$). Additional expansion of the particle emulsion beyond ε_{mf} is negligible for the range of particle sizes found in combustion systems (Gogolek and Grace, 1995).

As discussed in Section 7.3.2.1, a model is required to estimate the local $\delta(z)$ from $\Delta p(z)$ measurements (model illustrated in Figure 10). As shown in (18), the model depends not only on a measured estimate of the local voidage, $\varepsilon(z)$, but also on the emulsion voidage, ε_e. The local bubble fractions should integrate to give the overall bed-average bubble fraction ($\bar{\delta}$), which can be determined from the bed expansion. Although, as discussed in the previous paragraph, the emulsion voidage is approximately equal to the voidage at

minimum fluidization, when the bubble fractions calculated using (18) are integrated over the bed volume using the measured ε_{mf} for ε_e, they may deviate slightly from the measured $\bar{\delta}$. This could be due to limitations in the assumptions inherent in (16), such as small errors associated with neglecting friction or acceleration effects when using $\Delta p(z)$ to estimate $\varepsilon(z)$. Since we are interested in getting the best estimate of the local bubble fraction ($\delta(z)$) from the local voidage measurements, the value of ε_e will be specified such that when the bubble fractions from the model are integrated, the calculated overall bed-average bubble fraction ($\bar{\delta}$) matches that from bed-expansion measurements. ε_e is effectively being used to fit the δ model (Equation (18)) to match the overall bed-average bubble fraction. The measured value of ε_{mf}, from bed-expansion measurements, serves as a basis of comparison with the values of ε_e required to match $\bar{\delta}$. Individual values for ε_e were obtained for each u_o/u_{mf} condition tested, but due to the idealization of the model used to derive (18), it is difficult to justify using a variable ε_e. Hence, a single average value for ε_e was used to calculate the bubble-fraction profiles for all of the u_o/u_{mf} conditions tested. The details of these calculations are provided in the following two sections.

- Determination of ε_{mf}

The loose-packed voidage (ε_{lp}) can be calculated by dividing the mass of a particle sample by its loosely-packed volume to obtain the bulk density (i.e., $\rho_b = m_s/V_b$). The loose-packed voidage is then given by

$$\varepsilon_{lp} = 1 - \frac{\rho_b}{\rho_s}. \tag{19}$$

The loose-packed voidage of the polyethylene particles used in the cold model of the Tidd PFBC was measured outside the cold model using a flask and a balance. The loose-packed voidage was found to be ε_{lp}=0.55.

A more accurate estimate for the voidage at minimum fluidization (ε_{mf}) would be a corrected loose-packed voidage that accounts for the expansion of the emulsion that occurs between the loose-packed and minimum-bubbling conditions. This correction was estimated empirically, using the cold model, by measuring the bed level with no air flow (loose-packed condition) and the level at the point just before bubbles begin to form (minimum-bubbling condition). The minimum-bubbling point was determined from visual observations of the first appearance of bubbles at the front wall or the surface of the bed. The particles in the cold model are Geldart Group B (Geldart, 1973). Bubbles form at or only slightly above the minimum-fluidization velocity (u_{mf}) for particles in this category. The loose-packed voidage is related to the loose-packed height (H_{lp}) according to the following relationship.

$$\varepsilon_{lp} = 1 - \frac{(V_s/A_{xs})}{[H_{open} + (H_{lp} - H_{open}) \cdot (1 - \delta_T)]} = 0.55. \qquad (20)$$

H_{open} is the height of the open region below the tube bank and δ_T is the fraction of the cross-sectional area filled by tubes in the tube bank. The region from H_{open} to H_{lp} is filled with tubes. V_s/A_{xs}, the ratio of the volume of solids to the bed cross-sectional area, is constant regardless of the air flow through the bed and can be calculated using (20) and a measured H_{lp}. The minimum-fluidization voidage can then estimated by measuring the bed height at minimum-bubbling conditions (H_{mb}) and using the value for V_s/A_{xs} calculated from (20) in the following expression.

$$\varepsilon_{mf} = 1 - \frac{(V_s/A_{xs})}{[H_{open} + (H_{mb} - H_{open}) \cdot (1 - \delta_T)]}. \qquad (21)$$

Using (21) to evaluate the minimum-fluidization voidage for the cold-model bed material gives: ε_{mf}=0.58. This value of ε_{mf} provides a good estimate of the true emulsion voidage (ε_e) and serves as a basis of comparison with the emulsion voidages calculated below. These emulsion voidages, which were calculated such that the local bubble fractions given by (18) when integrated over the bed volume match the measured overall bed-average bubble fraction, are expected to be close to the measured ε_{mf}.

- Estimation of ε_e Required to Match the Overall Bed-Average Bubble Fraction

If it is assumed that bubbles are responsible for any bed expansion beyond the minimum bubbling point (i.e., ε_e is a constant), the bed-average bubble fraction ($\bar{\delta}$) can be calculated from bed-expansion measurements. For the special case where the bed height at minimum bubbling is greater than the height of the open area below the tube bank (i.e., $H_{mb} > H_{open}$), there are three contributions to the expanded bed volume (V_{exp}).

$$V_{exp} = V_{mb} + V_{tubes} + V_{bub} \,. \tag{22}$$

Equation (22) shows that the expanded bed volume consists of the original volume of the bed at the minimum-bubbling condition (V_{mb}), the volume of the tubes between H and H_{mb} (V_{tubes}), and the bubble volume (V_{bub}). Dividing (22) by V_{exp} and relating the bed volume to the bed height using relationships of the form $V_{exp}=H \cdot A_{xs}$ gives

$$1 = \frac{H_{mb}}{H} + \frac{(H - H_{mb}) \cdot \delta_T}{H} + \bar{\delta} \,, \tag{23}$$

where, again, δ_T is the fraction of the bed volume consisting of tubes for $H>H_{mb}$. The tube fraction (δ_T) for the cold model is 0.12. Solving (23) for $\bar{\delta}$ gives

$$\bar{\delta} = (1 - \delta_T) \cdot \left(1 - \frac{H_{mb}}{H} \right). \tag{24}$$

Equation (24) relates $\bar{\delta}$ to H and H_{mb} measurements. H_{mb} was measured by visually identifying and measuring the bed height at minimum-bubbling conditions. Due to the vigorous bubbling of the bed, it is not possible to measure H in the same manner. H is typically determined from the pressure profile in the bed. Figure 11 presents the pressure profile for one of the five conditions tested. As the figure demonstrates, the expanded bed height can be measured by linearly extrapolating the pressure profile to the height where the pressure equals the freeboard pressure (i.e., where $p-p_{fb}=0$).

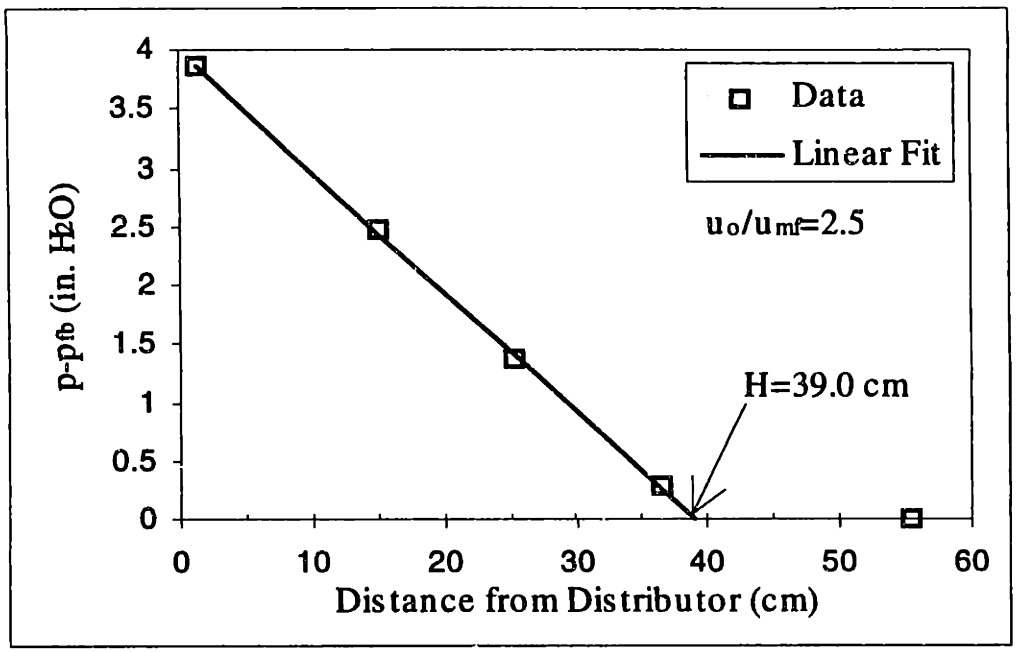

Figure 11: Sample Bed-Expansion Measurement

Bubble-property measurements were made at five different gas superficial velocities (u_o/u_{mf}=2.5, 2.8, 3.1, 3.4, and 3.83). The H/H_{mb} measurements and the values of $\bar{\delta}$, calculated using (24), are summarized in the Table 1. The bed-height measurements for all five test conditions are given in Appendix H.

Table 1: Summary of Overall Bubble Fractions for Test Conditions

u_o / u_{mf}	H / H_{mb}	$\bar{\delta}$
2.5	1.48	0.285
2.8	1.53	0.304
3.1	1.60	0.329
3.4	1.66	0.351
3.83	1.78	0.387

The emulsion voidage is calculated by determining the value of ε_e such that when $\delta(\varepsilon_e,\varepsilon(z))$ is integrated over the expanded particle volume ($V_{exp\text{-}s}$), it equals the average bed bubble fraction from bed-expansion measurements ($\bar{\delta}$ given in Table 1). $\varepsilon(z)$ is obtained from local pressure-drop measurements using (16). This integration can be accomplished by substituting (18) into

$$\bar{\delta} = \frac{1}{V_{exp\text{-}s}} \cdot \int_0^H \delta(\varepsilon_e, \varepsilon(z)) \cdot A(z) dz \tag{25}$$

and determining ε_e such that the right hand side of (25) integrates to be equal to the measured $\bar{\delta}$ listed in Table 1. The following example should clarify the procedure.

Again, consider the same case shown in Figure 11, where u_o/u_{mf}=2.5. As shown in Figure 12, the voidage is assumed to be constant over the intervals between pressure taps. The integral in (25) can then be evaluated using (18). The resulting expression is

$$\bar{\delta} = \frac{1}{H_{open} + (H - H_{open}) \cdot (1 - \delta_T)} \cdot \begin{bmatrix} \left(\frac{\varepsilon_1 - \varepsilon_e}{1 - \varepsilon_e}\right) \cdot z_1 + \left(\frac{\varepsilon_2 - \varepsilon_e}{1 - \varepsilon_e}\right) \cdot (H_{open} - z_1) + \\ \left(\frac{\varepsilon_2 - \varepsilon_e}{1 - \varepsilon_e}\right) \cdot (z_2 - H_{open}) \cdot (1 - \delta_T) + \\ \left(\frac{\varepsilon_3 - \varepsilon_e}{1 - \varepsilon_e}\right) \cdot (H - z_2) \cdot (1 - \delta_T) \end{bmatrix}. \tag{26}$$

The presence of the tubes alters the cross-sectional area with height (A(z)); the tube fraction (δ_T) is used to account for the area change.

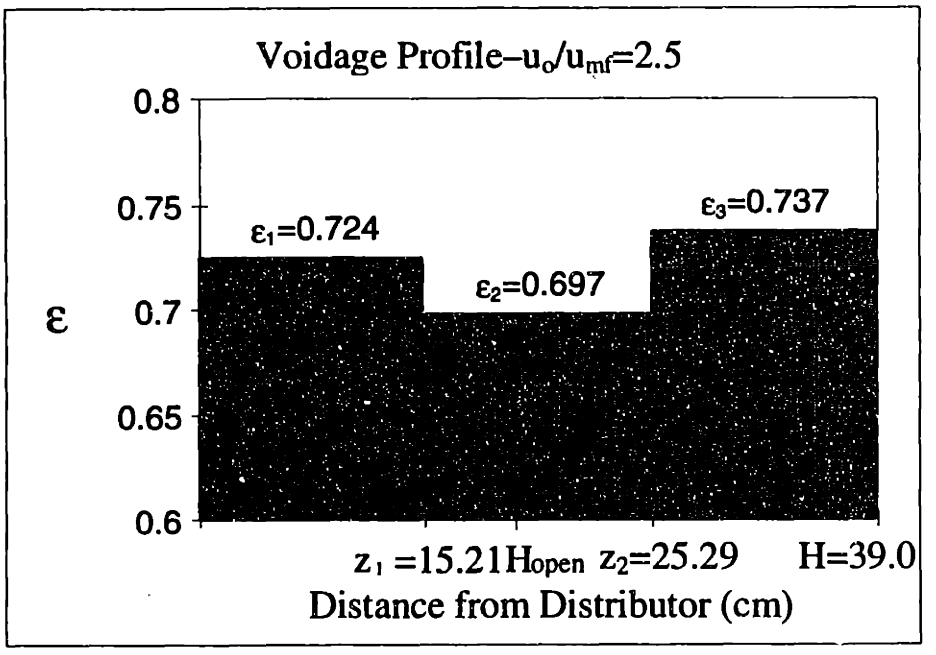

Figure 12: Sample Voidage Distribution to Illustrate Evaluation of ε_e

For this particular case, a value of ε_e=0.611 matches the overall bed bubble fraction of $\overline{\delta}$=0.285. Table 2 lists the emulsion voidages, calculated in the same manner as in the previous example, for all the conditions under consideration.

Table 2: Emulsion Voidages For Each Condition Under Consideration

u_o/u_{mf}	ε_e
2.5	0.611
2.8	0.618
3.1	0.625
3.4	0.636
3.83	0.647
	$\overline{\varepsilon}_e$ = 0.63

The average of the emulsion voidages is ε_e=0.63. As expected, this number is close to the estimated minimum-fluidization voidage of ε_{mf}=0.58. The values for ε_e approach ε_{mf} as u_o/u_{mf} is decreased. Rather than use a different emulsion voidage to calculate the local bubble fractions for each operating condition, the average value of 0.63 was used. As mentioned previously, idealizations in the model illustrated in Figure 10 make it difficult to justify varying ε_e for each condition. Also, there is more uncertainty for the ε_e values at higher u_o/u_{mf} since the highest pressure tap located within the bed is positioned at z=30.9 cm. Hence, the voidage measured between this tap and the one below it (ε_3) will be weighted over a larger section of the bed as it expands (i.e., $(H-z_2)$ will increase in (26)). This increased uncertainty also makes it difficult to justify using a variable ε_e. Using 0.63 for the emulsion voidage rather than 0.58, which is closer to the true emulsion voidage, should provide a better estimate of $\delta(z)$ since it provides better agreement with the independently-measured overall bed-average bubble fraction.

Finally, it is now possible to determine the bubble fraction profile ($\delta(z)$) that is used to set the bubble-probe threshold. For consistency, the u_o/u_{mf}=2.5 test condition will continue to serve as an illustrative example. Table 3 presents the calculated bubble-fraction profile. The $\varepsilon(z)$ values in Table 3 were calculated from pressure-drop measurements interpolated to correspond to the elevations of the optical probes. The detailed results of the bubble-fraction calculations are presented in Appendix G.

Table 3: Calculation of $\delta(z)$ Profile for u_o/u_{mf}=2.5 Case Using ε_e=0.63

Probe Elevation z (cm)	Interpolated $\varepsilon(z)$	$\delta(z)=\frac{\varepsilon(z)-\varepsilon_e}{1-\varepsilon_e}$
13.3	0.713	0.226
20.6	0.698	0.187
27.6	0.724	0.258
31.4	0.739	0.296

The procedure described in the preceding paragraphs demonstrates how the bubble fraction can be estimated from pressure-drop measurements.

- Using $\delta(z)$ from Pressure-Drop Measurements to Set the Optical-Probe Threshold

The bubble fraction measured using the optical probe should be the same as that from pressure-drop measurements. The local bubble fraction can be calculated from the optical probe output using

$$\delta = \frac{1}{T} \cdot \sum_{i=1}^{N_b} b_i . \tag{27}$$

N_b is the total number of bubbles detected during the sampling time, T, and b_i is the duration bubble i is present at the probe. The threshold, or cutoff, on the output is varied until the bubble fraction measured using the optical probe matches that determined using pressure-drop measurements (e.g., $\delta(z)$s listed in Table 3). Figure 13 illustrates the threshold. The figure shows a segment of the optical probe output, where again u_o/u_{mf}=2.5. The output has been converted to solid fraction using the calibration procedure described in Section 7.2.3. The threshold line shown on the figure represents the solid-fraction cutoff such that the bubble-fraction target, set using pressure-drop data, is matched by the optical-probe output.

In addition, Figure 13 highlights the need to define a threshold. The are many fluctuations in the signal at high solid fractions. The threshold defines the magnitude of the fluctuation considered to be due to the passage of a bubble.

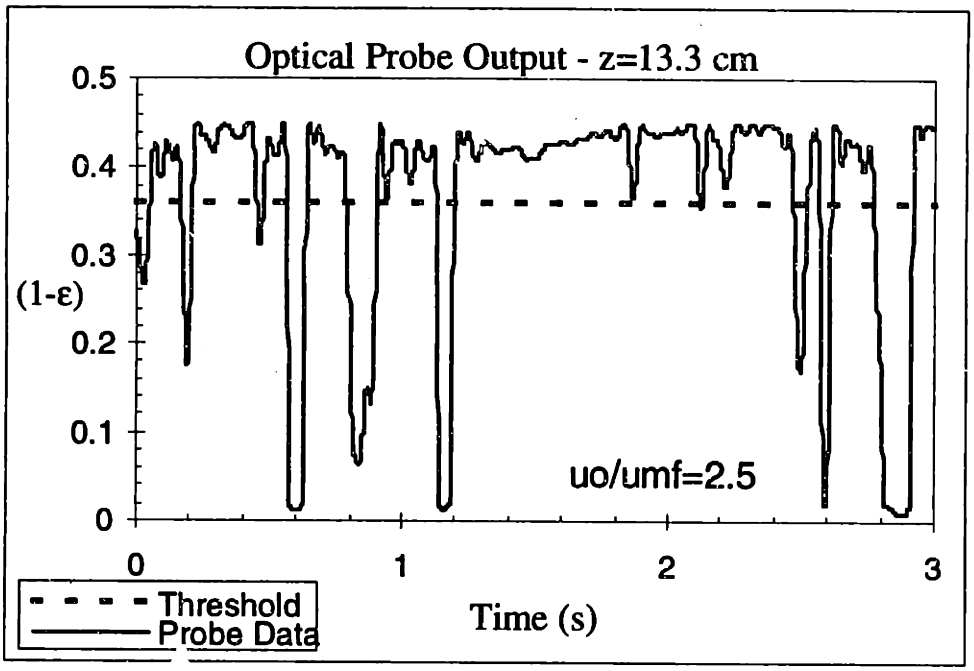

Figure 13: Sample Optical Probe Output with Threshold Shown

Figure 14 shows how the solid fraction threshold, which is used to specify the bubble mean pierced length and frequency, varies with the specified bubble fraction. The data used to generate Figure 14 is the same as that shown in Figure 13. The sensitivity of the bubble-probe measurements to the specified threshold (i.e., sensitivity of the measured bubble characteristics to the local bubble fraction estimates) is addressed in Section 7.4.4.

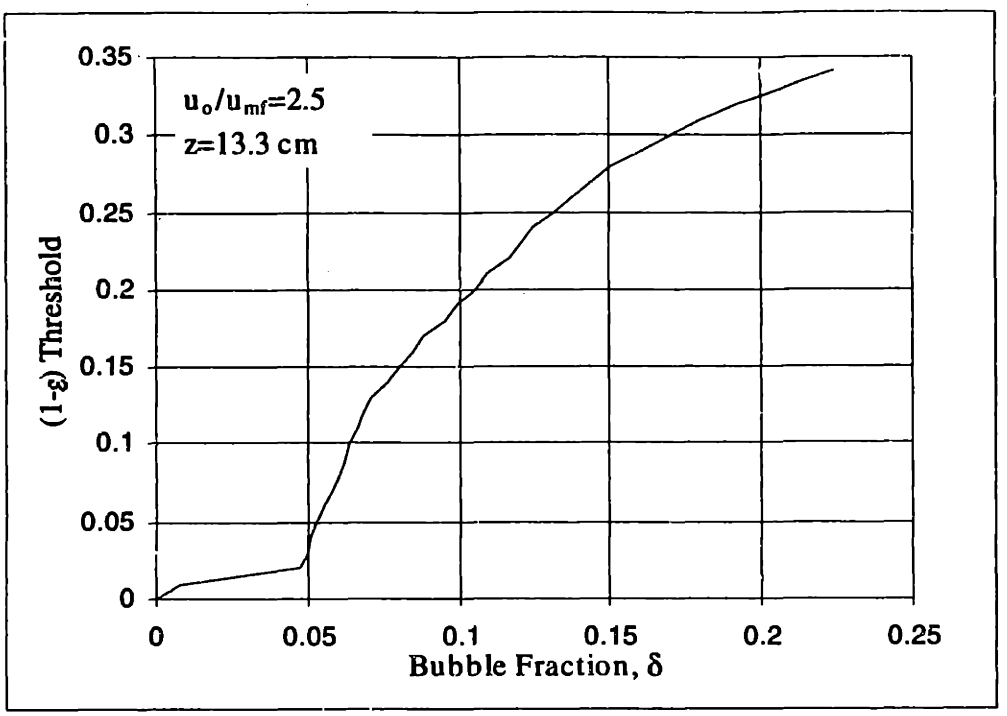

Figure 14: Variation of (1-ε) Threshold with Measured δ

7.3.2.3 Summary of Procedure for Setting Optical Probe Threshold

The procedure for setting the optical probe threshold described in the previous sections is potentially confusing and so it seems appropriate to briefly summarize the procedure. This summary is provided in the form of two figures. Figure 15 is a flowchart describing the steps of the procedure in words. The description provided in Figure 15 is then quantified in Figure 16, where the equations used in the procedure are summarized.

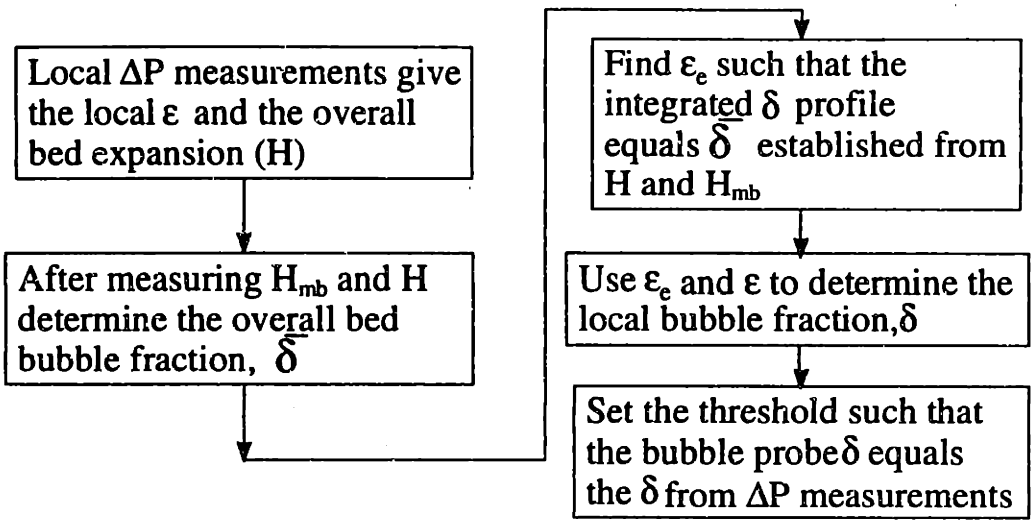

Figure 15: Flowchart of Procedure to Set Optical Probe Threshold

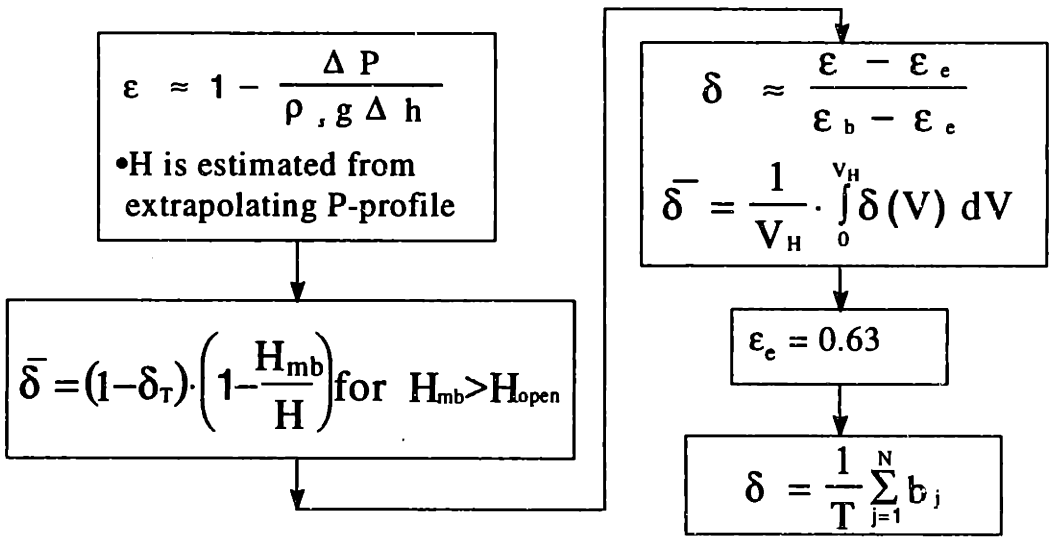

Figure 16: Flowchart Summarizing Expressions Used to Set Optical Probe Threshold

7.3.3 Bubble Size Determination

The bubble rise velocity (u_b) is a prerequisite to calculating the bubble size. Optical probes provide data to calculate what is commonly referred to as the mean pierced (or mean

chord) length, $\bar{l}_b$. The mean pierced length is calculated from the optical probe output using

$$\bar{l}_b = \frac{u_b}{N_b} \cdot \sum_{i=1}^{N_b} b_i , \tag{28}$$

where N_b is the number of bubbles detected and b_i is the time it takes bubble i to rise past the probe.

Most models and correlations are based on bubble diameter, not mean pierced length. Bubble diameter (d_B) can be estimated from mean pierced length measurements ($\bar{l}_b$) by assuming that the bubble has no preferred path and is spherically shaped. This relationship is obtained by integrating the equation for a circle of radius $d_B/2$ over its diameter, i.e.,

$$\bar{l}_b = 2 \cdot \left[\frac{1}{d_b} \cdot \int_{-d_b/2}^{d_b/2} \sqrt{(d_b/2)^2 - x^2}\, dx \right]. \tag{29}$$

Evaluating (29) gives

$$d_b = \frac{4}{\pi} \cdot \bar{l}_b , \tag{30}$$

which is a simple expression for estimating bubble diameter from mean pierced length measurements.

7.3.4 Bubble Frequency Determination

In addition to bubble size, bubble frequency is also important to solids mixing. Once a threshold is established, calculating the bubble frequency is straightforward. The bubble frequency is the number of bubbles which interact with the probe per unit time. The frequency can be calculated using

$$f_b = \frac{N_b}{T} , \tag{31}$$

where, again, N_b is the number of bubbles that interact with the probe during a total sampling time, T.

7.4 Optical Probe Results

Bubble characteristics were measured in the cold model at five superficial gas velocities (u_o/u_{mf}=2.5, 2.8, 3.1, 3.4, and 3.83). The u_o/u_{mf}=3.83 condition corresponds to the operating condition at which the scaling comparisons described in Chapter 4 were conducted. The intent was to measure the characteristics of the bubbles over a range of superficial velocities and then to develop a mixing model using both mixing and bubble data at a single superficial gas velocity. By developing a mechanistic model of the solids mixing process, based on the characteristics of the bubbles, it should then be possible to use the bubble properties at other superficial velocities to characterize the mixing at these conditions.

The optical probe data were acquired using the same PC-based digital data acquisition system described in Chapter 3. As mentioned in Werther and Molerus (1973a), the correlation between two bubble probe signals depends highly on the shape of the bubble pulses. The outputs of the optical probes were sampled every 0.002 s (f_{sample}=500 Hz). Based on measurements of the bubble mean pierced lengths and rise velocities, the bubble takes an average of roughly 0.07 s to pass the probe. Hence, the sampling rate is sufficient to provide, on average, over 30 data points to resolve the shape of the bubble pulses. Each run lasted 24 seconds (i.e., T=24.0 s), giving a total of 12000 points per run. The data were digitally low-pass filtered to eliminate high frequency noise. Filtering the data increased the correlation coefficients used to estimate the time lags for the bubble rise velocity measurements. The digital filter is illustrated in Figure 17.

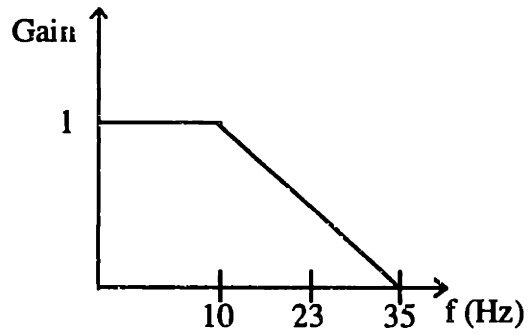

Figure 17: Graphical Illustration of Digital Filter Applied to Bubble Data

The bubble frequencies measured in this study range from 4-7 Hz. These frequencies are within the 0-10 Hz pass band of the digital filter shown in Figure 17, maintaining the hydrodynamic frequencies while attenuating noise in the signal. The width of the attenuation ramp is dictated by the sampling rate. The filter cutoff frequency of 23 Hz, corresponds to the midpoint of the ramp. The value of the cutoff frequency was specified so that for the 25 Hz attenuation ramp, there would be no attenuation of frequencies below 10 Hz.

In general, the bubble properties were determined from five 24 s runs. The highest u_o/u_{mf} case was the exception, where the bubble properties were determined from seven 24 s runs. Four additional runs were made for the four lowest u_o/u_{mf} cases to provide additional bubble-rise velocity data. Not all runs gave meaningful cross-correlation results at every level in the bed. The supplemental data were necessary to reduce the precision/random error in the bubble velocity measurements. When considering the quality of correlation between two probes, the two criterion were applied. The first was that the cross-correlation coefficient have a distinct peak, and the second was that the cross-correlation coefficient preferably be greater than 0.10.

The error bars shown on the plots in Sections 7.4.1-7.4.3 represent 95% confidence levels. These error bars reflect both bias and precision error where possible. A detailed discussion of the uncertainty analysis performed for each of the measurements is presented

in Appendix J. The results presented in graphical form in Sections 7.4.1-7.4.3 are tabulated in Appendix I.

7.4.1 Bubble Rise Velocity, u_b

Figure 18 presents the bubble rise velocity data, for all five test conditions, as a function of elevation above the distributor. The superficial gas velocity (u_o) ranges from 0.3 to 0.46 m/s for the five test conditions, and u_o-u_{mf} ranges from 0.18 to 0.34 m/s. The vertical dashed line represents location of the bottom of the tube bank. A single error bar, representing 95% confidence limits, is shown on the plot to provide an estimate of the uncertainty in the data. Figure 18 shows that the bubbles accelerate as they rise through the bed. As will be shown in Section 7.4.2, the larger bubbles rise faster. One would expect bubbles of the same size to rise faster the higher the gas superficial velocity. But in this case, the bubbles at the u_o/u_{mf}=3.1 condition rise the fastest. The higher superficial velocities appear to impede bubble growth, most likely due to increased bubble splitting, reducing the bubble rise velocity. In general, the bubble rise velocity data do not show a strong dependence on u_o/u_{mf}.

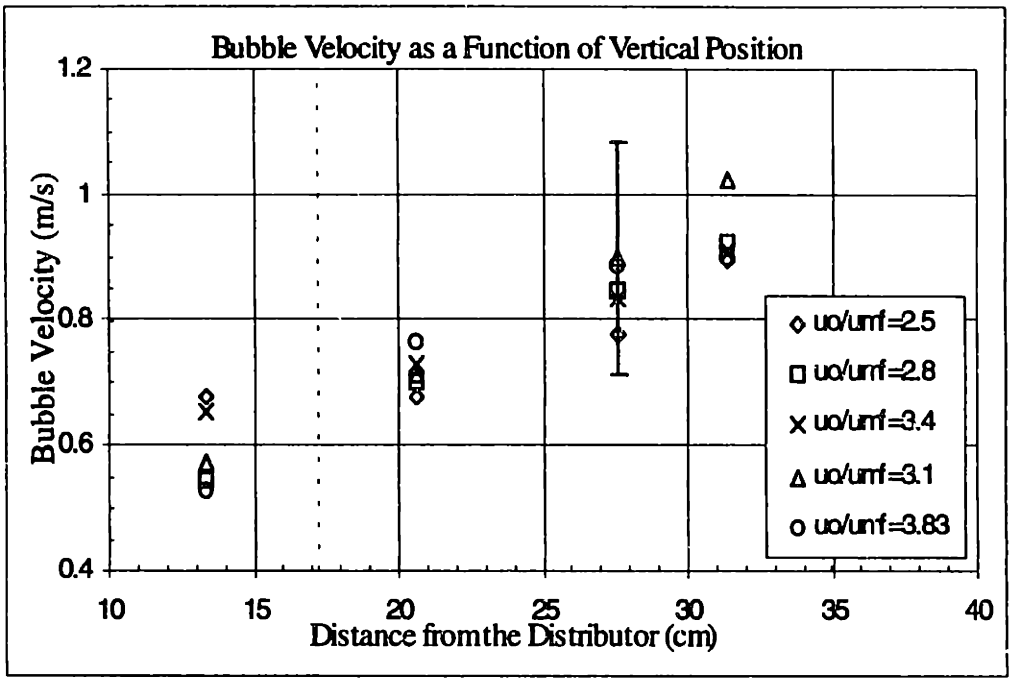

Figure 18: Bubble Rise Velocity Measurements as a Function of Position in the Bed

Figures 19-23 present the bubble rise velocity data as a function of distance from the distributor for each individual u_o/u_{mf} test condition. The figures include 95% confidence levels on the data. The details of the uncertainty analysis performed to arrive at these error estimates are described in Appendix J. Previous studies have shown that the average bubble rise velocity in a vigorously bubbling bed can be reasonably estimated using the following relationship.

$$u_b = u_o - u_{mf} + 0.711 \cdot \sqrt{g \cdot d_b} \,. \tag{32}$$

Davidson and Harrison (1963) first proposed using this expression for bubbles in fluidized beds. The predictions of (32) are plotted against the data in Figures 19-23. The predictions use the measured mean pierced lengths adjusted using (30) to estimate d_b. The predictions also account for the increased u_o in the upper part of the bed caused by the flow constriction created by the tubes (12% of the cross-sectional area). Also plotted on Figures 19-23, for comparison, is the single bubble form of (32), which does not include the excess gas velocity contribution (u_o-u_{mf}) (i.e., $u_b = 0.711\sqrt{g d_b}$). In general, (32) satisfactorily predicts the bubble rise data, but it predicts a much greater dependence on u_o/u_{mf} than the data show. This will become clear from the comparisons presented in

Section 7.4.2. The single bubble rise velocity expression does not depend upon (u_o-u_{mf}), but it clearly underpredicts the bubble rise velocity in the cold model.

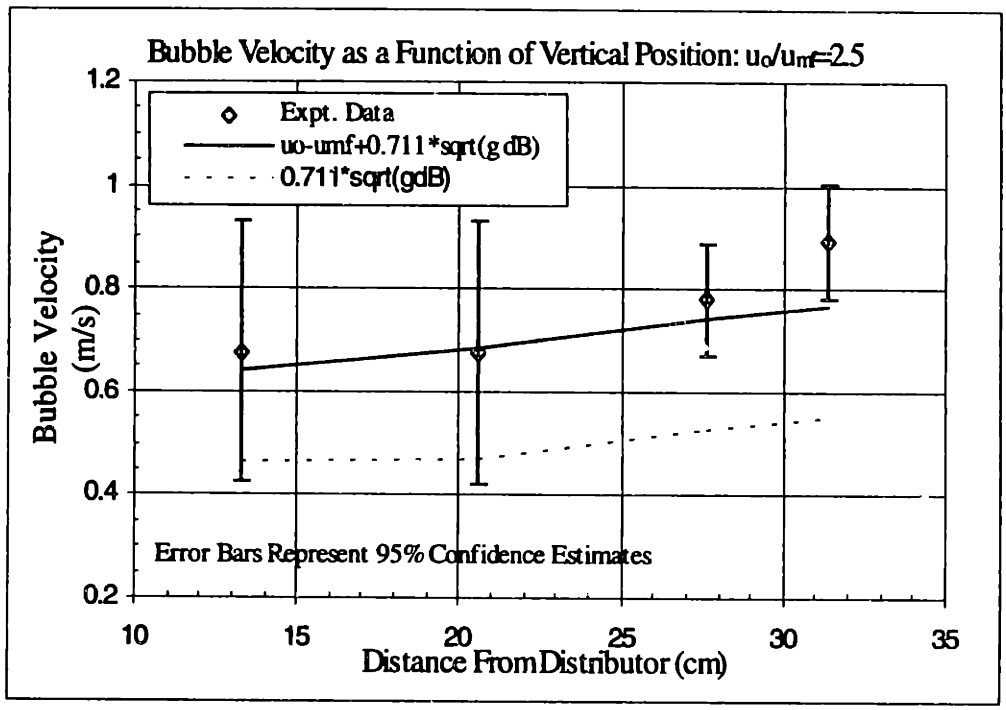

Figure 19: Bubble Velocity as a Function of Vertical Position: u_o/u_{mf}=2.5

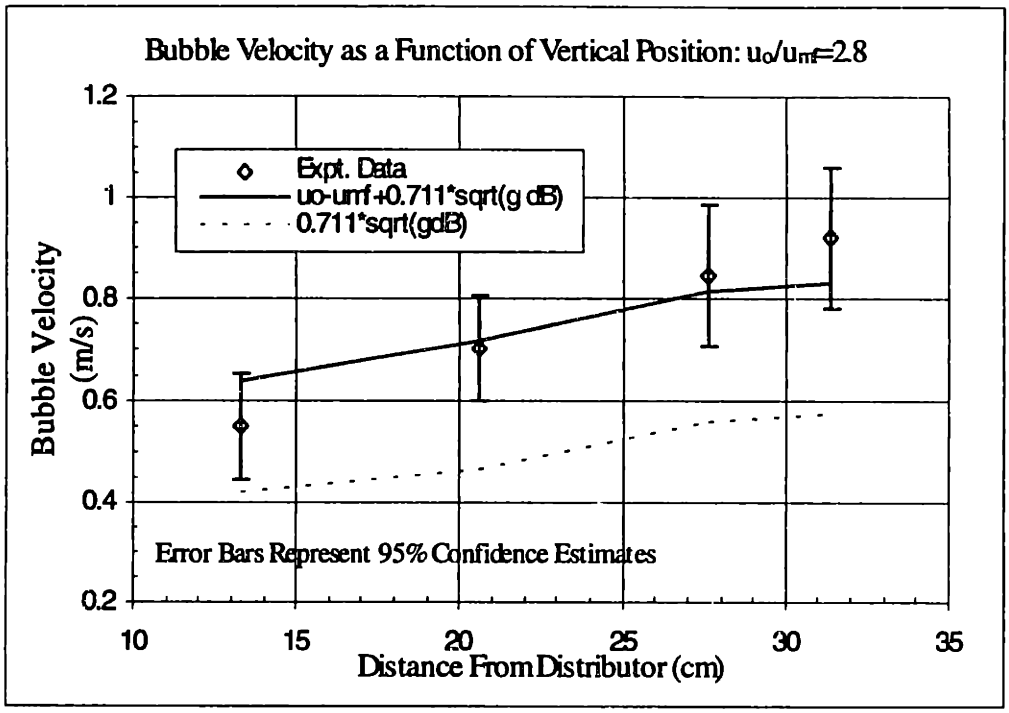

Figure 20: Bubble Velocity as a Function of Vertical Position: u_o/u_{mf}=2.8

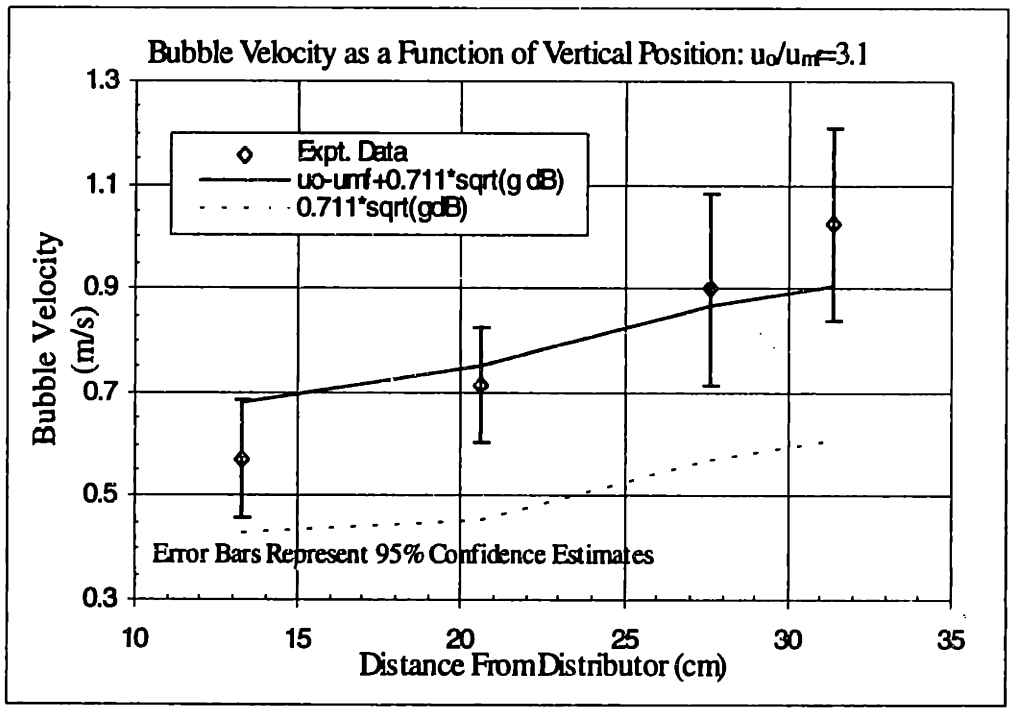

Figure 21: Bubble Velocity as a Function of Vertical Position: u_o/u_{mf}=3.1

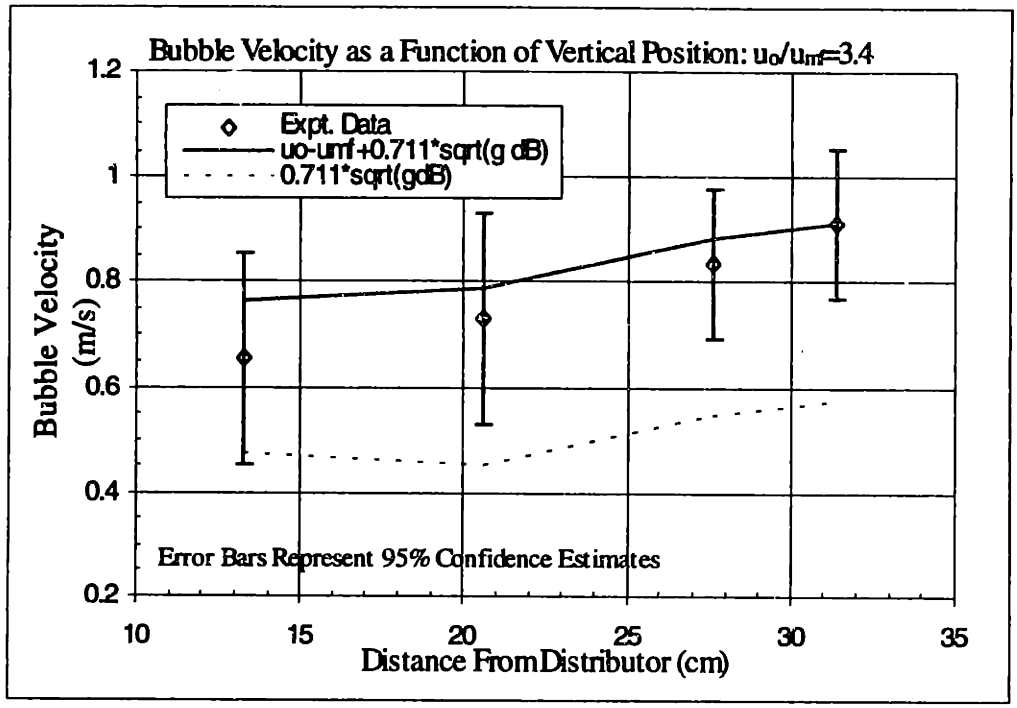

Figure 22: Bubble Velocity as a Function of Vertical Position: u_o/u_{mf}=3.4

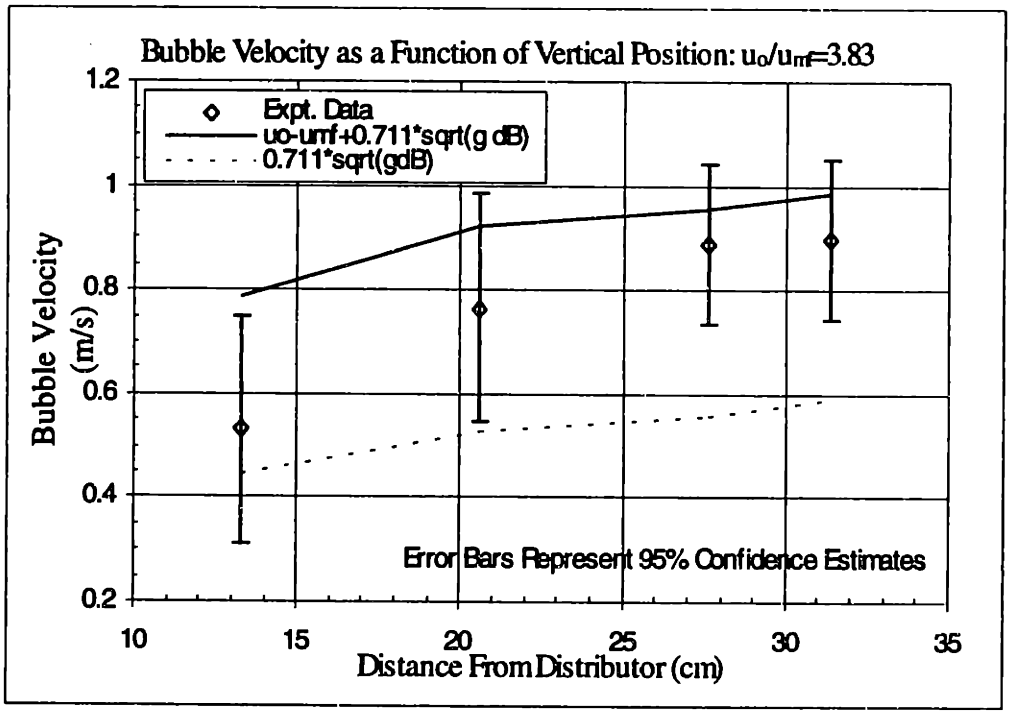

Figure 23: Bubble Velocity as a Function of Vertical Position: u_o/u_{mf}=3.83

7.4.2 Bubble Mean Pierced Length, $\bar{l}_b$

Figure 24 presents the mean pierced length data, for all five test conditions, as a function of elevation above the distributor. The vertical dashed line represents location of the bottom of the tube bank. A single error bar, representing 95% confidence limits, is shown on the plot to provide an estimate of the uncertainty in the data. Figure 24 shows that the bubbles appear to grow as they rise through the bed. It is also possible that the bubbles deform as they rise through the tube bank giving them a larger mean pierced length without an actual increase in bubble volume. As mentioned in Section 7.4.1, the largest bubbles, which correspond to u_o/u_{mf}=3.1, have the highest rise velocity. The presence of tubes in the bed tend to limit bubble growth, producing bubbles whose size is proportional to the tube spacing. The bubble size measured in the cold model is closely related to the spacing between the tubes. As with the bubble rise velocity, the bubble size measurements do not show a strong dependence on u_o/u_{mf}.

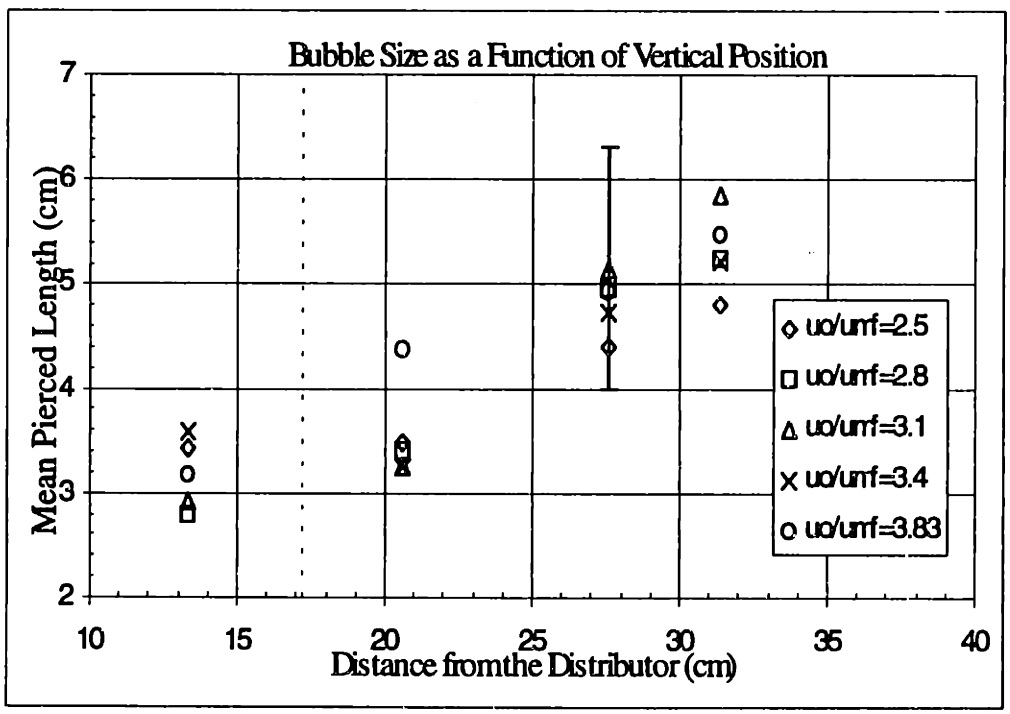

Figure 24: Bubble Size Measurements as a Function of Position in the Bed

Figure 25 is a plot of bubble rise velocity versus bubble diameter. According to (32), the bubble velocity should depend on the bubble diameter to the one-half power (i.e., $u_b - (u_o - u_{mf}) \propto \sqrt{d_b}$). The bubble velocity minus the excess gas velocity (u_b-(u_o-u_{mf})) is plotted on the ordinate of Figure 25 to evaluate the dependence of u_b on d_b for all five test conditions. Figure 25 also includes the dependence predicted by (32). The data exhibit the expected dependence on bubble diameter, within a rather large uncertainty band, lending support to the use of (32) to predict bubble velocity in PFBCs.

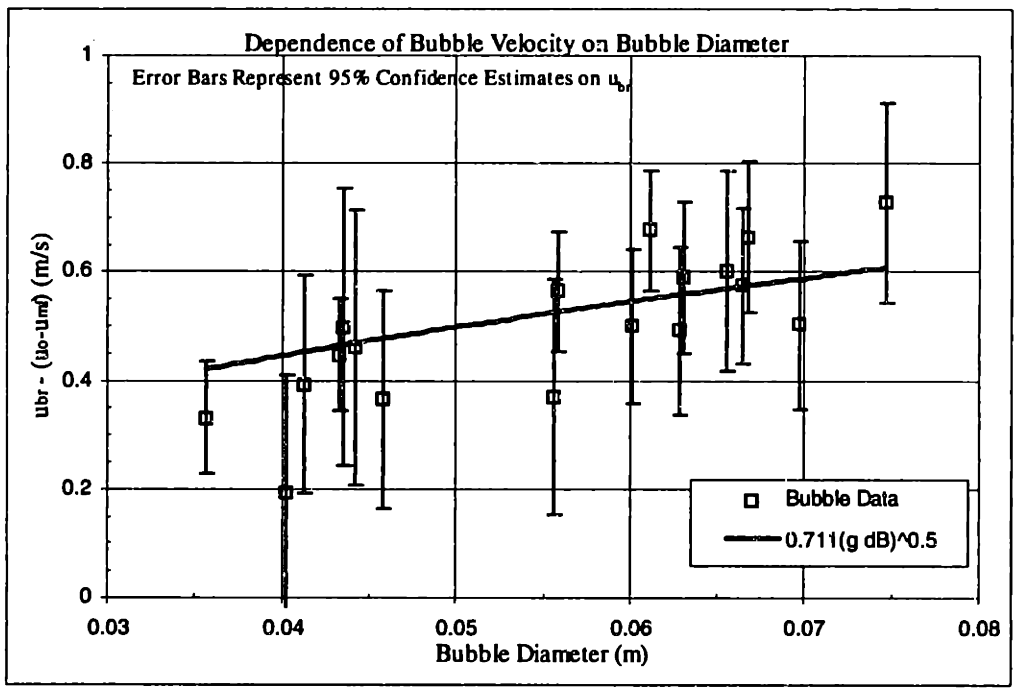

Figure 25: Dependence of Bubble Velocity on Bubble Diameter

Although (32) provides reasonable predictions of the bubble velocity as a function of bubble size, as mentioned in Section 7.4.1, the data do not show the same dependence on excess gas velocity (u_o-u_{mf}) as (32). This is apparent in Figure 26. Equation (32) suggests that the bubble rise velocity should increase with increasing u_o-u_{mf}, but as shown in Figure 26, the data show no dependence on excess gas velocity. Interestingly, the single-bubble

rise velocity expression ($u_b = 0.711\sqrt{g d_b}$), as shown in Figure 26, differs from the data by roughly a fixed amount.

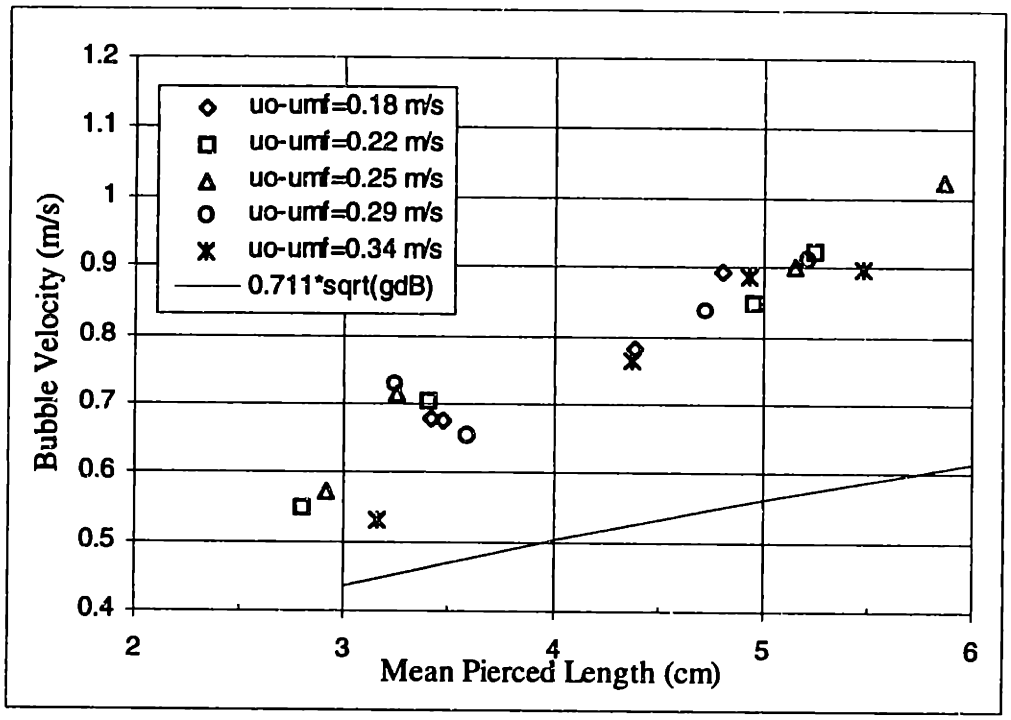

Figure 26: Dependence of Bubble Rise Velocity on Bubble Size

Figures 27-31 present the mean pierced length data as a function of distance from the distributor for each individual u_o/u_{mf} test condition. The figures include 95% confidence levels on the data. The details of the uncertainty analysis performed to arrive at these error estimates are described in Appendix J.

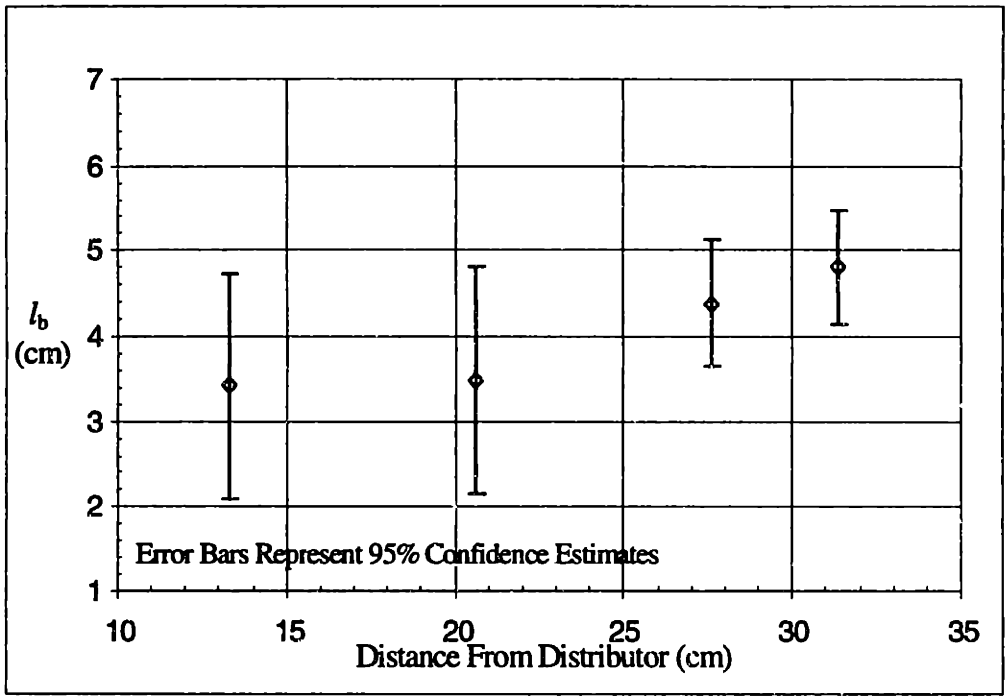

Figure 27: Bubble Size as a Function of Vertical Position: u_o/u_{mf}=2.5

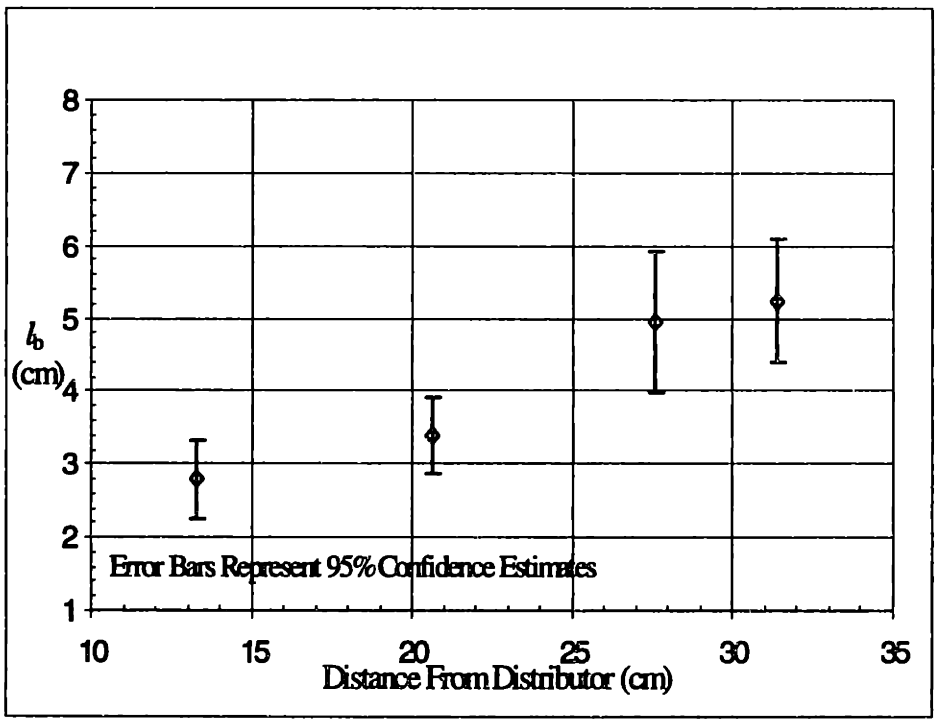

Figure 28: Bubble Size as a Function of Vertical Position: u_o/u_{mf}=2.8

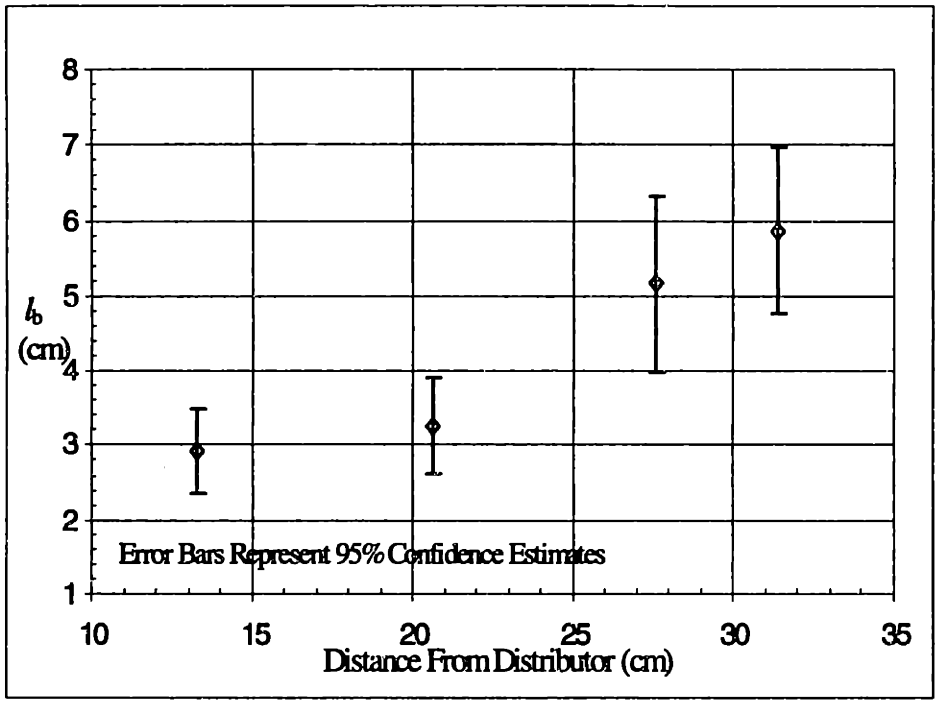

Figure 29: Bubble Size as a Function of Vertical Position: u_o/u_{mf}=3.1

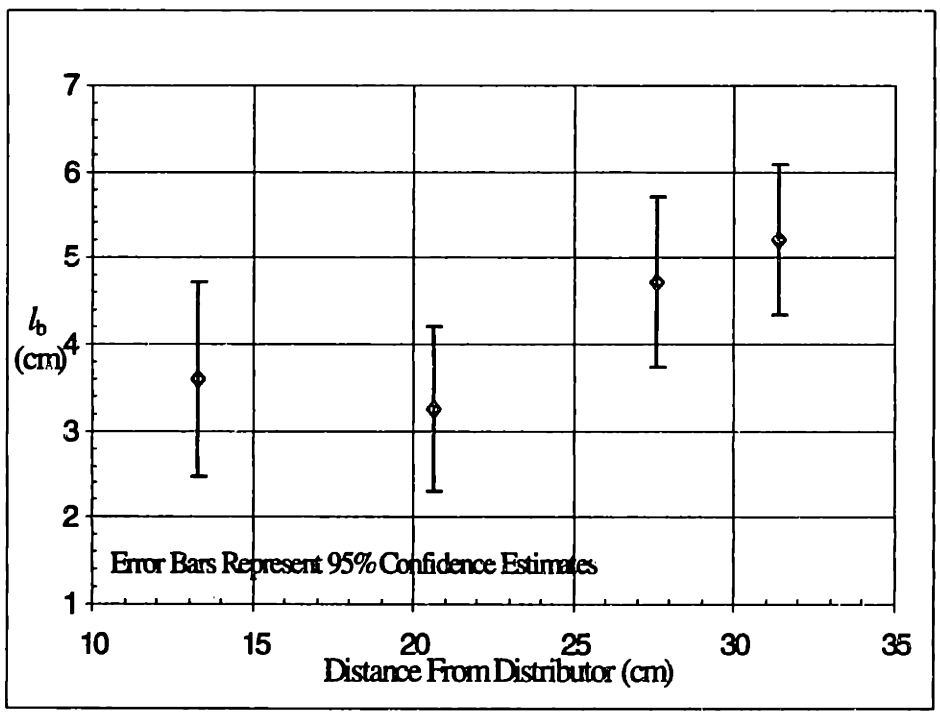

Figure 30: Bubble Size as a Function of Vertical Position: u_o/u_{mf}=3.4

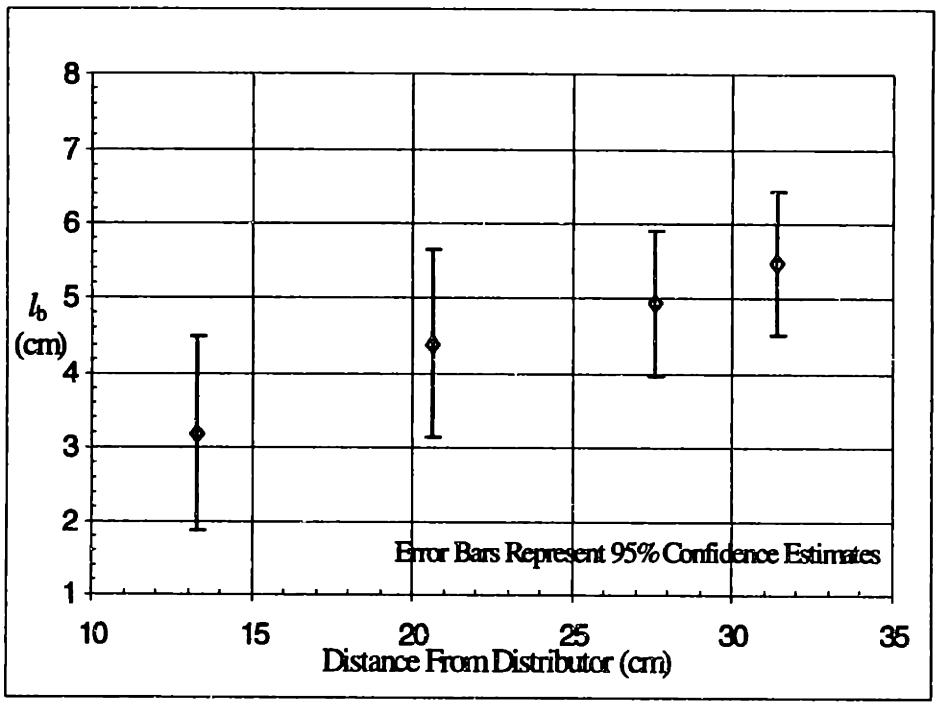

Figure 31: Bubble Size as a Function of Vertical Position: u_o/u_{mf}=3.83

7.4.3 Bubble Frequency, f_b

Figure 32 presents the bubble frequency data, for all five test conditions, as a function of elevation above the distributor. The vertical dashed line represents location of the bottom of the tube bank. A single error bar, representing 95% confidence limits, is shown on the plot to provide an estimate of the uncertainty in the data.

In contrast to the bubble velocity and bubble size data, the bubble frequency shows a strong dependence on u_o/u_{mf}. Vertically aligned chains of bubbles can produce very high local gas flows when the bubbles erupt at the bed surface. This gas through-flow reduces the number of bubbles required to carry the gas through the bed. The existence of bubble chains was evaluated by considering the cross-correlation coefficient of adjacent probe outputs at a time lag of 0. If bubbles were simultaneously present at both probes, the correlation of the two signals at zero time lag would be high. The data were found to

have no significant correlation at zero time lag. This suggests that bubble chains are not present in the bed, thus requiring an increasing number of bubbles to accommodate increasing excess gas velocities. This explains the strong dependence of the measured bubble frequencies on the gas superficial velocity. Gas through-flow is discussed further in Section 7.5.

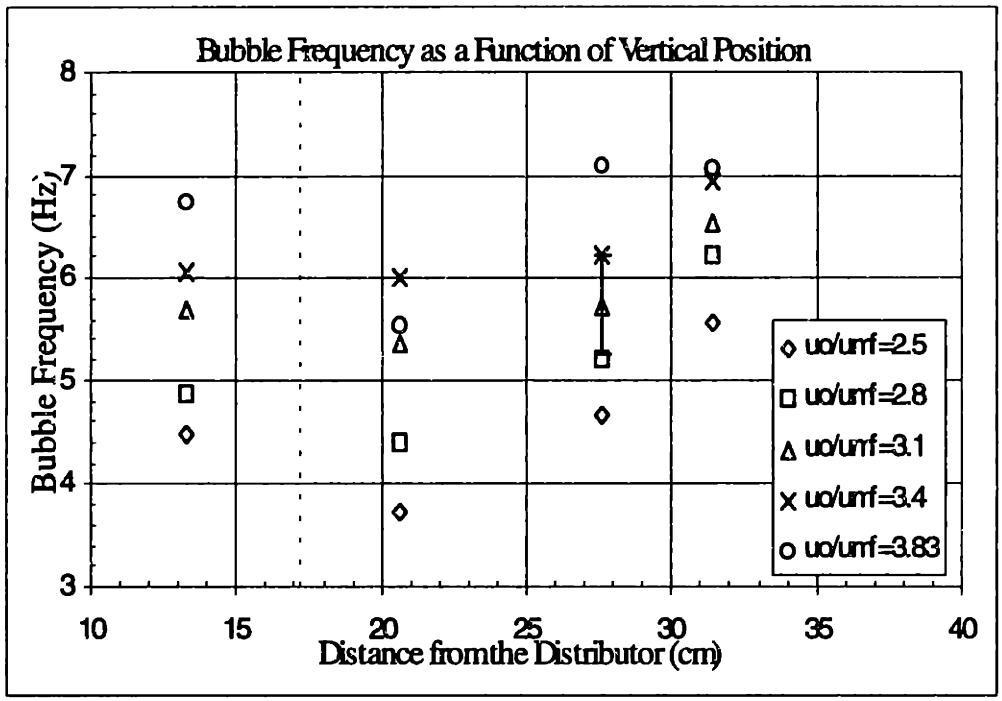

Figure 32: Bubble Frequency Measurements as a Function of Position in the Bed

The bubble mean pierced length increases with elevation from the distributor (see Figure 24). Assuming this implies that the bubbles grow due to coalescence, one would expect the bubble frequency to decrease in the upper portion of the bed. The bubble frequency data shown in Figure 32 do not exhibit this behavior. The dependence of the bubble frequency with height is similar to that of the bubble fraction (Appendix G), which is based on voidage estimates from pressure drop measurements. And the shape of the voidage profile was shown to be similar to the Tidd PFBC in Chapter 4. One possible explanation is that the bubbles coalesce in the bottom of the bed below the tube bank causing the initial reduction in f_b. But once the bubbles enter the tube bank, they split and deform due to the

tight tube spacing. This would produce bubbles with a higher height-to-width aspect ratio, giving them a larger mean pierced length with a smaller bubble volume. This would produce an increased bubble frequency in the top of the bed.

Figures 33-37 present the bubble frequency data as a function of distance from the distributor for each individual u_o/u_{mf} test condition. The figures include 95% confidence levels on the data. The details of the uncertainty analysis performed to arrive at these error estimates are described in Appendix J.

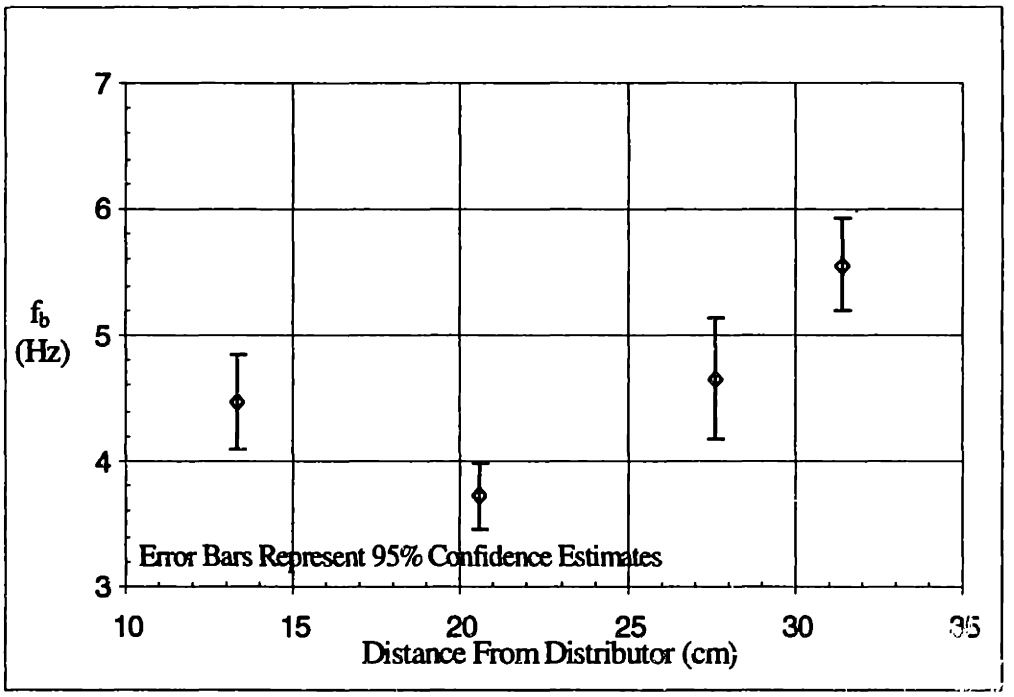

Figure 33: Bubble Frequency as a Function of Vertical Position: u_o/u_{mf}=2.5

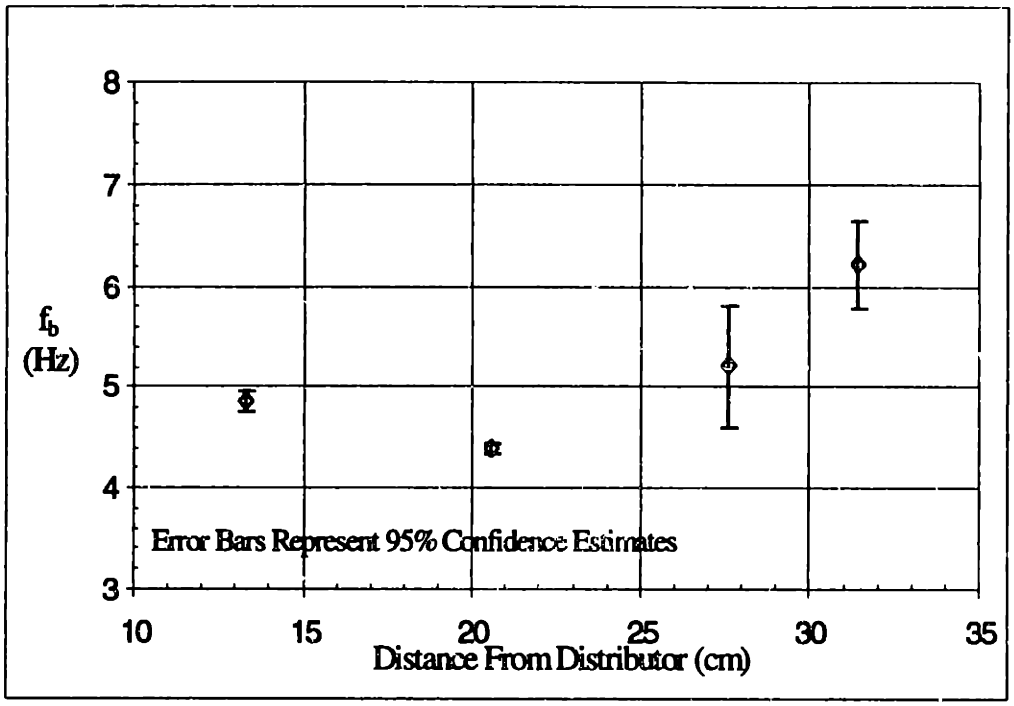

Figure 34: Bubble Frequency as a Function of Vertical Position: $u_o/u_{mf}=2.8$

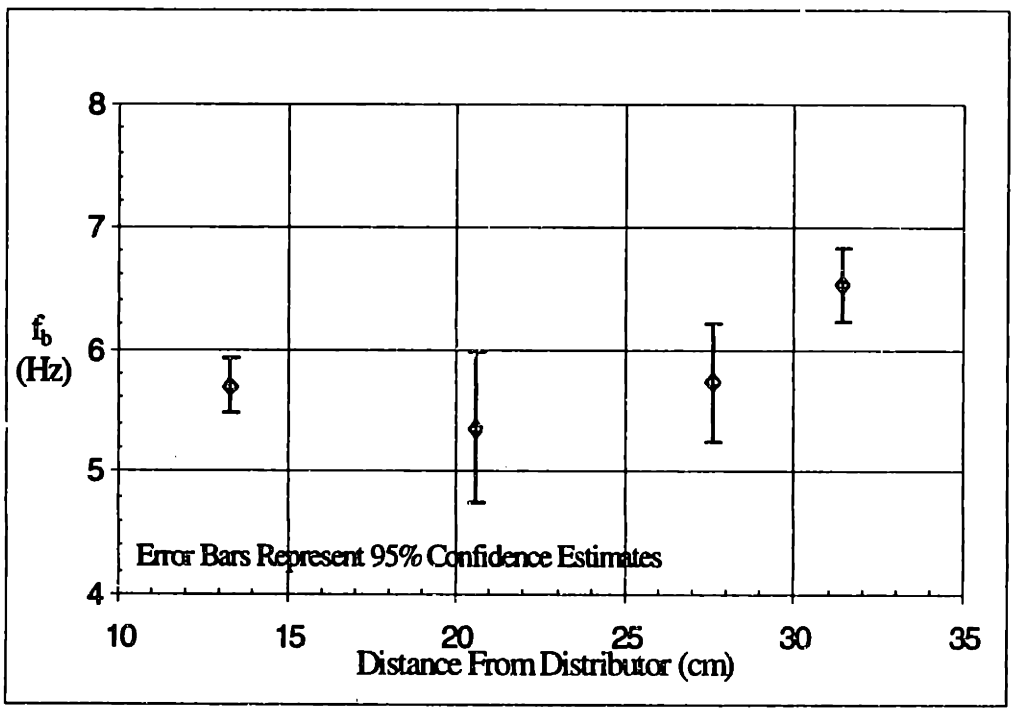

Figure 35: Bubble Frequency as a Function of Vertical Position: $u_o/u_{mf}=3.1$

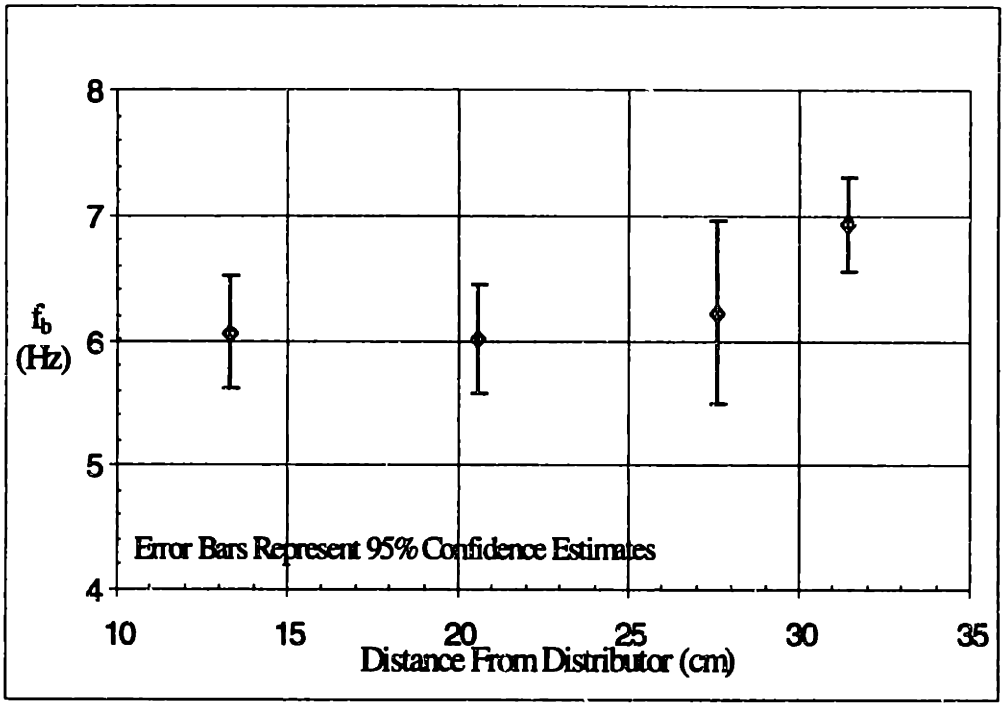

Figure 36: Bubble Frequency as a Function of Vertical Position: u_o/u_{mf}=3.4

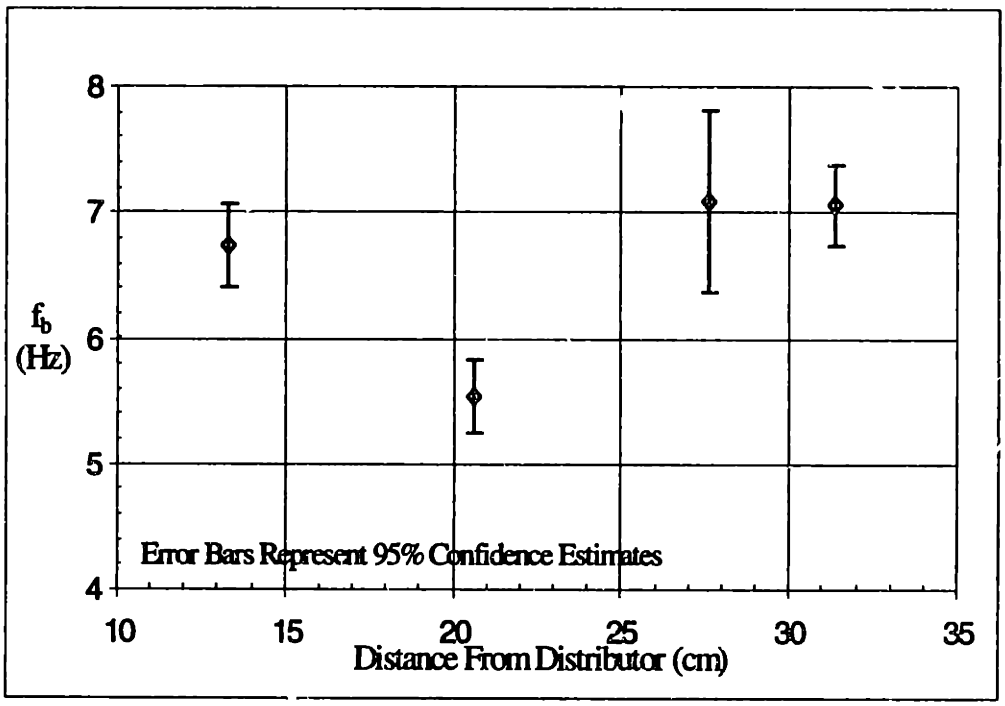

Figure 37: Bubble Frequency as a Function of Vertical Position: u_o/u_{mf}=3.83

7.4.4 Sensitivity of Bubble Probe Results to Threshold

The idealization inherent in the model used to derive (18) introduces some uncertainty in the bubble fractions calculated from the pressure-drop measurements. Since these measurements set the threshold that forms the basis for interpreting the optical probe output, it is important to understand how sensitive the bubble probe results are to the estimated bubble fractions.

The sensitivity of the bubble probe results to the bubble fraction estimate was evaluated for a representative sample of the data. The mean pierced length (l_b) and the bubble frequency (f_b) are the two measurements that depend on value of the bubble fraction. The threshold illustrated in Figure 13 was adjusted to provide a 10% higher local bubble fraction (δ). The effect of this change in δ on five l_b and f_b measurements was then evaluated. One point was chosen from each of the five u_o/u_{mf} test conditions, and all four probe elevations (z) are represented in the sample. The bubble fraction was increased by 10% to raise the threshold, illustrated in Figure 13, to a higher solid fraction. This causes the smaller amplitude fluctuations in the probe output to contribute to the number of bubbles measured (N_b) and the mean bubble duration time ($\overline{b}$). The results of the sensitivity study are summarized in Table 4.

Table 4: Sensitivity of Bubble Characteristics to a 10% Increase in Bubble Threshold

u_o/u_{mf}	z_p (cm)	$l_b(\delta)$ (cm)	$l_b(1.1\cdot\delta)$ (cm)	$l_b(\delta)$ / $l_b(1.1\cdot\delta)$	$f_b(\delta)$ (Hz)	$f_b(1.1\cdot\delta)$ (Hz)	$f_b(\delta)$ / $f_b(1.1\cdot\delta)$
2.5	31.4	4.80	4.91	0.98	5.56	5.93	0.94
2.8	27.6	4.96	4.80	1.03	5.21	5.91	0.88
3.1	13.3	2.91	3.00	0.97	5.70	6.09	0.94
3.4	20.6	3.25	3.42	0.95	6.02	6.43	0.94
3.83	20.6	4.37	4.58	0.95	5.54	5.76	0.96

Table 4 gives the values of the mean pierced length (l_b) and bubble frequency (f_b) based on a threshold set to match the true bubble fraction estimate (δ) and a 10% higher bubble fraction (i.e., $1.1 \cdot \delta$). The mean pierced length is less sensitive than the bubble frequency to the value of the bubble fraction. The largest effect on the mean pierced length was 5%. The largest change in the bubble frequency is 12%, but four of the five points experience a change of 6% or less. Based on the results of this study, it does not appear that the bubble probe results are excessively sensitive to the bubble fraction estimate.

7.5 Gas Flow Balance and Prediction of Bed Expansion

The gas flow through a fluidized bed is typically divided into three components: the flow through the particle emulsion, the visible bubble flow, and the gas flow through the bubble (Valenzuela and Glicksman, 1985). Mass conservation requires that

$$u_o = (1-\delta)u_e + Q''_b + \delta u_{tf}, \tag{33}$$

where:

u_e=superficial gas velocity through the particle emulsion,

Q''_b=visible bubble flow rate per unit cross-sectional area, and

u_{tf}=superficial gas through-flow velocity.

Typically, u_e is assumed to be equal to u_{mf}, and the gas through-flow is accounted for in terms of a through-flow coefficient, K, where K is defined as

$$K \equiv \frac{u_o - Q''_b}{u_{mf}}. \tag{34}$$

Substituting (34) into (33), assuming $u_e=u_{mf}$, and solving for u_{tf} gives

$$u_{tf} = \left(\frac{K-1+\delta}{\delta}\right) u_{mf}. \tag{35}$$

K=1 (i.e., $u_{tf}=u_{mf}$) corresponds to Toomey and Johnstone's (1952) original two-phase theory of fluidization, which assumes that all of the gas flow in excess of that required to fluidize the bed (i.e., $(u_o-u_{mf})A_{xs}$) passes through the bed in the form of bubbles. Alternatively, Davidson's (1961) model for an isolated bubble rising in an infinite bed

predicts that $u_{tf}=3u_e$, which assuming $u_e=u_{mf}$ corresponds to $K=1+2\delta$. More recently, Glicksman et al. (1991) proposed an expression for K that accounted for the low-resistance path for the gas flow that exists when large bubbles erupt at the surface of the bed.

The visible bubble flow (Q''_b) can be calculated using

$$Q''_b = \delta u_b , \tag{36}$$

such that (34) can be rewritten in the form

$$K = \frac{u_o - \delta u_b}{u_{mf}} . \tag{37}$$

Equation (37) implies that K can be estimated from experimental measurements of: u_o, δ, u_b, and u_{mf}. But Ks determined based on (37) are sensitive to the uncertainty associated with the assumption that $u_e=u_{mf}$, the associated uncertainty in the value of u_{mf}, along with the considerable uncertainty associated with measurements of δ and u_b. Hence, it is difficult to accurately estimate K based on experimental measurements. The uncertainty in K can be calculated by evaluating how the uncertainty in each of these measurements propagates. Using the approach presented by Beckwith et al. (1993), the uncertainty in K (U_k) is given by

$$U_k = \sqrt{\left(\frac{\partial K}{\partial u_o}U_{u_o}\right)^2 + \left(\frac{\partial K}{\partial \delta}U_\delta\right)^2 + \left(\frac{\partial K}{\partial u_b}U_{u_b}\right)^2 + \left(\frac{\partial K}{\partial u_{mf}}U_{u_{mf}}\right)^2} . \tag{38}$$

Evaluating (38) by differentiating (37) gives

$$U_k = \sqrt{\left(\frac{1}{u_{mf}}U_{u_o}\right)^2 + \left(-\frac{u_b}{u_{mf}}U_\delta\right)^2 + \left(-\frac{\delta}{u_{mf}}U_{u_b}\right)^2 + \left(-\frac{(u_o-\delta u_b)}{u_{mf}^2}U_{u_{mf}}\right)^2} . \tag{39}$$

As an example, consider the u_o/u_{mf} test condition where u_o=0.46 m/s, u_{mf}=0.12 m/s, u_b≈0.9 m/s, and $\bar{\delta}$ =0.39. If it is assumed that there is 5% uncertainty in u_o and 20% uncertainty in δ, u_b, and u_{mf}, which are reasonable assumptions, (39) gives that the uncertainty in K is 0.87. The bed average through-flow coefficient for this case is approximately 1.35, which corresponds to 64% uncertainty in K. The error in each of the quantities propagates, producing significant variability in the estimates of K from the optical probe data

presented in this chapter. Estimates of the local values of K for the five u_o/u_{mf} tested range from approximately 0 to 2.

If the four local "measured" Ks are averaged by integrating over the bed height, for a particular value of u_o/u_{mf}, these bed average through-flow coefficients are more well-behaved. Figure 38 is a plot of these average through-flow coefficients as a function of u_o/u_{mf}. The through-flow coefficients predicted by Davidson's (1961) isolated bubble model (i.e., $K=1+2\delta$) are included on the plot for comparison; K was evaluated using overall bed average bubble fractions ($\bar{\delta}$ given in Appendix H). The plot shows that the through-flow coefficients increase with increasing u_o/u_{mf}. Higher bubble fractions were observed in the cold model for higher u_o, which increases the opportunity for the gas to bypass the bed. It also seems reasonable to anticipate that the bubbles would tend to take on more ellipsoidal shapes as u_o is increased. Grace and Harrison (1969) showed that, theoretically, the bubble through-flow velocity increases with increasing bubble height-to-width aspect ratio. The values of the through-flow coefficients suggest that Toomey and Johnstone's (1952) two-phase theory of fluidization may be useful for analyzing the gas flow in PFBCs since K is close to 1. Glicksman et al. (1991) show that the two-phase theory overpredicts the bed expansion (i.e., underpredicts K) for atmospheric fluidized beds. But atmospheric fluidized bed combustors (AFBC) have shallower beds and sparser tube banks (larger bubbles) than PFBCs. This permits large amounts of gas to bypass the bed in the form of flow through the bubbles as they erupt at the bed surface. PFBCs, due to their high power densities and modest $\Delta p_{bed}/p_{bed}$, have deeper beds and tight tube banks. Their tighter tube banks keep bubbles small, reducing the gas through-flow.

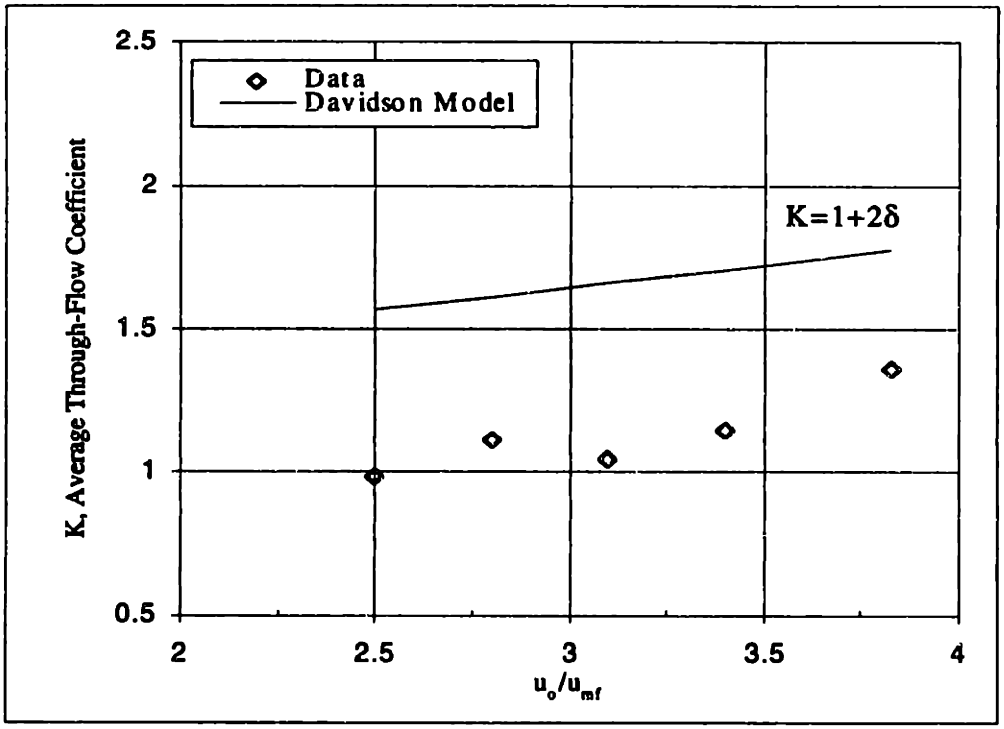

Figure 38: Bed Average Through-Flow Coefficient as a Function of u_o/u_{mf}

Bed expansion is closely related to the gas through-flow. Higher gas through-flow rates produce lower bed expansion since the bed has to expand less to accommodate the excess air flow. To evaluate the potential for using K=1 to analyze PFBC hydrodynamics, the measured bed expansions were compared against those predicted by the model of Glicksman et al. (1991) using K=1. The model requires an assumption for the bubble diameter in the tube bank. Based on the optical probe measurements, a value of 5.5 cm was assumed. Also, (24) was used, assuming H/H_{mb} was equivalent to H/H_{mf}, to calculate the expansion ratio (H/H_{mf}) since it accounts for the presence of the tubes. Figure 39 compares the dimensionless bed expansion measurements versus u_o/u_{mf} against predictions from Glicksman et al.'s (1991) bed expansion model assuming K=1. The agreement between the model and the data is very good, providing support for using K=1 to analyze PFBC hydrodynamics.

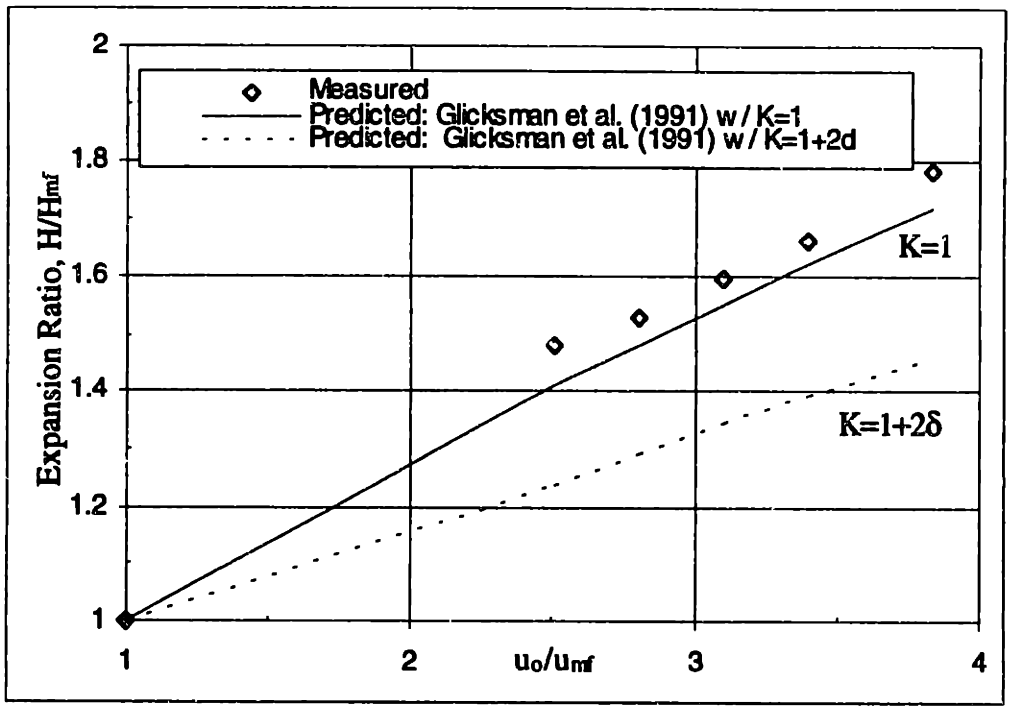

Figure 39: Comparison of Predicted and Experimental Expanded Bed Heights

7.6 Comparison of Data With Bubble Growth Models

Glicksman and McAndrews (1985) showed that bubbles are distributed uniformly across the cross-section of large-particle fluidized beds with horizontal tube banks. This uniformity permits the use of a one-dimensional bubble coalescence model, which is necessary to predict bubble growth. Glicksman et al. (1987) relate the bubble frequency to the coalescence rate using

$$\frac{d(f_b/A)}{dz} = -\frac{1}{2}\frac{(f_b/A)}{\Delta z_c}, \tag{40}$$

which states that if every bubble participates in one coalescence over a distance Δz_c–the average distance a bubble rises between coalescences–the number of bubbles will be halved. Nondimensionalizing (40) gives

$$-\frac{d_b}{(f_b/A)}\cdot\frac{d(f_b/A)}{dz} = \frac{d_b}{2\cdot\Delta z_c} = C(\delta). \tag{41}$$

$C(\delta)$ represents the dimensionless bubble coalescence rate, which has been found to be a function of the bubble fraction (δ). Several models have been proposed for $C(\delta)$. Using the Clift and Grace (1970) model, which has been found to be more appropriate for small particles, and assuming that the bubbles are distributed in a uniform cubic array (Glicksman et al., 1987) gives

$$C(\delta) \approx \frac{1}{2}\left(\frac{6}{\pi}\delta\right)^{1/3}. \tag{42}$$

Glicksman et al. (1987) found that (42) underpredicted the coalescence rate in large-particle beds under conditions representative of atmospheric fluidized beds. They proposed a statistical model whose results were closely approximated by

$$C(\delta) = 12(\delta)^{5/4}. \tag{43}$$

The coalescence models given by (42) and (43) can be used to compare predicted bubble growth against the bubble-size measurements made beneath the tube bank. Although, in order to evaluate $d_b(z)$ using (41), an expression for (f_b/A) as a function of d_b is necessary. The bubble frequency per unit area is related to the visible bubble flow (Q''_b) through

$$Q''_b = (f_b/A)\cdot V_{bub}, \tag{44}$$

where V_{bub} is the bubble volume. Assuming that the bubbles are spherical, substituting (44) into (34), and solving for (f_b/A) gives

$$\frac{f_b}{A} = \frac{u_o - K\cdot u_{mf}}{\frac{\pi}{6}d_b^3}. \tag{45}$$

In addition, since (42) and (43) are a function of the bubble fraction (δ), an expression for the dependence of the bubble fraction on the bubble diameter is also necessary. Substituting (32) into (37) and then solving for δ gives

$$\delta = \frac{u_o - K u_{mf}}{u_o - u_{mf} + 0.71\sqrt{g d_b}}. \tag{46}$$

Substituting (45) into (41) and integrating gives the following expression for calculating the bubble growth, $d_b(z)$;

$$\int_{d_{b_o}}^{d_b(z)} \frac{3}{C(\delta(d_b))} d(d_b) = \int_0^z dz \,. \tag{47}$$

d_{b_o} is the bubble size at the distributor (i.e., z=0); Glicksman et al. (1991) recommend

$$d_{b_o} = 3.69 \frac{(u_o - K u_{mf})^2}{g} \tag{48}$$

for the case where the predicted initial bubble size exceeds the average distributor orifice spacing. Hence, $d_b(z)$ can be calculated, in this case numerically, using (47) and either (42) or (43) in conjuction with (46) and (48).

Figure 40 presents a comparison of the measured and predicted bubble size 13.3 cm above the distributor over a range of u_o/u_{mf}. Both the Clift and Grace (1970) (Eqn. (42)) and Glicksman et al. (1987) (Eqn. (43)) coalescence models are compared against the bubble-size measurements. Based on the results presented in Figure 39, a through-flow coefficient (K) of unity was used in the bubble-growth calculations. As shown in the figure, the Glicksman et al. (1987) coalescence model significantly overpredicts the measured bubble growth. In contrast, the Clift and Grace (1970) model does a reasonable job predicting the bubble growth, even though Glicksman et al. (1987) found that it underpredicted bubble growth in large-particle fluidized beds.

The Glicksman et al. (1987) model was developed from data taken with much lower bubble fractions and higher solid-to-gas density ratios than were present in the cold model. These conditions are more representative of atmospheric fluidized bed combustors (AFBC) rather than PFBCs. Hence, the bubble-coalescence model that was found to predict bubble growth under conditions representative of AFBCs overpredicts bubble growth under PFBC conditions. This suggests that bubbles grow more slowly in PFBCs due to either lower coalescence rates or higher bubble splitting rates or some combination of the two. This is consistent with the experimental observations of many researchers on the effects of pressure on bubble size (e.g., see Chan et al., 1987). Yates (1996) recently

published a review article on the effects of temperature and pressure on gas-solid fluidization.

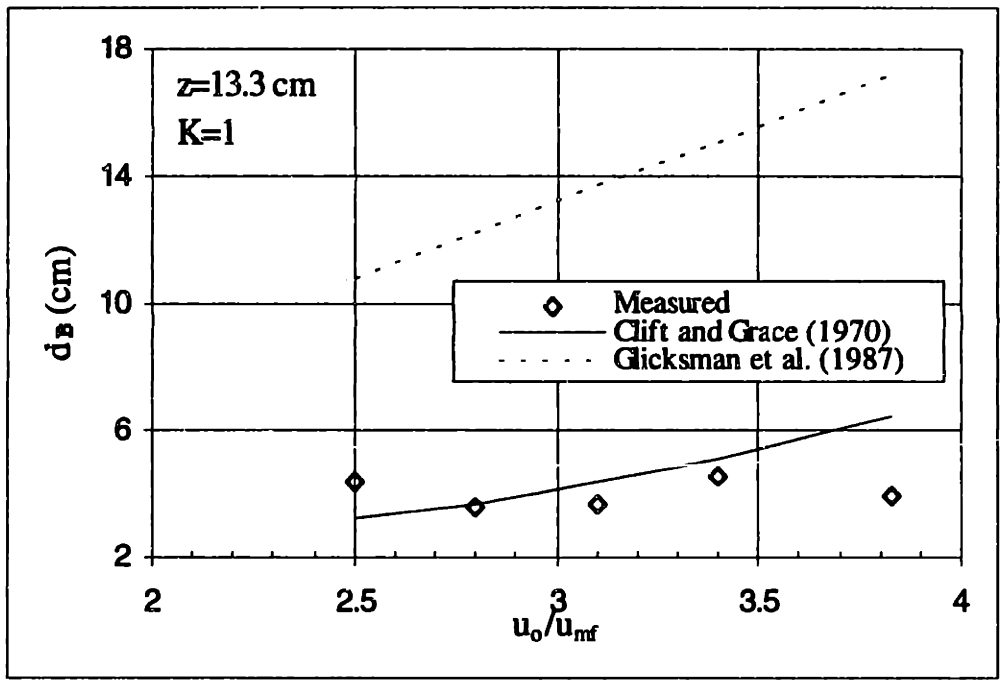

Figure 40: Comparison of Bubble-Size Measurements with Bubble-Growth Models

7.7 Nomenclature

A	optical probe calibration constant
A_{xs}	cross-sectional area
B	optical probe calibration constant
$\bar{b}$	mean time bubble is present at the optical probe
b_i	time bubble i is present the optical probe
$C(\delta)$	dimensionless bubble coalescence rate
d_B	bubble diameter
d_{b_o}	initial bubble size at the distributor
E_e	irradiance
f_b	bubble frequency
f_{sample}	sampling frequency
g	acceleration due to gravity=9.807 m/s^2
H	bed height
H_{lp}	height of bed under loose-packed conditions
H_{mb}	height of bed under minimum-bubbling conditions
H_{open}	height of open region below the tube bank
i_b	phototransistor base current
i_c	phototransistor collector current
i_{LED}	current flowing through the LED
K	through-flow coefficient
l_b	bubble mean pierced length
M	mass collected in optical probe calibration exercise
N	number of samples taken over time T
N_b	number of bubbles detected during time T
p	pressure
p_{bed}	bed pressure
P	power input
p_{fb}	freeboard pressure
Q''_b	visible bubble flowrate
r	lag number
R	LED circuit resistance
R_F	feedback resistor in the phototransistor circuit
$\hat{R}_x(0)$	sample mean square of x
$\hat{R}_y(0)$	sample mean square of y
$R_{xy}(\tau)$	cross-correlation function
t	collection time
T	sample record length
U_δ	uncertainty in δ
U_k	uncertainty in K
U_{ub}	uncertainty in u_b

U_{uo} uncertainty in u_o
U_{umf} uncertainty in u_{mf}
u_b bubble rise velocity
u_e superficial gas velocity through dense particle emulsion
u_{fall} fall velocity of particles in drop-tube apparatus
u_{mf} minimum fluidization velocity
u_o superficial gas velocity
u_{tf} superficial gas through-flow velocity
v_c phototransistor collector voltage
v_{ce} phototransistor collector-emitter voltage=v_c-v_e
v_e phototransistor emitter voltage
v_{LED} voltage drop across the LED
v_{in} input supply voltage
v_{out} output voltage from the phototransistor circuit
v_R voltage drop across LED-circuit resistor
V_{bub} bubble volume
V_{exp} expanded bed volume
V_s volume of solids
V_{tube} volume of tubes between H and H_{mb}
z distance above the distributor
z_p distance of optical probe from the distributor

Greek Symbols

β transistor current gain
δ bubble fraction
$\bar{\delta}$ overall bed bubble fraction
δ_T tube fraction
Δh distance between pressure taps
Δp differential pressure drop
Δp_{bed} pressure drop across the bed
Δt time between samples
Δz_c average distance bubble rises between coalescences
ε voidage
ε_b bubble voidage
ε_e emulsion voidage
ε_{lp} loose-packed voidage
ε_{mf} minimum fluidization voidage
$(1-\varepsilon)$ solid fraction
ρ_b bulk density
ρ_g fluidizing gas density
ρ_s particle solid density
$\hat{\rho}_{xy}$ sample cross-correlation coefficient
τ time lag = $r\Delta t$
τ_b most highly correlated time lag between optical probe output

7.8 References

Beckwith, T.G., Marangoni, R.D., and Lienhard, J.H., 1993, Mechanical Measurements, 5th Edition, Addison-Wesley, Reading, Massachusetts.

Bendat, J.S. and Piersol, A.G., 1986, Random Data - Analysis and Measurement Procedures, 2nd Edition, John Wiley & Sons, New York.

Chan, I.H., Sishtla, C., and Knowlton, T.M., 1987, "The Effect of Pressure on Bubble Parameters in Gas-Fluidized Beds," *Powder Technology*, 53, pp. 217-235.

Davidson, J.F., 1961, *Trans. Inst. Chem. Engrs.* (Great Britain), 39, p. 230.

Davidson, J.F. and Harrison, D., 1963, Fluidised Particles, Cambridge University Press, Cambridge.

Geldart, D. and Kelsey, J.R., 1972, "The Use of Capacitance Probes in Gas Fluidized Beds," *Powder Technology*, 6, pp. 45-50.

Geldart, D., 1973, "Types of Gas Fluidization," *Powder Technology*, 7, pp. 285-292.

Glicksman, L.R. and McAndrews, G., 1985, "Effect of Bed Width on the Hydrodynamics of Large Particle Fluidized Beds," *Powder Technology*, 42, pp. 159-167.

Glicksman, L.R., Lord, W.K., and Sakagami, M., 1987, "Bubble Properties in Large-Particle Fluidized Beds," *Chemical Engineering Science*, 42, 3, pp. 479-491.

Glicksman, L.R., Yule, T., and Dyrness, A., 1991, "Prediction of the Expansion of Fluidized Beds Containing Tubes," *Chemical Engineering Science*, 46, 7, pp. 1561-1571.

Gogolek, P.E.G. and Grace, J.R., 1995, "Fundamental Hydrodynamics Related to Pressurized Fluidized Bed Combustion," *Prog. Energy Combustion Science*, 21, pp. 419-451.

Grace, J.R. and Harrison, D., 1969, "The behavior of freely bubbling fluidized beds," *Chemical Engineering Science*, 24, pp. 497-508.

Horowitz, P. and Hill, W., 1989, The Art of Electronics, 2nd Edition, Cambridge University Press, Cambridge.

Kunii, D. and Levenspiel, O., 1968, "Bubbling Bed Model - Model for the Flow of Gas through a Fluidized Bed," *I&EC Fundamentals*, 7, 3, pp. 446-452.

Mainland, M.E. and Welty, J.R., 1995, "Use of Optical Probes to Characterize Bubble Behavior in Gas-Solid Fluidized Beds," *AIChE Journal*, 41, 2, pp. 223-228.

Morse, R.D. and Ballou, C.O., 1951, "The Uniformity of Fluidization, Its Measurement and Use," *Chemical Engineering Progress*, 47, pp. 199-211.

Riley, C.A. and Louge, M., 1989, "Quantitative Capacitive Measurements of Voidage in Gas-Solid Flows," *Particulate Science and Technology*, 7, pp. 51-59.

Toomey, R.D. and Johnstone, H.F., 1952, "Gaseous Fluidization of Solid Particles," *Chemical Engineering Progress*, 48, 5, pp. 220-226.

Valenzuela, J.A. and Glicksman, L.R., 1985, "Gas Flow Distribution in a Bubbling Fluidized Bed," *Powder Technology*, 44, pp. 103-113.

Werther, J. and Molerus, O., 1973a, "The Local Structure of Gas Fluidized Beds - I. A Statistically Based Measuring System," *International Journal of Multiphase Flow*, 1, pp. 103-122.

Werther, J. and Molerus, O., 1973b, "The Local Structure of Gas Fluidized Beds - II. The Spatial Distribution of Bubbles," *International Journal of Multiphase Flow*, 1, pp. 123-138.

Yasui, G. and Johanson, L.N., 1958, "Characteristics of Gas Pockets in Fluidized Beds," *AIChE Journal*, 4, pp. 445-452.

Yates, J.G., 1996, "Effects of Temperature and Pressure on Gas-Solid Fluidization," *Chemical Engineering Science*, 51, 2, pp. 167-205.

Yates, J.G. and Simons, S.J.R., 1994, "Experimental Methods in Fluidization Research," *International Journal of Multiphase Flow*, 20, Supplement, pp. 297-330.

8. Experimental Setup for Solids Mixing Studies

8.1 Thermal Tracer Technique

The thermal tracer technique involves using thermally-tagged bed particles as a tracer and following their motion by making temperature measurements at many locations in the bed. This technique was first used by Valenzuela (1982) in a two-dimensional bubbling bed, it has subsequently been employed by Westphalen (1993) to study lateral solids mixing in circulating fluidized beds. In both cases, the bed particles were heated to a temperature above the surrounding bed temperature. A similar technique was used by Bellgardt and Werther (1986), except that sublimating dry ice particles, rather than bed particles, were used as a tracer.

In the current study, a thermal tracer technique was used to investigate the solids mixing in the cold-scale model of the Tidd PFBC. In order to match the solid-to-gas density ratio, to satisfy the hydrodynamic scaling relationships, a granular polyethylene plastic was chosen as the cold-model bed material. Due to the low melting temperature of the plastic, it was not possible to heat the particles. Instead, the particles were cooled well below the bed temperature in a bath of liquid nitrogen. This approach, in addition to preserving the integrity of the particles, provides tracer particles with a larger temperature difference between themselves and the bed than was possible in previous studies.

Valenzuela (1982) identified several advantages of the thermal tracer technique over other approaches to studying solids mixing. Some of those advantages are discussed here.

1. The tracer particles are the bed particles, and hence their hydrodynamic behavior will reflect the true solids movement in the bed.
2. Thermal tracers come to thermal equilibrium with the bed within a few minutes after injection. This avoids the problem of elevated tracer background levels, and the need

to separate the tracer and the bed material. This is particularly important in the cold model, where the bed has a large particle inventory that has been carefully customized to scale the dimensionless particle size distribution of the Tidd PFBC. Solids mixing in fluidized beds is a stochastic phenomenon; as found by Fitzgerald et al. (1977), the solids do not mix exactly the same way each time an experiment is conducted. Hence, to properly characterize the mixing, experiments must be repeated many times. Changing the bed inventory between many experiments would require an unacceptable amount of time and effort.

3. The technique provides information on the transient characteristics of the mixing by following the motion of the tracer particles in time. An alternate approach to studying solids mixing is to introduce a tracer into the bed and after fluidizing the bed for a period of time the fluidization air is stopped suddenly. The distribution of the tracer concentration at that point in time is then determined by excavating the bed layer-by-layer. This tedious process would have to be repeated for many fluidization times to evaluate the transient characteristics of the mixing. Also, several measurements should be made for each time to characterize the average mixing behavior at that point in the transient. There is also the opportunity for additional solids motion to occur as the bed slumps.
4. Relatively small thermistor probes can be constructed to minimize their disturbance of the flow.

The one difficulty with the thermal tracer technique is that the temperature distribution measurements provided by the method can only be used to infer a rough estimate of the local tracer concentration.

8.1.1 Thermistor Probes

Thermistors are ceramic semiconductor devices whose resistance rises as their temperature drops (for negative-temperature-coefficient thermistors). Thermometrics

thermistor model AB6B2-GC16KA143L-37C was used in the thermistor probes. These thermistors have a resistance of approximately 30kΩ at 37 ° C. The thermistors were chosen because their small size provides a fast time response. Thermistors were used instead of thermocouples because thermocouples have a small electrical resistance and voltage output. This makes them susceptible to interference from static electricity in the bed and hence, unsuitable for use in this study. The thermistors consist of a 0.4 mm diameter bead sealed in a 2.5 mm long and 0.5 mm diameter cylindrical polyimide sleeve. The thermistor response time is discussed in Section 8.1.1.3.

The thermistor probe design is the same as that used by Westphalen (1993); some of Westphalen's probes were used in this study. Figure 1 illustrates the thermistor probe design. As shown in the figure, a single thermistor was first inserted into 20-gauge tubing and then epoxied into 3.2 mm steel tubing for additional support. A small amount of silicon sealant was used at the thermistor-tubing junction to prevent air and particle leakage. Care was taken to minimize the sealant in contact with the thermistor sleeve to prevent a reduction in response time. The 38-gauge nickel-alloy thermistor leads were run along the inside of the tubing and connected to a terminal block attached to the bottom of the probe. The terminal block served as a convenient, non-permanent way of connecting the thermistor probe to the supporting electrical bridge circuit described in Section 8.1.1.1.

The thermistor probes were installed in the polycarbonate front wall of the cold model. Compression fittings were used to hold the probes in position. Sixteen probes were installed in the cold model; the layout of the thermistor probe array is discussed in Section 8.1.1.4.

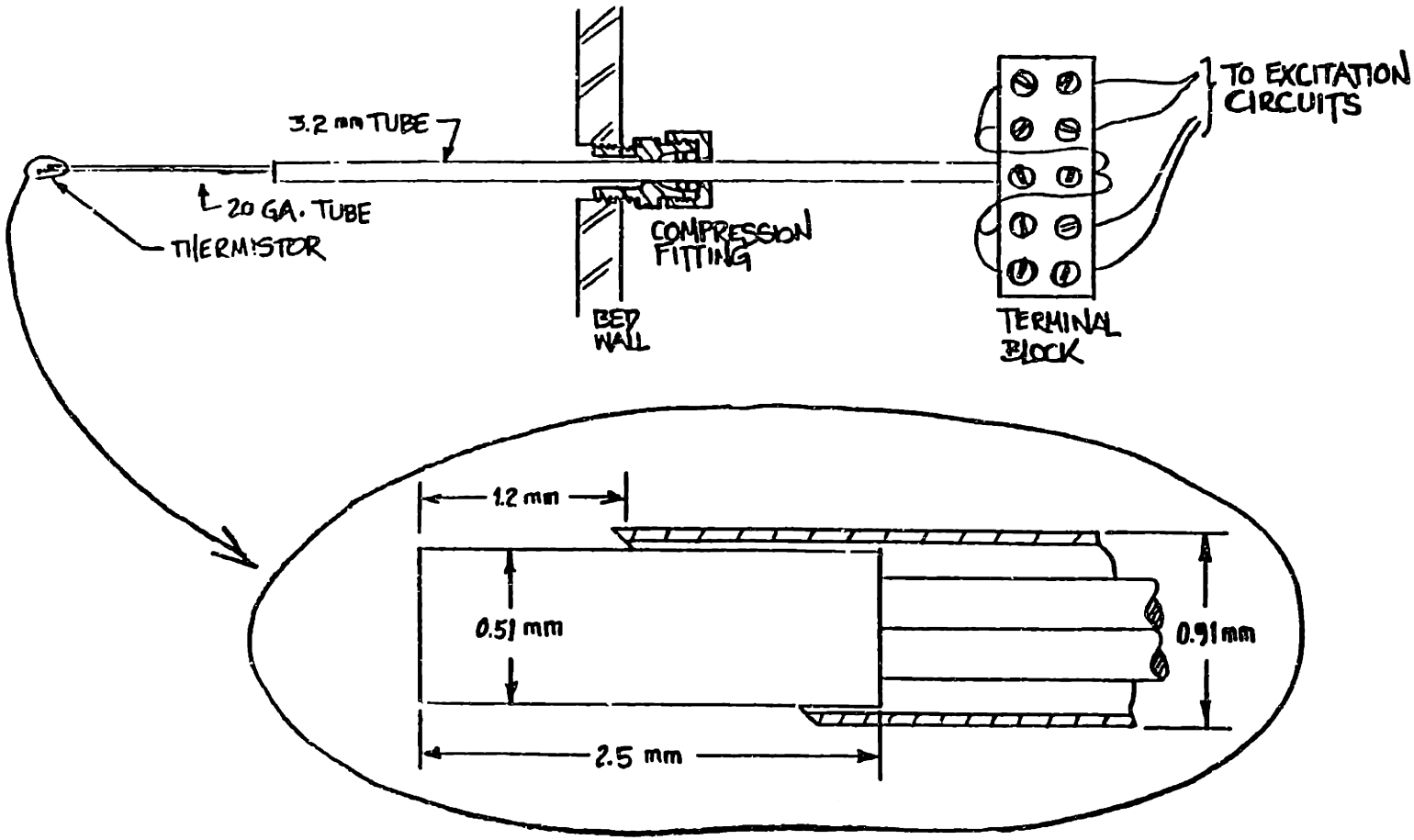

Figure 1: Thermistor Probe Construction [taken from Westphalen, (1993)]

8.1.1.1 Thermistor Circuits

A thermistor is a temperature-sensitive resistor. An external circuit is necessary to convert a thermistor's change in resistance to a voltage, which is a more convenient quantity to measure. The Wheatstone bridge circuit is a common choice for making resistance measurements. Figure 2 illustrates the Wheatstone bridge circuit. R_T represents the thermistor resistance; R_1, R_2, and R_3 are known resistances. The voltage measured by the meter shown in Figure 2 varies as R_T varies. If the meter draws no current, the voltage measured by the meter (e_M) has the following dependence on the resistances and the input voltage (e_{in}) (Beckwith et al., 1993).

$$e_M = e_{in} \cdot \left(\frac{R_2}{R_T + R_2} - \frac{R_3}{R_1 + R_3} \right). \quad (1)$$

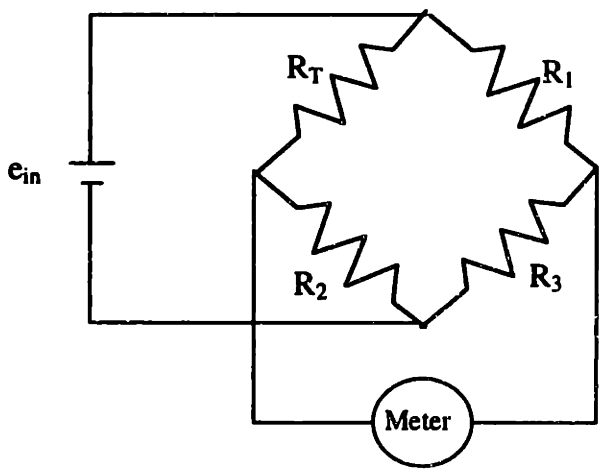

Figure 2: Wheatstone Bridge Circuit

Resistors R_2 and R_3 must be specified to minimize $i^2 R$ heating of the thermistor. Horowitz and Hill (1989) recommend that $i^2 R_T$ be kept below 1 mW to keep readings accurate within 1 °C. R_2 and R_3 were set to be 2.2 MΩ. For $e_{in} \approx 12$ V_{DC} and R_2=2.2 MΩ, the current through the thermistor is approximately 5.5 μA. The thermistors used in this study have a resistance (R_T) of around 30 kΩ at 37 °C. At this resistance, the value of

$i^2 R_T$ is roughly 1 μW, three orders of magnitude below Horowitz and Hill's (1989) recommendation. R_1 was set to be approximately 30 kΩ to be of comparable magnitude to the thermistor resistance.

The one problem with keeping the current through the resistor small is that the voltage drop across the thermistor is small. A differential amplifier was used to amplify the voltage output from the bridge circuit. The amplification circuit is shown in Figure 3. The two leads from the Wheatstone bridge circuit (shown going to the meter in Figure 2) provide the input to the amplification circuit (e_{i1} and e_{i2}). In Figure 3, R_1=R_2 and R_3=R_4. One-percent precision resistors were used to closely match the resistances. This was necessary to achieve a high common-mode rejection ratio. A LF411 operational amplifier (National Semiconductor) was used in the amplification circuit. For R_1=R_2 and R_3=R_4, the output voltage (e_o) is related to the input voltage difference by (Beckwith et al., 1993)

$$e_o = \left(\frac{R_3}{R_1}\right) \cdot (e_{i1} - e_{i2}), \tag{2}$$

where (R_3/R_1) is the amplifier gain. R_1 was set to be 100 kΩ and R_3 was chosen to be 1 MΩ, giving an amplifier gain of 10.

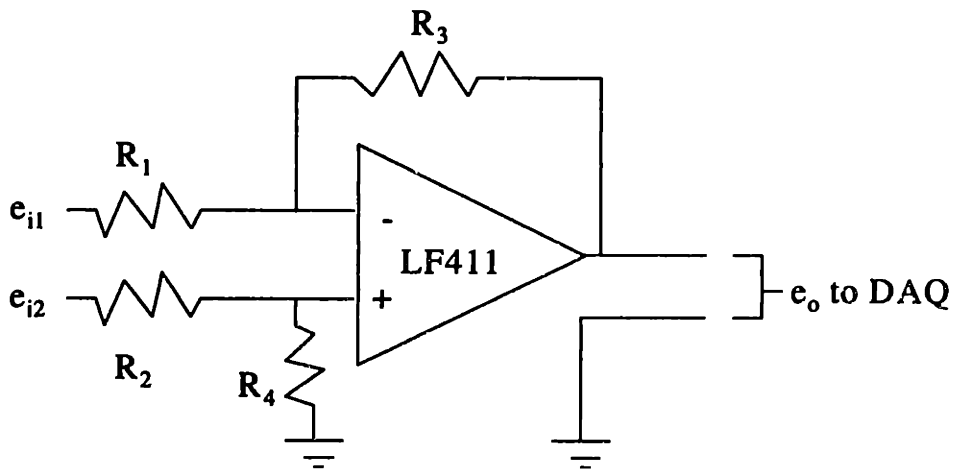

Figure 3: Differential Voltage Amplifier

Beyond amplifying the output from the bridge circuit, the differential amplifier serves two additional purposes. First, it increased the number of thermistor measurements that could be made. The data acquisition board used to record the voltage measurements from the bridge circuits has the capacity to measure up to 8 double-ended inputs or 16 single-ended inputs. The differential amplifier converts the double-ended output from the bridge circuit (voltage difference) to a single-ended output from the amplifier (voltage relative to common). This doubled the number of temperature measurements that could be made. Second, it served to isolate the data acquisition board from any static electricity generated in the bed.

8.1.1.2 Thermistor Calibration

The thermistor probes were calibrated by submersing them in a water bath. The temperature of the bath was measured using a mercury thermometer accurate to 0.1 °C. A temperature versus voltage calibration curve was constructed by varying the water bath temperature. This method was used to calibrate the probes over a temperature range of 5 to 45 °C. This was a sufficient calibration range for all the thermistor probes except thermistor 1; the thermistor positioned at the exit of the injector. The method for expanding the calibration range for thermistor 1 is described later in this section. Over this limited temperature range, a calibration curve of the form:

$$T(e_o) = A \cdot e_o^3 + B \cdot e_o^2 + C \cdot e_o + D \qquad (3)$$

was found to accurately fit the calibration data, where e_o is the output voltage from the thermistor circuit. The values of the calibration constants–A,B,C, and D–are given in Appendix K.

Thermistor 1 was used to identify the time of injection and the temperature of the injected particles. The tracer particles were cooled to roughly 100 °C below their initial temperature, requiring that the calibration of thermistor 1 be extended below 5 °C. The calibration range for thermistor 1 was extended using the setup shown in Figure 4.

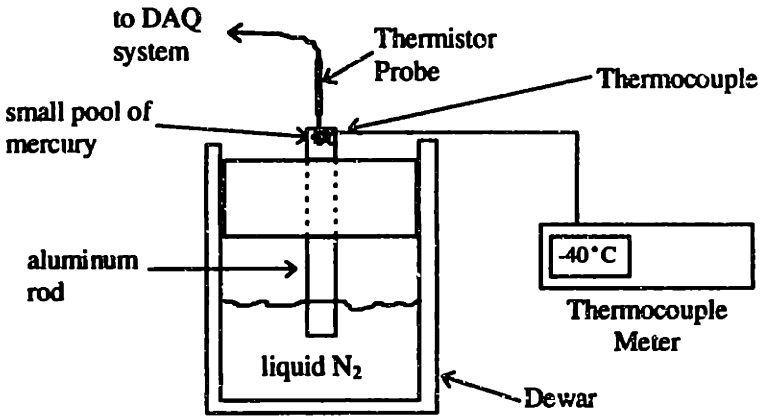

Figure 4: Calibration Setup for T<5 ° C

A small pool of mercury was formed on the hollowed-out end of an aluminum rod. The rod was supported in a piece of foam that fit inside a Dewar flask partially filled with liquid nitrogen. The temperature of the mercury was measured using a thermocouple connected to a thermocouple meter. The calibration for thermistor 1 was extended down to -40 ° C by immersing it in the mercury pool and changing the length of the rod immersed in the liquid nitrogen.

8.1.1.3 Thermistor Probe Time Response

Because of the finite thermal capacitance of the thermistor, a time lag exists between a change in the input to the thermistor and its response to that change. The thermistors used in this study are quite small and for typical heat transfer conditions can be treated as a lumped system (i.e., Bi<0.1). Thermal capacitance is the only a mode of storing energy in a lumped system. Systems with a single mode of energy storage are first-order systems whose time response can be characterized by a time constant, τ.

Westphalen (1993) conducted tests to evaluate the thermistor time constant under heat transfer conditions similar to those found in a circulating fluidized bed. He found that the

measured time constant was approximately 0.4 s. This result was shown to be relatively insensitive to solids flux. The experimental method was evaluated by constructing an analytical model of the thermistor-circuit system. The predicted time constants were consistent with the measured time constants and relatively insensitive to the assumed heat transfer coefficient (predicted time constants varied from approximately 0.3-0.5 s). The small sensitivity of the results to mass flux and heat transfer coefficient suggest that the time constant would not be significantly different under bubbling bed heat transfer conditions.

The time constant represents the amount of time it takes for a step-excited first-order system to proceed 63.2% of the way from its initial to its final state. The change in the temperature of a lumped body originally at a temperature of T_o, in response to a step change in the environment temperature (T_e) after a time τ, is given by (Mills, 1992)

$$\frac{T(\tau)-T_e}{T_o-T_e} = e^{-\frac{t}{\tau}}\Big|_{t=\tau} = 0.368. \qquad (4)$$

With the level of noise in the thermistor circuitry, detectable changes in temperature are limited to around 0.1 ° C. If it is assumed that the thermistor boundary condition changes every time a bubble passes and the maximum bubble frequency is 7 Hz, the thermistor needs to exhibit a detectable change in temperature in approximately 0.14 s (1/7 s). Using (4) with τ=0.4 s, the system will proceed 30% of the way from its initial to its final state in 0.14 s. For $T(0.14)-T_e$=0.1 ° C, T_o-T_e must be 0.14 ° C. Fitzgerald et al. (1977) found that injected tracer tends to remain in a clump. This would slow the rate at which the particles warm to the bed temperature. Considering the heat transfer to a single particle should provide a conservative estimate of the time it takes for the particles to return to the bed temperature. Assuming the particle is initially 100 ° C below the bed temperature, a simple analysis gives that the temperature of the particles remains at least 10 ° C below the bed temperature for over 11 seconds after injection. Particles with such a large temperature difference between themselves and the thermistor should have little difficulty producing a 0.14 ° C change in the thermistor temperature during time scales of interest.

8.1.1.4 Thermistor Array Configuration

Sixteen thermistor probes were installed in compression fittings in the cold model's clear polycarbonate front wall. Figure 5 shows the position of the thermistor probes relative to the bed wall and the distributor. Thermistor number 11 appears twice in the array, both in the row furthest above the distributor (as 11) and near the injector (as 11*). Tests were conducted with the probe in both positions to provide additional information on the mixing within the bed. The thermistor probes were inserted 10 cm into the bed, forming a two-dimensional measurement plane in vertical alignment with the injector.

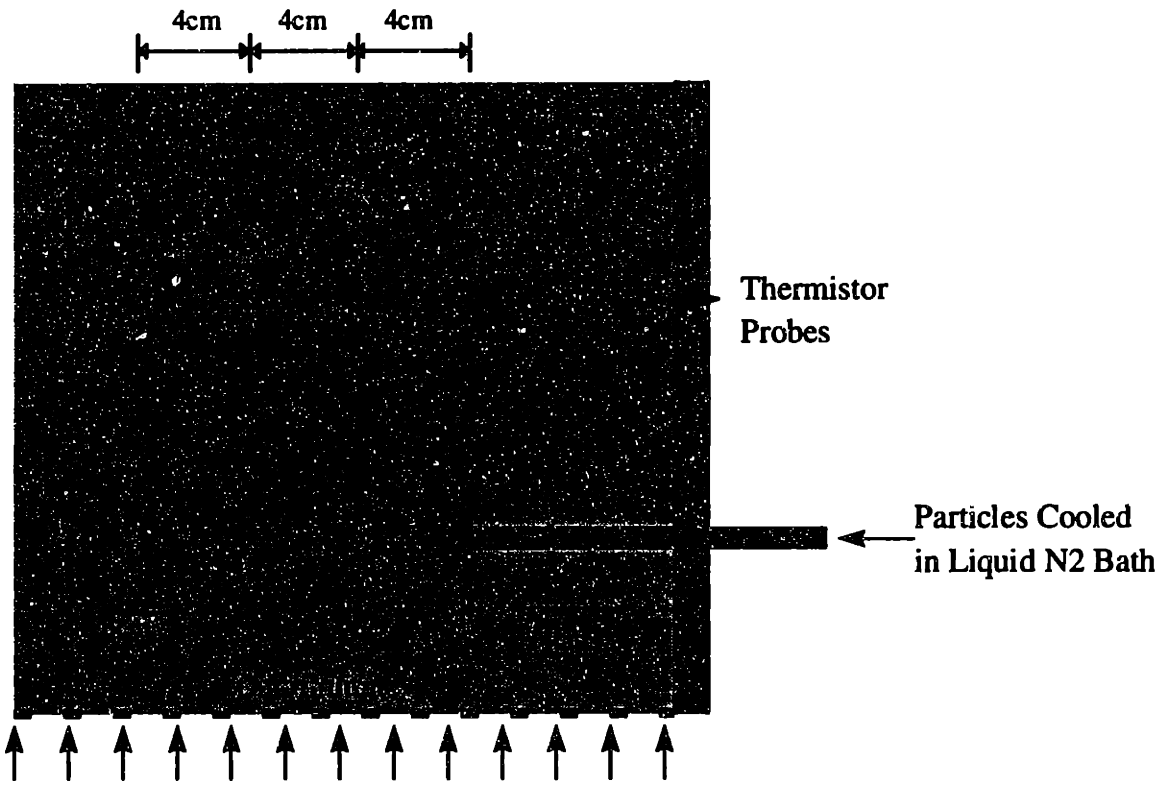

Figure 5: Thermistor Probe Layout

8.1.2 Thermal Tracer Injection

8.1.2.1 Injector Configuration

Figure 6 presents a side view of the tracer injector setup. The injector is positioned 8.5 cm above the distributor and, as shown in Figure 5, 14 cm in from the bed side wall. The injector is recessed 10 cm from the front panel of the bed, vertically aligned with the thermistors at the end of the probes. The injector is positioned and supported in the side wall by a compression fitting.

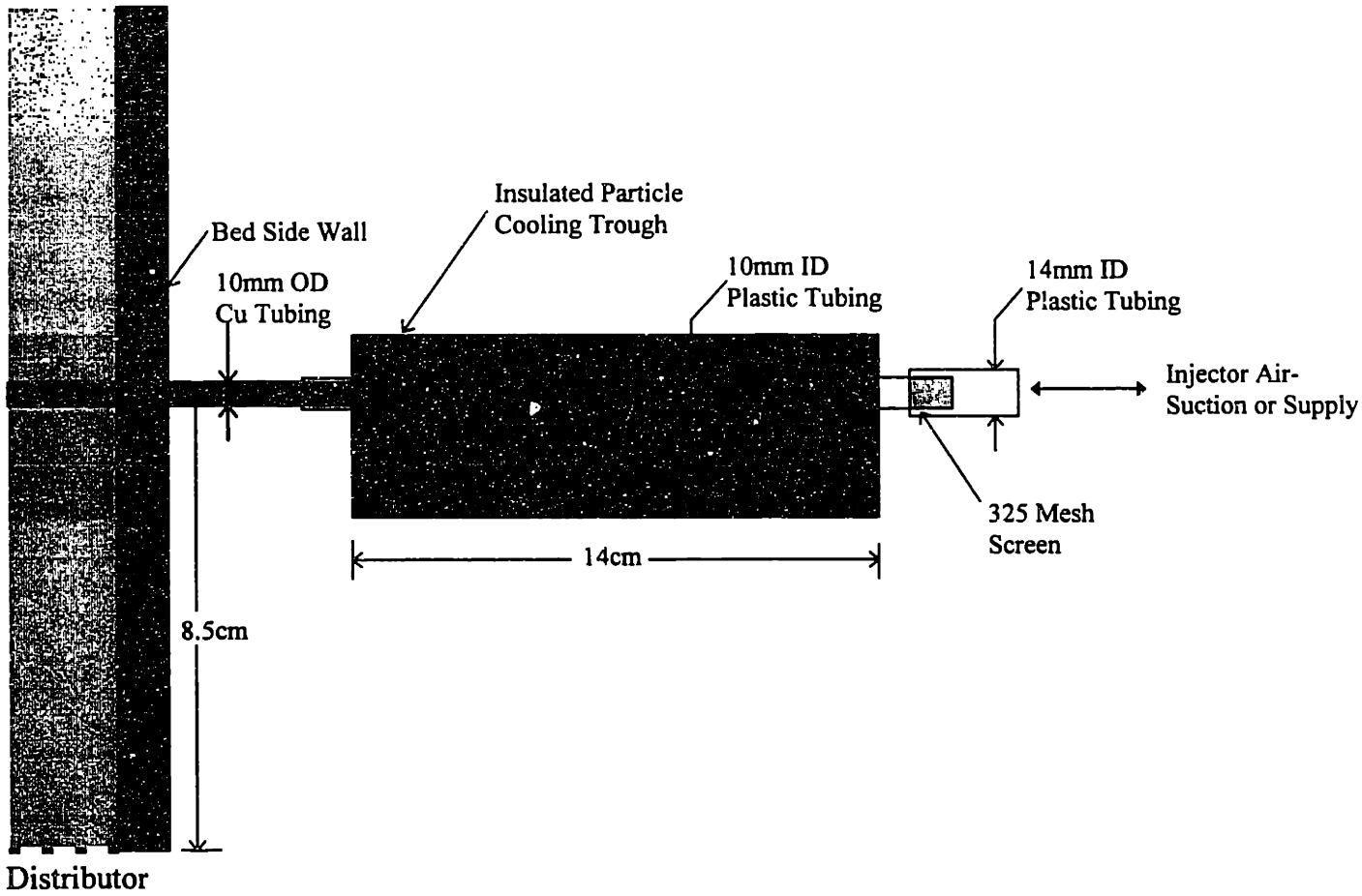

Figure 6: Side View of Tracer Injector Setup

The cooling trough is constructed of 3 mm thick polycarbonate plastic; the outside of the trough was covered with a spray foam insulation. The trough is 14 cm long, and the opening at its top is 6 cm across.

A 14 mm hole was drilled in each end of the trough to accommodate a piece of 10 mm ID flexible Tygon tubing. The tubing-trough interface was sealed with silicone sealant. A small amount of slack was left in the tubing to prevent cracking from shrinkage during its exposure to the liquid-nitrogen bath. Other types of rigid plastic tubing, such as polycarbonate, were found to fail when exposed to liquid nitrogen.

Particles are drawn from the bed into the cooling trough through a length of 10 mm OD copper tubing. The copper tubing fit snugly inside the plastic tubing in the cooling trough. By applying suction to the opposite end of the tubing, particles could be drawn through the copper tube into the tubing in the trough. The plastic tubing provided a way of cooling the bed particles without bringing them into direct contact with the liquid nitrogen. The particles were prevented from moving beyond the end of the tubing by covering it with a piece of 325 mesh screen. This permitted the suction/supply air but not the particles to pass through the end of the tubing.

The tubing supplying the injector air is a 14 mm ID flexible plastic tubing that fit snugly over the tubing in the trough. The screen was first placed on the end of the trough tubing and then held in place by inserting it inside the injector air supply line.

The injector air supply and suction setup is shown in Figure 7. In the configuration shown in the figure, when the valve is closed a suction is generated when air is forced through the top of the aspirator and out the nozzle. This suction was used to draw particles into the cooling trough. Once the particles were sufficiently cold, the valve was opened, and the loose end of the tubing connected to the valve (see Figure 7) was placed over the nozzle of the aspirator. In this configuration, air was supplied to the injector, forcing the chilled particles back into the bed.

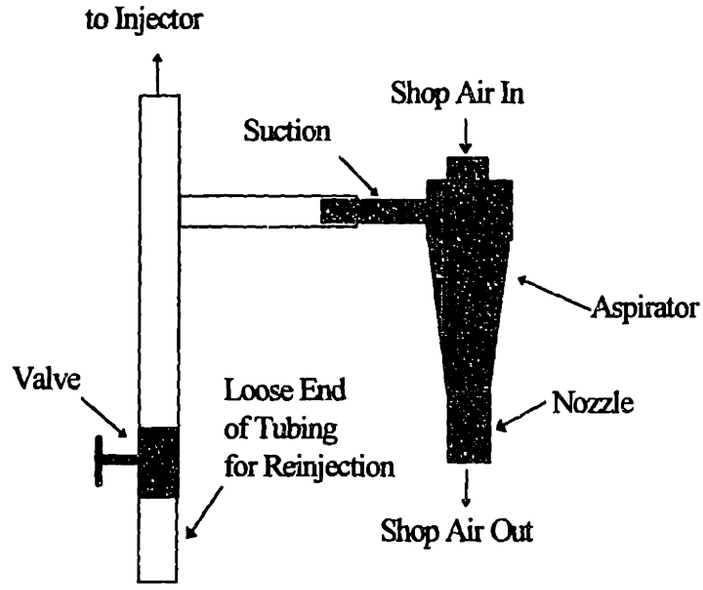

Figure 7: Injector Air-Suction and Supply Setup

8.1.2.2 Injection Procedure

The injector setup illustrated in Figures 6 and 7 serves three purposes: drawing particles from within the bed into the cooling trough, cooling the tracer particles well below the bed temperature, and injecting the chilled tracer particles back into the bed. The details of these three steps are summarized as follows.

1. With the bed running and the valve shown in Figure 7 closed, shop air is forced through the aspirator to draw particles into the cooling trough.

2. The cooling trough is filled with liquid nitrogen. The liquid level in the trough is kept high enough to keep the tube in the trough submerged. The particles are chilled in the liquid nitrogen for 5 minutes, providing tracer particles that are roughly 100 ° C below the bed temperature. (It was estimated that the particles had to be immersed in the

liquid nitrogen for approximately 5 minutes in order for their temperature to drop by 100 °C[1]; measurements support this estimate.)

3. The valve in Figure 7 is opened and the loose end of the tubing connected to the valve is inserted over the nozzle of the aspirator. Air is then forced through the aspirator at a velocity just sufficient to force the particles back into the bed. The injection velocity is minimized to eliminate the apparent lateral mixing produced by the injection process. The tracer particles did not appear to penetrate to thermistor 11* as a result of the particle momentum at injection (when thermistor 11* was positioned opposite the injector–see Figure 5). High-speed video measurements of the injection process showed that the injection velocity is approximately 0.3 m/s.

Tests were also conducted to estimate the maximum tracer particle injection velocity. High-speed video measurements showed that the maximum injection velocity was approximately 0.9 m/s.

[1] Gelperin and Einstein's (1971) expression for the thermal conductivity of a particle emulsion was used to estimate the thermal conductivity of the polyethylene particle-gas mixture. The thermal conductivity of the emulsion is low–$k_e \approx 0.028$ W/m-K. The high boiling heat transfer coefficient on the outside of the tubing, in conjunction with the low effective thermal conductivity produce a very highBiot number (~10^4). Modeling the particles as a convectively cooled cylinder with an ambient temperature of 77 K (Liq. N_2 T_{sat} at atm. pressure) indicates that after roughly 5 minutes the centerline temperature of the "cylinder" is 100° C below its initial temperature.

8.2 Nomenclature

Bi	Biot number–ratio of the conduction thermal resistance to the convection thermal resistance
e_{i1}	voltage input 1 from bridge circuit to differential amplifier
e_{i2}	voltage input 2 from bridge circuit to differential amplifier
e_{in}	bridge circuit input voltage
e_M	voltage measured by across the bridge circuit
e_o	output voltage
i	current
k_e	thermal conductivity of particle-gas emulsion
R	resistor resistance
R_T	thermistor resistance
t	time
T	temperature
T_e	environment temperature
To	initial temperature

Greek Symbols

τ	thermistor time constant

8.3 References

Beckwith, T.G., Marangoni, R.D., and Lienhard, J.H., 1993, Mechanical Measurements, 5th Edition, Addison-Wesley, Reading, Massachusetts.

Bellgardt, D. and Werther, J., 1986, "A Novel Method for the Investigation of Particle Mixing in Gas-Solid Systems," *Powder Technology*, 48, pp. 173-180.

Fitzgerald, T., Catipovic, N., and Jovanovic, G., 1977, "Solid Tracer Studies in a Tube-Filled Fluidized Bed," Proceedings of the Fifth International Conference on Fluidized Bed Combustion, 3, Washington, D.C., pp. 135-152.

Gelperin, N.I. and Einstein, V.G., 1971, "Heat Transfer", Chapter 10 in Fluidization, eds. J.F. Davidson and D. Harrison, Academic Press, London, pp.471-540.

Horowitz, P. and Hill, W., 1989, The Art of Electronics, 2nd Edition, Cambridge University Press, Cambridge.

Mills, A.F., 1992, Heat Transfer, Irwin, Boston, MA.

Valenzuela, J.A., 1982, Mixing of Solids in Bubbling Fluidized Beds and its Application to Fluidized Bed Combustors, Sc.D. Thesis, Massachusetts Institute of Technology.

Westphalen, D., 1993, Scaling and Lateral Solid Mixing in Circulating Fluidized Beds, Ph.D. Thesis, Massachusetts Institute of Technology.

This Page Intentionally Blank

9. Solids Mixing in Pressurized Bubbling Fluidized Bed Combustors

9.1 Thermal Tracer Data Analysis

The experimental setup described in Chapter 8 provides transient temperature measurements at 16 locations surrounding the thermal-tracer injection point. These temperature traces help address two questions: How quickly do the tracer particles disperse from the injection point? and, more importantly, What is the tracer concentration distribution as a function of time? The individual temperature traces for each thermistor probe can be evaluated to estimate the time it takes for the tracer particles to migrate to different positions in the bed. The magnitude of the temperature change experienced by a thermistor is shown to indicate the local tracer concentration.

9.1.1 Temperature Normalization

As discussed in Chapter 8, for two identical mixing experiments the solids will not mix in exactly the same way due to the stochastic nature of the bubble motion. For example, if a bubble passes by just as the tracer particles are injected into the bed, they will be quickly displaced upward. Whereas, if no bubble is present at the time of injection there will be a lag between the injection time and when the tracer begins to disperse. Similarly, if a bubble transporting tracer particles is in close proximity to a neighboring bubble they may coalesce, displacing the tracer laterally. But if the bubble transporting the tracer is far from other bubbles coalescence will not occur, producing primarily axial tracer motion. Essentially an infinite number of scenarios are possible, with each leading to the tracer being dispersed in a slightly different way. Hence, it is desirable to conduct several experiments and average the results to get a better estimate of the average mixing behavior. But variations in the bed and tracer temperatures between experiments makes direct averaging of the dimensional temperatures inappropriate. The dimensional

thermistor temperatures must be normalized to account for variations in the experimental test conditions.

As is typically done in heat transfer, the thermistor output are expressed in the form of a dimensionless temperature, Θ, given by

$$\Theta(t) \equiv \frac{T(t) - \overline{T}}{T_{inj} - \overline{T}}, \qquad (1)$$

where:

$\overline{T}$ =the average bed temperature measured by the thermistor prior to injection;

T(t)=the time-varying temperature measured by the thermistor; and

T_{inj}=the temperature of the thermal tracer particles at the time they are injected into the bed.

So, for example, at t=0, Θ=1 at the injector and Θ=0 in regions away from the injector where no tracer is present. Expressing the thermistor output in terms of Θ normalizes the data to account for variations in the injection temperature (T_{inj}) and the bed temperature ($\overline{T}$) between experiments. In addition, as will be shown in the next section, Θ provides a crude estimate of the tracer concentration for short times after injection.

9.1.1.1 Relationship Between Θ and the Tracer Concentration

The thermal tracer technique provides a convenient way of evaluating the effects of changing operating conditions and bed geometry on solids mixing. For these types of studies, Θ can be averaged from several mixing transients, for each configuration or condition tested, and then compared directly. But comparing thermal tracer data with the predictions from a mixing model requires a relationship between Θ and the tracer concentration.

Relating the dimensionless temperature (Θ), given by (1), to the local tracer concentration requires two assumptions.

1. *The thermistor measures a local mixture temperature.* The temperature measured by the thermistor will reflect an average temperature of the particles that surround it, both warm and cold. (The heat capacity (mc_p) of the air is much less than that of the particles causing it to quickly approach the local particle temperature.) But how closely this average temperature is to the thermodynamic mixture temperature is less clear. This is a rough approximation that introduces significant uncertainty in the relationship between Θ and the local tracer concentration.
2. *The energy transfer to the tracer particles is from the surrounding bed particles and not the air.* Coal devolatilizes in approximately 6 seconds in fluidized beds (Andrei et al., 1985); this corresponds to 3 seconds in the cold model (i.e., $t_{cold}=t_{hot}/2$ from scaling). For the first 3 seconds after injection, the temperature change of the particles due to energy transfer from the air should be modest.[1]. If the tracer particles are initially 100°C below the bed temperature and their temperature increases by 20°C after 3 seconds due to heating by the air, the error in Θ at the end of the 3 seconds is 20%. The error associated with this assumption is, most likely, much smaller than that associated with assumption 1.

Let m_1 and m_2 be the local mass fraction of tracer and the bed material, respectively. By mass conservation,

$$m_1 + m_2 = 1. \tag{2}$$

From conservation of energy,

$$u_{mix} = m_1 u_1 + m_2 u_2 , \tag{3}$$

where:

u_{mix}=the local specific internal energy corresponding to the temperature measured by the thermistor, T(t);

u_1=the specific internal energy of the tracer particles at T_{inj}; and

[1]Consider a volume of polyethylene tracer particles that are initially 100°C below the bed temperature. Further, assume that the dimensions of this particle volume are roughly equivalent to those of particles in the cooling trough (see Chapter 8). For an air flowrate through the particles corresponding to u_{mf}, where the air enters the particle volume at the bed temperature and leaves at the tracer injection temperature (i.e., 100°C colder), the particle temperature would rise 6°C after 3 seconds.

u_2=the specific internal energy of the bed particles at $\overline{T}$.

Substituting (2) into (3) gives

$$u_{mix} = m_1 u_1 + (1 - m_1) u_2 . \tag{4}$$

The temperature of the particles can be related to their internal energy by modeling them as a perfect incompressible substance. Under these assumptions, the specific internal energy is related to temperature by (Gyftopoulos and Beretta, 1990)

$$u(T) - u_{ref} = c(T - T_o), \tag{5}$$

where u_{ref} refers to the arbitrary reference state at T_o. Substituting (5) into (4) and solving for m_1, noting in this case that the tracer and the bed material have the same specific heat gives

$$m_1 = \frac{T(t) - \overline{T}}{T_{inj} - \overline{T}} . \tag{6}$$

Comparing (6) and (1) shows that, within the limitations of the previously discussed assumptions,

$$m_1 \approx \Theta . \tag{7}$$

Hence Θ can be used as a proxy for m_1. However, considering the assumptions required to arrive at (7), it is important to understand that this is only a crude approximation. Neglecting the thermal inertia of the thermistors adds additional uncertainty to (7) Technically, it is not necessary neglect thermistor thermal inertia since the time-response of the thermistor is known (see Chapter 8). However to correct for the lag in the response of the thermistor to a change in temperature requires that the rate of change of the thermistor temperature (i.e., dT/dt) be determined. It is virtually impossible to differentiate discrete data since small amounts of noise in the data cause the derivative to behave erratically. To alleviate this problem requires the construction of analytic fits of the data that can subsequently be differentiated. This approach is used to determine the injection temperature and is described further in Section 9.1.3. But to do this for all the thermistor output for all the runs would require a tremendous amount of effort to provide a slight improvement to a crude approximation.

9.1.2 Injection Time, t_0

The injection time is needed to identify the beginning of the mixing transient. As shown in Chapter 8, thermistor 1 was positioned at the exit of the injector. The injection time (t_0) was determined from the thermistor 1 temperature trace. Figure 1 gives a sample temperature trace from thermistor 1.

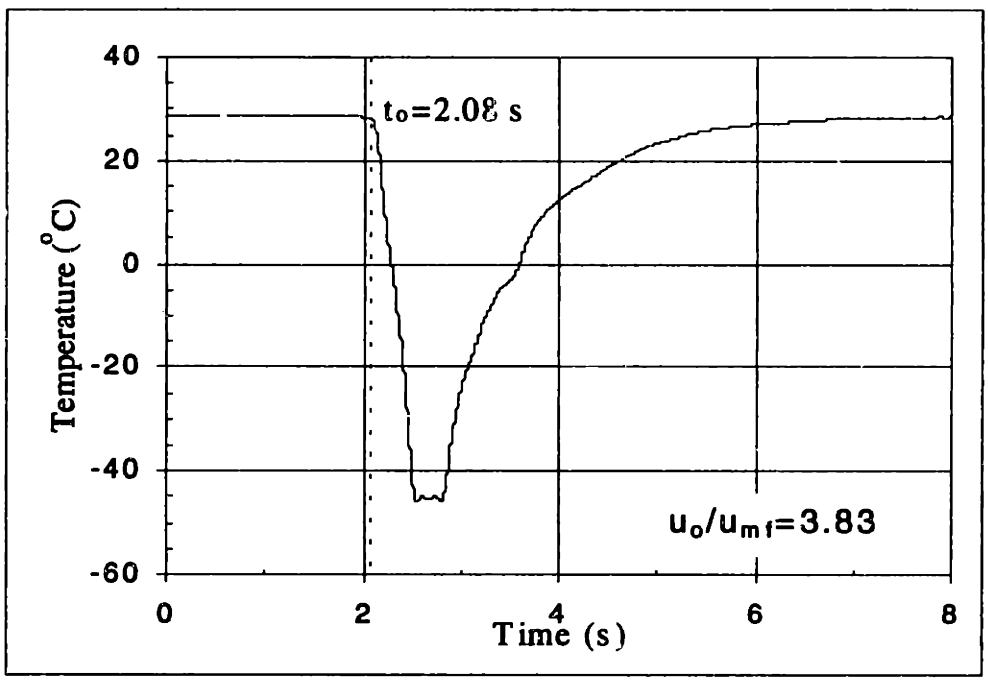

Figure 1: Sample Temperature Measured by Thermistor at Injector Exit

Figure 1 shows that thermistor 1 experiences a precipitous drop in temperature when the particles are injected. The dashed line in the figure marks the injection time, in this case, of t_0=2.08 seconds. The temperature trace flattens at approximately -50 ° C because the data acquisition board saturates at ±10 volts; -50 ° C corresponds to the -10 volt limit. Due to the thermal inertia of the thermistor, the temperature measured by the thermistor will lag behind the temperature of the surroundings. Hence, the minimum temperature

measured by the thermistor, which is lost due to the saturation of the data acquisition board, is not an accurate measure of the temperature of the injected particles. The determination of the tracer-particle injection temperature is discussed in Section 9.1.3.

9.1.3 Injection Temperature, T_{inj}

As mentioned in Sections 9.1.1.1 and 9.1.2, the thermal inertia of the thermistors causes their response to a change in temperature to lag behind the actual change in the temperature of the surroundings. Chapter 8, Section 8.1.1.3, discusses the time response of the thermistors. The thermistor is modeled as a first-order system whose time response is characterized by a time constant, τ. The time constant represents the time it takes for a step-excited first-order system to proceed 63.2% of the way from its initial to its final state. Westphalen (1993) measured the time constant of the thermistors used in this study, under heat transfer conditions typical of fluidized-beds, and found that $\tau \approx 0.4$ s.

The differential equation governing the response of the thermistor (T(t)) to a time-varying environment temperature ($T_e(t)$) is given by

$$\frac{dT}{dt} + \frac{1}{\tau} \cdot [T(t) - T_e(t)] = 0. \tag{8}$$

Solving (8) for $T_e(t)$ gives

$$T_e(t) = T(t) + \tau \cdot \frac{dT}{dt}. \tag{9}$$

Equation (9) shows that the measured temperature (T(t)) can be corrected using the thermistor time constant (τ) and the rate of change of the thermistor temperature (dT/dt), to infer the actual environment temperature ($T_e(t)$). Where, in this case, we are interested in correcting the thermistor output to estimate the tracer particle injection temperature (T_{inj}).

The following procedure was used to estimate the tracer particle injection temperature (T_{inj}).

1. Plot the output from thermistor 1 in the form shown in Figure 1.
2. Determine the slope of the thermistor response as the temperature drops past T=0 ° C. The slope is determined by fitting a line through the temperature data from +1 ° C to -1 ° C. The slope of this line gives an estimate of dT/dt at T=0 ° C.
3. Substituting T=0 ° C and dT/dt from step 2, along with τ=0.4 s from the measurements mentioned previously, into (9) gives an estimate of T_e at the time when T=0 ° C. As shown in Figure 1, this corresponds to approximately 0.2 s after the tracer particle injection commences. High-speed video measurements indicate that the injection velocity is approximately 0.3 m/s, and the length of the cylindrical volume of tracer particles in the cooling trough is 14 cm. Therefore, it should take roughly 0.4 s for all the tracer particles to enter the bed. Hence, at the time when the thermistor is registering 0 ° C it will still be responding to the injected tracer particles and $T_e \approx T_{inj}$.

Measurements indicate that typical tracer particle injection temperatures are more than 100 ° C below the bed temperature.

9.1.4 Delay Time, t_d

The time delay, t_d, is determined by inspecting a thermistor probe's temperature trace. This makes it somewhat subjective, but it provides a way of making qualitative comparisons of the axial and lateral particle dispersion rates as well as evaluating the effects of changing operating conditions.

Once the injection time (t_0) is known, and the tracer-particle arrival time (t_{arr}) is estimated from the probe output, the delay time is given by

$$t_d \equiv t_{arr} - t_0 . \qquad (10)$$

Figure 2 shows typical dimensionless temperature traces from thermistor probes 6 and 8; Thermistor 6 is positioned 5.5 cm directly above the injector and thermistor 8 is 7.5 cm above Thermistor 6. The time scale has been shifted by t_o, such that 0 on the abscissa of Figure 2 is the injection time. The vertical dashed lines identify the delay times for thermistors 6 and 8, for this particular run; the legend gives the numerical values of the delay times in case. The thermistor temperatures used to calculate Θ have not been corrected for the thermal inertia of the thermistors.

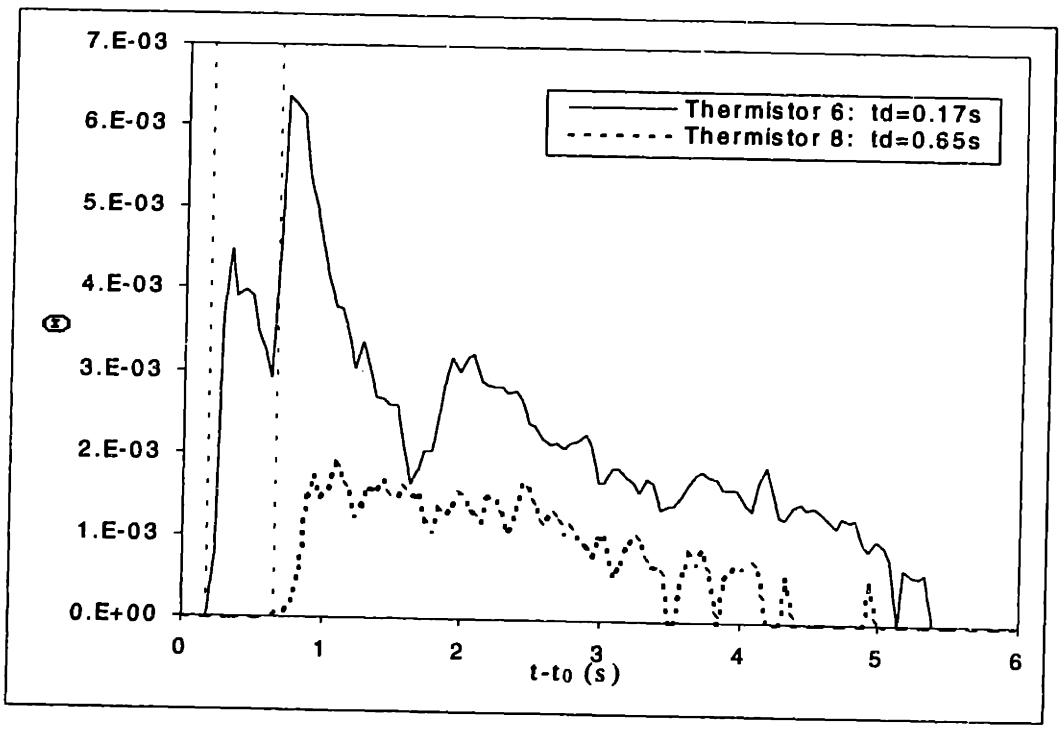

Figure 2: Dimensionless Temperature Traces With the Delay Time Shown

The delay time for an individual thermistor probe can vary between runs with the same operating condition. Probes that are distant from the injector do not always register the presence of tracer particles. These variations are due to random factors such as whether a bubble is present at the injector when the tracers are injected and the coalescence history of a bubble transporting tracer particles. Hence several runs are required to determine an average delay time.

9.2 Thermal Tracer Data

The personal-computer-based data acquisition system described in Chapter 3, Section 3.3.2, was used to sample the output of the sixteen thermistor probes. The thermistor output was sampled every 0.005 s (f_{sample}=200 Hz). This is much faster than either the hydrodynamic or thermistor-response time scales and hence, provided sufficient resolution of the thermistor output.

9.2.1 Time Delay Data

In this section, particle motion is referred to as particle dispersion rather than particle mixing. This distinction is made to distinguish between the maximum distance any particles move in a period of time, which is reflected by the time delay data, and the amount of particles that move different distances over a period of time. The latter is reflected by Θ, which was described in Section 9.1.1, and is used as the basis for the comparisons shown in Section 9.2.2.

The spatial distribution of time delays helps to answer the previously posed question of how quickly the tracer particles disperse from the injection point. More specifically, they provide some qualitative information on the relative axial and lateral tracer particle dispersion rates, as well as a way of assessing the effects of varying the gas superficial velocity on particle dispersion. A series of time delay measurements were made at two operating conditions–u_o/u_{mf}=2.5 and 3.83. These two conditions correspond to the minimum and maximum u_o/u_{mf} at which the bubble characteristics were measured (see Chapter 7). The u_o/u_{mf}=3.83 condition is the scaled Tidd PFBC operating condition.

Figures 3 and 4 show time delay contours for u_o/u_{mf}=2.5 and 3.83, respectively. The origin of the contour plots corresponds to the injector location. The arrow on the plots

identifies the injection location and direction. The contours in Figure 3 are the average of the time-delay results from 12 injections; Figure 4 is based on the average of 18 injections.

Figures 3 and 4 are plotted with the same spatial and time-delay scales. This permits a comparison between, not only the lateral and axial particle dispersion rates at a particular operating condition, but also the dispersion rates at two different superficial velocities. For short times, the relative particle dispersion rates (axial vs. lateral) are distorted due to the finite lateral penetration of the tracer particles at injection. In the cooling trough (see Chapter 8), the volume of tracer particles takes a 14 cm long cylindrical shape. When the particles are injected back into the bed, depending on how rapidly they are carried away from the injector exit relative to the injection rate, the tracer particles will be displaced laterally to make room for the particles behind them. In addition, high-speed video measurements indicate that the particles are introduced into the bed with an average velocity of 0.3 m/s. Hence the particle momentum also contributes to the lateral penetration distance of the tracer particles. This finite penetration creates a false lateral mixing in the vicinity of the injector. This is particularly apparent near the origin of Figure 3 where for short times the lateral mixing rate appears to be higher than the axial mixing rate. It is worse for the lower u_o/u_{mf} case because the frequency of bubbles passing the injector is lower, causing the tracer particles to be carried away from the exit of the injector at a lower rate. This is also the most likely cause of the peculiar behavior of the 0.6-0.8 s contour on Figure 3.

By comparing Figures 3 and 4, it is clear that increasing the superficial velocity increases the particle dispersion. As seen in Figure 4, for u_o/u_{mf}=3.83, after 1.2 s the tracer particles have dispersed throughout the measurement domain. However, as shown in Figure 3, it takes over 1.6 s to achieve comparable particle dispersion with u_o/u_{mf}=2.5. Based on the measurements presented in Chapter 7, the higher u_o/u_{mf} case has both higher bubble frequency and bubble fraction than the case with u_o/u_{mf}=2.5. Bubbles provide the primary motive force for solids mixing. Higher bubble frequency corresponds to a larger number of interactions between bubbles and the tracer particles producing greater axial particle

dispersion. Higher bubble fraction indicates that the bubbles are in closer proximity, making coalescence more likely, which increases lateral particle dispersion.

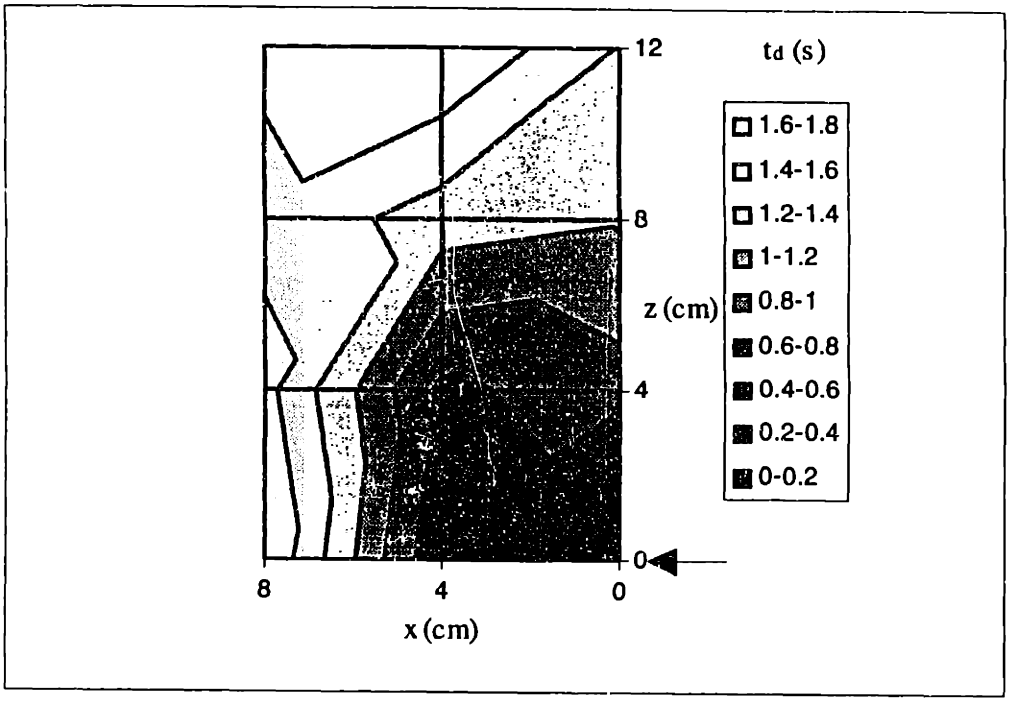

Figure 3: Time Delay Distribution for u_o/u_{mf}=2.5

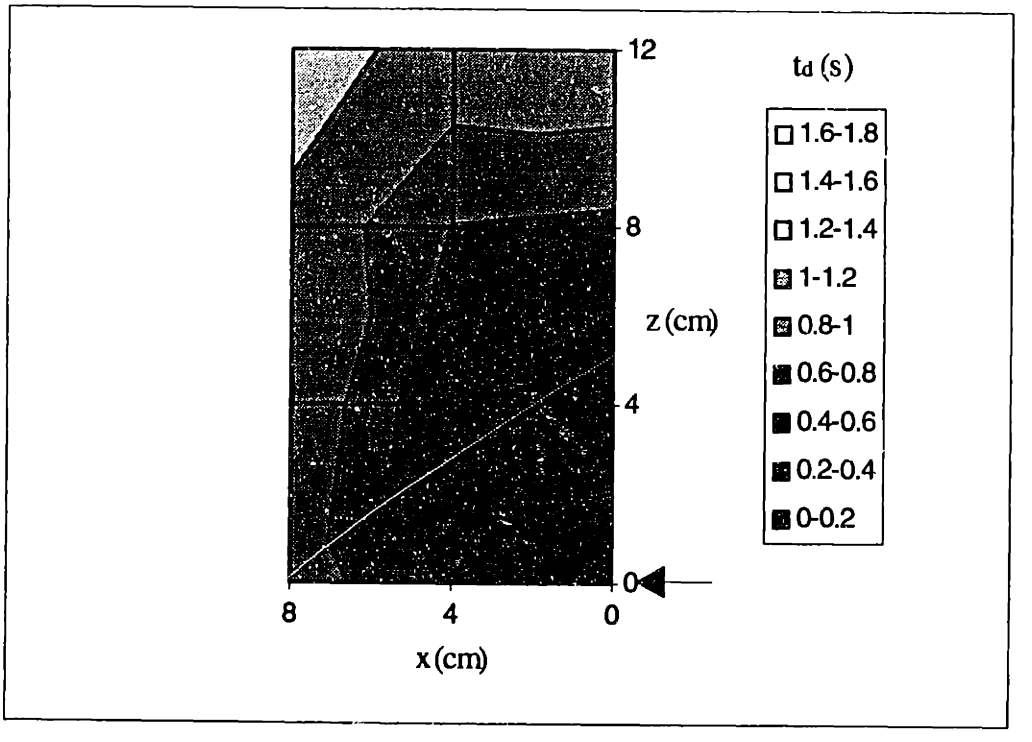

Figure 4: Time Delay Distribution for u_o/u_{mf}=3.83

Both Figures 3 and 4 show that the vertical particle dispersion rate is higher than the lateral dispersion rate. The measurement domain is 50% longer in the axial direction than it is in the lateral direction. Yet it takes the particles as long or longer to disperse to the lateral edge of the measurement domain (x=8 cm) than it does for them to reach the upper axial edge of the measurement domain (z=12 cm). The lateral particle dispersion shown in Figures 3 and 4 is also artificially enhanced by the finite lateral distance the particles travel when injected into the bed.

9.2.2 Thermal Tracer Mixing Data

The time delay measurements illustrate some important features of the solids mixing within the bed. For example, higher u_o/u_{mf} produces higher mixing rates, and axial mixing rates are higher than lateral mixing rates. But the time-delay measurements do not address the other more important question of: What is the tracer concentration distribution as a function of time? The dimensionless thermistor output (Θ) was shown in Section 9.1.1.1 to provide an approximate estimate for the local tracer concentration, making Θ useful for answering this question. Whereas in the previous section the emphasis was on the maximum distance particles move in a period of time, in the current section the interest is in evaluating the amount of particles that move different distances over a period of time.

Since the tracer distribution is of primary interest, contour plots of Θ over the measurement domain are used to illustrate the distribution at a point in time. The thermistors can credibly resolve changes in temperature as low as 0.1°C; temperature changes smaller than this begin to be obscured by noise in the electronics. Assuming that the tracer particles are 100°C below the bed temperature when they are injected (i.e., $\left(T_{inj} - \overline{T}\right) = -100\,°C$), a temperature change of 0.1°C (i.e., $\left(T - \overline{T}\right) = -0.1\,°C$) corresponds to Θ=0.001. Measurements of Θ<0.001 are shown on the contour plots in white, indicating that the tracer concentration is either zero or too small to measure.

Figures 5-10 present contour plots of Θ for u_o/u_{mf}=3.83. The plots are based on the average of the results from five mixing transients. The arrow in the figures indicates the injection location and direction, and the dashed line identifies the location of the bottom of the tube bank. The spatial and Θ scales are the same for all the plots to ease comparison of the results. Results out to approximately 3 seconds are presented since this corresponds to 6 seconds in the hot bed, which is roughly the time it takes for the coal to devolatilize.

Figures 5-10 present snapshots of the evolution of the tracer distribution as a function of time. In the previous section, the finite lateral penetration of the tracer particles at injection was discussed. This penetration is evident in Figure 6 where the first thermal tracer particles entering the bed were displaced laterally due to their momentum at injection and to make room for the tracer particles behind them, forming a "plume" of tracer at x=4 cm rather than directly above the injection point. Figure 6 shows that after a relatively short period of time (0.73 s), the particles have been displaced from the injector up to the base of the tube bank. Figure 7 shows the tracer particles from the injection feeding the center of the measurement domain, and the additional lateral mixing that takes place relative to Figure 6. Considering Figure 8, it is interesting that although the high concentration region in the center of the domain shown in Figure 7 has mixed laterally throughout the measurement domain, little additional axial mixing of the tracer is observed. Comparing Figures 6 and 8 shows that in the first 0.73 s the tracer dispersed very quickly axially up to the base of the tube bank (z=8 cm), but in more than double the amount time (after 1.6 s) little additional axial mixing of the tracer into the tube bank is evident. The tube bank appears to present a significant resistance to particle mixing. This is further supported by considering Figures 9 and 10 where the concentration of the tracer in the tube bank remains small. The flattening of the time-delay contours shown in Figure 4 at the base of the tube bank ($z \approx 9$ cm) may also be a manifestation of the resistance the tube bank offers to the motion of the solids.

Highley and Merrick (1971) and Chen et al. (1984) found that the presence of even a sparse tube bank significantly retards solids motion. The tube bank in the cold model of the Tidd PFBC is very tight, and therefore, based on the results of these previous studies, different mixing behavior would be expected within the tube bank than in the open region below the tube bank.

The Tidd PFBC experienced problems achieving adequate mixing near the fuel feed points, requiring the installation of baffles to improve the lateral fuel distribution (McDonald, 1992). The potential for problems such as this are highlighted by the mixing data from the cold-scale model.

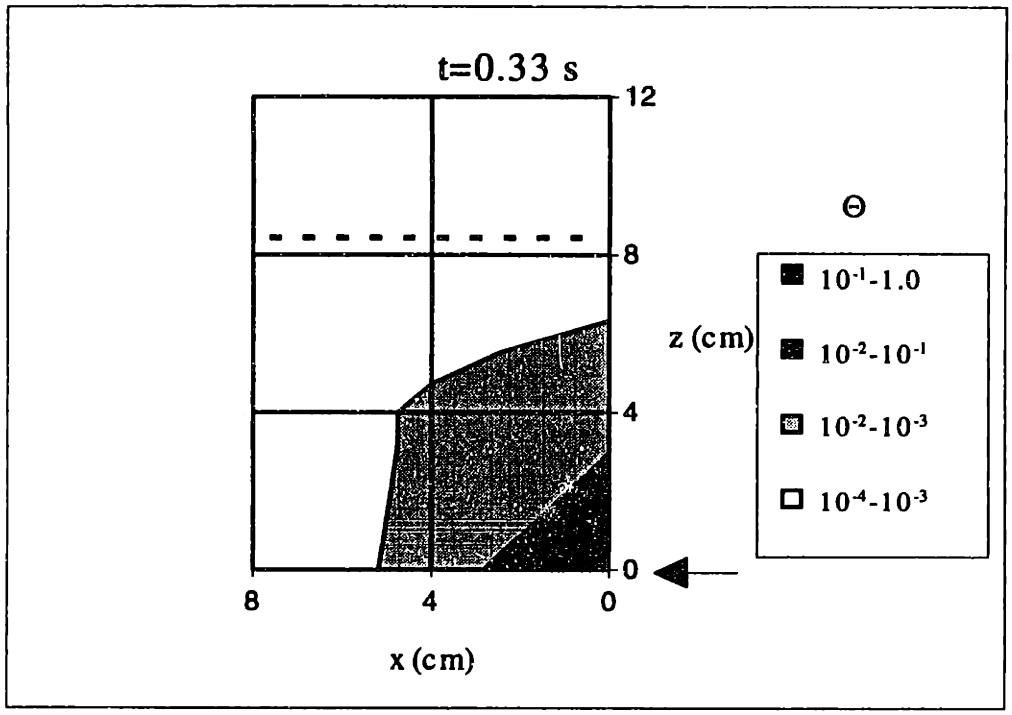

Figure 5: Θ Distribution 0.33 s After Injection–u_o/u_{mf}=3.83

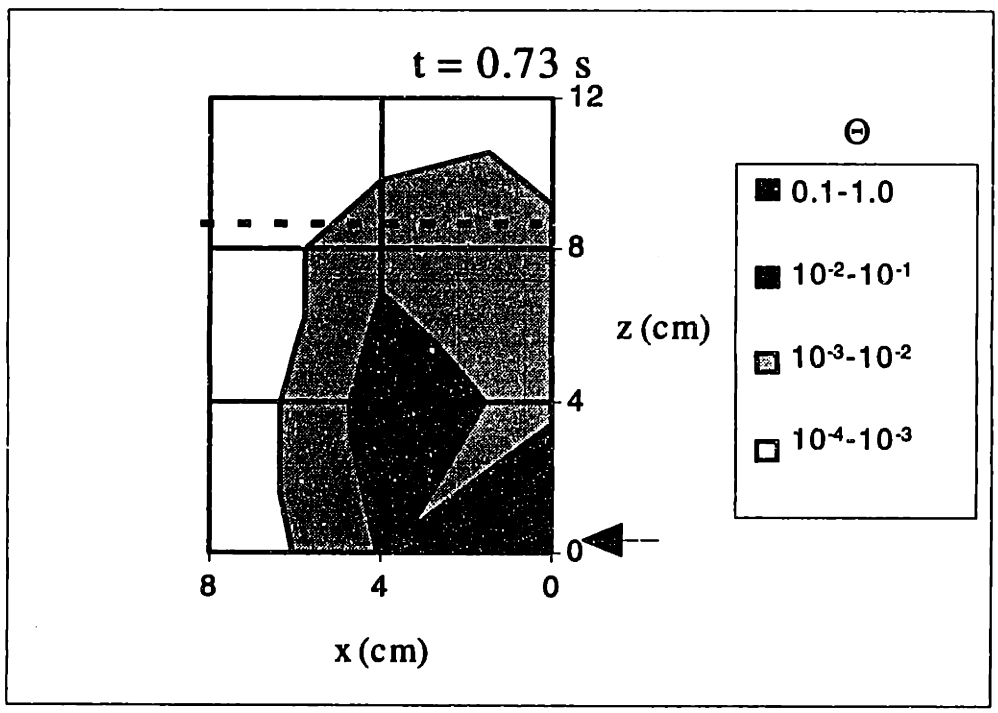

Figure 6: Θ Distribution 0.73 s After Injection–u_o/u_{mf}=3.83

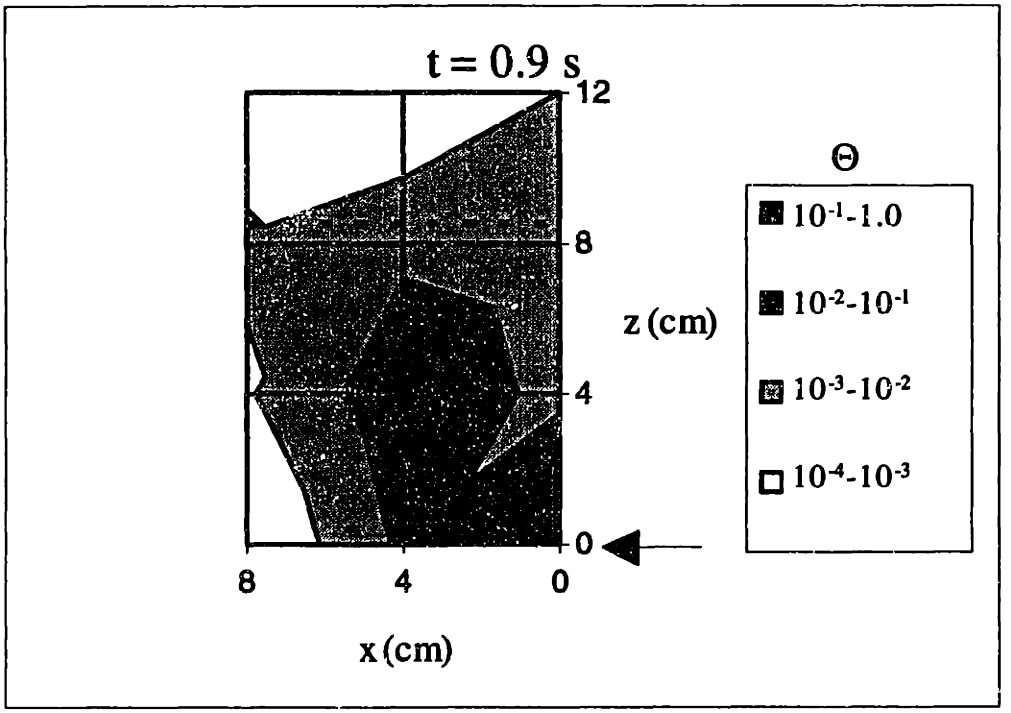

Figure 7: Θ Distribution 0.9 s After Injection–u_o/u_{mf}=3.83

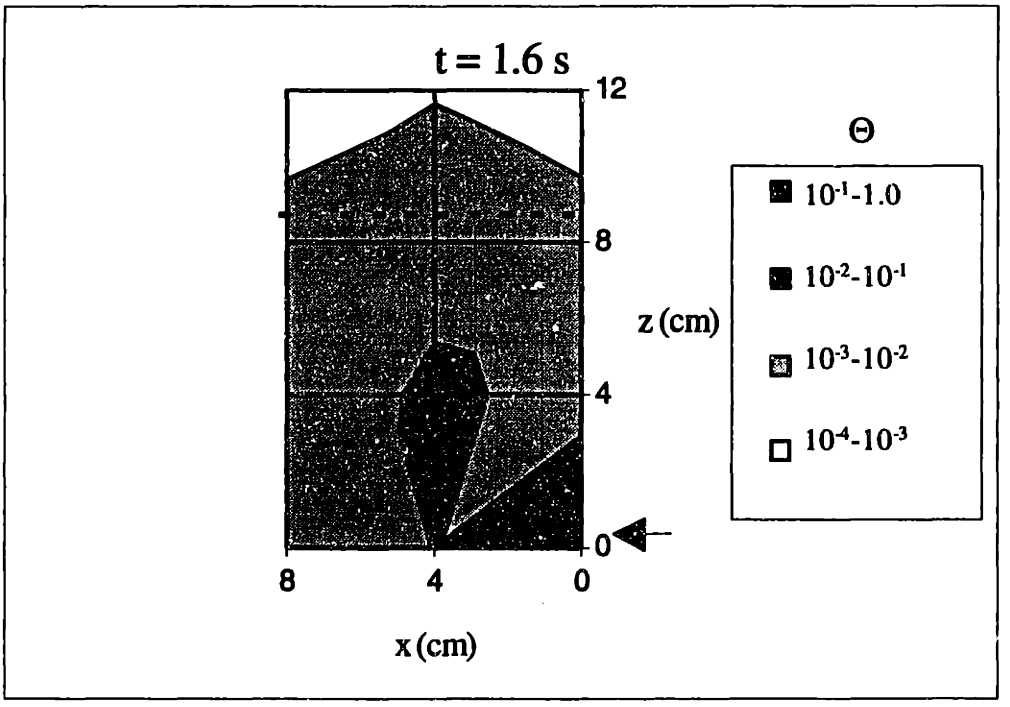

Figure 8: Θ Distribution 1.6 s After Injection–u_o/u_{mf}=3.83

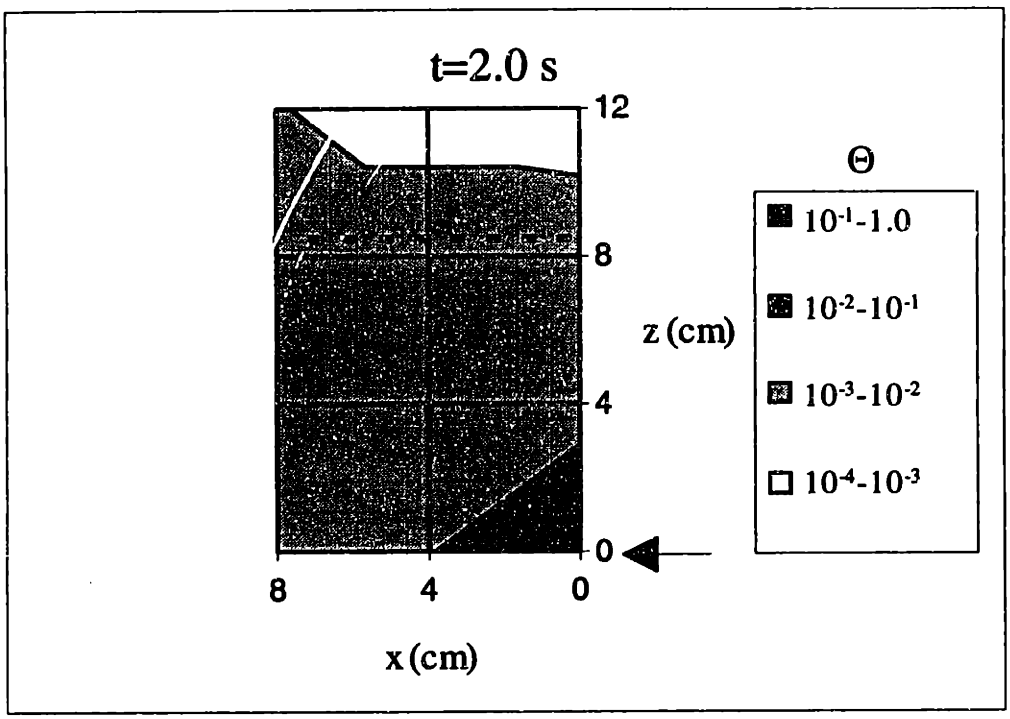

Figure 9: Θ Distribution 2.0 s After Injection–u_o/u_{mf}=3.83

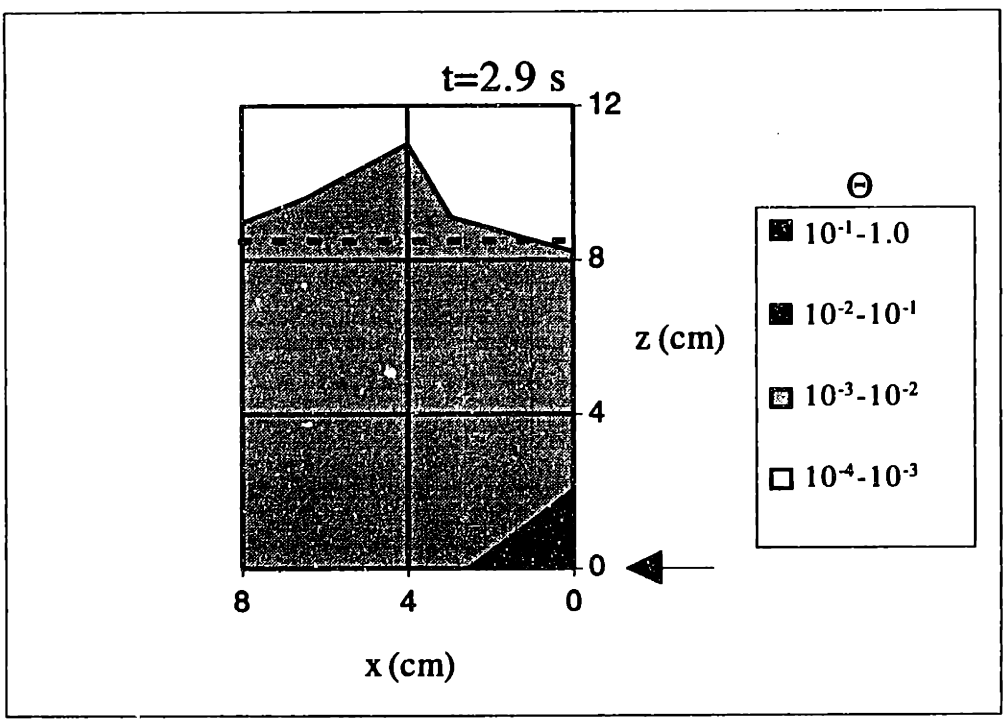

Figure 10: Θ Distribution 2.9 s After Injection–u_o/u_{mf}=3.83

It is also illuminating to compare the output from the thermistors at the same times in the mixing transient, but with different superficial velocities. Figures 11-13 are based on the average of five mixing transients with u_o/u_{mf}=2.5. Again, the spatial and Θ scales in these two figures are the same as those in Figures 5-10. The results in Figures 11-13 can be compared directly with the results shown in Figures 6, 8 and 9.

Comparing Figures 11-13 with Figures 6, 8 and 9, respectively, it is clear, for short times, that the tracer mixes much more slowly, at least below the tube bank, when u_o/u_{mf}=2.5 than it does when u_o/u_{mf}=3.83. However, as was the case with u_o/u_{mf}=3.83, once the tracer reaches the tube bank its motion appears to be impaired.

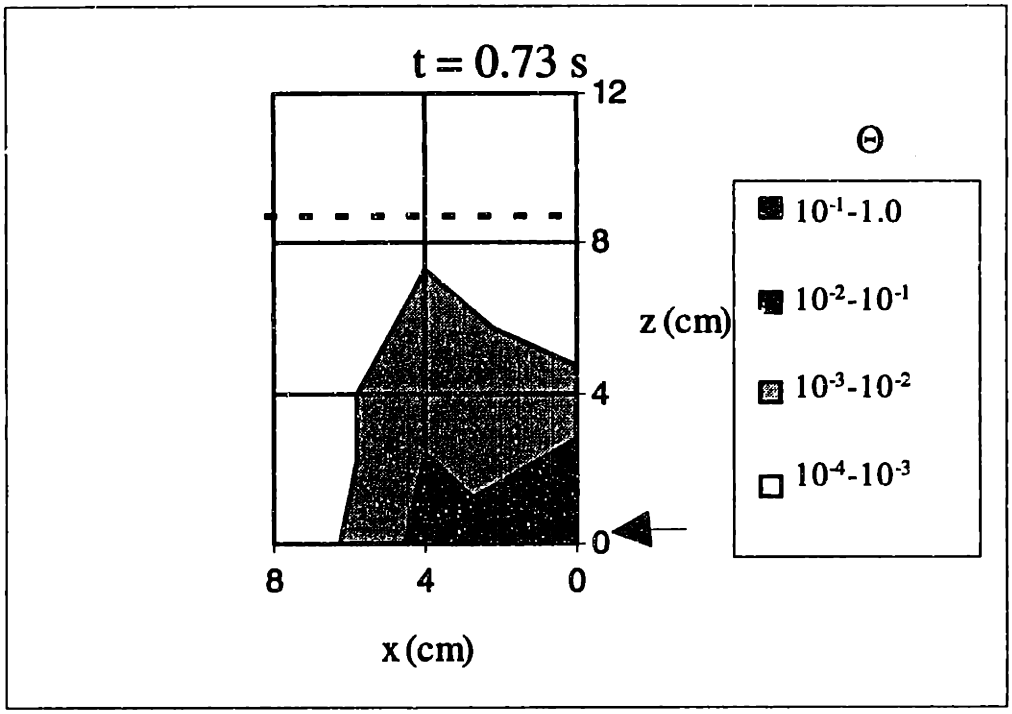

Figure 11: Θ Distribution 0.73 s After Injection–u_o/u_{mf}=2.5

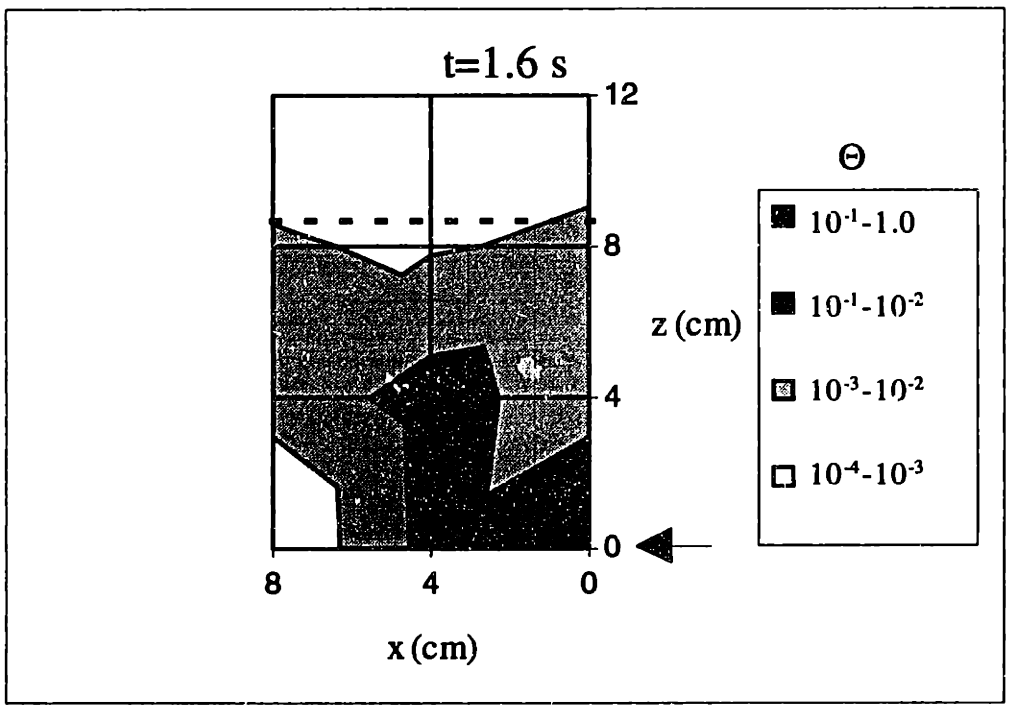

Figure 12: Θ Distribution 1.6 s After Injection–u_o/u_{mf}=2.5

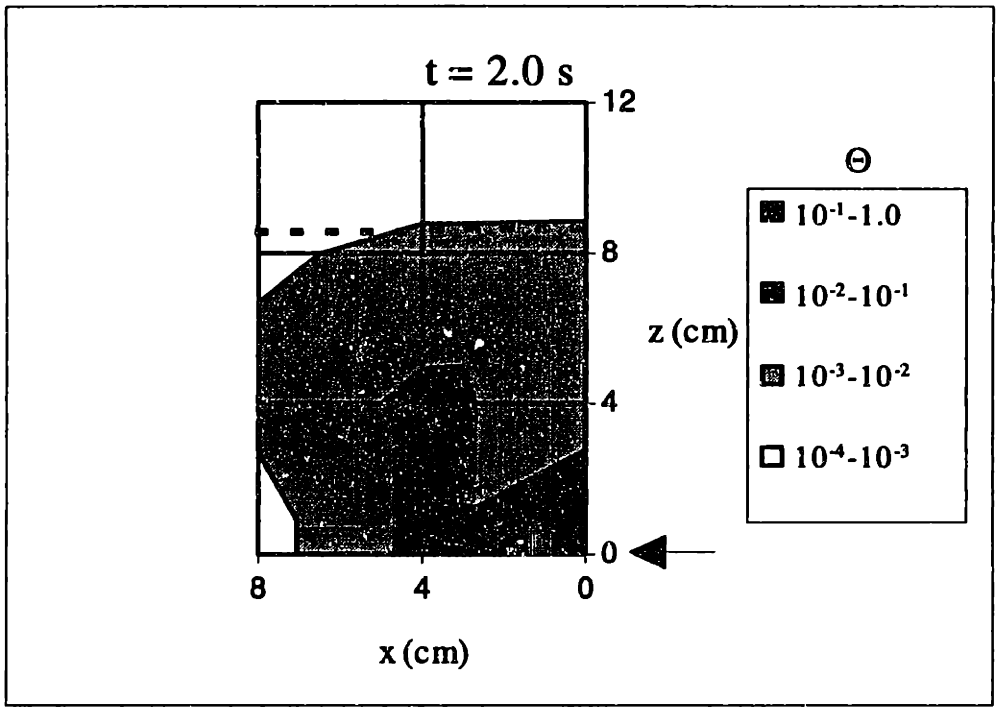

Figure 13: Θ Distribution 2.0 s After Injection–u_o/u_{mf}=2.5

9.3 Nomenclature

c_p specific heat
f_{sample} data acquisition sampling frequency
m mass
m_1 local tracer mass fraction
m_2 local bed material mass fraction
t time
t_{arr} tracer arrival time, time after tracer injection that the tracer reaches a thermistor relative to when the data acquisition system was activated
t_d delay time, time after tracer injection that the tracer reaches a thermistor
t_0 time after the data acquisition system is activated that the tracer particles are introduced into the bed
T temperature measured by the thermistor
$\overline{T}$ average bed temperature measured by a thermistor prior to injection
T_e temperature of the thermistor's environment
T_{inj} temperature of the injected tracer particles
T_o reference temperature
u_{ref} reference specific internal energy corresponding to T_o
u_{mix} specific internal energy of tracer/bed material mixture
u_1 specific internal energy of the tracer particles at T_{inj}
u_2 specific internal energy of the bed material at $\overline{T}$
u_{mf} minimum fluidization velocity
u_o gas superficial velocity
x lateral distance from injector
z axial distance above the injector

Greek Symbols

Θ dimensionless temperature measured by the thermistor
τ thermistor time constant

9.4 References

Andrei, M.A., Sarofim, A.F., and Beér, J.M., 1985, "Time-resolved Burnout of Coal Particles in a Fluidized Bed," *Combustion and Flame*, 61, pp. 17-27.

Chen, M.M., Chao, B.T., and Liljegren, J., 1984, "The Effects of Bed Internals on the Solids Velocity Distribution in Gas Fluidized Beds," *Proceedings of the Fourth International Conference on Fluidization*, eds. D. Kunii and R. Toei, Engineering Foundation, pp. 203-210.

Gyftopoulos, E.P. and Beretta, G.P., 1990, Thermodynamics: Foundations and Applications, Macmillan Publishing Company, New York.

Highley, J. and Merrick, D., 1971, "The Effect of the Spacing Between Solid Feed Points on the Performance of a Large Fluidized-Bed Reactor," *AIChE Symposium Series No. 116*, 67, pp. 219-227.

McDonald, D.K., 1992, "PFBC Plant Operations–TIDD," Babcock & Wilcox Technical Paper, BR-1498, presented to Power-Gen '92, Orlando, FL.

Westphalen, D., 1993, Scaling and Lateral Solid Mixing in Circulating Fluidized Beds, Ph.D. thesis, Massachusetts Institute of Technology.

This page intentionally blank

10. Modeling Solids Mixing in Bubbling Fluidized Beds

10.1 Solids Mixing Mechanisms

As discussed in Chapter 6, bubbles play a central role in the mixing of solids in bubbling fluidized beds. A detailed discussion of solids mixing mechanisms was presented in Section 6.2.1 to provide the motivation for studying bubble characteristics. These solids mixing mechanisms will be briefly reviewed to frame the mixing model development presented in Sections 10.2.1-10.2.3.

Figure 1 shows how particles, initially segregated into two layers, are displaced by the motion of a bubble. The figure illustrates the primary mechanisms of axial and lateral solids mixing within larger-particle ($d_p \geq 100$ μm) bubbling fluidized beds. Note that bubble motion is solely responsible for both axial and lateral solids mixing.

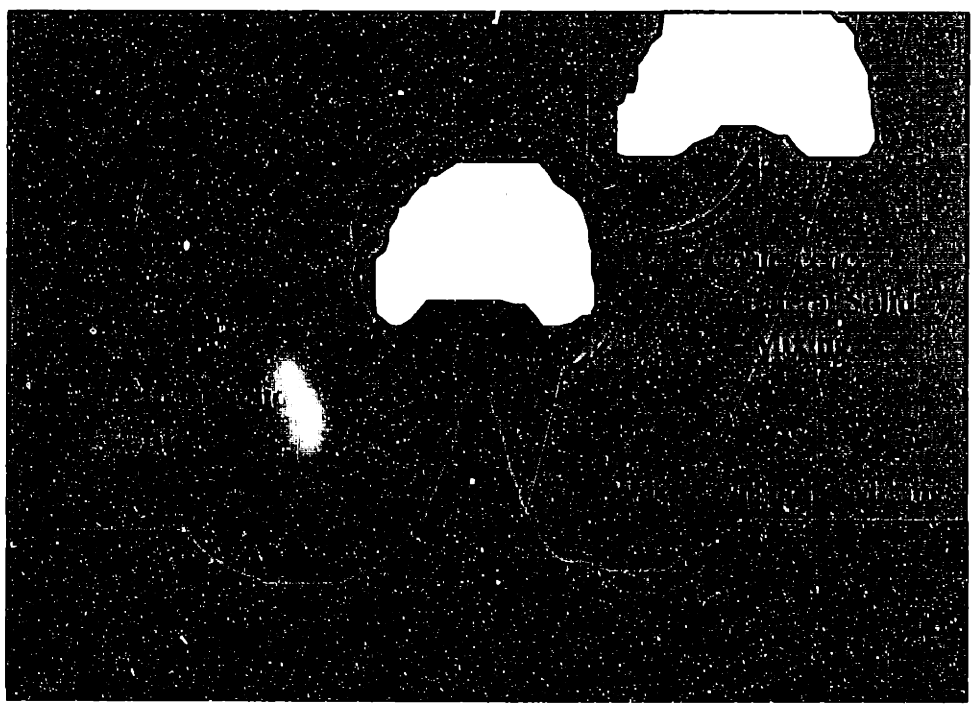

Figure 1: Mechanisms of Solids Mixing

As Figure 1 shows, axial mixing is produced by bubble-induced drift and wake transport. Solids mix laterally as bubbles move to coalescence with neighboring bubbles. And additional mixing takes place within the wake of the bubble. In general, inter-particle diffusion contributes negligibly to the solids mixing process.

According to inviscid flow theory (Lighthill, 1956), as a sphere moves through an unbounded ideal fluid, it displaces a volume equal to 50% of the volume of the sphere (Lighthill, 1956; Woollard and Potter, 1968). Both Woollard and Potter (1968) and Valenzuela and Glicksman (1983) estimated that the actual displaced volume is 30-40% of the bubble's volume. In contrast, Abrahami and Resnick (1974) and Cranfield (1978) measured a displaced volume that was approximately equal to the passing bubble's volume. Glicksman and McAndrews (1985) found that the combined wake and drift fraction varied between 0.55 and 1.10 for a large-particle fluidized bed with a bank of horizontal tubes.

Abrahami and Resnick (1974) concluded that the maximum height of the particle drift profile was always roughly 1.7 bubble diameters. Cranfield (1978) estimated the average upward particle displacement to be approximately one bubble diameter and the average downward displacement of the surrounding particles to be approximately one-eighth of a bubble diameter. These are average displacements, not the maximum height measured by Abrahami and Resnick (1974). Based on a sketch of the drift profile in Cranfield's (1978) paper, his drift-profile height appears to be consistent with that measured by Abrahami and Resnick (1974).

The mixing mechanisms illustrated in Figure 1, quantified using the experimental observations discussed in the previous two paragraphs, provide the physical foundation for the mixing model developed in Sections 10.2.1-10.2.3.

10.2 Solids Mixing Model

10.2.1 Axial Mixing Model

The model developed in this section is first described in words and figures to help clarify the physical assumptions of the model. This is then followed by the subsequent mathematical development of the model.

Figure 2 presents a side view of a model of the axial solids displacement produced by the passage of a single bubble. It is intended to represent the particle displacement due to bubble-induced drift and wake transport shown in Figure 1. The model assumes the particles are displaced upward a distance z_u. Bubbling fluidized beds experience no (significant) solids mass inflows or outflows. This imposes the requirement that there be no net mass flux across any level in the bed. To satisfy this requirement, particles displaced upward must be replaced by a downward flow of particles. Cranfield (1978) and Woollard and Potter (1968) found that the particles are displaced downward a distance z_d, which is much less than the upward displacement distance z_u. The difference in the magnitudes of z_u and z_d is illustrated in Figure 2. The approach to analyzing the axial mixing is to discretize the bed axially into Δz intervals of height z_d and then evaluate the concentration within that axial interval of the bed. But to evaluate the concentration within the interval requires consideration of how the bubble affects the contents of the interval. This is better visualized by considering a plan view of the model.

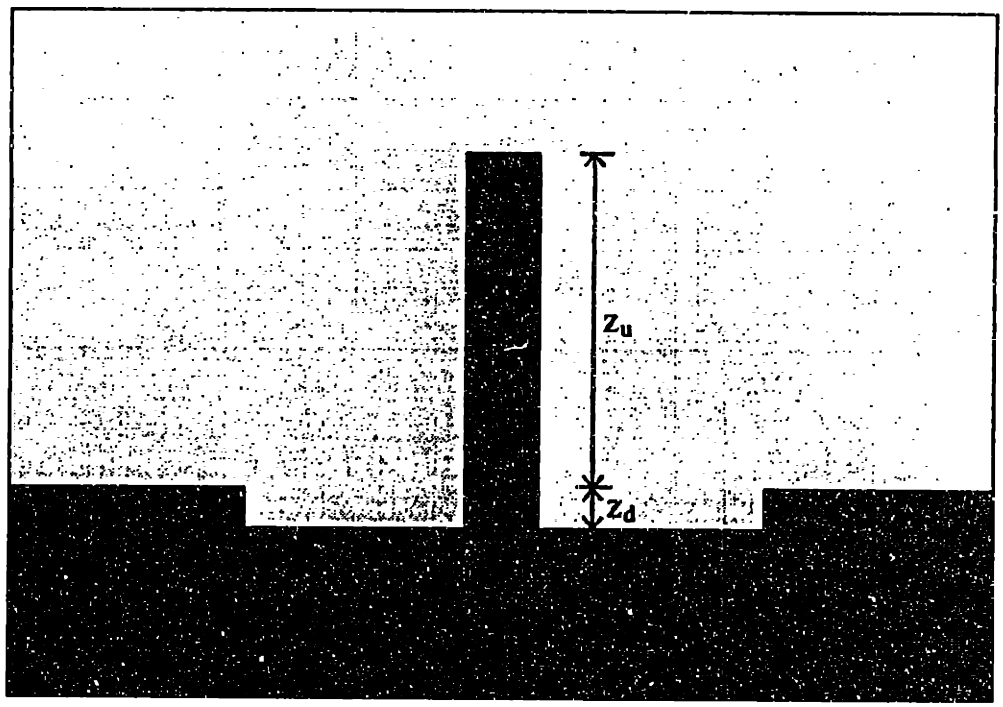

Figure 2: Model of Axial Solids Displacement Due to the Passage of a Single Bubble - Side View

Figure 3 presents the plan view (a view looking down on the surface of the bed) of the model illustrated in Figure 2. The area A, which is the entire area shown in Figure 3, represents the average cross-sectional area of the bed that contains a single bubble. (At this point only axial mixing is considered, therefore lateral variations are not modeled. Lateral mixing effects will be introduced in Section 10.2.2) This area is calculated from the bubble fraction, which represents the fraction of the cross-sectional area that is filled by bubbles, and the bubble diameter, which defines the cross sectional area of the bubble (i.e., $A=A_b/\delta$). After a bubble rises through this area (A), it is assumed that the bubble can influence concentration of an axial interval ($\Delta z=z_d$) in three ways. First, the bubble can exchange solids from its wake with the contents of the interval. The volume of this exchange is equal to $A_x \cdot z_d$, where A_x is the area within A that is affect by an exchange with a bubble. Note that A_x is less than the cross-sectional area of the bubble. Second, the interval can receive downflow from the interval directly above it, where A_d is the area within A that is affected by the downflow. And finally, the bubble can have no influence

on part of the interval, leaving it stagnant. A_s is the area within A that remains unchanged by the passage of a bubble. Hence, the area A consists of three sub-areas: A_s, A_d, and A_x.

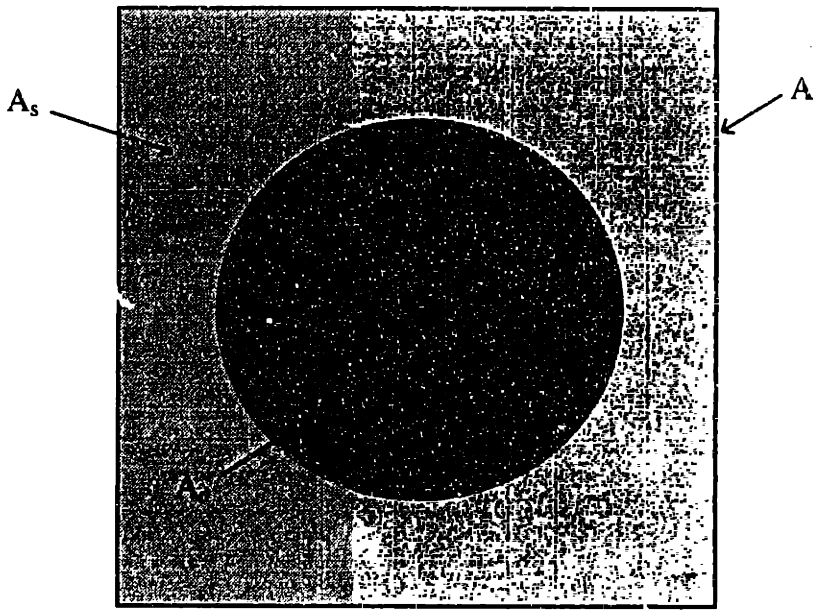

Figure 3: Model of Axial Solids Displacement Due to the Passage of a Single Bubble - Plan View

Figure 4 illustrates how a bubble is assumed to affect an axial interval of thickness z_d. Note that *intervals* will also be referred to as *elements*. Based on the model, an axial interval consists of three regions: exchange, downflow, and stagnant; the plan area for each of these regions corresponds to: A_x, A_d, and A_s, respectively. As a bubble rises through an interval, it picks up a volume of material ($A_x \cdot z_d$) and drops off an equal volume of material from a distance z_u below. The interval receives a downflow from the interval above it, while supplying the interval below it with a downflow of equal volume. The volume of the downflow is equal to the volume of material carried in the wake of the bubble. When the bubble reaches the surface of the bed, the contents of its wake provide the downflow into the axial interval at the bed surface. Similarly, the downflow from the interval at the bottom of the bed forms the wake of the bubble as it begins its rise through

the bed. Also, as shown in Figure 4, part of the interval can remain unaffected or stagnant due to the passage of the bubble. This process of bubbles rising through the bed, producing solids exchange between different intervals of the bed, repeats itself on a time step equal to the reciprocal of the bubble frequency (i.e., $\Delta t=1/f_b$). After the bubble passes, but prior to the passage of the subsequent bubble, the contents of each interval are assumed to mix perfectly. This model of axial solids mixing does not account for gross circulation of the solids in the bed, for example, due to a downflowing layer near the walls of the bed.

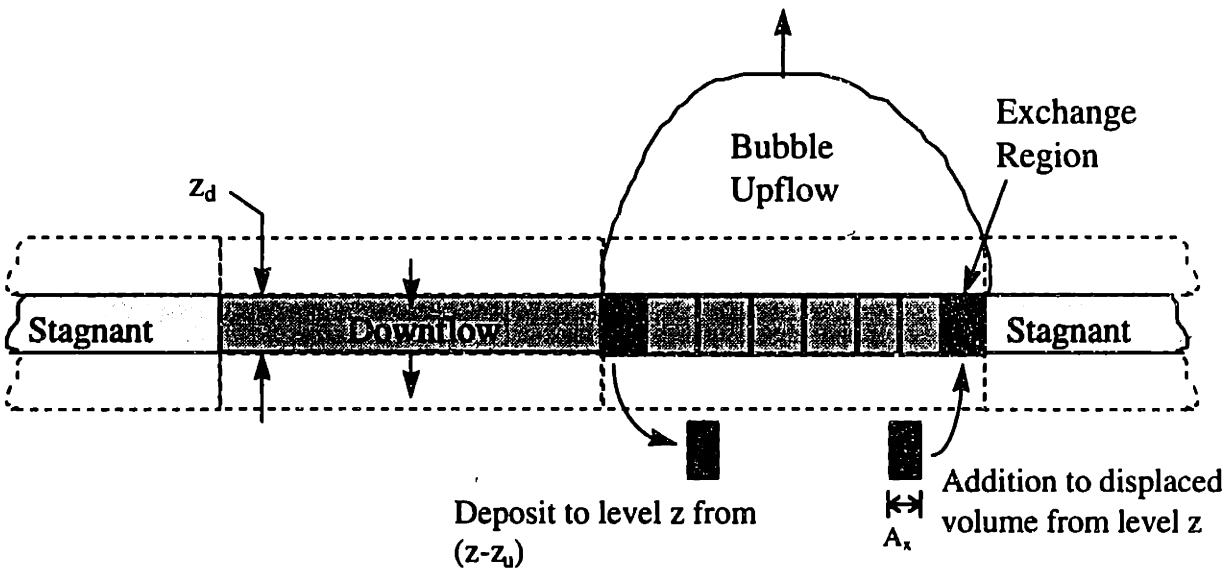

Figure 4: Effect of a Bubble on an Axial Interval

With this physical picture of the axial mixing model in mind, it is possible to proceed with the mathematical development of the model.

Assuming incompressibility, at any interval in the bed the volume of particles moving upward with the bubble (V_u) must be equal to the volume particles displaced downward into the interval (V_d), i.e.,

$$V_u=V_d=A_d \cdot z_d. \qquad (1)$$

This is because no particles leave the bed, and as mentioned previously, the volume of particles moving with the bubble when it reaches the surface of the bed supply the downflow region of the interval at the bed surface to satisfy mass conservation. (i.e., the downflow from the element "above" the surface interval is supplied by the volume of solids carried by the bubble.) As shown in Figure 4, the bubble picks up an exchange volume ($A_x \cdot z_d$) from each interval and deposits it in the axial interval a distance z_u above, hence

$$V_u = \left(\frac{z_u}{z_d}\right) \cdot (A_x \cdot z_d). \tag{2}$$

The ratio (z_u/z_d) is equal to the number of exchange volumes ($V_x=A_x \cdot z_d$) that are carried upward by the bubble. Equating the right hand sides of (1) and (2) gives

$$\frac{A_d}{A_x} = \frac{z_u}{z_d}. \tag{3}$$

Hence, at any level in the bed, the area affected by the downflowing region (A_d) is larger than that affected by the upflowing region (A_x) since $z_u > z_d$, as shown in Figure 2.

Assuming bubbles are uniformly distributed across the bed cross-section, a repeating area can be defined that characterizes the axial mixing behavior of the entire bed. This area is given by

$$A = \frac{A_b}{\delta} = \frac{\pi \cdot d_b^2}{4 \cdot \delta}, \tag{4}$$

where δ is the bubble fraction, and d_b is the bubble diameter. This A is the average cross-sectional area of the bed containing exactly one bubble. As shown in Figure 3, this repeating area (A) can be divided into three sub-areas: an exchange area, A_x; a downflow area, A_d; and a stagnant area, A_s, such that

$$A = A_x + A_d + A_s. \tag{5}$$

Dividing (5) by A provides the following area-ratio relationship

$$\alpha_x + \alpha_d + \alpha_s = 1, \tag{6}$$

where

$$\alpha_x \equiv \frac{A_x}{A}, \quad \alpha_d \equiv \frac{A_d}{A}, \quad \text{and} \quad \alpha_s \equiv \frac{A_s}{A}. \tag{7}$$

The area ratios given in (7) are important for calculating the mixture mass fraction at a level in the bed. This will be discussed further shortly.

The areas A_x and A_d depend on the volume of solids displaced by a bubble. Assuming the bubbles are spherical, their volume is given by

$$V_b = \frac{\pi}{6} d_b^3. \tag{8}$$

Define k_{vol} to be the volume of solids displaced upward by a bubble (V_u) divided by the bubble's volume. Hence,

$$k_{vol} = \frac{V_u}{V_b}. \tag{9}$$

Similarly, define k_{zu} to be the average distance particles are displaced upward by a bubble (z_u) divided by the bubble's diameter. And define k_{zd} to be the average distance particles are displaced downward by a bubble (z_d) divided by the bubble's diameter. Hence, k_{zu} and k_{zd} are given by

$$k_{zu} = \frac{z_u}{d_b} \text{ and } k_{zd} = \frac{z_d}{d_b}, \tag{10}$$

respectively. The requirement that there be no net mass flux at any level in the bed requires that the volume displaced upward equal the volume displaced downward (i.e., V_u=V_d). Considering Figure 2, the areas A_x and A_d required to calculate α_x and α_d in (7) can be expressed in terms of k_{vol}, k_{zu}, and k_{zd}, which are inputs to the model, using (1), (2), (9), and (10) to give:

$$A_x = \frac{V_u}{z_u} = \frac{k_{vol} \cdot V_b}{k_{zu} \cdot d_b} \tag{11}$$

and

$$A_d = \frac{V_u}{z_d} = \frac{k_{vol} \cdot V_b}{k_{zd} \cdot d_b}, \tag{12}$$

respectively. α_s can then be calculated using (6).

The lower limit for α_s is zero. This imposes a restriction on the maximum value of k_{vol} for specified k_{zu}, k_{zd}, and δ. The expression for k_{vol}^{max} is found by setting α_s=0 and substituting (4), (7), (11), and (12) into (6). The resulting expression is

$$k_{vol}^{max} = \frac{3 \cdot k_{zu} \cdot k_{zd}}{2 \cdot \delta \cdot (k_{zu} + k_{zd})}. \qquad (13)$$

This expression is included to highlight that mass conservation limits the upper value of k_{vol} input to the model; for specified values of δ, k_{zu} and k_{zd}; the value of k_{vol} input to the model must not exceed that given by (13).

As discussed previously, the approach to modeling the axial mixing process is to break the bed into discrete axial elements of height z_d (i.e., $\Delta z = z_d$). Bubble passage causes each element to receive particle volume of $V_x = A_x \cdot \Delta z$ from an element a distance z_u below, and to have an equal volume of its particles displaced upward a distance z_u. Each element also has a volume, $V_d = A_d \cdot \Delta z$, of its particles displaced downward a distance z_d while receiving an equal volume of particles from a distance z_d above. The two regions–exchange and downflow–supply each other at the bed bottom and surface to conserve mass. After the "passage" of a bubble, the contents of each axial element are perfectly mixed according to their contribution to the volume of the element ($V = \Delta z \cdot A$). Since Δz is the same for each of the three regions comprising the volume, (i.e., exchange, downflow, and stagnant) the mixture mass fraction of the volume is the sum of the mass fractions for each region weighted by their respective area ratio (i.e., α_x, α_d, and α_s). Bubble passage occurs on a time step of $\Delta t = 1/f_b$, where f_b is the frequency at which bubbles pass through area A. The process is best illustrated by a simple example.

Consider a fluidized bed which is $3d_b$ deep, and where, for simplicity, $z_u = d_b$ and $z_d = d_b/3$. Hence, (3) requires that $A_d/A_x = 3$. Figure 5 shows the contents of the each axial element prior to the passage of a bubble. Each element is broken into the three regions–exchange, downflow, and stagnant; subscripts on the interval numbers denote their region of origin.

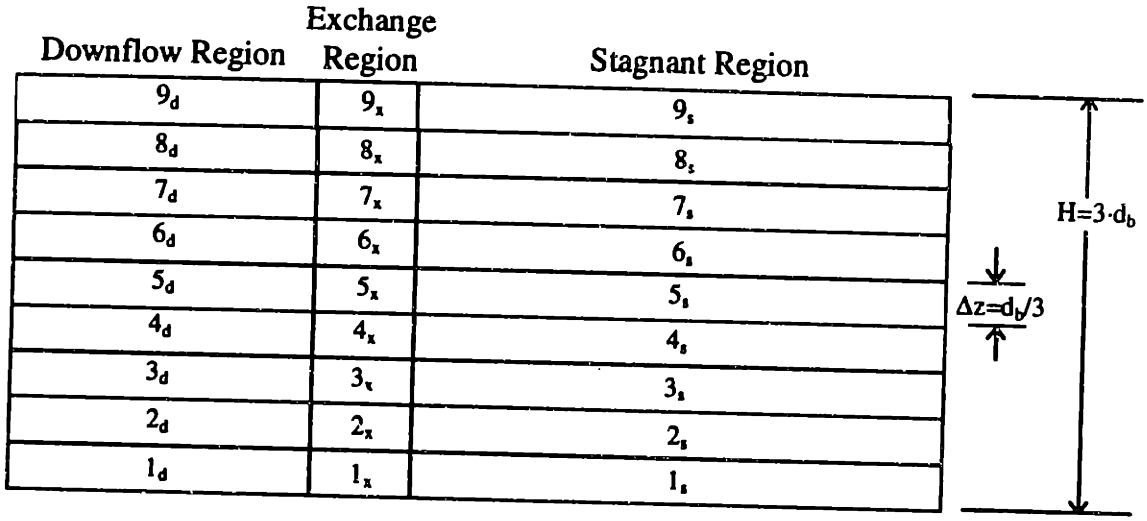

Figure 5: Contents of Bed Intervals Prior to Bubble Passage

Figure 6 shows the contents of each layer after the passage of a bubble. As discussed previously, the passage of the bubble shifts the contents in the exchange region up a distance z_u; remember that in this example $z_u=d_b$. The contents of the downflow region shift down a distance Δz, and the contents of the stagnant region remain unchanged. Note that the contents of the bubble "wake" at the surface of the bed (7_x, 8_x, and 9_x) supply the downflow region at the bed surface. Similarly, the downflow from interval 1 (i.e., 1_d) becomes the initial wake of the bubble entering the bottom of the bed, which supplies the exchange region. The arrows on Figure 6 illustrate the exchanges between the downflow and exchange regions at the top and bottom surfaces of the bed.

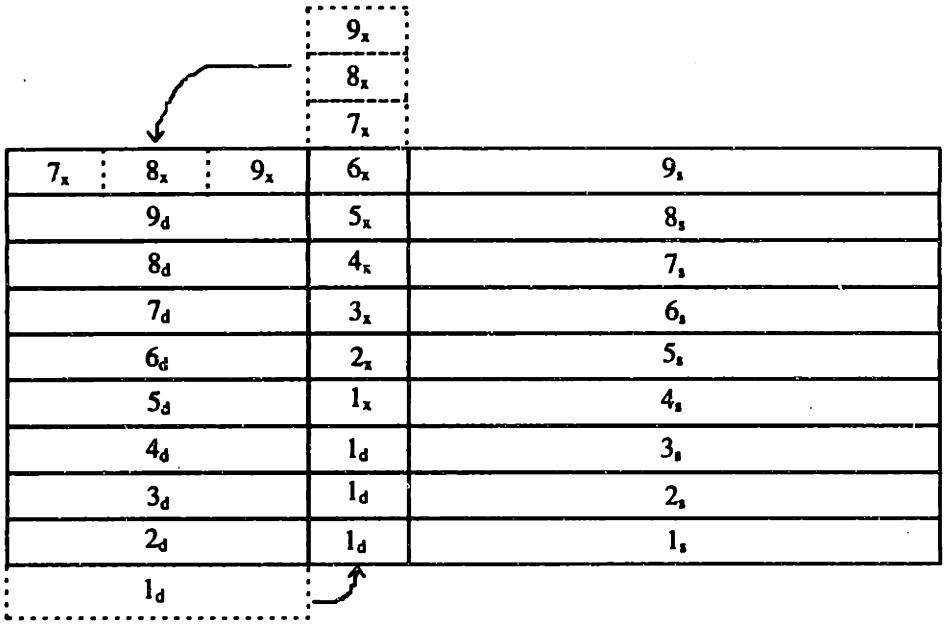

Figure 6: Contents of Bed Intervals After Bubble Passage

After the bubble passes, the contents of each interval are assumed to mix perfectly prior to the passage of the next bubble. Let m_l^p represent the mass fraction of species 1 at the current time step p, the mixture mass fraction in each interval is given by the following expressions. Define

$$n_{bot} \equiv \frac{\alpha_d}{\alpha_x}, \tag{14}$$

which, based on (3) and (7), is equal to z_u/z_d. For elements $i \le n_{bot}$,

$$m_{l_i}^p = \alpha_x \cdot m_{l_1}^{p-1} + \alpha_d \cdot m_{l_{i+1}}^{p-1} + \alpha_s \cdot m_{l_i}^{p-1}, \tag{15}$$

where $m_{l_i}^{p-1}$ is the mass fraction of species 1 in interval i, at the previous time step, p-1. Note that in Figure 6, the first 3 elements in the exchange region have a mass fraction of $m_{l_1}^{p-1}$ since $n_{bot}=3$ in this example (i.e., the bubble distributes the initial contents of its wake over the first n_{bot} elements). For the element at the surface of the bed, i=n,

$$m_{l_n}^p = \alpha_x \cdot m_{l_{n-nbot}}^{p-1} + \frac{\alpha_d}{n_{bot}} \cdot \sum_{j=0}^{(n_{bot}-1)} m_{l_{n-j}}^{p-1} + \alpha_s \cdot m_{l_n}^{p-1}. \tag{16}$$

Finally, for the intermediate elements where $n_{bot}<i<n$,

$$m_i^p = \alpha_x \cdot m_{i-nbot}^{p-1} + \alpha_d \cdot m_{i+1}^{p-1} + \alpha_s \cdot m_i^{p-1} . \quad (17)$$

These expressions should become clear by comparing the terms in each expression with the contents of each axial element shown in Figure 6. These expressions relate the mass fractions after the passage of a bubble (state shown in Figure 6) to a new state (shown in Figure 5) prior to the passage of the next bubble. This process repeats itself every $\Delta t=1/f_b$ seconds.

In the previous example, z_u/z_d was chosen to be 3 for simplicity. Based on the discussion in Section 10.1, $z_u \approx d_b$ and $z_d \approx d_b/8$ are more realistic choices.

10.2.1.1 Comparison of Axial Mixing Model Against Sitnai (1981) Data

Sitnai (1981) conducted solids mixing tests in a bubbling bed that conveniently isolated axial mixing effects. Most mixing studies have been conducted in high aspect-ratio beds with small particles and no tube bundle. The data from this study were obtained in an experimental rig that was representative of fluidized-bed combustors. Mixing data were taken in a 1.2 m x 1.2 m square bed with an array of tubes on approximately 10 cm centers. Silica sand with a mean particle size of 700 μm was used as the bed material, and 670 μm iron ore was used as a tracer. The size of the iron ore tracer was slightly smaller than the sand to provide approximately the same minimum fluidization velocity. Experiments were conducted by quickly distributing the iron ore tracer across the surface of the bed and then continuously drawing samples from different locations within the bed. The average sample composition was determined over 5 second intervals, providing the tracer concentration distribution as a function of time.

The Sitnai (1981) reference either provides, or makes it possible to roughly estimate, the input parameters for the axial mixing model. The model inputs and how they were specified are discussed below.

- Bubble Diameter, d_b

  Glicksman et al. (1987) found that the presence of a horizontal tube array in a large-particle fluidized bed tends to restrict bubble diameters to approximately the tube spacing. The tubes in Sitnai's (1981) experimental setup were arranged in a triangular arrangement on 10 cm centers, and thus, a bubble diameter of 10 cm was assumed.

- Bed Height, H

  Sitnai (1981) stated that the bed height for the experiments was 1.3-1.4 m. A bed height of 1.35 m was assumed.

- Bubble Fraction, δ

  The bubble fraction was given by Sitnai (1981) to be 0.12 and 0.18 for gas superficial velocities (u_o) of 0.6 m/s and 0.91 m/s, respectively. Presumably these estimates are based on bed expansion measurements.

- Bubble Frequency, f_b

  The bubble frequency can be estimated from predictions of the visible bubble flow. The visible bubble flow per unit area is given by

$$Q''_b = u_o - K \cdot u_{mf}, \tag{18}$$

  where K is the gas through-flow coefficient. Glicksman et al. (1991) proposed the following expression for K.

$$K = \exp\left[\delta \cdot \left(1.4 + \frac{7.6}{H/d_b}\right)\right]_{z=H}. \tag{19}$$

  The bubble frequency, f_b, is the number of bubbles passing through the area A (Figure 3) per unit time. This is expressed by

$$f_b = \frac{Q''_b \cdot A}{V_b}, \tag{20}$$

  where V_b is the bubble volume. Substituting (4), (8), and (18) into (20) gives

$$f_b = \frac{3 \cdot [u_o - K \cdot u_{mf}]}{2 \cdot d_b \cdot \delta}, \qquad (21)$$

where K is given by (19).

- Fraction of Bubble Volume Displaced, k_{vol}

  In the experimental studies discussed in 10.1, experimental estimates for k_{vol} ranged from 0.3 to 1.1. The value of k_{vol}=0.5 from potential flow theory appears to represent a reasonable compromise.

- Average Number of Bubble Diameters Particles are Displaced: k_{zu} and k_{zd}

  Cranfield's (1978) and Abrahami and Resnick's (1974) results suggest that a good estimate for k_{zu} is 1.0. Cranfield (1978) estimated that k_{zd} was roughly 1/8.

Although Sitnai (1981) sampled from many positions in the bed, the model is only compared against data taken from the middle of the bed. The model does not account for any gross circulation patterns within the bed. Thin downflowing layers are common at the walls of fluidized beds. Sitnai measured differences, at the same bed elevation, between the concentrations in the center of the bed and those at the wall.

Figure 7 compares the predicted and experimental concentration profiles as a function of time at a single elevation (z) in the bed, with a superficial velocity (u_o) of 0.6 m/s. m_1 represents the mass fraction of species 1 at an instant in time, while $m_{1\text{-}ss}$ is the concentration of species 1 if the contents of the bed were perfectly mixed. No effort was made to adjust parameters to fit the data in Figure 7. Considering the many rough assumptions, the agreement is very good.

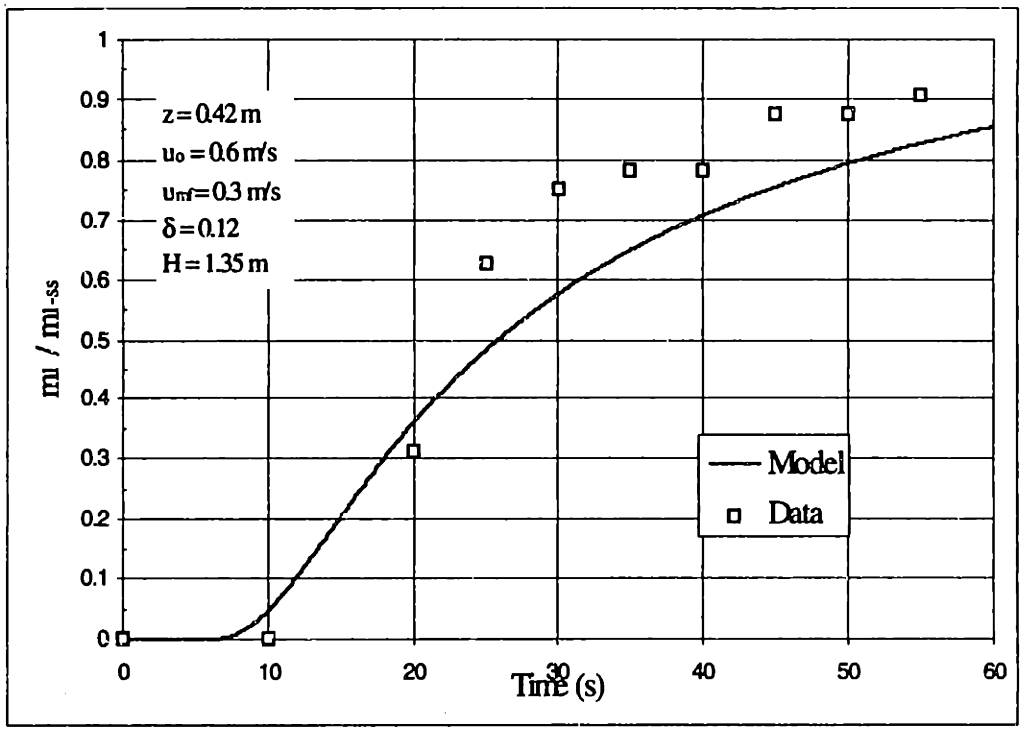

Figure 7: Comparison of Axial Mixing Model Predictions with Data–u_o=0.6 m/s

Figure 8 compares the model against concentration data with a superficial velocity of 0.91 m/s at two elevations in the bed. The agreement in this case is less satisfying.

One apparent contradiction is present in the data. The data shown in Figure 7 were sampled at an elevation of z=0.42 m with a superficial velocity of 0.6 m/s. One of the sets of data shown in Figure 8 was sampled at an elevation of z=0.63 m with a superficial velocity of 0.91 m/s. The concentration distribution for the case when u_o=0.6 m/s and z=0.42 m begins to develop earlier than the case when u_o=0.91 m/s and z=0.63 m. As the model predicts, one would expect the tracer concentration distribution at the same level in the bed to develop more quickly with u_o=0.91 m/s than when u_o=0.6 m/s. (This behavior was observed in the mixing data presented in Chapter 9.) Also, the tracer is initially spread across the surface of the bed, hence at the same u_o, one would expect the tracer to first appear at sampling ports higher in the bed (higher z). Both these expectations are contradicted by the data. In this case, the tracer appears earlier at the sampling port lower

in the bed for the test with lower superficial velocity. One possible explanation for this is the formation of gross circulation patterns in the bed as the superficial velocity is increased. The axial mixing model does not account for these effects.

The model consistently predicts that the concentration profile develops much more quickly than the data shows. Another problem with the predictions may be that the bubble frequency predicted by (21) may be too high. A lower bubble frequency would stretch the model concentration profile, but not change the magnitude of the predicted concentrations. It is encouraging that the model does a good job of predicting the magnitude of the concentrations. For example, at z=1.036 m, the model comes close to predicting the peak value of $m_l/m_{l\text{-}ss} \approx 2$ in the transient. Similarly, the model does a reasonable job of predicting the shape of the concentration time trace at z=0.626 m.

The results in Figures 7 and 8 suggest that better information on parameters like: k_{vol}, k_{zu}, k_{zd}, d_b, and f_b would produce more accurate predictions. Since the experiments had the tracer introduced at the top of the bed, the results of these comparisons are particularly sensitive to the value used for k_{zd}. The bubble measurements presented in Chapter 7 should help provide more accurate mixing predictions, through better information on d_b and f_b, in the current study on PFBCs. The presence of gross circulation patterns in the bed is another possible source of error in the predictions. Gross circulation of solids should be less important in PFBCs due to their tight tube bank configurations, although it may be present under the tube bank. Also, these experiments were conducted in a bed with tubes, while many of the input parameters such as: z_u, z_d, k_{vol}, etc., were obtained in open beds. There is currently no information available on the effect a tube bank has on these input parameters.

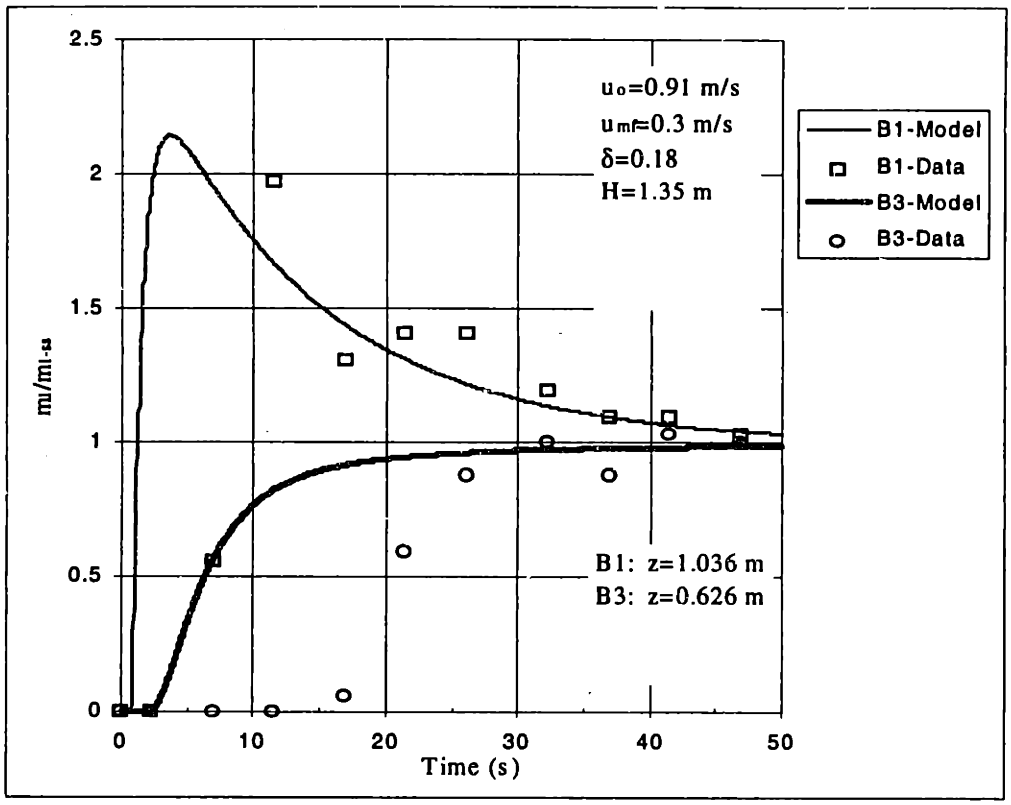

Figure 8: Comparison of Axial Mixing Model Predictions with Data–u_o=0.91m/s

10.2.2 Lateral Mixing Model

The lateral mixing model attributes all lateral mixing to the horizontal motion of bubbles as they move to coalesce with neighboring bubbles. This assumption is based on observations by Valenzuela and Glicksman (1984). In mixing experiments in a two-dimensional fluidized bed, they concluded that the horizontal displacement of solids was due primarily to lateral bubble motion. Hence, the mixing model attributes all the mixing of the solids to the bubble motion; the direction of the mixing (axial vs. lateral) depends on the direction of the bubble motion. Lateral mixing rates tend to be lower than axial mixing rates because of the preferential axial motion of bubbles rising to the surface of the bed.

The *lateral* mixing model does not account for the mixing that occurs in the splash zone, where erupting bubbles disperse the contents of their wakes across the surface of the bed.

The *axial* mixing model accounts for this to a limited degree, with ideal mixing over the area A, as discussed previously, but particles are most likely spread over a larger area than that defined by (4). One would expect coalescence rates, and thus lateral mixing rates, to be highest in the region below the tube bank. PFBC fuel feed points are typically positioned below the bottom of the tube bank. Since our primary interest is the mixing in the vicinity of the feed points, the boundary condition at the surface of the bed, particularly for the large bed depths found in PFBCs, should not be of significant importance.

10.2.2.1 Lateral Mixing Model Development

The lateral mixing model is based on three assumptions.

1. Bubbles are uniformly distributed across the cross-section of the bed. Glicksman and McAndrews (1985) showed that this was the case in large-particle fluidized beds.
2. Over a specified distance, Δz_c, each bubble participates in one coalescence (i.e., either as a coalescer or a coalescee) causing the number of bubbles at that level in the bed to be halved.
3. The volume of solids transported by bubbles at the time of coalescence (this will be referred to as the wake, although it includes contributions from drift as well), combine to form the new wake of the larger bubble resulting from the coalescence.
4. The solids entering an element are well mixed after each bubble passage.

The lateral mixing model builds on the framework developed for the axial mixing model. But now, rather than considering a single repeating area as defined by (4) with only the vertical axis discretized, it is now necessary to discretize the cross-section of the bed laterally as well. Figure 9 shows the cross-section of a bed of width, w, and depth, d, broken into discrete repeating units of area, A. Each of the repeating unit areas in Figure 9 contains a single bubble and corresponds to the area shown in Figure 3. But different

areas may have different solids concentrations, caused, for example, by the presence of a discrete solids feed point.

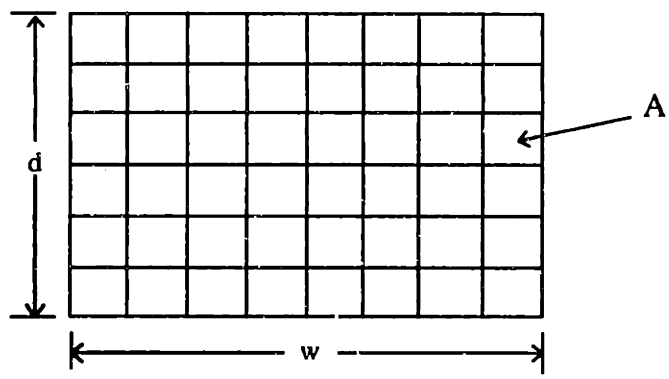

Figure 9: Discretized Fluidized Bed Cross-Section

When coalescence takes place at a particular elevation in the bed (z_c), the number of bubbles, and hence unit areas, is reduced by a factor of two (assumption 2). For example, the cross-section shown in Figure 9 would go from 48 bubbles to 24. According to assumption 1, the bubbles are uniformly distributed across the cross-section of the bed, both prior to and after coalescence. Figure 10 illustrates a discretized section of a bed cross-section after coalescence overlaid on top of the cross-section prior to coalescence.

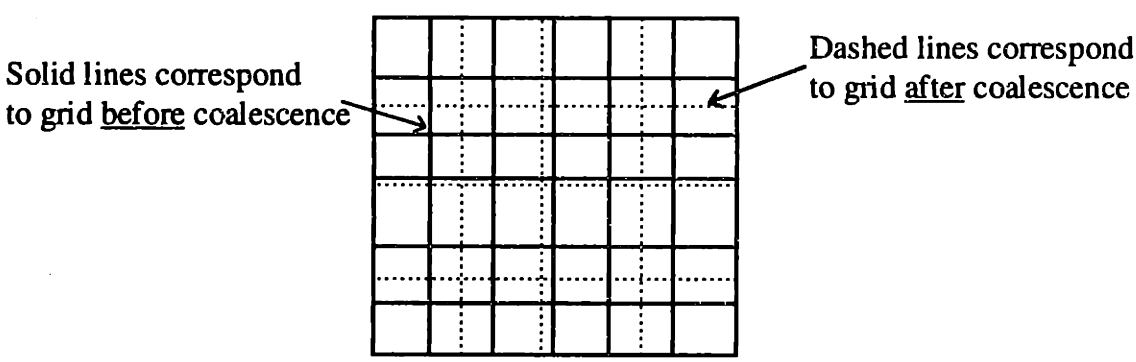

Figure 10: Comparison of Discretized Section of Bed Before and After Coalescence

As shown in the figure, the repeating areas after coalescence (defined by the dashed lines) are positioned above all of some, and part of other repeating areas in the grid before coalescence (defined by the solid lines). Note that each area corresponds to an element such as that shown in Figure 4. The procedure for discretizing the bed cross-section is presented in Section 10.2.3.1. Assumption 3 requires that the wakes of the bubbles in the areas prior to coalescence combine to form the wakes of the bubbles after coalescence. In the current model, lateral mixing is achieved by calculating the concentration of the post-coalescence wakes using the area-weighted average of the wake concentrations prior to coalescence. The weighting factors correspond to the fraction of an area of a pre-coalescence grid that lies below an area in the post-coalescence grid. This is shown more clearly in Figure 11.

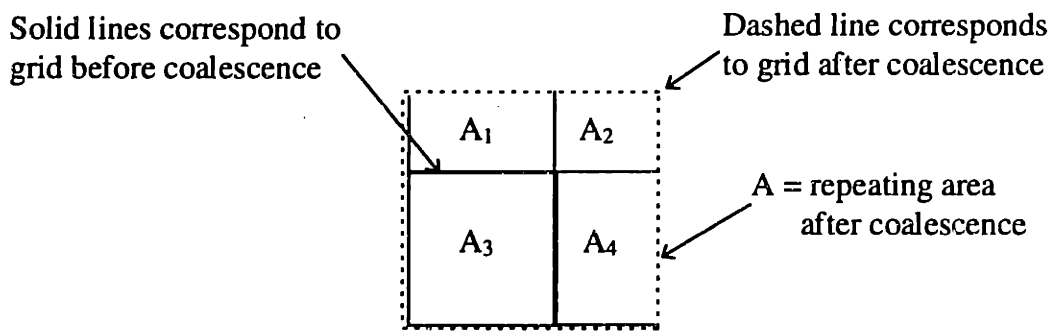

Figure 11: Area Weighting of Wake Flows

Using Figure 11 as an example, the mass fraction of species 1 in the wake of post-coalescence area A (m_{1w}^{A}) is given by

$$m_{1w}^{A} = m_{1w}^{A1}\left(\frac{A_1}{A}\right) + m_{1w}^{A2}\left(\frac{A_2}{A}\right) + m_{1w}^{A3}\left(\frac{A_3}{A}\right) + m_{1w}^{A4}\left(\frac{A_4}{A}\right), \qquad (22)$$

where, for example, m_{1w}^{A1} is the mass fraction of species 1 in the wake of the element of which area A_1 is a part. In this instance, A_1, for example, is the area of an element in the pre-coalescence grid that lies below A–the element area in the post-coalescence grid whose wake concentration is being evaluated.

Recall from the discussion of the axial mixing model that each vertical element experiences a downflow from the element above. The downflow between post- and pre-coalescence grids requires an area weighting similar to (22). Figure 12 illustrates the area relationships between the downflow from the grid after coalescence to the grid prior to coalescence. The subscripts ac and pc refer to after-coalescence and prior-to-coalescence, respectively. The dashed lines, which form larger areas (A_{ac}), correspond to the grid after coalescence. The solid lines, which form the smaller grid (A_{pc}), correspond to the grid prior to coalescence.

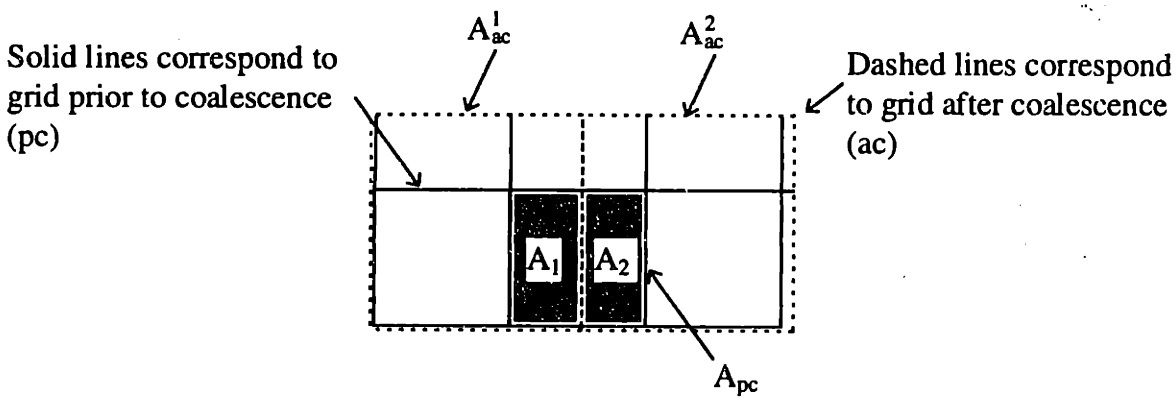

Figure 12: Area Weighting of Downflows

The concentration of the downflow into area A_{pc} from elements in the after-coalescence grid is given by

$$m_1^{A_{pc}} = m_1^{A^1_{ac}}\left(\frac{A_1}{A_{pc}}\right) + m_1^{A^2_{ac}}\left(\frac{A_2}{A_{pc}}\right), \tag{23}$$

where:

$m_1^{A^1_{ac}}$ =the mass concentration of species 1 in area A^1_{ac};

$m_1^{A^2_{ac}}$ =the mass concentration of species 1 in area A^2_{ac};

A_1=the part of area A^1_{ac} positioned over A_{pc}; and

A_2=the part of area A^2_{ac} positioned over A_{pc}.

Lateral mixing occurs as bubbles coalesce. The lateral mixing model accounts for this by reducing the number of bubbles in half at a specified coalescence elevations (z_{c_j}). The wakes of the bubbles prior to coalescence combine to form the wakes of the bubbles after coalescence. The concentrations of the bubble wakes in the elements after coalescence are a function of the concentrations of the bubble wakes in the prior-to-coalescence elements that lie below the after-coalescence element, as shown in the development of (22). Similarly, the downflow from the larger after-coalescence elements is distributed amongst the prior-to-coalescence elements that lie directly below them. The concentration of the downflow that a prior-to-coalescence receives is determine following the approach used to develop (23). These exchanges between different spaced grids at an elevation in the bed are used in conjunction with the axial mixing model, developed in Section 10.2.1, to create an integrated solids mixing model. The development of this integrated model is presented in Section 10.2.3.

10.2.3 Integrated Solids Mixing Model

It is now possible to use the axial and lateral mixing models discussed in Sections 10.2.1 and 10.2.2 to construct an integrated three-dimensional bubbling-bed mixing model. As with the axial mixing model, the features of the integrated solids mixing model will first be described in words and then developed mathematically.

The integrated model views the bubbling bed as a progression of bubbles rising axially and then coalescing, rising axially and then coalescing, etc. Only axial mixing occurs while the bubbles rise; lateral mixing occurs at the point of coalescence. Hence, the model consists of axial mixing regions, whose boundaries are defined by coalescence elevations (z_c) and the top and bottom of the bed. Figure 13 illustrates the integrated mixing model.

As shown in Figure 13, the bed is broken into a set of axial mixing regions. Each region is constructed of elements, such as the one shown in Figure 4. These elements are the

"bricks" that form a region. In the axial mixing model, these bricks were only stacked one on top of the other. Here, regions are constructed of these elements by not only stacking them axially but also by filling the region laterally with these stacks of elements. The elements in these stacks do not interact laterally within a region, only at the boundaries of a region.

The coalescence elevations (z_c) shown in Figure 13 are inputs to the model that are determined from a coalescence model; this will be described further in Section 10.2.3.1.3. The cross-section of each region is discretized as shown in Figure 9, and each area, A, within the cross-section, has its own exchange, downflow, and stagnant regions (see Figure 3). The wakes of the bubbles leaving the elements on the top surface of a region combine to form the initial bubble wakes in the region above it. The concentrations of the initial bubble wakes are determined using the approach used to derive (22). The downflows from the elements on the bottom surface of a region provide the downflows into the elements on the upper surface of the region below it. The concentrations for the downflows into each element are determined using the approach used to develop (23). Figure 13 also shows that at the top surface of the bed (Region n), the bubble wakes in each area, A, supply the downflow region for that area. And at the bottom of the bed (Region 1), the downflow from each area, A, provides the initial bubble wake for that area. The boundary conditions at the top and bottom of the bed are applied for each element across the bed cross-section in exactly the same way they were applied for the axial mixing model.

Figure 14 presents a more detailed schematic of an individual axial mixing region. The figure shows how the stacks of elements fill the cross-section of the bed. A single element within a stack is identified. Note that each element is the basic building block illustrated in Figures 3 and 4.

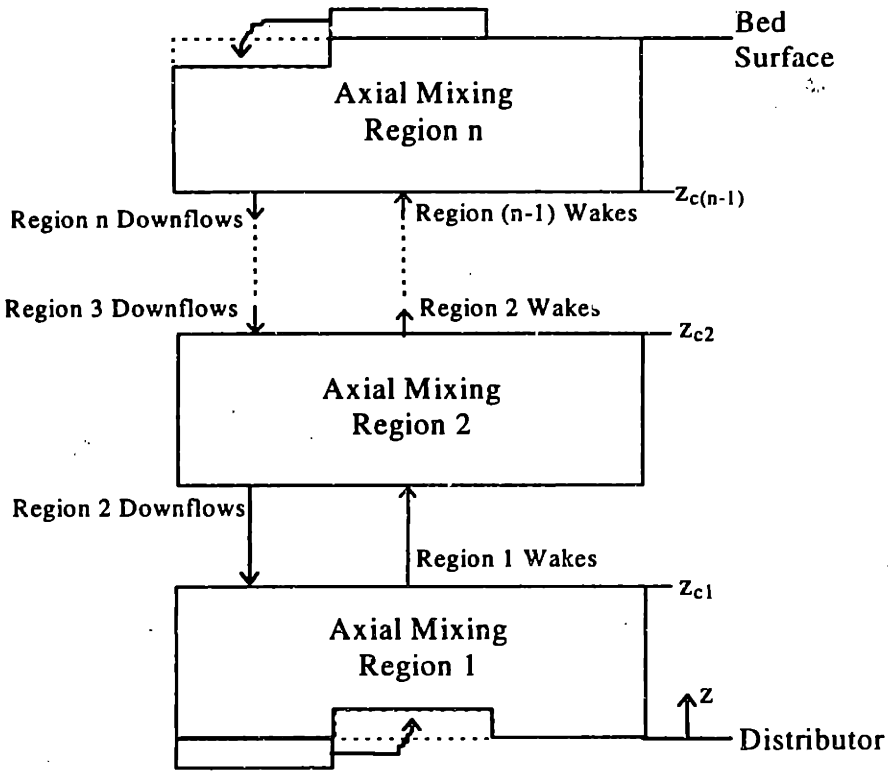

Figure 13: Illustration of Integrated Mixing Model

As just discussed, the wake and downflow concentrations *received* by each element on a region's boundary are calculated from the concentrations of the wakes and downflows *leaving* elements on the surface of adjacent regions. The wake and downflow concentrations received are determined using the area-weighting demonstrated in (22) and (23). The following set of expressions are for the wake and downflow concentrations entering and leaving the elements on the surfaces of a region.

Due to the many indices and subscripts that are required to distinguish between different mass fractions (m), a brief nomenclature list is provided before proceeding. As mentioned previously, regions are constructed of stacks of elements. The index k is used to identify an element's axial position within the stack.

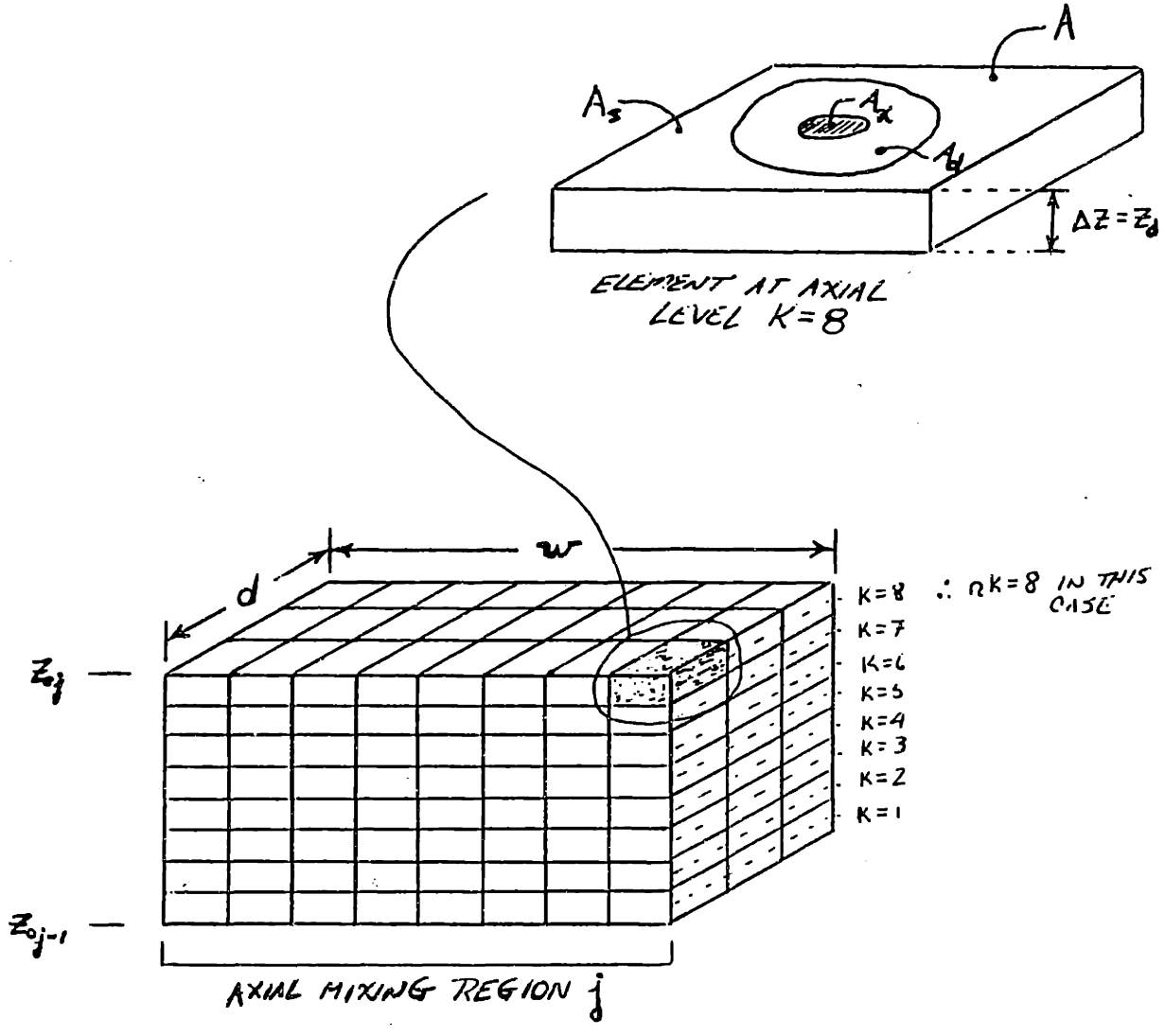

Figure 14: Definition of Elements and Regions

m_{1w_j} ≡ the mass fraction of species 1 in the wake leaving an element on the upper surface of Region j.

m_{1w_0} ≡ is the mass fraction of the wake entering the bottom of Region 1.

m_{1k_j} ≡ the mass fraction of species 1 in an element at axial level k within Region j. So for example, m_{1l_j} is the mass fraction of species 1 in an element on the bottom of Region j.

m_{1d_j} ≡ the mass fraction of species 1 in the downflow entering an element on the upper surface of Region j.

In addition to this already complicated list of subscripts, each element on a region's surface has two additional indices reflecting its coordinates on the surface (e.g., see Figure 14). Each region is constructed of many "stacks" of elements. These indices identify which stack an element resides in. These indices are omitted to avoid further complication of the nomenclature.

The composition of a wake leaving an element on the surface of Region j depends on whether the number of axial elements in the region is larger than n_{bot}, defined by (14). If nk is the number of axial elements in Region j, for $nk \le n_{bot}$,

$$m_{1w_j} = \frac{1}{n_{bot}} \cdot \left((n_{bot} - nk) \cdot m_{1l_j} + \sum_{k=1}^{nk} m_{1k_j} \right). \tag{24}$$

Otherwise, if $nk > n_{bot}$,

$$m_{1w_j} = \frac{1}{n_{bot}} \cdot \sum_{k=1}^{n_{bot}} m_{1(nk-k+1)_j}. \tag{25}$$

The concentration of the "wake" entering Region 1 (m_{1w_0}) is given by

$$m_{1w_0} = m_{1l_1}, \tag{26}$$

where m_{1l_1} is the concentration of species 1 in axial element 1 of Region 1.

The concentration of the downflow from an element on the bottom surface of Region j+1 to the top surface Region j (m_{1d_j}) is given by

$$m_{1d_j} = m_{1l(j+1)}, \tag{27}$$

where $m_{1l(j+1)}$ is the mass fraction of species 1 in axial element 1 of region (j+1). The exception to this occurs at the bed surface (Region n) where

$$m_{ld_n} = m_{lw_n}; \tag{28}$$

i.e., the wake of an element on the surface of Region n supplies its own downflow region.

Let nx_j represent the number of elements across the bed width in Region j. Similarly, let ny_j represent the number of elements spanning the bed depth in Region j. According to Assumption 3 in Section 10.2.2.1, the bubbles "wake" volumes prior to coalescence combine to form the wakes of the larger post-coalescence bubbles. If V_{u_j} represents the volume transported by a bubble in Region j, in order to ensure mass conservation, $V_{u_{j+1}}$ must satisfy

$$V_{u_{j+1}} = V_{u_j} \cdot \frac{nx_j \cdot ny_j}{nx_{j+1} \cdot ny_{j+1}}. \tag{29}$$

The ratio on the right hand side of (29) is ideally 2, since according to assumption 2 of Section 10.2.2.1, the number of bubbles is reduced in half as a result of the coalescence. Equation (29) is required to ensure that mass is conserved, because it may not be possible to specify nx and ny such that the ratio is exactly 2. The initial assumption for V_{u_1} in Region 1 is given by (8) and (9), based on an assumed k_{vol} and a calculated initial bubble diameter (see Section 10.2.3.1.2). If bubble volume is assumed to be conserved in the coalescence, the ratio of displaced to bubble volume (k_{vol}) will remain constant throughout the bed.

10.2.3.1 Mixing Model Inputs

Sections 10.2.3.1.1-10.2.3.1.3 provide a discussion of the inputs to the integrated mixing model. Sample output from the model is presented in Section 10.3. The predictions in Section 10.3 correspond to the cold model operating at the scaled Tidd PFBC operating

condition. The inputs for these predictions are used as examples in Sections 10.2.3.1.1-10.2.3.1.3.

10.2.3.1.1 Axial Mixing Model Inputs

The axial mixing model inputs were discussed in detail in Section 10.2.1.1. They are summarized briefly again here in the context of the results presented in Section 10.3.

- Bubble Diameter, d_b

  Bubble diameter calculations are discussed in detail in Section 10.2.3.1.2.

- Bed Height, H

  Bed height typically is estimated from pressure drop measurements. Alternatively, if data are not available, Glicksman et al. (1991) present a model for predicting the expanded bed height. The bed expansion measurements from the cold model of the Tidd PFBC (Chapter 7) suggest that a through-flow coefficient (K) of 1 should be used in the Glicksman et al. (1991) model for predicting PFBC bed expansion. The cold-model expanded bed height (H) at the conditions under consideration was measured to be 47.1 cm.

- Bubble Fraction, δ

  Overall bed average bubble fraction ($\overline{\delta}$) is typically inferred from bed expansion measurements. The overall bed average bubble fraction ($\overline{\delta}$) for the cold model was found to be 0.39.

- Bubble Frequency, f_b

  If no data are available on bubble frequency in a bed, (21) should provide a rough estimate for f_b. Bubble frequency was measured in the cold model (see Chapter 7). These measurements will be used for the predictions in Section 10.3.

Bubble probes measure the frequency of bubbles passing through an area surrounding the probe. It is therefore necessary to estimate this measurement area. Once this area is specified, the probe bubble frequency can be corrected to give the frequency of bubbles passing through the repeating area A, given by (4). Ideally, a bubble probe at a point should be able to sense bubbles passing within one bubble diameter of the probe as illustrated in Figure 15.

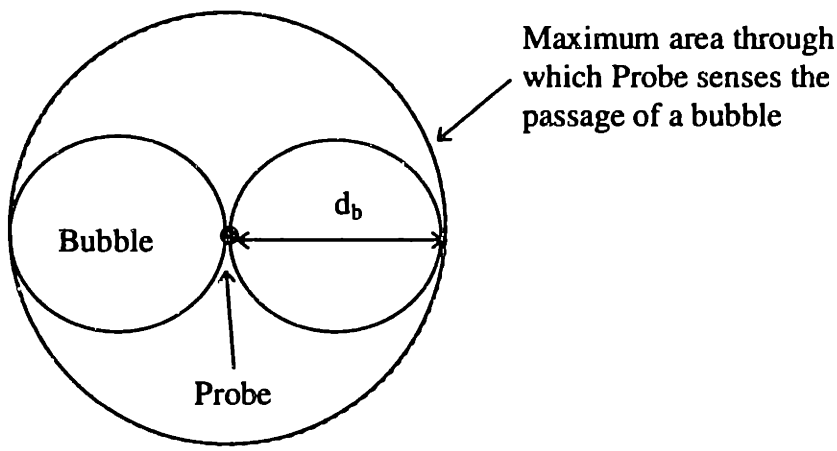

Figure 15: Maximum Area Over Which a Point Probe Could Record Bubble Passage

For uniformly distributed bubbles, the bubble frequency per unit area is constant. Using the area shown in Figure 15 gives

$$f''_b = \frac{f_b^{probe}}{\pi d_b^2} = \text{constant}. \tag{30}$$

Using (4) and (30), the bubble frequency through A that provides the same f''_b as measured with the bubble probe is given by

$$f_b = \frac{f_b^{probe}}{4 \cdot \delta}. \tag{31}$$

The probe used in this study was not a point probe, which reduces the measurement area of the probe. This is illustrated in Figure 16.

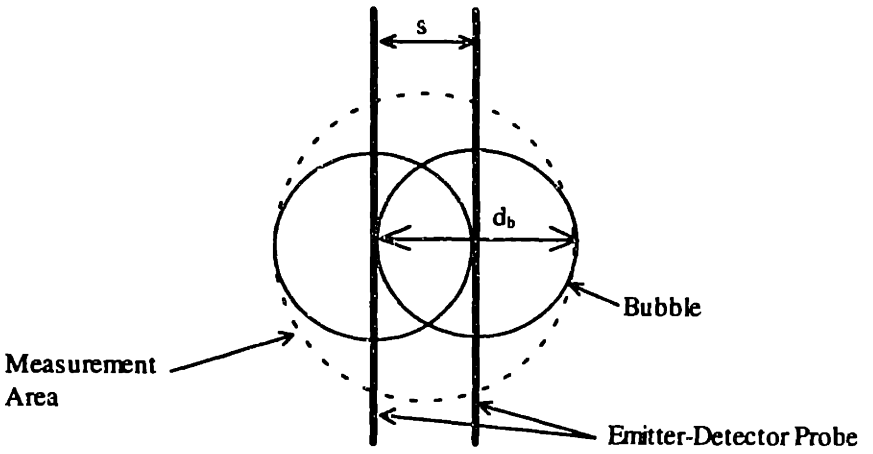

Figure 16: Area over Which Emitter-Detector Probe Could Record Bubble Passage

Rewriting (30) for the measurement area shown in Figure 16 gives

$$f''_b = \frac{f_b^{probe}}{\pi\left(d_b - \frac{s}{2}\right)^2} = constant. \tag{32}$$

Using (4) and (32), the bubble frequency through A that provides the same f''_b as measured with the bubble probe is given by

$$f_b = f_b^{probe} \frac{d_b^2}{4\delta \cdot \left(d_b - \frac{s}{2}\right)^2}, \tag{33}$$

which converges to (31) when s=0.

The cold model bubble frequency at the conditions under consideration was measured to be $f_b^{probe} \approx 7$ Hz.

- k_{vol}

  k_{vol} was assumed to be 0.5.

- k_{zu} and k_{zd}

  k_{zu} and k_{zd} were assumed to be 1.0 and 1/8, respectively.

10.2.3.1.2 Bubble Diameter in Each Region

The mixing model requires that a bubble diameter be specified for each region. Once an initial bubble diameter is specified for Region 1 (d_{b1}), the bubble diameters in subsequent regions are easily calculated if bubble volume is assumed to be conserved.

Kunii and Levenspiel (1991) give two expressions for calculating the bubble size at the distributor. If $d_{b1} \leq l_{or}$, where l_{or} is the spacing between adjacent holes in the distributor, they recommend

$$d_{b1} = \frac{1.30}{g^{0.2}} \cdot \left(\frac{u_o - u_{mf}}{N_{or}} \right)^{0.4} . \tag{34}$$

N_{or} is the number of orifice holes per unit area. At higher gas flow rates, where $d_{b1} > l_{or}$, Kunii and Levenspiel (1991) recommend

$$d_{b1} = \frac{2.78}{g} \cdot (u_o - u_{mf})^2 \tag{35}$$

Equation (35) results from an analysis given by Miwa et al. (1972).

Assuming bubble volume is conserved in a coalescence, the bubble size in Region j, d_{bj}, is related to the bubble size in Region (j-1) through

$$d_{bj} = \sqrt[3]{2} \cdot d_{bj-1} = 1.26 \cdot d_{bj-1} . \tag{36}$$

In the cold model of the Tidd PFBC, the distance between the holes in the distributor (l_{or}) is 0.5 cm, and there are approximately 0.43 holes/cm^2 (N_{or}). The cold model operates at a superficial velocity of 0.46 m/s, with a minimum fluidization velocity of 0.12 m/s. These conditions correspond to the scaled Tidd PFBC operating conditions. Calculating d_{b1} at these conditions using both (34) and (35), shows that $d_{b1} > l_{or}$ and therefore (35) is the

appropriate expression to use to calculate d_{b1}. The resulting initial bubble size is d_{b1}=3.3 cm. Equation (36) gives the bubble diameters in the remaining regions. Table 1 gives estimates of the bubble diameters in Regions 1-4. The description of how the elevations at which bubble coalescence takes place (z_c) are specified is provided in the next section.

Table 1: Estimated Bubble Sizes in the Cold Model

Region,j	d_{bj} (cm)
1	3.28
2	4.13
3	5.20
4	6.55

10.2.3.1.3 Bubble Coalescence Rate

Glicksman and McAndrews (1985) showed that bubbles are distributed randomly/uniformly across the cross-section of large-particle fluidized beds with horizontal tube banks. This uniformity permits the use of a one-dimensional bubble coalescence model. Glicksman et al. (1987) relate the bubble frequency to the coalescence rate using

$$\frac{d(f_b/A)}{dz} = -\frac{1}{2}\frac{(f_b/A)}{\Delta z_c}. \tag{37}$$

This expression states that if every bubble participates in one coalescence over a distance Δz_c–the average distance a bubble rises between coalescences–the number of bubbles will be reduced in half. Expressing (37) in dimensionless form gives

$$-\frac{d_b}{(f_b/A)}\cdot\frac{d(f_b/A)}{dz} = \frac{d_b}{2\cdot\Delta z_c} = C(\delta). \tag{38}$$

$C(\delta)$ represents the dimensionless coalescence rate, which has been found to be a function of the bubble fraction (δ). Several models have been proposed for $C(\delta)$. Using the Clift

and Grace (1970) model, which is more appropriate for small particles, and assuming that the bubbles are distributed in a uniform cubic array (Glicksman et al., 1987) gives

$$C(\delta) \approx \frac{1}{2}\left(\frac{6}{\pi}\delta\right)^{1/3} . \tag{39}$$

Glicksman et al. (1987) found that (39) underpredicted the coalescence rate in large-particle fluidized beds and proposed a statistical coalescence model. They showed that the results of this model were closely approximated by

$$C(\delta) = 12(\delta)^{5/4} . \tag{40}$$

PFBCs tend to have deep beds, and their tight tube banks keep bubbles small. These two factors tend to minimize gas through-flow, producing high bubble fractions. Although one would expect (40) to be more appropriate for the larger particles used in PFBCs, the high bubble fractions cause (40) to predict unrealistically high coalescence rates. For example, the cold model bed average bubble fraction ($\bar{\delta}$) at the Tidd PFBC operating condition is 0.39. Using (38) and (40), the number of bubbles would be reduced by a factor of 2 after rising a distance of $d_b/7.4$. At this rate, neglecting bubble splitting, the bubbles would quickly grow very large, and the number of bubbles in the bed would become unrealistically small. Equation (39) appears to predict more reasonable coalescence rates for PFBCs, but further study is needed to better quantify bubble coalescence and splitting under these conditions.

The lateral mixing model requires an estimate of the elevations at which coalescence occurs (z_{c_j}). Thus, a coalescence model is required to establish the input to the mixing model, but it is not an integral part of the mixing model framework. Different coalescence models can be used depending on the situation under consideration.

When modeling the solids mixing in the cold-scale model of the Tidd PFBC, the bubble size measurements discussed in Chapter 7, provide additional information to guide the choice of dimensionless coalescence rates. In particular, they show that for $u_o/u_{mf}=3.83$, d_b is approximately 5 cm at the bottom of the tube bank. Using an overall bed bubble

fraction of 0.39, (39) predicts C(0.39)=0.453. At this coalescence rate, the bottom of the tube bank lies in Region 4 where d_b is 6.6 cm (see Table 1). Hence, even (39) appears to predict too high a coalescence rate, at least when (35) is used to calculate d_{b_1}. The divergence may also be because the bubbles split as well as coalesce.

The approach taken here is to use (38) and estimate a value for C(δ) such that in the distance between the distributor and the bottom of the tube bank, the bubble grows to match the measured bubble size at the base of the tube bank. For example, Table 1 gives estimates of the bubble size in the first four regions of the cold model. The bottom of the cold model tube bank corresponds to z=17.2 cm. The data from Chapter 7 suggest that, at these conditions, at an elevation of 13 cm, $d_b \approx 4$ cm and at 17 cm, $d_b \approx 5$ cm. It seems reasonable to assume that the coalescence that causes the bubble diameter to grow from 4 to 5 cm in diameter occurs at an elevation of roughly 15 cm. Using (38) and the results in Table 1, a dimensionless coalescence rate of $C(\delta) \approx 0.25$ satisfies this condition. Using $C(\delta) \approx 0.25$ and (38), the elevations in the cold model at which coalescence occurs (z_{c_j}) can be calculated. Table 2 summarizes the results.

Table 2: Summary of Model Inputs for Cold Model of Tidd PFBC

Region	d_b (cm)	z_{c_j} (cm)	nx_j	ny_j
1	3.28	6.55	18	10
2	4.13	14.81	13	7
3	5.20	25.22	9	5
4	6.55	—	6	4

Table 2 also includes values for nx_j and ny_j, the number of elements across the width and depth of the bed, respectively, for a Region j. The procedure for determining nx_j and ny_j is best illustrated by going through the calculations that were followed to arrive at the values given in Table 2. But first, it is important to understand that regardless of the values for nx_j and ny_j, each region must sit directly over the region below it and directly under the

region above it so that mass is conserved. In other words, each region must be exactly w wide and d deep. Hence, the exact width (Δx_j) and depth (Δy_j) of the elements in Region j must satisfy

$$\Delta x_j = \frac{w}{nx_j} \text{ and } \Delta y_j = \frac{d}{ny_j}. \tag{41}$$

The bed width and depth are inputs to the model. The cold model of the Tidd PFBC is 85 cm wide and 46 cm deep. There are two additional guidelines that are important but subordinate to the requirement expressed by (41). The first guideline is that the number of elements be reduced by a factor of two after a coalescence (i.e., in going from Region j to Region j+1), to satisfy (37). Deviations from an exact reduction by a factor of 2 are corrected for by (29). The second guideline is that the elements be approximately square to keep the bubbles distributed as uniformly as possible across the cross-section of the bed.

The size and number of elements across the bed cross-section in Region 1 forms the starting point from which the size and number of elements in higher regions are determined. Beginning with Region 1, the area of an element (A) in Region 1 is estimated using (4), the bubble fraction (δ), and the bubble diameter at the distributor (d_{b_1}). (See Section 10.2.3.1 for a discussion on the model inputs.) For d_{b_1}=3.28 cm and δ=0.39, (4) gives an element area of 21.67 cm^2. Using this area to estimate the dimensions of the element assuming that the area is square gives: $\Delta x_1 = \Delta y_1 \approx \sqrt{A_1}$ =4.65 cm. Dividing the width (w) and depth (d) of the bed by these dimensions provides an estimate of the number of elements that will fit across the bed cross-section. This gives that $w/\Delta x_1 = 18.28$ and $d/\Delta y_1 = 9.89$. Rounding these numbers off to provide an integer number of elements gives: nx_1=18 and ny_1=10 (180 bubbles), which are the numbers for Region 1 in Table 2. Equation (41) then requires that Δx_1=4.72 cm and Δy_1=4.60 cm, satisfying the objective of keeping the elements as square as possible.

The number of elements across the width and depth of the bed for Region 2 must be approximately half those in Region 1. Region 1 had 180 bubbles, hence, Region 2 should have 90 bubbles. The area of an element in Region 2 is estimated by dividing the bed cross-sectional area into 90 elements. Dividing the product of the bed width and depth by 90 gives an element area of 43.44 cm^2, which assuming the elements are square corresponds to $\Delta x_2 = \Delta y_2 \approx 6.59$ cm. Now, as with Region 1, dividing the width (w) and depth (d) of the bed by Δx_2 and Δy_2 to estimate the number of elements that will fit across the bed cross-section gives: $w/\Delta x_1 = 12.90$ and $d/\Delta y_1 = 6.98$. Again, rounding these numbers off to provide an integer number of elements gives: nx_1=13 and ny_1=7 (91 bubbles). Equation (41) requires that Δx_1=6.54 cm and Δy_1=6.57 cm, providing approximately square elements. For Region 3 and subsequent regions, the number of bubbles is halved from that in the previous region, and the procedure followed for Region 2 is repeated.

10.2.4 Calculational Procedure

The following steps summarize the procedure for implementing the mixing model described in the previous sections.

1. Calculate the element width (Δx_j) and depth (Δy_j) using (41).
2. Calculate the wake and downflow area-weighting ratios illustrated in Figures 11 and 12, and used in (22) and (23).
3. Estimate the frequency of bubbles passing through A using either (21) or (31). The time step for the simulation is given by $\Delta t = 1/f_b$.
4. Calculate the area ratios given in (7), using Equations (6), (8), (11), and (12). Calculate n_{bot} using (14).
5. Set the initial conditions for the mass fraction of species 1 in each element, for each Region j, i.e., $m_1(i,jj,k)_j$. Where indices i, jj, and k represent an element's (x,y,z) position within Region j.
6. Repeat the following calculations for each time step.

a) Calculate the "new" concentrations for each element in each region. The new concentrations are given by (15)-(17). The exchange region concentrations consist of the original contents of the axial elements and the wake concentrations given by (24)-(26). The concentrations in the downflow region consist of the original contents in the axial elements, and the downflow concentrations given by (27)-(28). The contributions of the wake and downflows from elements in adjacent regions are determined using the area ratios calculated in Step 2.

b) Reset the "old" concentrations equal to the "new" concentrations to serve as the initial condition for the next time step.

c) Increment the time by Δt and return to step 6a).

10.3 Sample Model Output

The integrated mixing model was run using the inputs described in Section 10.2.3.1. The mass fraction distribution of species 1 (m_1) was calculated as a function of time. Initially, m_1 was specified to be 1.0 in an element located in the middle of the bed, 8.5 cm above the distributor; the surrounding elements had m_1=0. This initial condition was chosen to simulate coal input for a short period of time with all the mixing due to the bubble motion (i.e., negligible inlet jet momentum). The m_1 distribution results are shown at three different times in Figures 17-19. The origin (0,0) shown on the figures corresponds the point where m_1 was initially 1.0.

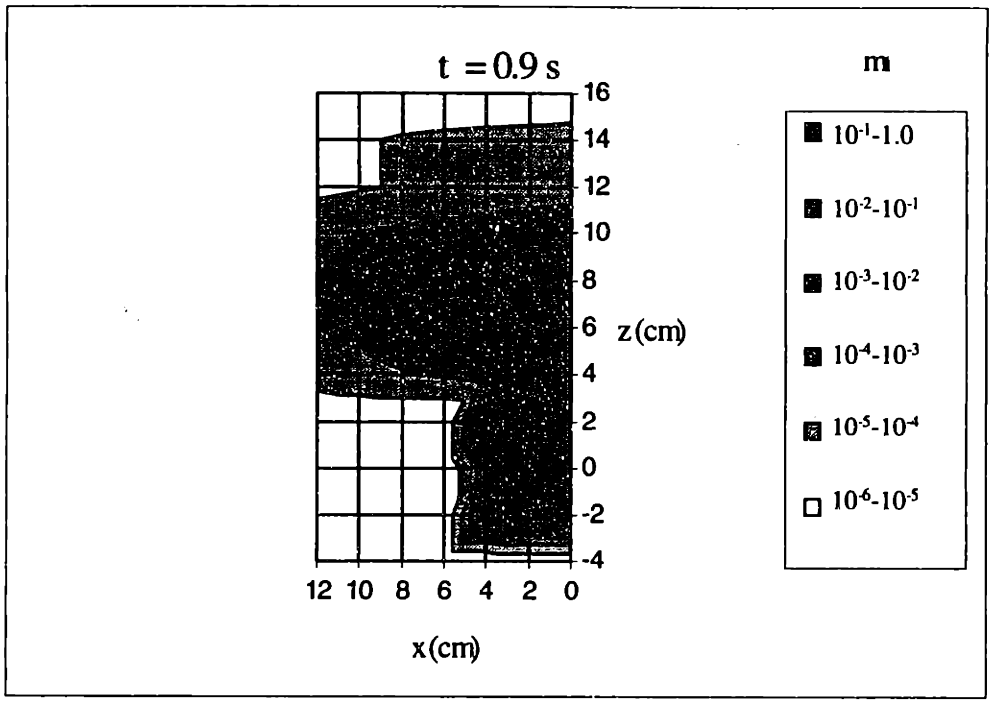

Figure 17: Distribution of Predicted m_1 after 0.9s

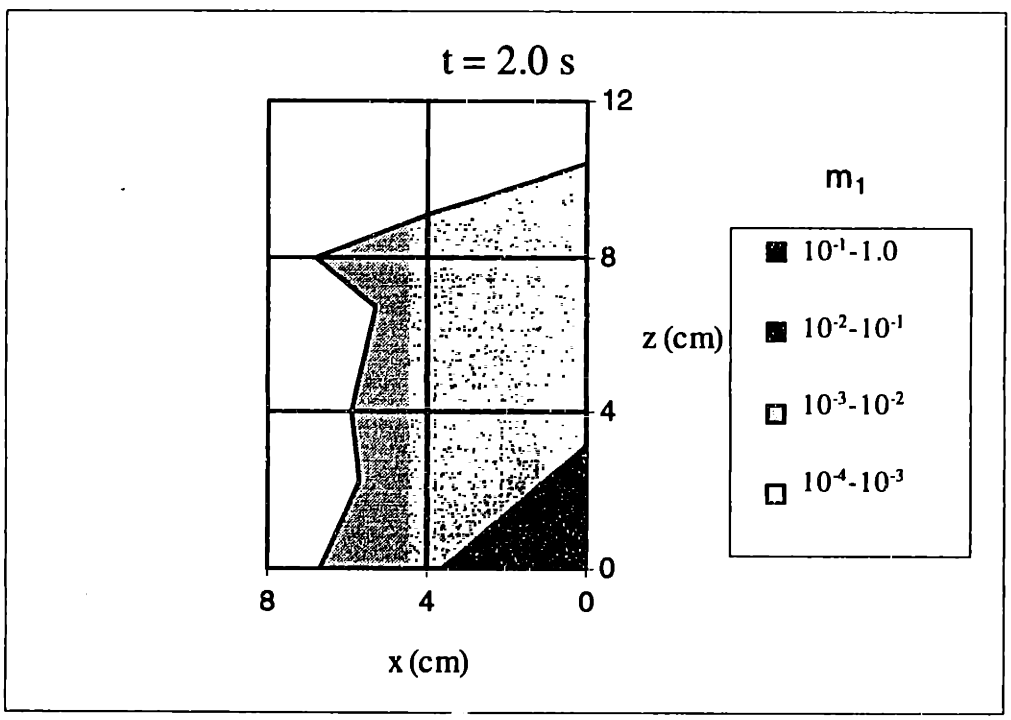

Figure 18: Distribution of Predicted m_1 after 2.0s

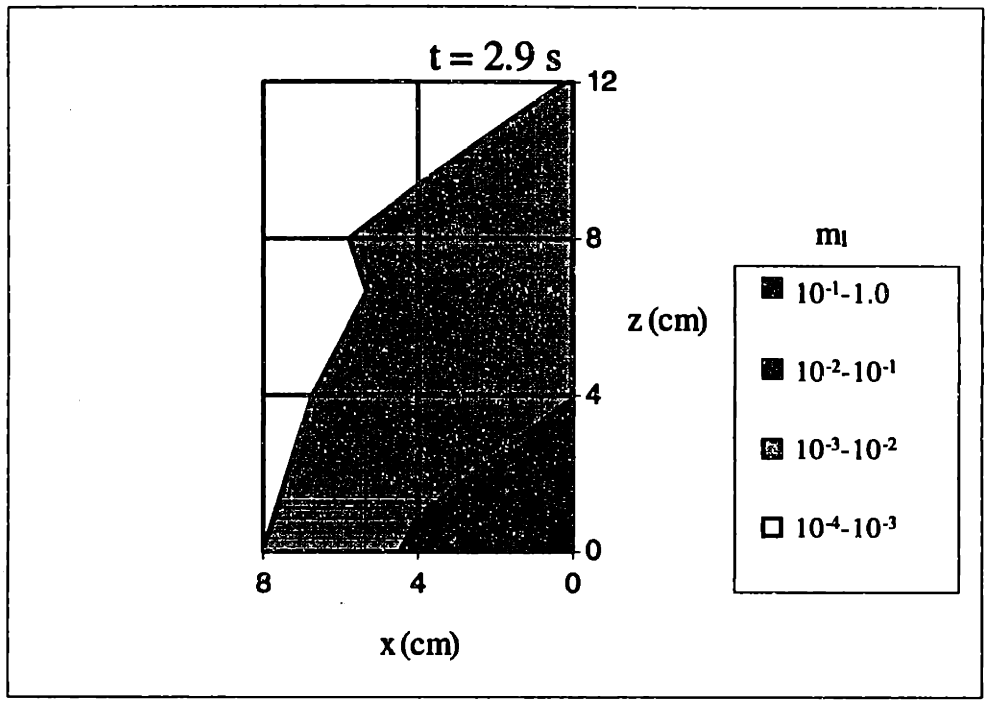

Figure 19: Distribution of Predicted m_i after 2.9s

In general, Figures 17-19 exhibit the expected behavior. In particular, the initial contents of the element at the origin are mixed axially and laterally with the surrounding bed material. Axial mixing rates are higher than lateral mixing rates, and upward mixing rates are faster than downward mixing rates, as shown in Figure 17. The strong lateral mixing exhibited at z≈5cm in Figure 17 is due to the presence of the boundary (z_{c_2}) between Regions 2 and 3. All the lateral mixing occurs at this one elevation in the bed. For short times, when there are large concentration gradients, these high concentration regions are dispersed laterally at the one level in the bed. Once the concentration gradients are smaller, this false discontinuity vanishes. Hence, using fixed region boundaries (z_{c_j}) causes the mixing rates to be overpredicted for short times. This overprediction of the short-time mixing is further exacerbated by the assumption of perfect mixing within an element, since most of the element contains no species 1. These unrealistically high short-time mixing rates are apparent in Figure 17, which requires two more m_i decades than Figures 18 and 19. For longer times, the effects of the fixed boundaries should "average

out". The behavior exhibited in Figures 18 and 19 seem to support this conclusion. The model is flexible enough that it could accommodate time-varying region boundaries (i.e., $z_{c_j}(t)$) if desired. Although this would require mapping the "old" concentration distribution to the "new" grid, which would significantly complicate the model.

Comparing the concentration near the origin in Figures 17 and 18 shows that it has an oscillatory character. This oscillatory behavior is shown more clearly in Figure 20, which gives the concentration at the origin as a function of time. The figure shows that for short times, before the tracer at the origin and the surroundings mix more thoroughly, solids exchange, due to the bubble motion, can produce concentration fluctuations. Fitzgerald et al.'s (1977) experimental observations suggested that a tracer moves in clumps, which subsequently break into smaller clumps. This mechanism of solid movement is essentially that used in the current mixing model. As discussed by Valenzuela and Glicksman (1984), an oscillatory component was observed in the mixing studies of de Groot (1967), Babu (1971), and Highley and Merrick (1971). This behavior in the data highlights the inadequacy of diffusion models, which would predict that solids disperse uniformly away from an injection point.

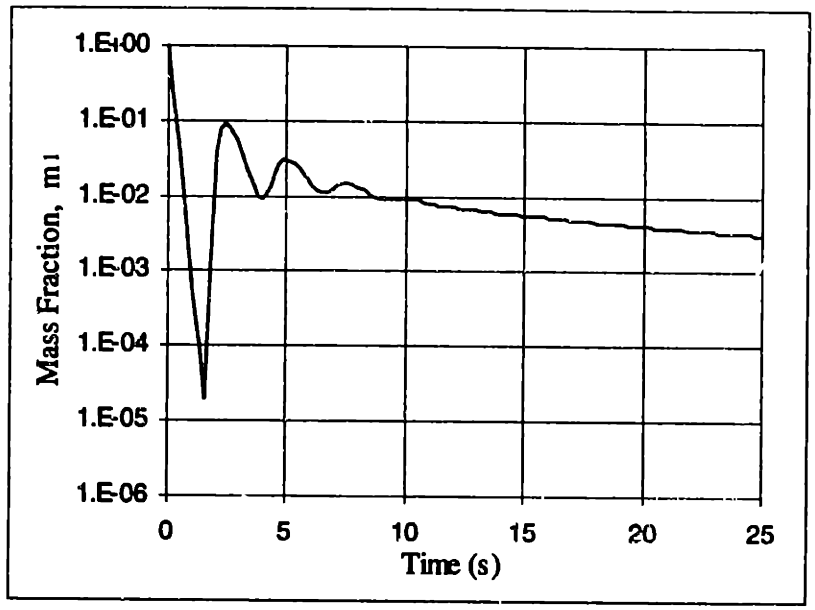

Figure 20: Oscillations in $m_1(t)$ at the Origin

10.4 Comparison of Mixing Model Output with Thermal Tracer Data

Based on the development presented in Chapter 9, the dimensionless thermistor temperature (Θ) provides a crude proxy for the tracer mass fraction (m_1). The mixing model output presented in Section 10.3 are a simulation of the same conditions as the thermal tracer mixing data taken with u_o/u_{mf}=3.83. Hence, contour plots of the mass fraction distribution predicted by the model can be directly compared with the contour plots of the dimensionless thermistor temperature (Θ).

Figures 21 and 22 present contour plots of Θ from the thermal tracer data. The arrow in the figures indicates the injection location and direction, and the dashed line identifies the location of the bottom of the tube bank. Figures 21 and 22 can be compared directly with Figures 18 and 19. The spatial and Θ/m_1 scales are the same for the pairs of plots to ease comparison of the results.

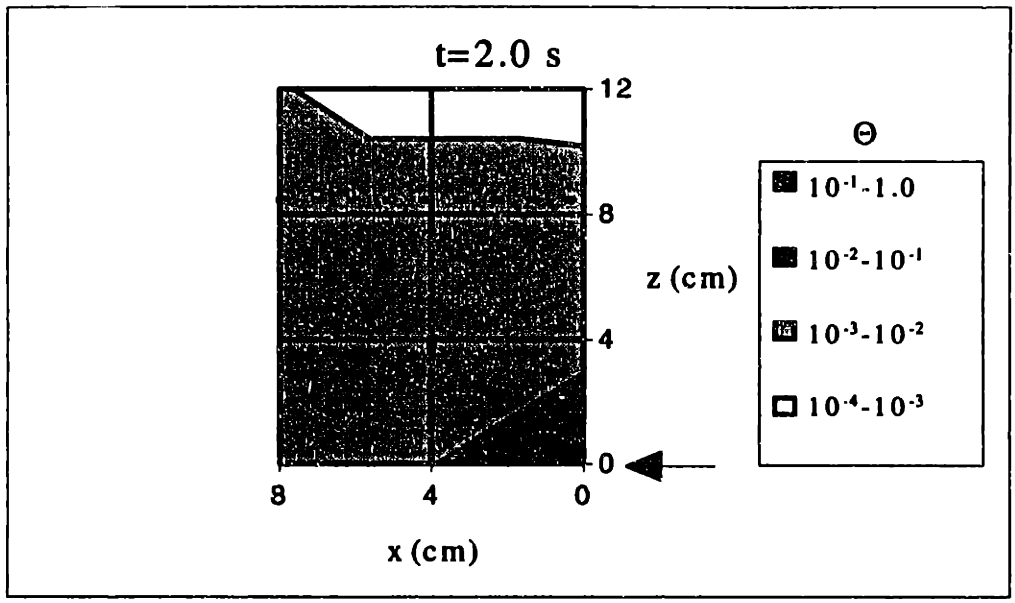

Figure 21: Measured Θ Distribution 2.0 s After Injection–u_o/u_{mf}=3.83

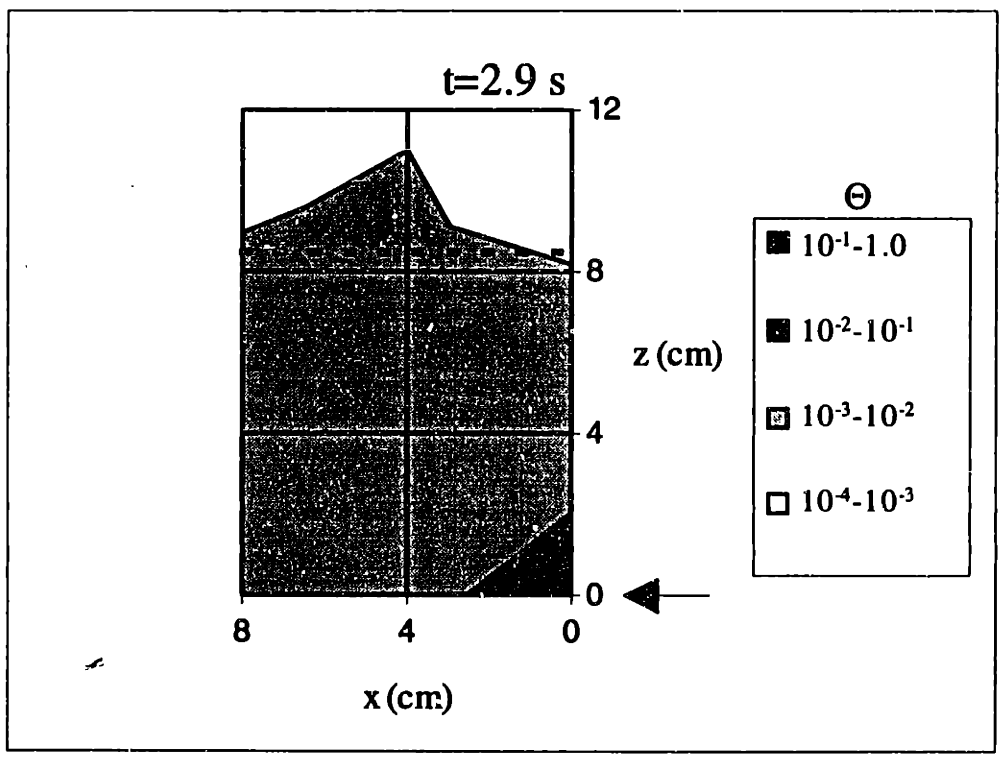

Figure 22: Measured Θ Distribution 2.9 s After Injection–u_o/u_{mf}=3.83

A comparison of Figures 18 and 21, and Figures 19 and 22 is encouraging, particularly considering how roughly Θ is expected to represent m_l. The model appears to do a reasonable job of predicting the thermal tracer data, with no attempts to "tune" the model inputs. The thermal tracer data exhibit greater lateral mixing, but these data also include some "false" lateral mixing due to the injection effects discussed in Chapter 9. The model also does not account for the presence of the tube bank and its effects on the solids mixing. Comparing Figures 19 and 22 shows that the model continues to mix solids up into the region where the tube bank is located (indicated by the dashed line on Figure 22). But, as discussed in Chapter 9, the tube bank appears to significantly impede solids motion.

It is difficult to compare the output from the model with the time-delay data presented in Chapter 9, Section 9.2.1. In addition to the crude relationship between the mass fraction predicted by the model (m_l) and the dimensionless temperature measured by the thermistors (Θ), it is necessary to estimate the tracer concentration at which the thermistors would indicate that the tracer has arrived at a particular bed location. In other words, it is necessary to define a m_l threshold on the model's predictions that corresponds to the point where the thermistor first senses the presence of the thermal tracer particles. The time-delay measurements were based on an inspection of each thermistor probe's temperature trace, making the measurements somewhat subjective and further complicating comparisons with the model. However, with these difficulties in mind, the time-delay data presented in Chapter 9 will be compared with the output of the model.

As discussed in Chapter 9, Section 9.2.2, the thermistors can credibly resolve temperature changes as low as 0.1°C. Assuming that the tracer particles are 100°C below the bed temperature, a temperature change of 0.1°C corresponds to Θ=0.001. The analysis in Chapter 9, Section 9.1.1.1 suggests that $m_l \approx \Theta$. Hence, a threshold of m_l=0.001 will be used to estimate the concentration at which the thermistors would first sense the presence of the tracer particles.

Figure 23 is a plot of the predicted time-delay contours that corresponds to the measurements presented in Figure 4 in Chapter 9–the contours are shaded the same to permit direct comparison of the two plots. A comparison of the plots shows that the model overpredicts the delay times (underpredicts the mixing). This is particularly true at locations offset from the vertical axis (i.e., $x > 0$). This is due to several factors. The first is because the model underpredicts mixing for short times due to the assumption of perfect mixing within each element. It is also due to a limited understanding of the bubble splitting and coalescence behavior within PFBCs, which limits the model's ability to predict lateral solids mixing. In addition, remember that there is some artificial lateral mixing produced by the tracer injection momentum, which is not accounted for in the model simulation. The uncertainty in the mass fraction threshold used to predict the time delays also contributes to the deviations between the output of the model and the thermistor measurements.

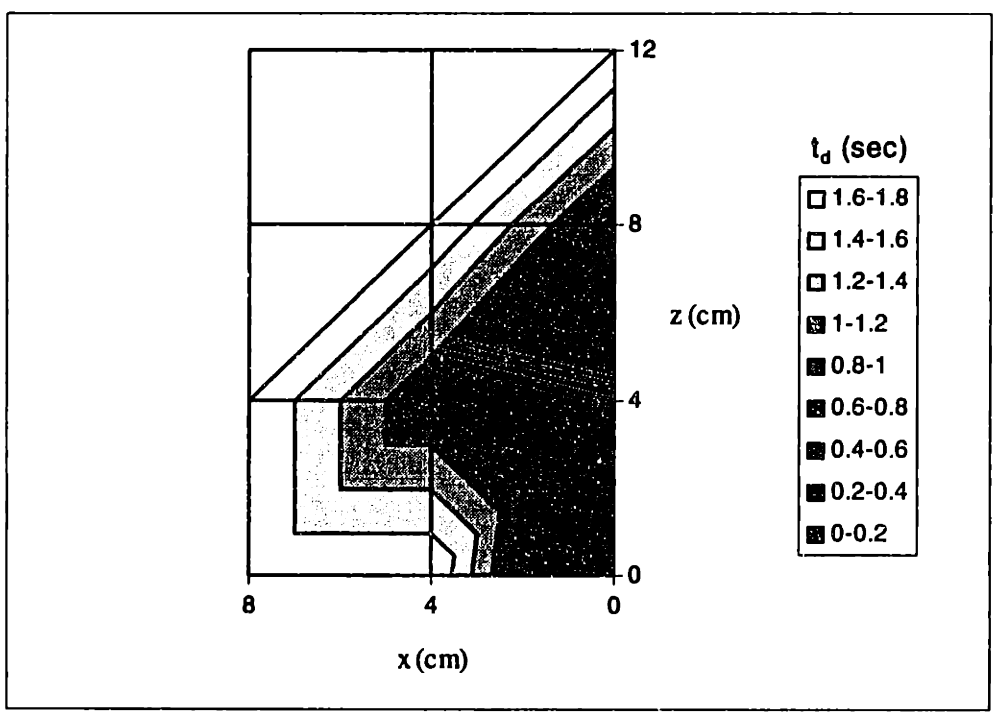

Figure 23: Predicted Time Delays–u_o/u_{mf}=3.83

10.5 Advantages of Mixing Model Over Previous Models

The most significant advantage of the proposed mixing model is that it models the mixing process in terms of the mechanisms that have been shown to be responsible for solids mixing in bubbling beds. The diffusion model (described in Chapter 6), although simpler to implement, does not the correctly model of the physics of solids mixing in bubbling fluidized beds. This is reflected in the large variations and contradictions in diffusion coefficient measurements. The counter-current mixing model, also described in Chapter 6, is a better representation of the physics of solids mixing, but it relies on specifying nonphysical exchange coefficients. These exchange coefficients are not known *a priori* with any better accuracy than a diffusion coefficient. The current model requires inputs whose rough magnitudes are known. So that where diffusion coefficients have been found to vary by many orders of magnitude, it is known, for example, that the upward displacement of particles is on the order of the bubble diameter. Similarly, as shown in Section 10.2.3.1, it is possible to make reasonable estimates for all the inputs to the model.

The other advantage of the model is its flexibility. For example, bubble splitting could be incorporated into the model in the same way bubble coalescence is handled. It would also be possible to use a coalescence model to specify mean coalescence elevations, and then the actual coalescence elevations could be specified randomly about the mean elevation for each time step. This would significantly complicate the geometry of the model since the grid would change as a function of time, requiring the concentration from previous time steps to need to be mapped to the new grid. This is not a trivial task, but the framework of the model is flexible enough to accommodate this enhancement if desired.

10.6 Nomenclature

A	unit area containing a single bubble
A_{ac}	unit area after coalescence
A_b	cross-sectional area of a bubble$=\pi d_b^2/4$
A_d	area within A that experiences a downflow from interval above
A_{pc}	unit area prior to coalescence
A_s	area within A that is unaffected by passage of the bubble
A_x	area within A that experiences an exchange with the bubble wake
$C(\delta)$	dimensionless bubble-coalescence rate
d	bed depth
d_b	bubble diameter
d_{b_1}	bubble diameter in Region 1, i.e., initial bubble diameter at distributor
d_p	mean particle diameter
f_b	bubble frequency
f''_b	bubble frequency per unit area
f_b^{probe}	bubble frequency measured by probe
H	bed height
K	gas through-flow coefficient
k_{vol}	volume of solids displaced upward by bubble divided by the bubble volume
k_{zd}	the average distance particles are displace downward (z_d) divided by d_b
k_{zu}	the average distance particles are displace upward (z_u) divided by d_b
l_{or}	spacing between adjacent holes in the distributor
m_1	mass fraction of species 1
m_{1w}	mass fraction of species 1 in the wake of a post-coalescence area A
m_{1d}	mass fraction of species 1 in the downflow to a pre-coalescence area A
$m_{1\text{-}ss}$	steady-state mass fraction of species 1
n_{bot}	α_d/α_x
N_{or}	number of distributor orifice holes per unit area
nx_j	number of elements spanning the bed width in Region j
ny_j	number of elements spanning the bed depth in Region j
Q''_b	visible bubble flow rate per unit area
s	spacing between emitter and detector in emitter-detector optical probe
t	time
t_d	delay time
u_{mf}	minimum fluidization velocity
u_o	gas superficial velocity
V_b	bubble volume
V_d	volume of particles displaced downward as bubble passes by
V_u	volume of particles moving upward with the bubble
w	bed width
z	axial position
z_c	axial coalescence elevation

z_d distance surrounding particles are displaced downward due to bubble passage
z_u distance particles are diplaced upward due to bubble passage

Greek Symbols

α_d fraction of area A consisting of area A_d
α_s fraction of area A consisting of area A_s
α_x fraction of area A consisting of area A_x
δ bubble fraction
$\bar{\delta}$ bed average bubble fraction
Δt time between bubble passages
Δz axial element thickness
Δz_c average distance bubble rises between participating in a coalescence
Θ dimensionless thermistor temperature

10.7 References

Abrahami, S.N. and Resnick, W., 1974, "Fluidised Bed Behavior Near Incipient Fluidisation in a Three-Dimensional Bed," *Transactions of the Institution of Chemical Engineers (Great Britain)*, 52, pp. 80-87.

Babu, S.P., 1971, "Fluidization Characteristics and Solids Mixing in Batch Operated Tapered and Non-Tapered Gas Fluidized Beds," Ph.D. Thesis, Illinois Institute of Technology.

Clift, R. and Grace, J.R., 1970, "Bubble Interaction in Fluidized Beds," *Chemical Engineering Progress Symposium Series No. 66*, p. 14.

Cranfield, R.R., 1978, "Solids Mixing in Fluidized Beds of Large Particles," Fluidization: Application to Coal Conversion Processes, *AIChE Symposium Series No. 176*, 74, pp. 54-59.

de Groot, J.H., Proc. 1967, "Scaling up of Gas-Fluidized Bed Reactors," International Symposium on Fluidization, Eindhoven, Amsterdam, pp. 348-361.

Fitzgerald, T., Catepovic, N., and Jovanovic, G., 1977, "Solid Tracer Studies in a Tube Filled Fluidized Bed," Fifth International Conference on Fluidization, Washington, p. 135.

Glicksman, L.R. and McAndrews, G., 1985, "The Effect of Bed Width on the Hydrodynamics of Large Particle Fluidized Beds," *Powder Technology*, 42, pp. 159-167.

Glicksman, L.R., Lord, W.K., and Sakagami, M., 1987, "Bubble Properties in Large-Particle Fluidized Beds," *Chemical Engineering Science*, 42, 3, pp. 479-491.

Glicksman, L.R., Yule, T., and Dymess, A., 1991, "Prediction of the Expansion of Fluidized Beds Containing Tubes," *Chemical Engineering Science*, 46, 7, pp. 1561-1571.

Highley, J. and Merrick, D., 1971, "The Effects of the Spacing Between Solid Feed Points on the Performance of a Large Fluidized Bed Reactor," *AIChE Symposium Series No. 116*, 67, pp. 219-227.

Kunii, D. and Levenspiel, O., 1991, Fluidization Engineering, Second Edition, Butterworth-Heinemann, Boston.

Lighthill, M.J., 1956, "Drift," *Journal of Fluid Mechanics*, 1, pp. 31-53.

Miwa, K., Mori, S., Kato, T., Muchi, I., 1972, "Behavior of bubbles in a gaseous fluidized bed," *International Chemical Engineering*, 12, 1, pp. 187-194.

Sitnai, O., 1981, "Solids Mixing in a Fluidized Bed with Horizontal Tubes," *Ind. Eng. Chem. Process Des. Dev.*, 20, 3, pp. 533-538.

Woollard, I.N.M. and Potter, O.E., 1968, "Solids Mixing in Fluidized Beds," *AIChE Journal*, 14, 3, pp. 388-391.

Valenzuela, J.A. and Glicksman, L.R., 1984, "An Experimental Study of Solids Mixing in a Freely Bubbling Two-Dimensional Fluidized Bed," *Powder Technology*, 38, pp. 63-72.

This page intentionally blank

11. Conclusions and Recommendations

There were to two primary objectives of this study. The first was to verify a set of hydrodynamic scaling parameters for use with commercial bubbling pressurized fluidized bed combustors (PFBC). The conclusions of this work are presented in Section 11.1. This study's second objective was to investigate the solids mixing in PFBCs, with particular emphasis on the mixing in the vicinity of the fuel feed point. The conclusions from the solids mixing work are provided in Section 11.2.

11.1 Conclusions of Hydrodynamic Scaling Studies

11.1.1 Hydrodynamic Scaling of the Tidd PFBC

A quarter-scale cold model of American Electric Power's 70 MW_e Tidd PFBC has been constructed based on a simplified set of scaling parameters. Comparisons of the statistical characteristics of time-varying pressure drop data from the cold model and the Tidd PFBC indicate that the hydrodynamics of the two beds are similar. The excellent agreement between the dimensionless probability density functions, the mean solid fraction profiles, and the bed expansions provide a verification of the simplified set of scaling laws for large-scale commercial pressurized bubbling beds.

As discussed in Chapter 3, only a section of the Tidd cross-section is represented by the cold model. The decision to only scale a section of the combustor was based on previous work that showed that the distribution of bubbles is nearly uniform in large-particle beds with an array of horizontal tubes. The results of this scaling study validate this decision. Hence, an additional conclusion of this study is that in large-particle beds with tight tube arrays, it is more important to scale the tube bundle geometry than the overall cross-

sectional dimensions of the bed. Although, the scaled section should have a diameter that is at least 3-4 times larger than the maximum bubble size.

In addition to a statistical analysis of the time-varying pressure drop data from the two beds, power spectral densities of the data were also calculated. Comparisons of the power spectral densities between the two beds show that the Tidd power spectrum contains peaks at distinct frequencies that are not present in the cold model power spectrum. Based on previous experience, the presence of the peaks in the power spectrum is unusual, and the peaks are of high enough frequency to conclude that their source is not the bed hydrodynamics. One possible explanation is that forces on the tubes in the Tidd PFBC may be exciting the natural frequencies of the tube bank. Although, any vibrations within the bed appear to be structurally insignificant, and do not appear to have any significant effect on the overall bed hydrodynamics. Another possibility is that the pressure lines themselves are the source of the peaks in the Tidd power spectrum. The Tidd pressure lines are extremely long ($\approx$15 m), and the pressure taps protrude into the bed. The possibility exists that the flow past the pressure tap excites the harmonic frequencies of the pressure lines. Estimates of the pressure line harmonic frequencies coincide very closely with the peak frequencies in the Tidd power spectrum.

11.1.2 Importance of the Solid-to-Gas Density Ratio for Scaling Bubbling Fluidized Beds

An additional study was conducted to assess the importance of matching the solid-to-gas density ratio when scaling bubbling fluidized beds. Previous work has shown that matching the density ratio is essential for scaling circulating fluidized beds, but some controversy remained over the importance of the parameter for scaling bubbling fluidized beds. Hydrodynamic scaling comparisons were conducted with all the scaling parameters matched with the exception of the solid-to-gas density ratio. The comparisons indicate that in order to reliably scale the hydrodynamics of bubbling fluidized beds it is essential to match the solid-to-gas density ratio. The density ratio also appears to influence the nature

of the transition from the bubbling to the slugging regimes of fluidization. Results suggest that, for the materials tested, the lower density ratio material experiences transition from bubbling to slugging over a broader range of u_o/u_{mf}.

11.2 Conclusions of Solids Mixing Studies

As discussed in Section 11.1, the cold model of the Tidd PFBC was shown to be hydrodynamically similar to the hot Tidd combustor. Hence, the cold model provides a convenient and powerful platform for conducting detailed studies of PFBC hydrodynamics. Previous studies have shown that bubbles play a central role in the mixing of solids in bubbling fluidized beds, prompting an investigation of the characteristics of the bubbles in the cold model. Subsequently, the cold model was used to investigate solids mixing in the feed-point region at the bottom of the bed; these studies were conducted using a thermal tracer technique. Finally, an original solids mixing model has been developed. The model is based on the underlying mechanisms of solids mixing in bubbling fluidized beds.

11.2.1 PFBC Bubble Characteristics

A unique optical probe design has been developed to measure the characteristics of the bubbles in the cold-scale model of the Tidd PFBC. The design minimizes the intrusion of the probe into the flowfield by integrating the probe's optoelectronic components into the tubes used to simulate presence of tube bank in the Tidd PFBC. The optical probes were used to measure the characteristics of the bubbles in the bed, such as their velocity, size, and frequency. Measurements were made at four vertical locations in the bed, for five gas superficial velocities.

The vertical bubble dimensions were measured, and the bubble rise velocity was calculated using Davidson and Harrison's (1963) bubble rise velocity expression assuming the bubbles were spherical. Davidson and Harrison's (1963) bubble rise velocity expression was found to approximately predict the bubble rise velocity in the cold model, although the data show no dependence on excess gas velocity (u_o-u_{mf}), in contrast to Davidson and Harrison's (1963) expression. The bubble size within the tube bank was found to be on the order of the spacing between the tubes. The bubble frequency shows a strong dependence on gas superficial velocity.

Most of the excess gas flow appears to pass through the bed in the form of bubbles. A gas through-flow coefficient of 1, which corresponds to Toomey and Johnstone's (1952) original two-phase theory of fluidization, was found to provide the best prediction of the bed expansion measurements in the cold model. Pressurized fluidized beds tend to have tight tube banks that keep the bubbles small relative to the bed depth, limiting the gas through-flow .

A comparison of the bubble-size measurements with an existing bubble growth model, which has been demonstrated to accurately predict bubble growth under conditions more typical of atmospheric fluidized beds, is shown to dramatically overpredict the bubble growth in the region below the cold-model tube bank. This suggests that bubbles grow more slowly in pressurized beds or that the bubbles split as well as coalesce, which is consistent with the observations of other researchers. The bubble size within the tube bank was found to be on the order of the spacing of the tubes.

In addition to providing information on the bubble characteristics of PFBCs, the bubble measurements were used to provide inputs to the mechanistic mixing model discussed in Section 11.2.3.

11.2.2 Thermal Tracer Mixing Results

A thermal tracer technique has been implemented in the cold model of the Tidd PFBC. The technique involves thermally tagging bed particles, injecting them back into the bed, and tracking their motion using an array of thermistors.

The thermal tracer data suggest that there are distinct differences in how the solids mix below the tube bank versus within the tube bank. As found in other studies, the tube bank appears to severely impair solids mixing. This is also consistent with early observations in the Tidd PFBC where extra measures were required to ensure adequate lateral mixing of the fuel. Tube banks in PFBCs tend to be deep and tightly spaced due to their high power density. It is therefore, most likely, not practical to increase the tube spacing or reduce the bed depth. Hence, adequate mixing below the tube bank appears to be paramount to the successful operation of the bed.

In general, higher gas superficial velocities produce both higher axial and lateral mixing rates. Increasing the gas superficial velocity leads to higher visible bubble flowrates, which correspond to higher bubble frequencies and bubble fractions. The increased bubble frequency produces a higher rate of bubble interaction with the solids in the bed, increasing the axial mixing. Higher bubble fractions correspond to a reduced spacing between bubbles, producing a higher rate of bubble coalescence and hence lateral mixing. Therefore, higher superficial velocities will produce increased mixing rates, particularly below the tube bank.

As mentioned previously, the mixing below the tube bank is critical. Introducing the coal as low in the bed as possible would make it possible to take maximum advantage of the higher mixing rates below the tube bank. Bubbles are smaller closer to the distributor and coalesce after rising shorter distances. Thus there are a higher number of coalescences per axial distance closer to the distributor, providing increased lateral mixing.

Frequently, the size of the region below the tube bank is limited by concerns over erosion. Bubbles grow as they rise through the tube-free region. Larger bubbles rise faster, transporting larger wakes with greater momentum. When the bubbles reach the bottom of the tube bank the wakes collide with the tubes at the bottom of the tube bank, producing the potential for significant erosion. But as just discussed, bubble growth appears to occur much more slowly in pressurized beds than in atmospheric beds, suggesting that this tube-free zone below the tube bank could be increased in size without increasing the potential for erosion. Increasing the size of this region would provide a larger area for the fuel and the sorbent to mix, improving the overall solids mixing characteristics of the bed.

Finally, the combination of the thermal tracer technique and the cold-scale model, which simulates the hydrodynamics of a hot combustor, is shown to be a useful approach for evaluating the effects of varying superficial velocity on the solids mixing. This suggests that this approach would also be useful for evaluating the effects of varying other operating conditions or the bed geometry on the solids mixing.

11.2.3 Mechanistic Solids Mixing Model

A mechanistic model of solids mixing in bubbling fluidized beds has been developed. The model is based on the basic mechanisms that have been identified for solids motion in bubbling beds. In particular, it views solids mixing as consisting of solids being displaced due to the passage of bubbles through the bed. Axial solids mixing is due to bubbles transporting solids vertically as they rise towards the bed surface. Lateral solids mixing is attributed to the lateral motion of bubbles as they move to coalesce with neighboring bubbles. Comparisons of the model with data from a previous study and the thermal tracer data are encouraging. Reasonable agreement with the data are achieved for longer times without adjusting the parameters of the model to fit the data. This is also due to the use of measured bubble properties as inputs to the model. Due to the assumptions of the model, it tends to overpredict mixing rates for short times.

11.3 Recommendations for Future Work

Much work remains to better understand how solids mix in pressurized fluidized beds. The results from this study indicate that the tube bank severely restricts solids mixing. However, more work needs to be done to evaluate the effect of the tube bank on the mixing, and to possibly identify tube bank geometries that provide better solids mixing performance within the tube bank.

The mechanistic model developed in this study highlights, through its inputs, what variables need to be better understood to reliably predict solids mixing. In particular, many of the inputs to the model such as the volume of particles transported by a bubble, and the upward and downward distances a bubble displaces solids are based on idealized single-bubble experiments. Much more information is needed on the solids motion produced by a bubble in a vigorously bubbling bed, both with and without tubes, with the effects of the tubes being particularly important.

Much of the work on solids mixing is motivated by the desire to avoid the formation of plumes of volatiles above the feedpoints in fluidized-bed combustors. But gas mixing is also important. Just as the cold model provides a convenient platform for investigating solids mixing in PFBC, it also would be useful for conducting gas mixing studies.

The cold model of the Tidd PFBC, in combination with the thermal tracer technique, also provides the unique capacity to conduct experimental studies of novel solids-feed and distributor designs for the augmentation of lateral mixing. Studies such as these would provide useful design information for next-generation PFBC designs.

11.4 References

Davidson, J.F. and Harrison,D., 1963, Fluidized Particles, Cambridge University Press, Cambridge.

Toomey, R.D. and Johnstone, H.F., 1952, "Gaseous Fluidization of Solid Particles," Chemical Engineering Progress, 48, 5, pp. 220-226.

APPENDICES

Appendix A – Model of Tidd PFBC Pressure Lines[1]

The pressure-sensing lines for the Tidd PFBC are quite long, raising concerns over their effect on the fidelity of the pressure signal. A mathematical model of the pressure lines was mentioned in Chapter 3 to evaluate their frequency response. A more detailed description of the model is provided in this appendix.

A lumped-parameter model was developed for the pressure line shown in Figure 1. The pressure line has a diameter, d, and length, *l*. Of primary interest is the effect the line has on a time-varying input pressure signal, or in other words, How closely does $p_{out}(t)$ represent $p_{in}(t)$?

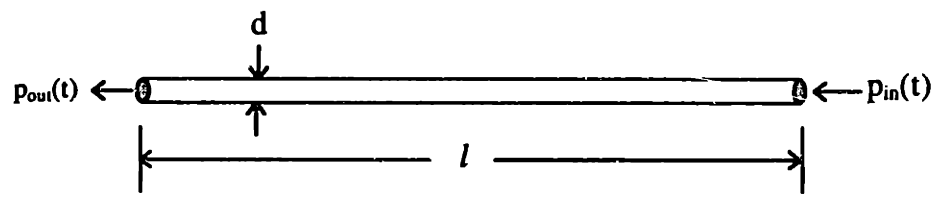

Figure 1: Illustration of Pressure Line

The model includes three fluid-system elements: inertance, capacitance, and resistance. The fluid inertance (I) accounts for the inertia of the fluid. For a circular line of diameter, d, the inertance is given by

$$I = \frac{\rho_g l}{A} = \frac{4\rho_g l}{\pi d^2}. \qquad (1)$$

If the pressure line is rigid, energy is stored through compression of the air in the line. The fluid capacitance (C_f) for a compressible fluid in a rigid container can be expressed as

[1] The model of the pressure lines was developed using the approach and constitutive relationships presented by: Rowell, D. and Wormley, D.N., 1994, System Dynamics: An Introduction, Course Notes for: 2.02 *Introduction to System Dynamics*, Department of Mechanical Engineering, Massachusetts Institute of Technology.

$$C_f = \frac{\pi d^2 l}{4 \cdot \gamma \cdot p}, \tag{2}$$

where:

p=absolute air pressure and

$\gamma = c_p/c_v = 1.4$ for air.

Finally, assuming laminar flow in the pressure line, the fluid resistance can be modeled as

$$R_f = \frac{128 \mu l}{\pi d^4}; \tag{3}$$

μ is the dynamic viscosity of the air.

State equations can be developed for the system shown in Figure 1 using either the linear-graph methods discussed by Rowell and Wormley (1994)[2] or other similar techniques such as the bond-graph methods presented by Rosenberg and Karnopp (1983)[3]. The resulting state equations, expressed in state-matrix form, are

$$\frac{d}{dt}\begin{bmatrix} Q \\ p \end{bmatrix} = \begin{bmatrix} -\frac{R_f}{I} & -\frac{1}{I} \\ \frac{1}{C_f} & 0 \end{bmatrix}\begin{bmatrix} Q \\ p \end{bmatrix} + \begin{bmatrix} \frac{1}{I} \\ 0 \end{bmatrix} p_{in}(t). \tag{4}$$

The two state variables are pressure, p, and volumetric flowrate, Q. The output pressure–the pressure at the transducer–is the dynamic quantity of interest. Hence, the output equation is

$$p = \begin{bmatrix} 0 & 1 \end{bmatrix}\begin{bmatrix} Q \\ p \end{bmatrix} + [0] p_{in}(t). \tag{5}$$

Equations (4) and (5) are expressed in the standard form commonly used in system dynamics. Software packages, such as MATLAB[4], directly accept the column vectors and matrices in (4) and (5) as inputs.

---

[2] Rowell, D. and Wormley, D.N., 1994, System Dynamics: An Introduction, Course Notes for: 2.02 *Introduction to System Dynamics*, Department of Mechanical Engineering, Massachusetts Institute of Technology.

[3] Rosenberg, R.C. and Karnopp, D.C., 1983, Introduction to Physical System Dynamics, McGraw-Hill, Inc., New York.

[4] The MathWorks, Inc., Natick, MA.

Equation (4) consists of two first-order differential equations because the pressure line model is a second-order system. This is equivalent to saying that it has two independent energy storage elements–fluid inertance and capacitance. Fluid resistance can only dissipate energy. Second-order system transient response is characterized by two parameters–the undamped natural frequency (ω_n) and the damping ratio (ζ). The undamped natural frequency and damping ratio for the system described by (4) are given by

$$\omega_n = \sqrt{\frac{1}{I \cdot C_f}} \tag{6}$$

and

$$\zeta = \frac{R_f}{2}\sqrt{\frac{C_f}{I}}, \tag{7}$$

respectively. Substituting (1) and (2) into (6) and introducing the ideal-gas equation of state gives

$$\omega_n = \sqrt{\frac{\gamma \cdot R \cdot T}{l^2}}, \tag{8}$$

where R is the ideal gas constant, which for air equals 287 J/kg-K, and T is absolute temperature (K).

Appendix B – Measurement of Particle Sphericity

Particle sphericity (ϕ_s) is defined as (Kunii and Levenspiel, 1991)[5]:

$$\phi_s \equiv \left(\frac{\text{surface area of sphere}}{\text{surface area of particle}} \right)_{\text{of equivalent volume}}.$$

The sphericities of both the Tidd and cold-model bed materials were determined following the approach described by Chang and Louge (1992)[6]. Particles from both beds were randomly distributed across the surface of microscope slides coated with epoxy. Magnified pictures were taken of the particles on the slides and digital images were generated from the photographs. Image 1.47, image-analysis software developed by the U.S. National Institutes of Health, was used to measure the projected area (A) and the apparent circumference (P) of many particles. Chang and Louge (1992) give that

$$\phi_s \approx C^2 = \frac{4\pi A}{P^2}, \tag{9}$$

where C is the apparent particle circularity. The sphericity of each individual particle was calculated, and then an average sphericity was determined for the particle sample. The average sphericity of the dolomite in the Tidd PFBC was 0.82, while the average sphericity of the polyethylene used in the cold model was measured to be 0.85.

---

[5] Kunii, D. and Levenspiel, O., 1991, Fluidization Engineering, Second Edition, Butterworth-Heinemann, Boston.

[6] Chang, H. and Louge, M., 1992, "Fluid Dynamic Similarity of Circulating Fluidized Beds," *Powder Technology*, 70, pp. 259-270.

Appendix C – Tidd PFBC and Cold Model Particle Size Distributions

The particle size distributions for the Tidd PFBC and the cold model were determined by sieve analysis. The analysis involves sieving a sample of the particles to determine what fraction of the sample's mass (x_i) is collected between sieves whose mean aperture is $\bar{d}_{p_i}$. The surface-volume mean particle diameter (d_p) was calculated using

$$d_p = \frac{1}{\sum_i \frac{x_i}{\bar{d}_{p_i}}}. \qquad (10)$$

- Tidd PFBC Particle Size Distribution

The Tidd PFBC particle size distribution is given in the Table 1. Using (10) to calculate the mean particle diameter gives $d_p = 851\mu m$.

Table 1: Tidd Particle Size Distribution

$\bar{d}_{p_i}$ (μm)	Mass Fraction, x_i
2000	0.0086
1700	0.1442
1200	0.3251
855	0.2616
605	0.1744
428	0.0807
268	0.0032
113	0.0022

- Cold Model Particle Size Distribution

The cold model particle size distribution is given in Table 2. Using (10) to calculate the mean particle diameter gives $d_p = 609\mu m$.

Table 2: Cold Model Particle Size Distribution

$\bar{d}_{p_i}$ (μm)	Mass Fraction, x_i
1700	0.0381
1200	0.1669
855	0.3133
605	0.2167
428	0.1903
268	0.0688
113	0.0059

Appendix D – Mean and Standard Deviation of Solid Fraction Data from Tidd PFBC and Cold Model

Table 3 summarizes the Tidd PFBC and the cold model operating conditions for the scaling comparisons given in Table 4.

Table 3: Summary of Tidd PFBC and Cold Model Operating Conditions

	Tidd PFBC	MIT Cold Model
T (K)	1135	311
p (Pa-abs)	9.04×10^5	1.013×10^5
μ (kg/m-s)	4.6×10^{-5}	1.9×10^{-5}
ρ_g (kg/m^3)	2.8	1.1
ρ_s (kg/m^3)	2513	918
ϕ_s	0.82	0.85
u_{mf} (m/s)	0.24	0.12
u_o (m/s)	0.91	0.46
D (m)	3.4	0.85
d_p (μm)	851	609
H_b (m)	2.13	0.53

Table 4 summarizes the mean and the standard deviation (σ) of the solid fraction calculated from the time-varying pressure drop data taken from the Tidd PFBC and the cold model.

Table 4: Summary of Statistics on Time-Varying Solid Fraction Data

y/H	Tidd mean (1-ε)	Tidd σ of (1-ε)	Cold Model mean (1-ε)	Cold Model σ of (1-ε)
0.09			0.203	
0.22	0.278	0.100	0.267	0.042
0.34	0.246	0.046	0.246	0.039
0.50	0.188	0.018	0.192	0.015

As shown in Table 4, and discussed in Section 4.3.1, it was not possible to acquire time-varying data in the bottom of the Tidd PFBC due to a plugged pressure tap. Steady pressure drop data from Tidd's Plant Operational Performance System (POPS) were used to estimate the mean solid fraction in the bottom of the Tidd PFBC. Table 5 summarizes the solid fraction profile from the POPS pressure drop measurements.

Table 5: Summary of POPS Data Solid Fraction Profile

y/H	Tidd POPS mean (1-ε)
0.06	0.22
0.19	0.28
0.34	0.27
0.59	0.14

The information in Tables 4 and 5 was used to generate Figure 1 in Chapter 4.

Appendix E – Particle Size Distributions for ρ_s/ρ_g Studies

The particle size distributions for the polyethylene and limestone particles were determined by sieve analysis. The analysis involves sieving a representative sample of the particles to determine what fraction of the sample's mass (x_i) is collected between sieves whose mean aperture is $\bar{d}_{p_i}$. The surface-volume mean particle diameter (d_p) was calculated using

$$d_p = \frac{1}{\sum_i \frac{x_i}{\bar{d}_{p_i}}}. \qquad (11)$$

- Polyethylene Particles

The particle size distribution of the polyethylene particles is given in Table 6. Using (11) to calculate the mean particle diameter gives $d_p = 653\mu m$.

Table 6: Polyethylene Particle Size Distribution

$\bar{d}_{p_i}$ (μm)	Mass Fraction, x_i
1200	0.1897
855	0.3117
605	0.3008
428	0.1626
268	0.0352

- Limestone Particles

The particle size distribution of the limestone particles is given in Table 7. Using (11) to calculate the mean particle diameter gives $d_p = 379\mu m$.

Table 7: Limestone Particle Size Distribution

$\overline{d}_{p_i}$ (μm)	Mass Fraction, x_i
855	0.0866
605	0.2568
428	0.3032
268	0.3277
143	0.0257

Appendix F – Internal Angle of Friction Measurements for ρ_s/ρ_g Studies

The internal angle of friction characterizes the frictional forces within a granular substance. The bin-flow method described by Zenz and Othmer[7] was used to measure the internal angle of friction of the two types of particles used here. Figure 2 shows the experimental apparatus used to measure the internal angle of friction.

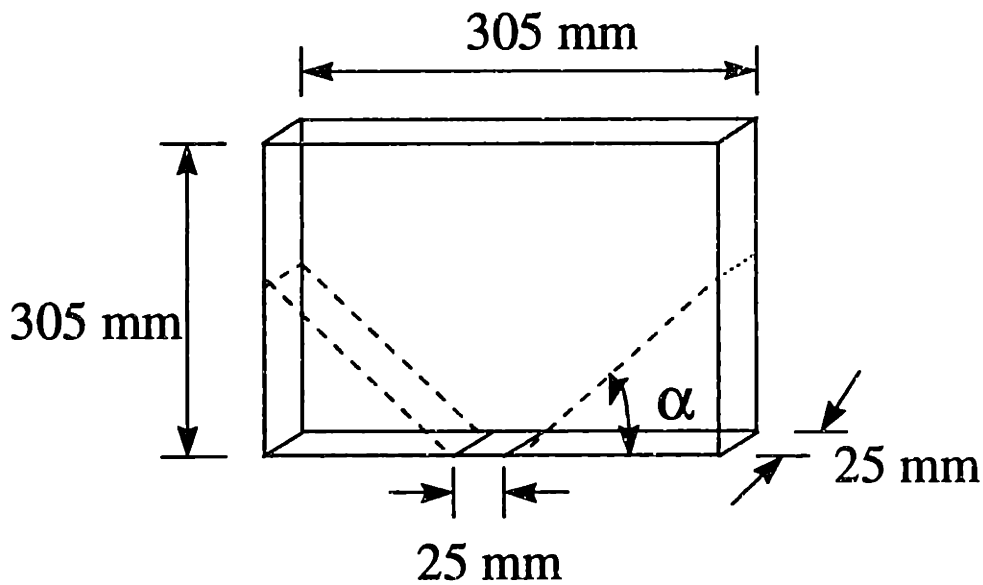

Figure 2: Internal Angle of Friction Measurement Apparatus

The apparatus consists of a bin 305 mm high, 305 mm wide, and 25 mm deep; the bin was constructed of 3 mm thick polycarbonate plastic. A 25 mm by 25 mm square opening was located in the center of the bottom of the apparatus. The opening was covered with a piece of 3 mm thick polycarbonate that served as a "trap door" to permit particles to drain through the hole when desired. The apparatus shown in Figure 2 was attached to a frame positioned over a container to collect particles as they flowed out the hole in the bottom of the bin. The bin was loosely filled with the particles whose internal angle of friction was

[7] Zenz, F.A. and Othmer, D.F., 1960, Fluidization and Fluid-Particle Systems, Reinhold Publishing Corporation, New York.

to be evaluated. When the opening in the bottom of the bin was uncovered, particles flowed through the hole until the frictional force between the particles balanced the force of gravity. The upper surface of the particles that remain in the bin (shown as a dashed line in Figure 2) are at an angle α relative to the horizontal. This angle corresponds to the internal angle of friction for the particles.

The internal angle of friction for the granular polyethylene was found to be

$$\alpha_{poly}=36°.$$

The internal angle of friction for the limestone was measured to be

$$\alpha_{lime}=40°.$$

The upper surface of the particles that remain in the bin is not perfectly linear, which introduces some uncertainty in the measurements. This uncertainty is estimated to be ±2 degrees. The test was repeated several times for both types of particles; the results were quite repeatable.

Appendix G – Bubble Fraction Data

Using the model developed in Section 7.3.2.1, the local bubble fraction can be estimated from pressure-drop measurements. The pressure-drop measurements were made across four levels in the cold-scale model for the five u_o/u_{mf} test conditions. A table is provided for each operating condition. The table first includes: the midpoint elevation between the pressure taps (z), the distance between the taps (Δh), the pressure drop measurements (Δp), and the local voidage (ε). The optical probe elevations do not coincide with the position where the voidage measurements were made. The local bubble fraction depends on the local voidage. So the voidage at the optical probes was estimated by interpolating between the pressure-drop voidage measurements. The last three columns of the table give the probe elevations (z_p), the interpolated probe voidage (ε_p), and the bubble fraction (δ). The calculations were made using a cold-model particle solid density (ρ_s) of 918 kg/m^3, a fluidizing air density (ρ_g) of 1 kg/m^3, and an emulsion voidage (ε_e) of 0.63.

- u_o/u_{mf}=2.5

z (cm)	Δh (cm)	Δp (in. H_2O)	ε	z_p (cm)	ε_p	δ
8.22	13.97	1.394	0.724	13.3	0.713	0.226
20.21	10.08	1.106	0.697	20.6	0.698	0.187
30.93	11.35	1.080	0.737	27.6	0.724	0.258
46.06	18.93	0.273	0.960	31.4	0.739	0.296

- u_o/u_{mf}=2.8

z (cm)	Δh (cm)	Δp (in. H_2O)	ε	z_p (cm)	ε_p	δ
8.22	13.97	1.358	0.731	13.3	0.720	0.246
20.21	10.08	1.077	0.705	20.6	0.707	0.210
30.93	11.35	1.001	0.756	27.6	0.740	0.300
46.06	18.93	0.411	0.940	31.4	0.759	0.349

- u_o/u_{mf}=3.1

z (cm)	Δh (cm)	Δp (in. H_2O)	ε	z_p (cm)	ε_p	δ
8.22	13.97	1.260	0.751	13.3	0.737	0.290
20.21	10.08	1.032	0.717	20.6	0.719	0.242
30.93	11.35	0.969	0.764	27.6	0.749	0.325
46.06	18.93	0.546	0.920	31.4	0.766	0.369

- u_o/u_{mf}=3.4

z (cm)	Δh (cm)	Δp (in. H_2O)	ε	z_p (cm)	ε_p	δ
8.22	13.97	1.145	0.774	13.3	0.754	0.336
20.21	10.08	0.997	0.727	20.6	0.728	0.267
30.93	11.35	0.929	0.774	27.6	0.759	0.351
46.06	18.93	0.657	0.904	31.4	0.776	0.396

- u_o/u_{mf}=3.83

z (cm)	Δh (cm)	Δp (in. H_2O)	ε	z_p (cm)	ε_p	δ
8.22	13.97	0.999	0.802	13.3	0.778	0.402
20.21	10.08	0.929	0.745	20.6	0.747	0.317
30.93	11.35	0.879	0.786	27.6	0.773	0.389
46.06	18.93	0.841	0.877	31.4	0.788	0.428

Figure 3 is a plot of all the bubble fraction data as a function of vertical position. The cold model has small bubbles relative to the depth of the bed; this prevents significant gas flow through bubbles bursting at the bed surface. Due to the limited gas through-flow, increasing gas flow requires an increasing number of bubbles to carry the gas to the bed's surface. This is reflected in the strong dependence of bubble fraction on the superficial velocity.

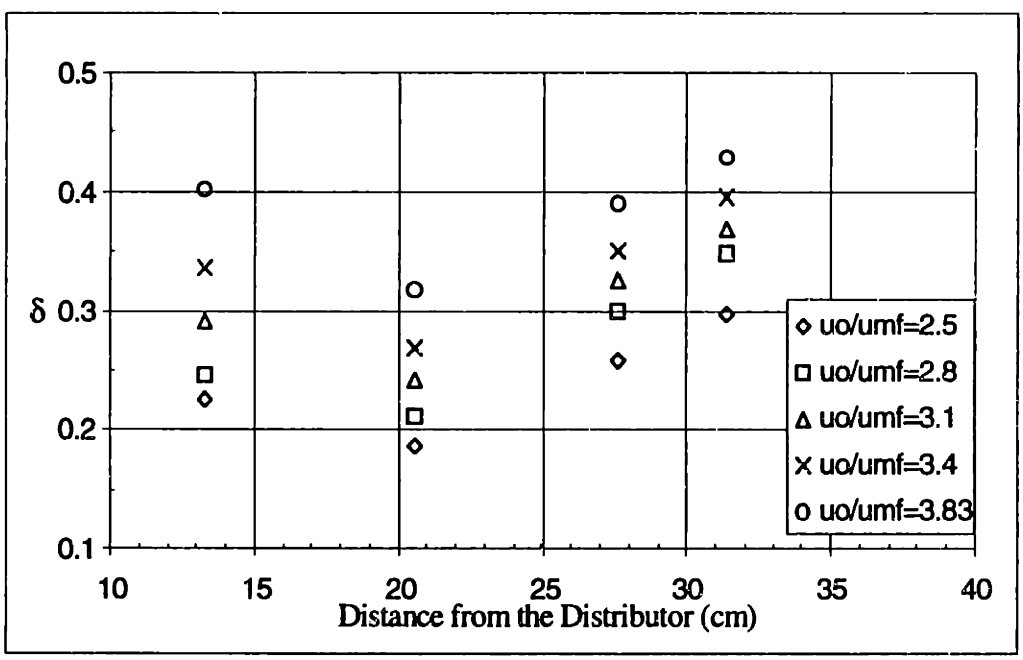

Figure 3: Bubble Fraction Profiles for Five Conditions Tested

Appendix H – Bed Height Measurements

The expanded bed height (H) is used to determine the emulsion voidage (ε_e). It was shown that the expanded bed height can be found from measurements of the vertical pressure distribution in the bed. The following five tables give the pressure distributions used to determine H for each of the test conditions. They also include the resulting bed height (H), the ratio of the expanded bed height to the bed height at minimum bubbling conditions (H/H_{mb}), the average bed bubble fraction ($\bar{\delta}$), and the emulsion voidage estimated for each condition. The average of these five emulsion voidages was used to calculate the bubble fraction profiles given in Appendix G.

- u_o/u_{mf}=2.5

Tap	z (cm)	$p-p_{fb}$ (in. H_2O)	H (cm)	H/H_{mb}	$\bar{\delta}$	ε_e
1	1.27	3.853	39.02	1.478	0.285	0.611
2	15.16	2.460				
3	25.25	1.353				
4	36.6	0.273				
5	55.52	0				

- u_o/u_{mf}=2.8

Tap	z (cm)	p-p_{fb} (in. H_2O)	H (cm)	H/H_{mb}	$\bar{\delta}$	ε_e
1	1.27	3.846	40.35	1.528	0.304	0.618
2	15.16	2.488				
3	25.25	1.412				
4	36.6	0.411				
5	55.52	0				

- u_o/u_{mf}=3.1

Tap	z (cm)	p-p_{fb} (in. H_2O)	H (cm)	H/H_{mb}	$\bar{\delta}$	ε_e
1	1.27	3.807	42.15	1.597	0.329	0.625
2	15.16	2.547				
3	25.25	1.515				
4	36.6	0.546				
5	55.52	0				

- u_o/u_{mf}=3.4

Tap	z (cm)	p-p_{fb} (in. H_2O)	H (cm)	H/H_{mb}	$\bar{\delta}$	ε_e
1	1.27	3.728	43.89	1.662	0.351	0.636
2	15.16	2.583				
3	25.25	1.586				
4	36.6	0.657				
5	55.52	0				

- u_o/u_{mf}=3.83

Tap	z (cm)	$p-p_{fb}$ (in. H_2O)	H (cm)	H/H_{mb}	$\bar{\delta}$	ε_e
1	1.27	3.648	47.08	1.783	0.387	0.647
2	15.16	2.649				
3	25.25	1.720				
4	36.6	0.841				
5	55.52	0				

Appendix I – Tabulated Optical Probe Data

The following five tables give the numerical values for the bubble characteristics plotted in Sections 7.4.1-7.4.3. U_{ub}, U_l, and U_f, represent the 95% confidence limits for the bubble: velocity, mean pierced length, and frequency, respectively.

- u_o/u_{mf}=2.5

z (cm)	u_b (m/s)	U_{ub} (m/s)	l_b (cm)	U_l (cm)	f_b (Hz)	U_f (Hz)
13.3	0.678	0.254	3.417	1.318	4.475	0.369
20.6	0.676	0.254	3.476	1.330	3.717	0.257
27.6	0.780	0.110	4.386	0.737	4.650	0.478
31.4	0.893	0.110	4.801	0.662	5.559	0.358

- u_o/u_{mf}=2.8

z (cm)	u_b (m/s)	U_{ub} (m/s)	l_b (cm)	U_l (cm)	f_b (Hz)	U_f (Hz)
13.3	0.546	0.104	2.800	0.538	4.859	0.101
20.6	0.703	0.104	3.400	0.513	4.392	0.059
27.6	0.846	0.140	4.955	0.982	5.209	0.611
31.4	0.921	0.140	5.244	0.854	6.209	0.427

- u_o/u_{mf}=3.1

z (cm)	u_b (m/s)	U_{ub} (m/s)	l_b (cm)	U_l (cm)	f_b (Hz)	U_f (Hz)
13.3	0.572	0.111	2.914	0.574	5.700	0.230
20.6	0.715	0.111	3.252	0.640	5.350	0.609
27.6	0.899	0.185	5.148	1.164	5.725	0.478
31.4	1.025	0.185	5.863	1.108	6.526	0.296

- u_o/u_{mf}=3.4

z (cm)	u_b (m/s)	U_{ub} (m/s)	l_b (cm)	U_l (cm)	f_b (Hz)	U_f (Hz)
13.3	0.653	0.201	3.594	1.131	6.059	0.446
20.6	0.729	0.201	3.246	0.944	6.017	0.443
27.6	0.836	0.142	4.727	0.989	6.217	0.731
31.4	0.911	0.142	5.215	0.875	6.926	0.377

- u_o/u_{mf}=3.83

z (cm)	u_b (m/s)	U_{ub} (m/s)	l_b (cm)	U_l (cm)	f_b (Hz)	U_f (Hz)
13.3	0.530	0.218	3.161	1.308	6.733	0.329
20.6	0.765	0.218	4.373	1.260	5.536	0.283
27.6	0.887	0.154	4.932	0.995	7.084	0.729
31.4	0.898	0.154	5.473	0.968	7.060	0.315

Appendix J – Bubble Characteristics Uncertainty Analysis

The figures presenting the bubble characteristics measurements in Chapter 7 include errors bars representing 95% confidence intervals on the measurements. (Statistically, 95% confidence intervals indicate that the odds are 1 in 20 that the true value of the measured quantity lies outside the interval.) The purpose of this appendix is to describe how these uncertainty estimates were established. The following approach to uncertainty analysis is discussed in detail in Beckwith et al. (1993)[8].

Two types of error - precision and bias error - have been considered when estimating the total uncertainty in the bubble measurements. Precision or random error is reflected in variations in an instrument's repeated measurements of the same quantity. Bias errors are systematic errors, such as limited measurement resolution, that occur in the same manner for each measurement.

The approach to estimating the uncertainty in the bubble measurements is similar for all the bubble properties. After a detailed description of the uncertainty analysis for the bubble rise velocity measurements, the subsequent discussion for the remaining bubble properties is more brief.

- **Uncertainty in Mean Bubble Rise Velocity Measurements**

The mean bubble rise velocity (u_b) is calculated using $u_b = \Delta h/\tau_b$, where Δh is the measured distance between the probes and τ_b is the mean time lag. The uncertainty estimates for u_b account for bias uncertainty in the measurement of Δh and the precision uncertainty due to variations in the time-lag measurements.

[8] Beckwith, T.G., Marangoni, R.D., and Lienhard, J.H., 1993, Mechanical Measurements, 5th Edition, Addison-Wesley, Reading, Massachusetts.

The mean time lag (τ_b) was calculated using

$$\tau_b = \frac{1}{n_\tau} \cdot \sum_{i=1}^{n_\tau} \tau_{b_i}, \tag{12}$$

where n_τ was a relatively small sample 4 to 9 time lag measurements. To estimate precision uncertainty in the case where n_τ is less than approximately 30, the statistics of the t-distribution must be employed. The precision uncertainty in this case is given by

$$\tau_b - P_\tau < \bar{\tau}_b < \tau_b + P_\tau, \tag{13}$$

where $\bar{\tau}_b$ is the true mean time lag, and P_τ is the precision uncertainty in τ_b. P_τ is a statistical quantity given by

$$P_\tau = t_{\alpha/2,\nu} \cdot \frac{\sigma_\tau}{\sqrt{n_\tau}}, \tag{14}$$

where:

α = 1-c where c is the confidence level (e.g. c=0.95 for 95% confidence),

$\nu = n_\tau - 1$,

$t_{\alpha/2,\nu}$ = the t-statistic, and

σ_τ = the standard deviation of the τ_b measurements.

The values of $t_{\alpha/2,\nu}$ are tabulated; see for example Beckwith et al. (1993) or Bendat and Piersol (1986)[9].

Some bias uncertainty exists in the measurement of Δh ($B_{\Delta h}$). This uncertainty was estimated to be

$$B_{\Delta h} = \pm 0.002 \text{ m}. \tag{15}$$

The bubble rise velocity is calculated from two independent measurements, each of which have their own uncertainty. To estimate the uncertainty in u_b, we need to consider how the uncertainty in each of the measurements propagates. Consider a quantity κ that is a function of x and y. The uncertainty in κ (U_κ) is given by

[9] Bendat, J.S. and Piersol, A.G., 1986, Random Data - Analysis and Measurement Procedures, 2nd Edition, John Wiley & Sons, New York.

$$U_\kappa = \sqrt{\left(U_x \cdot \frac{\partial \kappa}{\partial x}\right)^2 + \left(U_y \cdot \frac{\partial \kappa}{\partial y}\right)^2}, \tag{16}$$

where U_x and U_y are the total uncertainty in x and y, respectively. Note that U_x, for example, can include both bias (B_x) and precision (P_x) uncertainty. B_x and P_x combine to give U_x according to

$$U_x = \sqrt{P_x^2 + B_x^2}. \tag{17}$$

Using $u_b = \Delta h/\tau_b$ and (16), the uncertainty in the bubble velocity (U_{ub}) is found to be

$$U_{ub} = \sqrt{\left(B_{\Delta h} \cdot \frac{1}{\tau_b}\right)^2 + \left[P_\tau \cdot \left(\frac{-\Delta h}{\tau_b^{\,2}}\right)\right]^2}. \tag{18}$$

- **Uncertainty in Bubble Size Measurements**

The mean pierced length ($\bar{l}_b$) characterize the bubble size, and it was calculated using

$$\bar{l}_b = u_b \cdot \bar{b}, \tag{19}$$

where $\bar{b}$ is the mean time it takes for a bubble to rise past the probe. The error bars on the figures presenting the mean pierced length measurements represent the 95% confidence limits. These uncertainty estimates include both the uncertainty in the bubble rise velocity, given by (18), and the precision and bias uncertainty in the mean bubble duration time.

A relatively small sample of $\bar{b}$ measurements were available, typically 5. (Although each $\bar{b}$ measurement is the average of over a hundred bubble duration times.). Hence, (14) was used to evaluate the precision uncertainty in the mean duration time (P_b). A small bias uncertainty exists due to the finite sampling rate of 500 Hz (Δt=0.002s). The bias uncertainty in $\bar{b}$ (B_b) was estimated to be

$$B_b = \pm 0.001 \text{ s}. \tag{20}$$

The total uncertainty in the mean duration time (U_b) was then calculated using (17).

The total uncertainty in the mean pierced length measurements was determined using (16) in conjunction with (19) to give

$$U_l = \sqrt{(U_{ub} \cdot \bar{b})^2 + (U_b \cdot u_b)^2} \,. \tag{21}$$

- **Uncertainty in Bubble Frequency Measurements**

The 95% confidence intervals shown on the figures presenting the bubble frequency measurements in Chapter 7 reflect the precision uncertainty in the bubble frequency measurements. The mean values shown in the figures are typically the average of 5 to 7 measurements. The precision uncertainty in f (P_f) was evaluated using Equation (14).

Appendix K – Thermistor Calibration Constants

Over a limited temperature range, the thermistor temperature-voltage calibration data can be fit in the form

$$T(e_o) = A \cdot e_o^3 + B \cdot e_o^2 + C \cdot e_o + D .$$

The calibration constants for each of the sixteen thermistors for temperatures between 5 and 45°C are given in Table 8.

Table 8: Thermistor Calibration Constants–5°C<T<45°C

Thermistor	A	B	C	D
1	15.5	25.8	31.1	18.2
2	0.279	1.09	6.22	17.2
3	0.261	1.16	6.26	18.1
4	0.569	0.316	6.06	11.9
5	0.466	0.787	5.95	14.2
6	0.311	1.13	6.21	17.3
7	0.328	1.02	5.95	15.5
8	0.426	0.906	5.94	14.2
9	0.306	1.08	6.18	15.8
10	0.351	1.09	6.34	16.5
11	0.505	0.525	5.86	13.1
12	0.398	0.990	6.04	15.3
13	0.389	0.866	5.83	15.0
14	0.31	1.05	5.97	16.6
15	0.523	0.798	5.82	13.5
16	1.97	1.98	12.6	13.5